Master thesis

Path Integral Monte Carlo Simulations of Correlated Bosons and Fermions in Traps

by

Tobias Dornheim

October 2014

Institut für Theoretische Physik und Astrophysik
der Christian-Albrechts-Universität zu Kiel

Erster Gutachter:	Prof. Dr. Michael Bonitz
Zweiter Gutachter:	Priv.-Doz. Dr. Kai Roßnagel

Abstract

The worm algorithm path integral Monte Carlo technique (WA-PIMC), which delivers quasi-exact ab initio results in thermodynamic equilibrium, is applied to the simulation of mutually repelling quantum particles in traps. The investigated aspects of bosons include superfluidity, i.e., the change of the moment of inertia due to quantum effects (NCRI), spatial correlations and the quantum breathing mode, which, despite being a dynamic quantity, can be estimated from equilibrium data with a sum-rule formalism and the reconstruction of the spectrum from an imaginary time correlation function. Finally, the PIMC simulation of fermions is discussed and the notorious fermion sign problem compared to a conceptually different approach, namely CPIMC.

Kurzfassung

Die Wurm-Algorithmus Pfadintegral Monte Carlo Methode (WA-PIMC), welche die Berechnung quasi exakter ab-initio Ergebnisse im thermodynamischen Gleichgewicht erlaubt, wird verwendet, um repulsiv wechselwirkende Quantenteilchen in Fallen zu simulieren. Die untersuchten Eigenschaften von Bosonen beinhalten Superfluidität, genauer die Änderung des Trägheitsmoments durch Quanteneffekte, räumliche Korrelationen und die Quanten-Breathing-mode, welche, obwohl es sich um eine dynamische Größe handelt, aus Gleichgewichtsdaten sowohl mit einem Summenregelformalismus als auch durch die Rekonstruktion eines Spektrums aus einer imaginärzeitigen Korrelationsfunktion betrachtet werden kann. Schließlich werden PIMC Simulationen von Fermionen diskutiert und das berüchtigte fermionische Vorzeichenproblem wird mit dem konzeptuell verschiedenen CPIMC Zugang verglichen.

Contents

Anyone who attempts to generate random numbers by deterministic means is, of course, living in a state of sin.

– John von Neumann, 1951

1 Introduction

1.1 Motivation

Monte **C**arlo (MC) simulations, i.e., the application of random numbers for numerical calculations, are widespread among various fields, including sociology and economics, e.g. [1][1], biology and medicine, e.g. [2], and quantum physics and chemistry, e.g. [3]. The latter category comprises ground state methods such as Variational and Diffusion MC [4] and approaches for finite temperature like the widely used **P**ath **I**ntegral **M**onte **C**arlo (PIMC) technique, for a review see [5]. PIMC is based on the Metropolis algorithm [6] and allows for the ab initio calculation of quasi-exact ensemble averages of quantum particles at, in principle, arbitrary coupling strength and temperature and is arguably the most successful tool for the investigation of strongly correlated Bose and Boltzmannon (i.e., particles without exchange) systems. However, the application of Quantum Monte Carlo methods to Fermi systems is a notoriously difficult task due to the well known fermion sign problem, see e.g. [7], which might render even small systems unfeasible.

In this work, the **W**orm **A**lgorithm (WA) path integral Monte Carlo technique [8], which is a particularly advantageous realization of PIMC, is implemented for the numerical treatment of correlated bosons and fermions in harmonic traps. Spatially confined quantum systems are a contemporary research field and exhibit many interesting features like Bose Einstein condensation, e.g. [9], and collective oscillations, e.g. [10]. However, many questions remain unsufficiently addressed and it is the goal of this thesis to provide an overview about different research aspects of trapped quantum particles. New results include the investigation of superfluidity in $2D$ and $3D$ systems, the characterization of spatial correlations via the consideration of a novel center-two particle correlation function [11], which has been successfully applied to classical systems, and the computation of the quantum breathing mode for Bose systems from equilibrium expectation values using an improved sum-rule approach [12]. In addition, the possibility to reconstruct the spectral function from an imaginary time correlation function, which is a well known approach to other non-equilibrium quantities like the dynamic structure factor and the single particle spectrum [13], is investigated. Special attention is paid to fermions and the aforementioned sign problem from PIMC is compared to a conceptually different approach, namely CPIMC [14].

Experimental realizations include ultracold gases in traps [15, 16], electrons in quantum dots [17] and electron-hole bilayers, e.g. [18] and references therein. In addition, charged bosons are predicted to exist within the core of neutron stars, where both protons and neutrons form Cooper pairs (BCS-BEC crossover) [19, 20] and the core of helium white dwarfs [21, 22].

[1] The blue numbers indicate hyperlinks to references, equations, figures and footnotes.

1.2 Outline

- **1: Introduction**

- **2: Path integral Monte Carlo**
  All theoretical aspects of PIMC are described in detail, starting with a brief introduction of ensemble averages and the connection to imaginary time path integrals. The Metropolis algorithm allows for the generation of random configurations according to a distribution with an unknown normalization and provides the basis for all updates of the Worm Algorithm, which are elaborately derived. The chapter finishes with the discussion of the calculation of observables and the corresponding error analysis, including the binning analysis for the treatment of autocorrelation effects.

- **3: Implementation of PIMC**
  Several practical aspects concerning the implementation of PIMC in C++ are discussed and the validity of the developed code is checked by comparisons to analytical results and another code. Afterwards, the usual WA-PIMC method is extended with some improvements and special attention paid to the inhomogeneity of trapped quantum particles. Finally, a brief summary of the capabilities of the presented PIMC implementation is given.

- **4: General properties of confined bosons**
  The chapter starts with a short discussion of three different phases of mutually repelling bosons, namely solid, fluid and superfluid behaviour. The latter topic is elaborated with the investigation of superfluidity in $3D$ and $2D$ Coulomb-systems and the influence of the additional dimension on the former is analyzed. In addition, a local superfluid density estimator provides insight into the inhomogeneity of the superfluid phase transition. Finally, spatial correlations are discussed and a novel center two-particle correlation function [11] is applied to quantum systems.

- **5: The quantum breathing mode**
  The quantum breathing mode, i.e., the system's response to a monopole perturbation, serves as an example for the calculation of dynamic properties from PIMC data. A compact revision of the linear response formalism is followed by the introduction of the sum-rules which allow for the expression of an upper bound to the frequency of interest solely in terms of equilibrium expectation values. The chapter finishes with a discussion of the reconstruction of spectral functions from imaginary time correlation functions.

- **6: Simulation of fermions**
  The ab initio simulation of fermions is a particularly challenging topic since quantum Monte Carlo methods suffer from the notorious fermion sign problem. The brief presentation of results for Coulomb- and dipole-interacting fermions and comparisons to bosonic properties is followed by the comparison of PIMC to other methods. Special attention is paid to a recently developed **C**onfiguration **P**ath **I**ntegral **M**onte **C**arlo (CPIMC) technique [14] and the sign problem is investigated with both PIMC and CPIMC.

- **7: Conclusion**

2 Path integral Monte Carlo

In this section, all theoretical aspects of the **P**ath **I**ntegral **M**onte **C**arlo method are covered in detail, starting with a problem statement (2.1) and a short introduction to the imaginary time path integral picture. After a brief discussion of particle exchange (2.2), the Metropolis algorithm, which allows for the generation of random configurations according to a distribution with an unknown normalization, is explained in detail (2.3). The latter provides the basis of the worm algorithm (2.4), which is used to efficiently generate configurations of particles in the canonical, grandcanonical and an even more extended ensemble. Finally, a short introduction to the calculation of physical observables (2.5) is complemented by the explanation of the error analysis of Monte Carlo data (2.6), including autocorrelation effects.

2.1 The path integral picture

In the following subsection, some principles of statistical physics and the connection between expectation values and imaginary time path integrals are introduced based on the textbooks by Nolting [23] and Bonitz and Semkat [24].

The system of interest is given by N particles in a volume V at temperature T, where all three quantities are fixed, hence, a canonical ensemble. The particles are assumed to be distinguishable, and the otherwise needed (anti-)symmetrization with respect to particle exchange will be introduced later. Of fundamental interest are the expectation values of (arbitrary) observables $\hat{A}$ in thermodynamic equilibrium, which are given by

$$\langle \hat{A} \rangle = \frac{1}{Z} \mathrm{Tr}\left(\hat{\rho}\hat{A}\right) \quad ,$$

with the partition function

$$Z = \mathrm{Tr}\left(\hat{\rho}\right) \quad , \tag{1}$$

the density operator

$$\hat{\rho} = e^{-\beta \hat{H}} \quad , \tag{2}$$

and the inverse temperature $\beta = 1/k_\mathrm{B}T$. The trace in Eq. (1) is defined as the sum (or integral in the continuum case) over the diagonal elements of $\hat{\rho}$, i.e.,

$$Z = \sum_k \langle k| \hat{\rho} |k\rangle = \int \mathrm{d}\mathbf{R} \ \langle \mathbf{R}| \hat{\rho} |\mathbf{R}\rangle = \int \mathrm{d}\mathbf{R} \ \rho(\mathbf{R}, \mathbf{R}, \beta) \quad . \tag{3}$$

The first equality assumes a discrete set of basis functions $|k\rangle$ while the second one applies to the continuous spatial representation, where the variable $\mathbf{R}$ includes the coordinates of all N particles: $\mathbf{R} = (\mathbf{r}_1, \ldots, \mathbf{r}_N)^T$. The definition of the density operator's matrix elements $\rho(\mathbf{R}_1, \mathbf{R}_2, \beta)$ directly follows from the third equality. The Hamiltonian $\hat{H}$ can be expressed as the sum of the kinetic and potential energy contributions, respectively:

$$\hat{H} = \hat{T} + \hat{V} \quad .$$

The main obstacle is the fact that the density operator from Eq. (2) cannot be factorized since $\hat{T}$ and $\hat{V}$ do not commute:

$$\hat{\rho} = e^{-\beta(\hat{T}+\hat{V})} = e^{-\beta\hat{T}} e^{-\beta\hat{V}} e^{-\beta\hat{C}} \quad .$$

The operator $\hat{C}$ can be deduced from the Baker-Campbell-Hausdorff formula [25] as the infinite series

$$\hat{C} = \frac{\beta}{2}[\hat{V},\hat{T}] - \beta^2\left(\frac{1}{6}[\hat{V},[\hat{V},\hat{T}]] - \frac{1}{3}[[\hat{V},\hat{T}],\hat{T}]\right) + \dots \quad . \tag{4}$$

It directly follows from Eq. (4) that the primitive approximation,

$$\hat{\rho} \approx e^{-\beta\hat{T}}e^{-\beta\hat{V}} \quad , \tag{5}$$

becomes more inaccurate for decreasing temperature T, i.e., in the regime where quantum mechanical effects are no longer negligible.

A widely used solution to this problem has been proposed by Feynman and makes use of the group property of the density operator [26]:

$$\hat{\rho} = e^{-\beta\hat{H}} = \prod_{i=0}^{P-1} e^{-\epsilon\hat{H}} \quad ,$$

with the definition $\epsilon = \beta/P$. Inserting this identity into the spatial representation of the partition function Z from Eq. (3) yields

$$Z = \int \mathrm{d}\mathbf{R}\ \langle\mathbf{R}|\prod_{i=0}^{P-1} e^{-\epsilon\hat{H}}|\mathbf{R}\rangle \tag{6}$$

$$= \int \mathrm{d}\mathbf{R}\mathrm{d}\mathbf{R}_1\dots\mathrm{d}\mathbf{R}_{P-1}\,\langle\mathbf{R}|e^{-\epsilon\hat{H}}|\mathbf{R}_1\rangle\langle\mathbf{R}_1|e^{-\epsilon\hat{H}}|\mathbf{R}_2\rangle\dots\langle\mathbf{R}_{P-1}|e^{-\epsilon\hat{H}}|\mathbf{R}\rangle \quad , \tag{7}$$

where, for the second equality, $P-1$ unities of the form

$$\hat{1} = \int \mathrm{d}\mathbf{R}_i\ |\mathbf{R}_i\rangle\langle\mathbf{R}_i| \tag{8}$$

have been inserted between the factors in Eq. (6). This means that the partition function, which was originally given as the trace over low T matrix elements of $\hat{\rho}$, can instead be expressed as the trace over the product of P matrix elements $\rho(\mathbf{R}_1,\mathbf{R}_2,\epsilon)$ at P times the temperature:

$$Z = \int \prod_{i=0}^{P-1} \mathrm{d}\mathbf{R}_i\ \rho(\mathbf{R}_i,\mathbf{R}_{i+1},\epsilon) \quad , \tag{9}$$

with $\mathbf{R}_P = \mathbf{R}_0$. It is important to note that the matrix elements in Eq. (9), which is still exact, are yet unknown. The desired improvement compared to Eq. (3) is that the high T elements, $\rho(\mathbf{R}_1,\mathbf{R}_2,\epsilon)$, can be reasonably approximated by analytical expressions, justified by the Trotter formula [27]:

$$e^{-(\hat{A}+\hat{B})} = \lim_{P\to\infty}\left(e^{-\frac{\hat{A}}{P}}e^{-\frac{\hat{B}}{P}}\right)^P \quad . \tag{10}$$

Eq. (10) implies that the primitive approximation from Eq. (5) becomes exact for the limit of infinitely many factors or, in other words, that the resulting error can be made arbitrarily small. The following subsection 2.1.1 elaborates the connection to the path integral picture in the imaginary time.

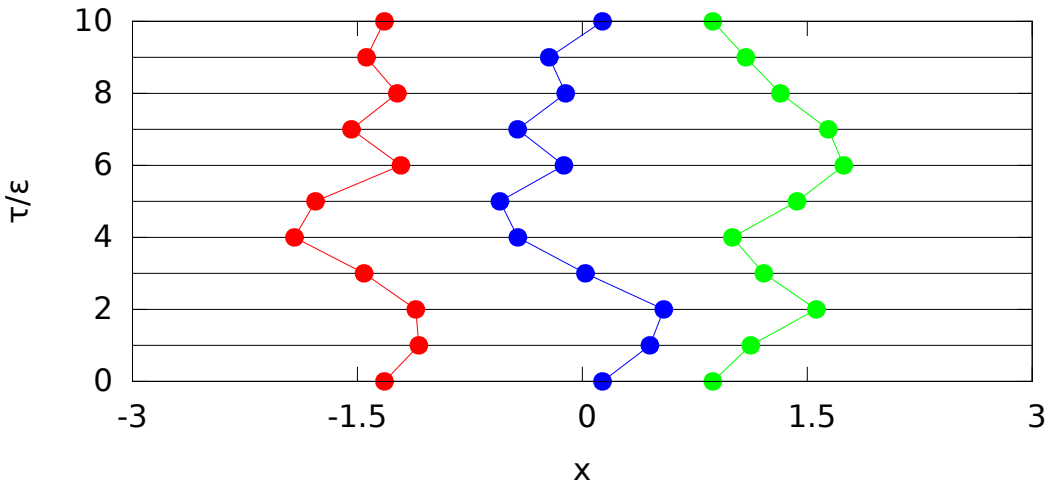

Figure 1: ***Illustration of the path integral picture:*** The imaginary time τ in units of discretization steps ϵ is plotted over the spatial coordinate x. The red, blue and green curve correspond to the paths of three different particles.

2.1.1 Imaginary time path integrals

In thermodynamic equilibrium, where the Hamiltonian is, by definition, time-independent, the time evolution operator is given by

$$\hat{U}(t_2, t_1) = \exp\left(-\frac{i}{\hbar}\hat{H}(t_2 - t_1)\right) \quad ,$$

which only depends on the time difference $t = t_2 - t_1$:

$$\hat{U}(t) = \exp\left(-\frac{i}{\hbar}\hat{H}t\right) \quad .$$

The definition $\tau := -i\hbar\beta$ yields that the calculation of ensemble averages using the canonical density operator $\hat{\rho}$ is equivalent to a propagation in the imaginary time τ:

$$\hat{U}(\tau) = \exp\left(-\frac{i}{\hbar}\hat{H}\tau\right) = \exp\left(-\frac{i}{\hbar}\hat{H}(-i\hbar\beta)\right) = \exp\left(-\beta\hat{H}\right) \quad .$$

Therefore, the expression for the partition function Z from Eq. (9) corresponds to the integral over all closed paths in the imaginary time from $\tau = 0$ to $\tau = -i\hbar\beta$, and each factor $e^{-\epsilon\hat{H}}$ to the propagator of one discretized (imaginary-) time step. For convenience, in the following the modified imaginary time $\tau \to \tau/(-i\hbar)$ will be used. This means that the paths simply range from $\tau = 0$ to $\tau = \beta$. The imaginary time path integral picture of the ensemble averaging is illustrated in Fig. 1, where the imaginary time τ is plotted in units of the discretization steps ϵ over some spatial coordinate[2] x. The red, blue and green curve symbolize the paths of three different particles. The number of factors is chosen as $P = 10$, which means that ten time slices appear in the path integral visualization and the particle coordinates for $\tau = 0$ and $\tau = 10\epsilon = \beta$ are equal. Hence, the paths are closed or, equivalently, periodic in imaginary time. The integration

[2]The definition of the system of units is given in section 3.1.

over the $\mathbf{R}_i$ in Eq. (9) yields that all possible configurations $\{\mathbf{X}\} = \{\mathbf{R}_0, \mathbf{R}_1, \ldots, \mathbf{R}_{P-1}\}$ on all P time slices are included in Z, according to their corresponding weight $W(\mathbf{X})$. The generation of such configurations with a probability distribution with an unknown normalization (i.e., Z itself) can be achieved with the Metropolis algorithm [6], which will be explained in section 2.3. However, first one needs to derive an appropriate analytical expression for the matrix element $\rho(\mathbf{R}_1, \mathbf{R}_2, \epsilon)$. This will be the topic of the following subsection.

2.1.2 The primitive approximation

The high temperature matrix element in the primitive approximation is given by

$$\rho(\mathbf{R}_1, \mathbf{R}_2, \epsilon) = \langle \mathbf{R}_1 | \, e^{-\epsilon \hat{T}} e^{-\epsilon \hat{V}} \, | \mathbf{R}_2 \rangle \qquad . \tag{11}$$

However, this expression is still not useful to sample correctly distributed configurations $\{\mathbf{X}\}$. The first step towards an analytical expression is the insertion of the unity operator from Eq. (8) into (11):

$$\rho(\mathbf{R}_1, \mathbf{R}_2, \epsilon) = \int \mathrm{d}\tilde{\mathbf{R}} \, \langle \mathbf{R}_1 | \, e^{-\epsilon \hat{T}} \, | \tilde{\mathbf{R}} \rangle \, \langle \tilde{\mathbf{R}} | \, e^{-\epsilon \hat{V}} \, | \mathbf{R}_2 \rangle \qquad , \tag{12}$$

which is nothing else than the integration over the kinetic and potential matrix element:

$$\rho(\mathbf{R}_1, \mathbf{R}_2, \epsilon) = \int \mathrm{d}\tilde{\mathbf{R}} \; \rho_{\mathrm{kin}}(\mathbf{R}_1, \tilde{\mathbf{R}}, \epsilon) \rho_{\mathrm{pot}}(\tilde{\mathbf{R}}, \mathbf{R}_2, \epsilon) \qquad . \tag{13}$$

The first term corresponds to the free particle density matrix (i.e., $\hat{V} = 0$), which is known as [28]

$$\rho_{\mathrm{kin}}(\mathbf{R}_1, \mathbf{R}_2, \epsilon) = \left(\frac{m}{2\pi\epsilon\hbar^2} \right)^{Nd/2} \exp\left(-\frac{m}{2\epsilon\hbar^2} \left(\mathbf{R}_1 - \mathbf{R}_2 \right)^2 \right) \qquad , \tag{14}$$

with d being the dimensionality of the system. The prefactor in Eq. (14) can be identified with the thermal de Broglie wavelength [29] at the inverse temperature ϵ which is a measure for the quantum mechanical extension of a particle and given by

$$\lambda_\epsilon = \frac{2\pi\hbar}{\sqrt{2\pi m k_{\mathrm{B}} T_\epsilon}} \qquad . \tag{15}$$

The expression (15) implies that a particle's extension increases with decreasing temperature T as it is expected. Inserting λ_ϵ into the free particle density matrix gives

$$\rho_{\mathrm{kin}}(\mathbf{R}_1, \mathbf{R}_2, \epsilon) = \frac{1}{\lambda_\epsilon^{Nd}} \exp\left(-\frac{\pi}{\lambda_\epsilon^2} \left(\mathbf{R}_1 - \mathbf{R}_2 \right)^2 \right) \qquad . \tag{16}$$

The reconsideration of the definition of $\mathbf{R}_i$ as the coordinate vector of all N particles finally gives

$$\rho_{\mathrm{kin}}(\mathbf{R}_1, \mathbf{R}_2, \epsilon) = \frac{1}{\lambda_\epsilon^{Nd}} \exp\left(-\frac{\pi}{\lambda_\epsilon^2} \sum_{k=1}^{N} \left(\mathbf{r}_{k,1} - \mathbf{r}_{k,2} \right)^2 \right) \qquad , \tag{17}$$

which is the product of N single particle kinetic density matrices:

$$\rho_{\mathrm{kin}}(\mathbf{R}_1, \mathbf{R}_2, \epsilon) = \prod_{k=1}^{N} \rho_{\mathrm{kin}}(\mathbf{r}_{k,1}, \mathbf{r}_{k,2}, \epsilon) \qquad . \tag{18}$$

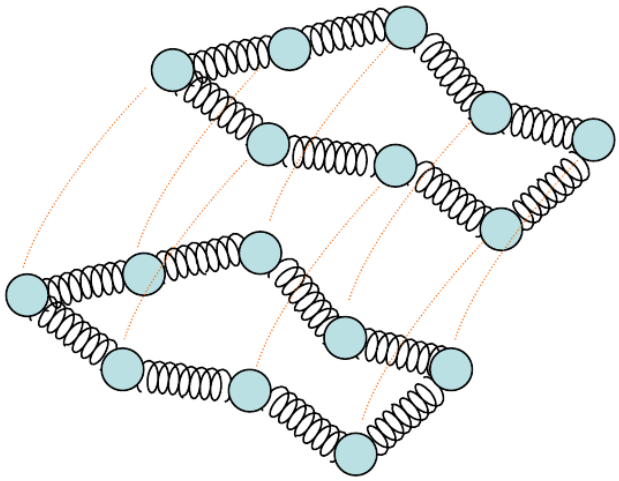

Figure 2: ***Illustration of the classical isomorphism:*** Two particles are expressed in the path integral picture on $P = 8$ imaginary time slices, symbolized by the turquoise circles. The springs correspond to the kinetic and the orange connections to the potential matrix elements. The figure has been obtained from Sakkos et al. [32].

The potential matrix element, i.e., the second term in Eq. (13), is given by

$$\rho_{\mathrm{pot}}(\mathbf{R}_1, \mathbf{R}_2, \epsilon) = \langle \mathbf{R}_1 | \, e^{-\epsilon \hat{V}} \, | \mathbf{R}_2 \rangle \qquad . \tag{19}$$

The potential energy operator $\hat{V}$ is assumed to be diagonal in coordinate representation, which makes Eq. (19) to

$$\rho_{\mathrm{pot}}(\mathbf{R}_1, \mathbf{R}_2, \epsilon) = \delta(\mathbf{R}_1 - \mathbf{R}_2) \, \langle \mathbf{R}_1 | \, e^{-\epsilon \hat{V}} \, | \mathbf{R}_2 \rangle \qquad , \tag{20}$$

with the Dirac distribution $\delta(\mathbf{R}_1 - \mathbf{R}_2)$, see e.g. [30]. Inserting this expression into Eq. (13) yields

$$\begin{aligned} \rho(\mathbf{R}_1, \mathbf{R}_2, \epsilon) &= \int \mathrm{d}\tilde{\mathbf{R}} \; \rho_{\mathrm{kin}}(\mathbf{R_1}, \tilde{\mathbf{R}}, \epsilon) \delta(\tilde{\mathbf{R}} - \mathbf{R}_2) \rho_{\mathrm{pot}}(\tilde{\mathbf{R}}, \mathbf{R}_2, \epsilon) \\ &= \rho_{\mathrm{kin}}(\mathbf{R}_1, \mathbf{R}_2, \epsilon) \rho_{\mathrm{pot}}(\mathbf{R}_2, \mathbf{R}_2, \epsilon) \qquad . \end{aligned}$$

The resulting diagonal potential matrix element corresponds to the evaluation of the potential energy on a single time slice:

$$\rho_{\mathrm{pot}}(\mathbf{R}_2, \mathbf{R}_2, \epsilon) = \exp\left(-\epsilon V(\mathbf{R}_2)\right) \qquad . \tag{21}$$

The final expression for the density matrix element $\rho(\mathbf{R}_1, \mathbf{R}_2, \epsilon)$ in the primitive approximation is often illustrated as an isomorphism to classical ringpolymers [31]. This is illustrated in Fig. 2, where a configuration of two particles in the path integral picture is shown for $P = 8$ imaginary time slices. The particle position for each τ is illustrated by turquoise circles which are denoted as beads. Beads of the same particle on adjacent time slices effectively interact via the gaussian from Eq. (17), as illustrated by the springs. The cheapest configuration corresponds to classical particles, which means that all beads are on the same position and the particles form a straight line in the τ-x-plane. Beads from different particles on the same time slice interact via the pair

interaction $V_{\text{int}}(\mathbf{r}_{1,k}, \mathbf{r}_{2,k})$. This is illustrated by the orangely dotted connections. Finally, it should be noted that these polymers are closed, which is due to the periodicity in imaginary time. Hence, particles in the path integral picture can be mapped onto a classical system of interacting ringpolymers.

The main result of this subsection is an analytical expression for the density matrix elements in the partition function from Eq. (9). The latter reads

$$Z = \int \mathrm{d}\mathbf{R}_0 \ldots \mathrm{d}\mathbf{R}_{P-1} \frac{1}{\lambda_\beta^{dN}} \prod_{i=0}^{P-1} \exp\left(-\frac{\pi}{\lambda_\epsilon^2} \sum_{k=1}^{N} \left(\mathbf{r}_{k,i} - \mathbf{r}_{k,i+1}\right)^2 - \epsilon V(\mathbf{R}_i) \right) \quad . \tag{22}$$

Eq. (22) is simply the integral over the weights $W(\mathbf{X})$

$$Z = \int \mathrm{d}\mathbf{X}\ W(\mathbf{X}) \quad , \tag{23}$$

with the meta variable $\mathbf{X} = \{\mathbf{R}_0, \ldots, \mathbf{R}_{P-1}\}$ containing the coordinates of all N particles on P time slices. It should be noted that $W(\mathbf{X}) \geq 0$ applies for all possible configurations $\mathbf{X}$, which makes them directly accessible to being sampled with the Monte Carlo Metropolis algorithm. The consideration of particle exchange, however, can destroy this desireable property. For completeness, it is reported that there exist higher order factorization schemes of the density operator which require less time slices for the same magnitude of the error [33]. Sakkos et al. [34] have implemented such an approach into their path integral Monte Carlo code and have been able to achieve an effective sixth order scaling by the empirical choice of some free parameters. However, this seemingly great advantage comes at a high price since the explicit evaluation of all forces and the introduction of ancilla time slices is needed. This significantly increases the computational effort of the higher order schemes and restricts them to very low temperatures, where their more favourable scaling compensates for the former.

2.2 Particle exchange in the path integral picture

In the preceding sections, all N particles have been assumed to be distinguishable, which means that particle exchange is strictly forbidden. For N indistinguishable particles, however, the wavefunction or, equivalently, all operators must be symmetric or antisymmetric under exchange for bosons and fermions, respectively. Thus, the partition function reads [28]

$$Z = \frac{1}{N!} \sum_{\{\pi\}} (\pm 1)^{\pi_l} \int \mathrm{d}\mathbf{R}_0, \ldots, \mathrm{d}\mathbf{R}_{P-1} \prod_{i=0}^{P-1} \rho(\mathbf{R}_i, \hat{\pi}\mathbf{R}_{i+1}, \epsilon) \quad , \tag{24}$$

with the exchange operator $\hat{\pi}$, the set of all possible permutations $\{\pi\}$ and the permutation length π_l, which is given by the number of pair permutations. The plus and minus sign in Eq. (24) refer to bosons and fermions, respectively. This means that, for fermionic particles, the weights from Eq. (23) can be both positive and negative which leads to the infamous fermion sign problem, see e.g. [7]. The latter makes the PIMC simulation of fermions much harder since positive and negative contributions might nearly cancel, which causes extremely large relative errors. Simulation results for fermions and a discussion of the sign problem can be found in section 6. For bosons, all weights in Eq. (24) remain positive which makes them perfectly accessible to the Metropolis algorithm.

The depiction of particle exchange in the path integral picture is illustrated in the figures 3 and 4. The left image of Fig. 3 shows a configuration of two particles with their paths plotted in

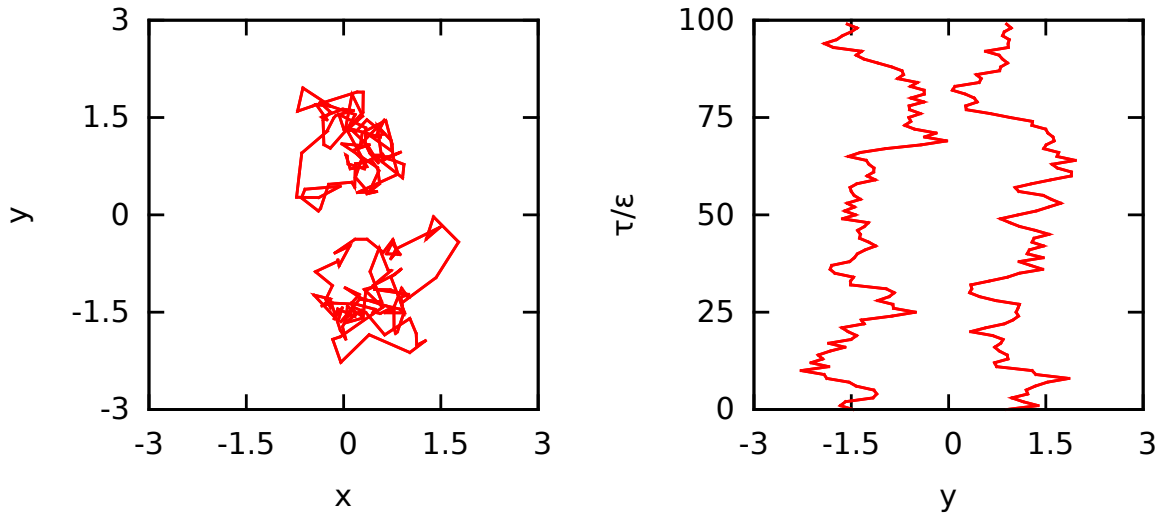

Figure 3: ***Two particles without exchange:*** In the left image, the paths of two particles are plotted in the x-y-plane. The right image shows the same configuration for the imaginary time τ in units of ϵ, plotted over y.

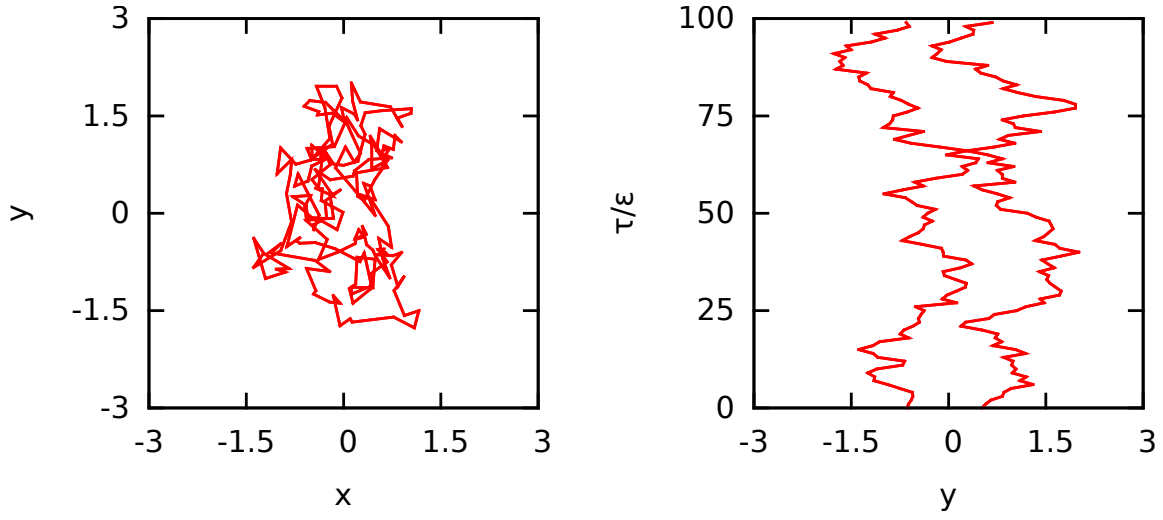

Figure 4: ***Two particles with exchange:*** In the left image, the paths of two particles which form an exchange cycle are plotted in the x-y-plane. The right image shows the same configuration for the imaginary time τ in units of ϵ, plotted over y.

the x-y-plane. The paths of the two particles are not connected with each other, which means that they do not form an exchange cycle. In the right image, the same configuration is shown and the imaginary time τ in units of ϵ is plotted over the spatial coordinate y. Again, the two paths are not connected. Fig. 4 shows the same plots as Fig. 3 with the only difference being that the two particles form an exchange cycle. This means that the paths of the two particles are connected with each other and, therefore, form a single trajectory. In the imaginary time plot, the exchange is nicely illustrated at $\tau \approx 65\epsilon$ where the two paths intersect each other.

Finally, it should be noted that, for highly degenerate systems, macroscopic trajectories involving a large number of particles can occur. These are directly connected to the esitmation of superfluidity in the path integral picture [35] and a more detailed discussion of superfluidity can be found in section 4.2.

2.3 Metropolis algorithm

The Metropolis algorithm [6] is the heart of the path integral Monte Carlo method and allows to sample configurations $\mathbf{X}$ according to a probability distribution $P(\mathbf{X})$ with an unknown normalization Z. This exactly corresponds to the problem statement of PIMC which is to sample all possible closed paths and exchange cycles in the imaginary time according to the density matrix $\rho(\mathbf{R}_1, \mathbf{R}_2, \beta)$, where the normalization is given by the (unknown) partition function:

$$\int \mathrm{d}\mathbf{R}\ \frac{\rho(\mathbf{R}, \mathbf{R}, \beta)}{Z} = 1 \qquad .$$

To achieve this goal, the detailed balance equation is imposed:

$$P(\mathbf{X} \to \tilde{\mathbf{X}}) = P(\tilde{\mathbf{X}} \to \mathbf{X}) \qquad . \tag{25}$$

Equation (25) states that the number of transitions P between every two configurations, $\mathbf{X}$ and $\tilde{\mathbf{X}}$, is the same in both directions. This certainly is an unnecessary rigorous restriction, but there exists a simple solution. For the generalized Metropolis algorithm, see e.g. [28], the quantity P is divided into three steps

$$P(\mathbf{X} \to \tilde{\mathbf{X}}) = W(\mathbf{X}) T(\mathbf{X} \to \tilde{\mathbf{X}}) A(\mathbf{X} \to \tilde{\mathbf{X}}) \qquad , \tag{26}$$

where $W(\mathbf{X})$ denotes the probability to occupy a particular state $\mathbf{X}$, $T(\mathbf{X} \to \tilde{\mathbf{X}})$ the transition probability, i.e., the probability to generate the configuration $\tilde{\mathbf{X}}$ starting from $\mathbf{X}$, and $A(\mathbf{X} \to \tilde{\mathbf{X}})$ the probability to accept the proposed new configuration $\tilde{\mathbf{X}}$. Inserting Eq. (26) into (25) yields the generalized detailed balance equation

$$W(\mathbf{X}) T(\mathbf{X} \to \tilde{\mathbf{X}}) A(\mathbf{X} \to \tilde{\mathbf{X}}) = W(\tilde{\mathbf{X}}) T(\tilde{\mathbf{X}} \to \mathbf{X}) A(\tilde{\mathbf{X}} \to \mathbf{X}) \qquad , \tag{27}$$

which is the starting point for the derivation of all updates of the PIMC worm algorithm [8], as described in detail in section 2.4. The famous solution by Metropolis et al. [6] to Eq. (27) for the acceptance probability of a proposed update is given by

$$A(\mathbf{X} \to \tilde{\mathbf{X}}) = \min\left(1, \frac{W(\tilde{\mathbf{X}}) T(\tilde{\mathbf{X}} \to \mathbf{X})}{W(\mathbf{X}) T(\mathbf{X} \to \tilde{\mathbf{X}})}\right) \qquad , \tag{28}$$

which can be easily verified by inserting the expression for $A(\mathbf{X} \to \tilde{\mathbf{X}})$ into the generalized detailed balance equation and considering the two cases $W(\tilde{X}) T(\tilde{\mathbf{X}} \to \mathbf{X}) > W(\mathbf{X}) T(\mathbf{X} \to \tilde{\mathbf{X}})$ and vice versa. Since the normalization Z is the same for both $W(\mathbf{X})$ and $W(\tilde{\mathbf{X}})$, it cancels in Eq. (28) and, thus, is not needed.

A practical implementation of the Metropolis algorithm can be formulated as follows:

1. Start with an (arbitrary) initial configuration $\mathbf{X}_0$.
2. Generate a new configuration $\tilde{\mathbf{X}}$ according to $T(\mathbf{X}_i \to \tilde{\mathbf{X}})$.
3. Calculate the acceptance probability $A(\mathbf{X}_i \to \tilde{\mathbf{X}})$ using Eq. (28). Draw a random number $\alpha \in [0, 1)$. If $\alpha \leq A(\mathbf{X}_i \to \tilde{\mathbf{X}})$, then the configuration is updated to $\mathbf{X}_{i+1} = \tilde{\mathbf{X}}$, otherwise the update is rejected, and the new configuration is equal to the old one: $\mathbf{X}_{i+1} = \mathbf{X}_i$.
4. Repeat steps 2 and 3 until you have generated the desired number of configurations.

Given an ergodic set of updates $\{c_i(\mathbf{X} \to \tilde{\mathbf{X}})\}$, the algorithm will generate a Markov chain of configurations $\{\mathbf{X}\}$ which are distributed according to $W(\mathbf{X})$. Ergodicity means that (i) the probability to go from $\mathbf{X}$ to $\tilde{\mathbf{X}}$ may only depend on $\mathbf{X}$ itself and (ii) all configurations must be reachable in a finite number of updates. A segment of such a Markov chain may look like

$$\mathbf{X}_0 = \mathbf{A} \to \mathbf{X}_1 = \mathbf{B} \to \mathbf{X}_2 = \mathbf{B} \to \mathbf{X}_3 = \mathbf{B} \to \mathbf{X}_4 = \mathbf{C} \to \dots \quad .$$

After starting with the initial configuration $\mathbf{X}_0 = \mathbf{A}$, a new one $\mathbf{B}$ is sampled and the update is accepted. However, the next two updates are rejected and, hence, $\mathbf{X}_1 = \mathbf{X}_2 = \mathbf{X}_3$ because the configuration is not changed. The fourth update is accepted again, and the configuration is changed to $\mathbf{X}_4 = \mathbf{C}$. It is very important to understand that, although for a rejected update $\mathbf{X} \to \tilde{\mathbf{X}}$ the configuration is not changed, $\mathbf{X}$ is still counted as a member of the Markov chain. Including only configurations after successful updates will result in completely wrong results.

2.4 Worm algorithm

The **W**orm **A**lgorithm (WA) by Boninsegni et al. [8] is a very advantageous realization of the Metropolis algorithm applied to the problem of generating correctly distributed paths in the imaginary time. However, instead of operating in the canonical ensemble like usual PIMC implementations, see e.g. [5] and [36], it works in an extended configuration space, allowing the particle number N to fluctuate and even the possibility of one open trajectory, the so called worm. The change of N corresponds to the grand canonical ensemble, where, instead of the particle number, the chemical potential μ serves as the third fixed input parameter. The grand canonical partition function $Z_{\mathrm{GC}}(\mu, V, T)$ is related to its canonical counterpart $Z_{\mathrm{C}}(N, V, T)$ by [23]

$$Z_{\mathrm{GC}}(\mu, V, T) = \sum_{N=1}^{\infty} \exp\left(\beta\mu N\right) Z_{\mathrm{C}}(N, V, T) \quad .$$

Hence, the worm algorithm allows for the calculation of additional quantities like the compressibility κ, which is linked to the particle number fluctuation [37], and, in addition, also of the **M**atsubara **G**reen **f**unction (MGF) $G(\mathbf{r_1}, \mathbf{r_2}, \tau)$ as explained below.

Nevertheless, the main benefits of the WA are the prevention of critical slowing down phenomena that occur near phase transitions and can cause extremely large autocorrelation times (see section 2.6) and, therefore, large statistical errors [38] and the significantly enhanced performance of the sampling of particle exchange. The idea of the extended configuration space is illustrated in Fig. 5. The left picture shows an open path in the x-y-plane and the symbols $\Psi^\dagger$ and Ψ correspond to the creation and annihilation field operator, respectively, which are defined as

$$\Psi^\dagger(\mathbf{r}, \tau) = \sum_j \hat{a}_j^\dagger(\tau)\phi_j^*(\mathbf{r}) \qquad \text{and} \qquad \Psi(\mathbf{r}, \tau) = \sum_j \hat{a}_j(\tau)\phi_j(\mathbf{r}) \quad .$$

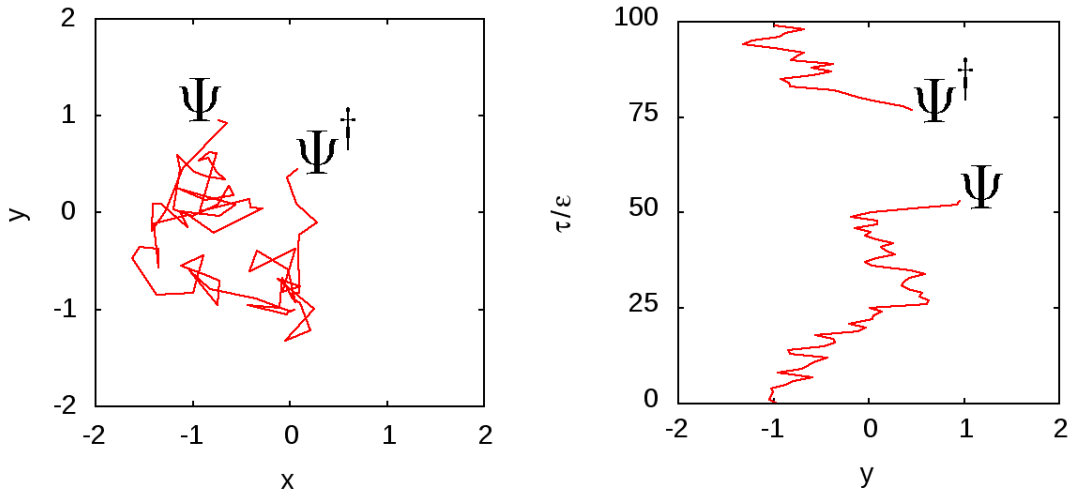

Figure 5: ***Illustration of the worm trajectories:*** In the left picture, an open trajectory of a single particle is plotted in the x-y-plane. The symbols $\Psi^\dagger$ and Ψ correspond to the creation and annihilation field operator, respectively. The right picture shows the same configuration for the imaginary time τ in units of ϵ plotted over y.

Here, $\hat{a}_j^\dagger$ and $\hat{a}_j$ denote the usual creation and annihilation operator from second quantization, see e.g. [39], corresponding to an orbital $|j\rangle$ and it hold $\phi_j^*(\mathbf{r}) = \langle j|\mathbf{r}\rangle$ and $\phi_j(\mathbf{r}) = \langle \mathbf{r}|j\rangle$. Therefore, the field operators create or destroy a particle at the position $\mathbf{r}$ and time slice τ. The right picture from Fig. 5 shows the same configuration in the τ-y-plane and yields the following interpretation: At $\tau = 77\epsilon$, a particle is created by $\Psi^\dagger$ and propagates in the imaginary time until $\tau = 53\epsilon$, where it is annihilated by Ψ. The former time slice is often denoted as the worm's tail, or Masha, and the latter as its head, or Ira. The sampling of such open path trajectories is directly connected to the Matsubara Green function,

$$G(\mathbf{r}_1, \mathbf{r}_2, \tau) = \langle \hat{T}\Psi(\mathbf{r}_2, \tau)\Psi^\dagger(\mathbf{r}_1, 0)\rangle \quad , \tag{29}$$

where $\hat{T}$ denotes the usual time ordering operator. In thermodynamic equilibrium, Eq. (29) only depends on the time difference between the application of $\Psi^\dagger$ and Ψ, and, for the computation of the average, all configurations with one open path are taken into account. For completeness, it is mentioned that the MGF is connected to a system's single particle excitation spectrum by a Laplace transform, which means that dynamical information can be reconstructed from equilibrium expectation values, as explained e.g. in [13].

The extension of the configuration space makes it necessary to consider a generalized partition function

$$Z_{\mathrm{tot}}(\mu, V, T) = Z_{\mathrm{GC}}(\mu, V, T) + \tilde{Z}(\mu, V, T) \quad ,$$

given by the sum of the closed path (i.e., grand canonical) and open path normalization. The latter might be expressed as

$$\tilde{Z} = C Z_{\mathrm{GC}}(\mu, V, T) \sum_{\tau_{\Psi^\dagger}} \sum_{\tau_\Psi} \int \mathrm{d}\mathbf{r}_{\Psi^\dagger} \mathrm{d}\mathbf{r}_\Psi \; G(\mathbf{r}_\Psi, \mathbf{r}_{\Psi^\dagger}, \tau_\Psi - \tau_{\Psi^\dagger}) \quad . \tag{30}$$

Here, C is an, in principle, arbitrary constant that determines the ratio of diagonal (closed path) and off-diagonal (open path) configurations and can be used to enhance the performance of the algorithm.

The next step is to find a suitable update scheme for the Metropolis algorithm to generate all possible configurations of the extended ensemble. In section 2.4.1, an efficient path sampling technique which is the main ingredient for most updates of the WA is introduced. Afterwards, all used updates are derived in section 2.4.2 from the detailed balance equation. Finally, it is shown in section 2.5.1 how canonical data can be extracted from simulations in the extended ensemble.

2.4.1 Path sampling schemes

Consider an open path configuration as pictured in Fig. 5. In order to switch between the off-diagonal and diagonal sector, it is necessary to sample a connecting path between the time slices τ_Ψ and $\tau_{\Psi^\dagger}$. For simplicity, it is assumed that new path segments are sampled beginning from the worm's head, i.e., forward in the imaginary time, although one is, in principle, free to move the tail as well. The trivial approach is to generate one new bead at a time at a random position inside some volume V. The inverse move from the new configuration $\tilde{\mathbf{X}}$ back to $\mathbf{X}$ will be the removal of that particular bead. This gives the transition probabilities

$$T(\mathbf{X} \to \tilde{\mathbf{X}}) = \frac{1}{V} \qquad \text{and} \qquad T(\tilde{\mathbf{X}} \to \mathbf{X}) = 1 \qquad ,$$

since there is no free parameter for the annihilation of the last bead. The ratio of the configuration weights can only be affected on the particular time slice because the rest of the configuration remains unchanged:

$$\frac{W(\tilde{\mathbf{X}})}{W(\mathbf{X})} = e^{\epsilon\mu} e^{\epsilon \Delta V(\mathbf{X}\to\tilde{\mathbf{X}})} \rho_{\text{kin}}(\mathbf{r}_{k,i}, \mathbf{r}_{k,i+1}, \epsilon) \qquad , \tag{31}$$

where $\mathbf{r}_{k,i}$ and $\mathbf{r}_{k,i+1}$ denote the old and new position of the head, respectively, and $\Delta V(\mathbf{X} \to \tilde{\mathbf{X}})$ the change in the potential energy. The acceptance ratio for this simple advance update directly follows from Eq. (28) as

$$A(\mathbf{X} \to \tilde{\mathbf{X}}) = \min\left(1, e^{\epsilon\mu} e^{\epsilon \Delta V(\mathbf{X}\to\tilde{\mathbf{X}})} \rho_{\text{kin}}(\mathbf{r}_{k,i}, \mathbf{r}_{k,i+1}, \epsilon) V\right) \qquad . \tag{32}$$

However, the mean acceptance probability will be very low since the gaussian from $\rho_{\text{kin}}(...)$ will quickly approach zero for large distances between $\mathbf{r}_{k,i}$ and $\mathbf{r}_{k,i+1}$. Therefore, it is much better to make use of the free choice of $T(\mathbf{X} \to \tilde{\mathbf{X}})$ and try to eliminate as much of the ratio (31) as possible to achieve acceptance probabilities A close to unity for both the update and the inverse move. This idea is called importance sampling. A simple enhancement of Eq. (32) is to sample the new position from the kinetic density matrix itself, i.e., gaussian distributed around the old position:

$$T(\mathbf{X} \to \tilde{\mathbf{X}}) = \rho_{\text{kin}}(\mathbf{r}_{k,i}, \mathbf{r}_{k,i+1}, \epsilon) \qquad .$$

This gives an acceptance probability of

$$A(\mathbf{X} \to \tilde{\mathbf{X}}) = \min\left(1, e^{\epsilon\mu} e^{\epsilon \Delta V(\mathbf{X}\to\tilde{\mathbf{X}})}\right) \qquad . \tag{33}$$

The remaining factor due to the change in $V(\mathbf{X})$ cannot be removed in general because the required normalization is not known in advance. The next obstacle to be considered is the inefficiency of single slice moves in large systems. This means that adjacent configurations in the generated Markov chain will be very correlated with each other since they are nearly the

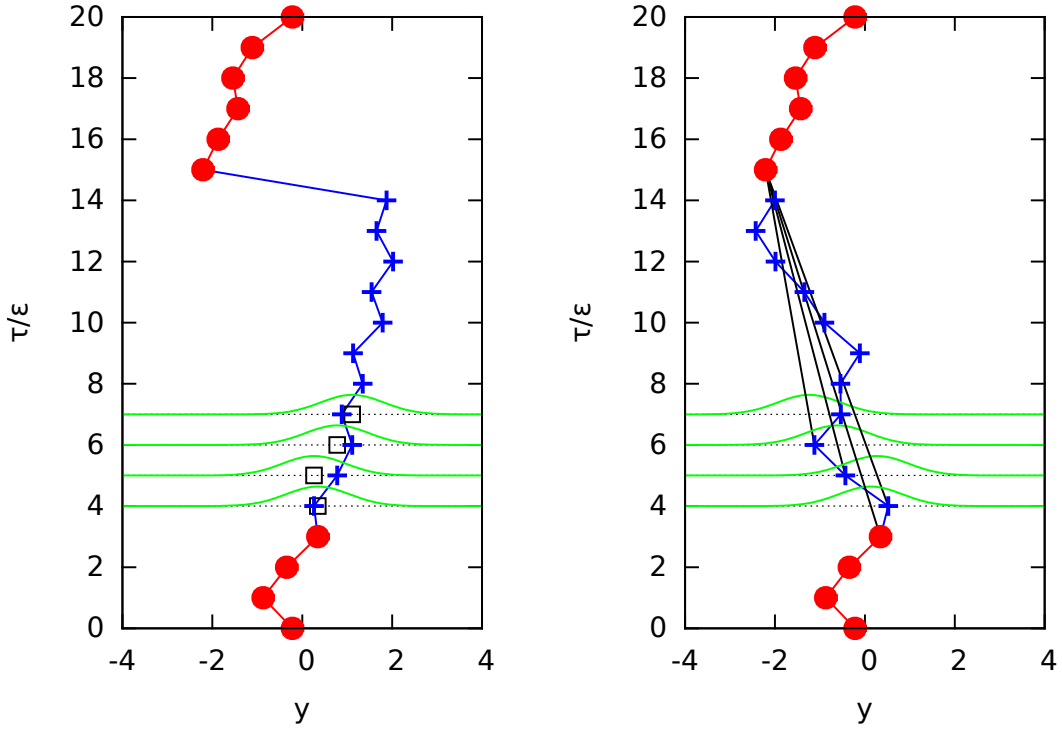

Figure 6: ***Illustration of path sampling schemes:*** An off-diagonal configuration is plotted in the y-τ-plane. The red configuration corresponds to $\mathbf{X}$ before the update and the blue trajectory is the new path. The green gaussians symbolize the probability distribution of the new coordinates. The left picture illustrates the naive sampling directly from ρ_{kin} and the right one the more sophisticated approach.

same. However, this problem can be easily overcome by the introduction of multislice moves. The starting point is again an open configuration like in Fig. 5, but the new update will generate M new beads in a single step. All new coordinates will be sampled according to the kinetic density matrix:

$$T(\mathbf{X} \to \tilde{\mathbf{X}}) = \prod_{i=0}^{M-1} \rho_{\text{kin}}(\mathbf{r}_{k,i}, \mathbf{r}_{k,i+1}, \epsilon) \quad . \tag{34}$$

The acceptance ratio is, in analogy to Eq. (33), given by

$$A(\mathbf{X} \to \tilde{\mathbf{X}}) = e^{\epsilon \Delta V(\mathbf{X} \to \tilde{\mathbf{X}})} e^{M \epsilon \mu} \quad . \tag{35}$$

The sampling procedure is illustrated in the left picture of Fig. 6, where the y-τ-plane is visualized. The red trajectory corresponds to the configuration $\mathbf{X}$ before the update. The blue points are the new coordinates which have been sampled according to Eq. (34). The green gaussians symbolize the probability distribution for each new coordinate, centered around the position of the bead on the previous time slice, i.e., the black squares. The problem with this kind of sampling scheme is due to the fact that the creation of the M missing beads, based on the Eqs. (34) and (35), is not sufficient to account for a change between diagonal and off-diagonal sector. The missing contribution (for further details see the WA update *Close*) is the

kinetic density matrix which connects the last new bead with the worm's tail, i.e., the time slices $\tau = 14\epsilon$ and $\tau = 15\epsilon$ in Fig. 6. The sampling of the new path is completely independent from $\mathbf{r}_{\Psi\dagger}$. This means that the last sampled bead might be very far away from the tail's position, as it is indeed the case in the pictured example. However, such a large spatial difference between adjacent beads is severely punished by ρ_{kin}, and a transition to the diagonal sector will not be possible in this case.

A much better alternative to Eq. (34) is the widely used bisection method. The kinetic part of the ratio of the weights is given by

$$\frac{W_{\text{kin}}(\tilde{\mathbf{X}})}{W_{\text{kin}}(\mathbf{X})} = \prod_{i=0}^{M} \rho_{\text{kin}}(\mathbf{r}_{k,i}, \mathbf{r}_{k,i+1}, \epsilon) \quad . \tag{36}$$

For a better sampling scheme, each of the factors in Eq. (36) is complemented with additional terms [40]:

$$\begin{aligned} T(\mathbf{X} \to \tilde{\mathbf{X}}) \quad = \quad & \frac{\rho_{\text{kin}}(\mathbf{r}_0, \mathbf{r}_1, \epsilon)\rho_{\text{kin}}(\mathbf{r}_1, \mathbf{r}_{M+1}, M\epsilon)}{\rho_{\text{kin}}\left(\mathbf{r}_0, \mathbf{r}_{M+1}, (M+1)\epsilon\right)} \times \\ & \frac{\rho_{\text{kin}}(\mathbf{r}_1, \mathbf{r}_2, \epsilon)\rho_{\text{kin}}(\mathbf{r}_2, \mathbf{r}_{M+1}, (M-1)\epsilon)}{\rho_{\text{kin}}\left(\mathbf{r}_1, \mathbf{r}_{M+1}, M\epsilon\right)} \times \ldots \\ & \ldots \times \frac{\rho_{\text{kin}}(\mathbf{r}_{M-1}, \mathbf{r}_M, \epsilon)\rho_{\text{kin}}(\mathbf{r}_M, \mathbf{r}_{M+1}, \epsilon)}{\rho_{\text{kin}}\left(\mathbf{r}_{M-1}, \mathbf{r}_{M+1}, 2\epsilon\right)} \quad . \end{aligned} \tag{37}$$

The difference between Eqs. (36) and (37) is the denominator of the first factor since all other new terms cancel. To recognize the important advantage of the latter, one might consider a single one of the fractions which give the probability distribution for the sampling of an intermediate coordinate x_i, $i \in [1, M]$:

$$P(x_i) = \frac{1}{\sqrt{2\pi}\sigma_i} \exp\left(-\frac{(x_i - \xi_i)^2}{2\sigma_i^2}\right) \quad . \tag{38}$$

Equation (38) is a gaussian distribution with the variance

$$\sigma_i = \sqrt{\frac{\alpha_i}{2\pi}}\lambda_\epsilon, \quad , \quad \alpha_i = \frac{M+1-i}{M+2-i}$$

around the position

$$\xi_i = \alpha_i x_{i-1} + (1-\alpha_i)x_{M+1} \quad ,$$

which is the intersection of the time slice τ_i with the line connecting x_{i-1} with x_{M+1}. This more sophisticated sampling scheme is illustrated in the right image of Fig. 6. The red and blue paths again represent the old and new trajectory, respectively, and the green gaussians the probability distribution $P(x_i)$ of the new coordinates. This time, however, the $P(x_i)$ are centered around the straigt black lines which connect the last bead with the tail. The great advantage of this bisection technique is that the end point of the new trajectory which, in the case of a closing update, is the worm's tail is explicitly taken into account, so that no large gaps like in the left image of the figure might appear. Therefore, Eqs. (37) and (38) provide the basis of most updates of the worm algorithm as explained in the following section.

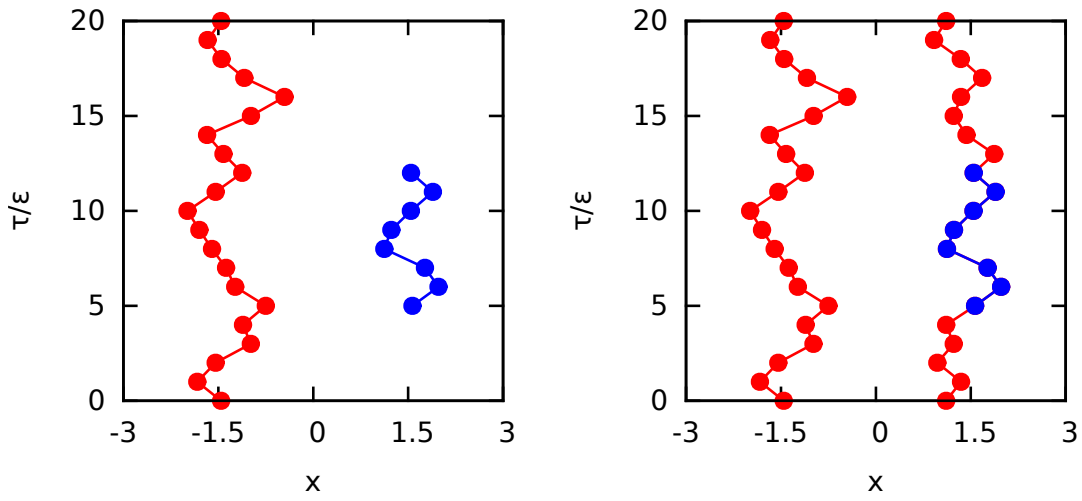

Figure 7: ***Illustration of Insert/Remove and Open/Close:*** Two configurations are plotted in the x-τ-plane. The left picture visualizes the updates *Insert*/*Remove*. The red path corresponds to some unaffected pre-existing particle and the blue piece of trajectory is the inserted or removed worm. The right picture shows the *Open*/*Close* update and the blue segment corresponds to the new ($\rightarrow$ close) or removed ($\rightarrow$ open) beads.

2.4.2 Updates of the worm algorithm

A working path integral Monte Carlo algorithm must provide an ergodic set of updates fulfilling the detailed balance Eq. (27). However, in order to have a more flexible scheme, the update set from Boninsegni et al. [8] is complemented by two additional updates, namely *Move* and *Bisection*.

1. ***Insert*** and ***Remove***: The update *Insert* causes the insertion of a new worm into a formerly closed configuration, as it is pictured in the left image of Fig. 7, in the following steps:

   - Select a time slice $\tau_{\Psi^\dagger} \in [0, P-1]$ at random.
   - Sample the position of the tail $\mathbf{r}_{\Psi^\dagger}$ uniformly inside some predefined volume V.
   - Randomly select the length $\tilde{M} \in [1, M]$ of the new worm. The maximum number of changed beads, M, is a free algorithmic parameter.
   - Sample the position of the worm's head $\mathbf{r}_\Psi$ from $\rho_{\text{kin}}(\mathbf{r}_{\Psi^\dagger}, \mathbf{r}_\Psi, \tilde{M}\epsilon)$.
   - Connect the head and the tail with $\tilde{M}-1$ new beads according to the bisection method from Eq. (37).

   These five steps lead to the transition probability

$$T_{\text{Insert}}(\mathbf{X} \rightarrow \tilde{\mathbf{X}}) = \frac{\rho_{\text{kin}}(\mathbf{r}_{\Psi^\dagger}, \mathbf{r}_\Psi, \tilde{M}\epsilon)}{PVM} \frac{\prod_{i=1}^{\tilde{M}} \rho_{\text{kin}}(\mathbf{r}_i, \mathbf{r}_{i+1}, \epsilon)}{\rho_{\text{kin}}(\mathbf{r}_{\Psi^\dagger}, \mathbf{r}_\Psi, \tilde{M}\epsilon)} \quad , \tag{39}$$

   with $\mathbf{r}_1 = \mathbf{r}_{\Psi^\dagger}$ and $\mathbf{r}_{\tilde{M}+1} = \mathbf{r}_\Psi$. The random selection of the head's position causes the matrix elements $\rho_{\text{kin}}(\mathbf{r}_{\Psi^\dagger}, \mathbf{r}_\Psi, \tilde{M}\epsilon)$ to cancel. The ratio of the new and old configuration

weights is given by

$$\frac{W(\tilde{\mathbf{X}})}{W(\mathbf{X})} = e^{\tilde{M}\epsilon\mu} e^{\epsilon\Delta V(\mathbf{X}\to\tilde{\mathbf{X}})} \prod_{i=1}^{\tilde{M}} \rho(\mathbf{r}_i, \mathbf{r}_{i+1}, \epsilon) \quad . \tag{40}$$

The transition probability for the inverse update, i.e., the removal of an existing worm, is simpy given by $T_{\text{Remove}}(\tilde{\mathbf{X}} \to \mathbf{X}) = 1$, since there is no degree of freedom. Inserting Eqs. (39) and (40) into the Metropolis solution (28) yields the acceptance probabilities

$$\begin{aligned} A_{\text{Insert}}(\mathbf{X} \to \tilde{\mathbf{X}}) &= \min\left(1, CVPM e^{\tilde{M}\epsilon\mu} e^{\epsilon\Delta V(\mathbf{X}\to\tilde{\mathbf{X}})}\right) \quad \text{and} \\ A_{\text{Remove}}(\tilde{\mathbf{X}} \to \mathbf{X}) &= \min\left(1, \frac{1}{CVPM} e^{-\tilde{M}\epsilon\mu} e^{-\epsilon\Delta V(\mathbf{X}\to\tilde{\mathbf{X}})}\right) \quad , \end{aligned}$$

where the constant C controls the ratio of the diagonal and off-diagonal sector and can be optimized to enhance the performance. Finally, it should be noted that *Insert* is only possible in a diagonal configuration and *Remove* requires the presence of a worm with less than $M+1$ beads and a tail which is located within V. The removal of $l > M+1$ beads or $\mathbf{r}_{\Psi\dagger}$ not being within the volume in which a particle can be inserted would violate the detailed balance equation since the reverse move is not possible.

2. ***Close*** and ***Open***: The update *Close* samples the missing connection between the head and tail and, hence, causes a transition from the off- to the diagonal sector. This is illustrated in the right image of Fig. 7, where the red paths symbolize the pre-existing configuration and the blue piece of trajectory corresponds to the new connection between head and tail.

   - Sample the $\tilde{M}-1$ missing beads according to the bisection scheme from Eq. (37).

   This gives the transition probability

$$T_{\text{Close}}(\mathbf{X} \to \tilde{\mathbf{X}}) = \frac{\prod_{i=1}^{\tilde{M}} \rho(\mathbf{r}_i, \mathbf{r}_{i+1}, \epsilon)}{\rho(\mathbf{r}_{\Psi\dagger}, \mathbf{r}_{\Psi}, \tilde{M}\epsilon)} \quad ,$$

   with $\mathbf{r}_1 = \mathbf{r}_\Psi$ and $\mathbf{r}_{\tilde{M}+1} = \mathbf{r}_{\Psi\dagger}$. The ratio of the configuration weights is given by

$$\frac{W(\tilde{\mathbf{X}})}{W(\mathbf{X})} = e^{\tilde{M}\epsilon\mu} e^{\epsilon\Delta V(\mathbf{X}\to\tilde{\mathbf{X}})} \prod_{i=1}^{\tilde{M}} \rho(\mathbf{r}_i, \mathbf{r}_{i+1}, \epsilon) \quad .$$

   The *Open* update erases existing connections from a closed configuration and involves the following steps

   - Choose the new head at random from all N_{beads} existing beads.
   - Select the number of beads to be erased uniformly as $\tilde{M} \in [0, M-1]$.

   The resulting transition probability is given by

$$T_{\text{Open}}(\tilde{\mathbf{X}} \to \mathbf{X}) = \frac{1}{N_{\text{beads}} M} \quad .$$

   Thus, the solution of the detailed balance equation is given by

$$\begin{aligned} A_{\text{Close}}(\mathbf{X} \to \tilde{\mathbf{X}}) &= \min\left(1, \frac{\rho(\mathbf{r}_{\Psi\dagger}, \mathbf{r}_{\Psi}, \tilde{M}\epsilon) e^{\tilde{M}\epsilon\mu} e^{\epsilon\Delta V(\mathbf{X}\to\tilde{\mathbf{X}})}}{CMN_{\text{beads}}}\right) \\ A_{\text{Open}}(\tilde{\mathbf{X}} \to \mathbf{X}) &= \min\left(1, \frac{CMN_{\text{beads}} e^{-\tilde{M}\epsilon\mu} e^{-\epsilon\Delta V(\mathbf{X}\to\tilde{\mathbf{X}})}}{\rho(\mathbf{r}_{\Psi\dagger}, \mathbf{r}_{\Psi}, \tilde{M}\epsilon)}\right) \quad , \end{aligned}$$

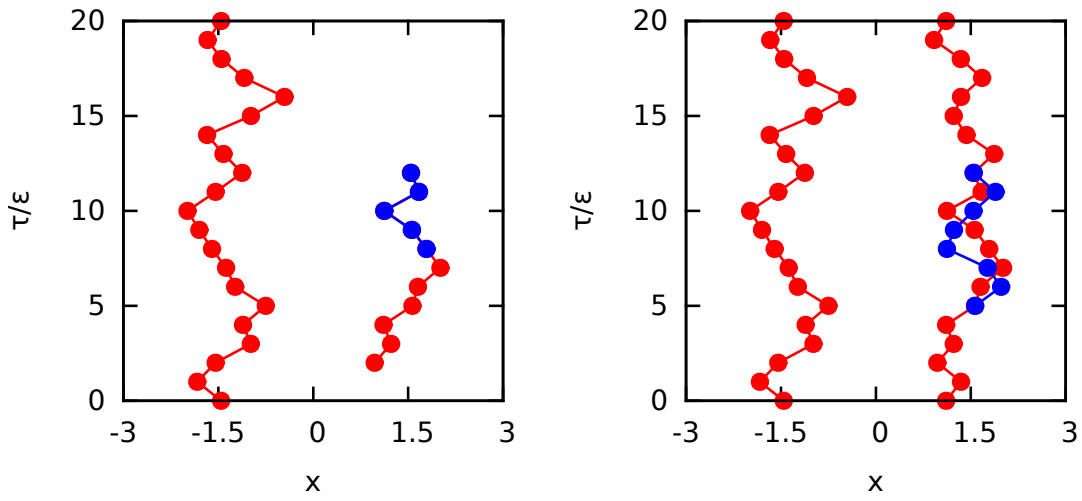

Figure 8: ***Illustration of Advance/Recede and Bisection:*** Two configurations are plotted in the x-τ-plane. The left picture corresponds to the *Advance*/*Recede* update where the red paths symbolize the pre-existing configuration and the blue beads the new/deleted piece of trajectory. The right image shows the *Bisection* update where a part of one pre-existing red path is replaced by the new blue beads.

with the same constant C as in the *Insert* and *Remove* update. Configurations with $l > M-1$ missing links cannot be closed due to the lack of an inverse update.

3. ***Advance*** and ***Recede***: The *Advance* update moves the worm's head forward in imaginary time by generating $\tilde{M}$ new beads. This is illustrated in the left image of Fig. 8 by the blue piece of trajectory and implemented as follows:

   - Select the number of new beads $\tilde{M} \in [1, M]$.
   - Sample the position of the new head, $\mathbf{r}_{\tilde{M}}$, from $\rho(\mathbf{r}_\Psi, \mathbf{r}_{\tilde{M}}, \tilde{M}\epsilon)$.
   - Connect the old and new head according to the usual bisection scheme from Eq. (37).

   The transition probability is given by

$$T_{\text{Advance}}(\mathbf{X} \to \tilde{\mathbf{X}}) = \frac{\rho(\mathbf{r}_\Psi, \mathbf{r}_{\tilde{M}}, \tilde{M}\epsilon)}{M} \frac{\prod_{i=0}^{\tilde{M}-1} \rho(\mathbf{r}_i, \mathbf{r}_{i+1}, \epsilon)}{\rho(\mathbf{r}_\Psi, \mathbf{r}_{\tilde{M}}, \tilde{M}\epsilon)} \quad ,$$

   with $\mathbf{r}_0 = \mathbf{r}_\Psi$. The ratio of the old and new configuration weights is calculated as

$$\frac{W(\tilde{\mathbf{X}})}{W(\mathbf{X})} = e^{\tilde{M}\epsilon\mu} e^{\epsilon \Delta V(\mathbf{X} \to \tilde{\mathbf{X}})} \prod_{i=0}^{\tilde{M}-1} \rho(\mathbf{r}_i, \mathbf{r}_{i+1}, \epsilon) \quad .$$

   The inverse update *Recede* moves the head backwards in τ by deleting $\tilde{M}$ existing beads:

   - Select the number of beads to be deleted as $\tilde{M} \in [1, M]$.
   - Erase the last $\tilde{M}$ beads, starting from the head.

This results in the transition probability

$$T_{\text{Recede}}(\tilde{\mathbf{X}} \to \mathbf{X}) = \frac{1}{M} \quad .$$

Hence, the Metropolis solution for the acceptance probability is given by

$$\begin{aligned} A_{\text{Advance}}(\mathbf{X} \to \tilde{\mathbf{X}}) &= \min\left(1, e^{\tilde{M}\epsilon\mu} e^{\epsilon\Delta V(\mathbf{X}\to\tilde{\mathbf{X}})}\right) \quad \text{and} \\ A_{\text{Recede}}(\tilde{\mathbf{X}} \to \mathbf{X}) &= \min\left(1, e^{-\tilde{M}\epsilon\mu} e^{-\epsilon\Delta V(\mathbf{X}\to\tilde{\mathbf{X}})}\right) \quad . \end{aligned}$$

Both updates are only applicable to off-diagonal configurations since an existing worm is needed.

4. ***Bisection***: This update is both applicable to diagonal and off-diagonal configurations and is in detailed balance with itself. The idea is to change the position of $\tilde{M}$ beads by erasing them and closing the trajectory immediately afterwards, as it is illustrated in the right image of Fig. 8. Thus, it can be viewed as a combination of the updates *Open* and *Close*, but without any restrictions on the present configuration.

   - Select the number of beads to be changed as $\tilde{M} \in [1, \overline{M}]$.
   - Select the first bead of this set randomly from all existing ones in the present configuration.
   - Erase the beads and resample them according to the usual bisection scheme from Eq. (37).

   The parameter $\overline{M}$ does not have to be equal to M and can be optimized to enhance the performance. Since the update is self-balanced and conserves the number of variables, the acceptance probability is simply given by the ratio of the configuration weights:

$$A_{\text{Bisection}}(\mathbf{X} \to \tilde{\mathbf{X}}) = \min\left(1, e^{\epsilon\Delta V(\mathbf{X}\to\tilde{\mathbf{X}})}\right) \quad .$$

   Although, in principle, not needed, the *Bisection* update is expected to considerably decrease the autocorrelation time since all parts of the trajectories are updated regardless of the worm itself.

5. ***Move***: Like the *Bisection* update, the single particle move is, in principle, applicable to both diagonal and off-diagonal configurations and self-balanced as well. The only requirement is a closed piece of trajectory consisting of exactly P beads, i.e., a single particle which is not involved in any exchange cycles. The proposal to move more than one particle at once would be much less efficient and, therefore, is not included.

   - Select a single particle from the existing configuration. If there is not one, the update is rejected.
   - Calculate the particle's displacement randomly as $\mathbf{d} \in [-\mathbf{d}_{\max}, \mathbf{d}_{\max}]$.
   - Move the particle by adding $\mathbf{d}$ to the position of all P beads.

   As for the *Bisection* update, the acceptance probability is simply given by

$$A_{\text{Move}}(\mathbf{X} \to \tilde{\mathbf{X}}) = \min\left(1, e^{\epsilon\Delta V(\mathbf{X}\to\tilde{\mathbf{X}})}\right) \quad .$$

   The single particle move is especially useful in quasi-classical systems with no or only small exchange effects.

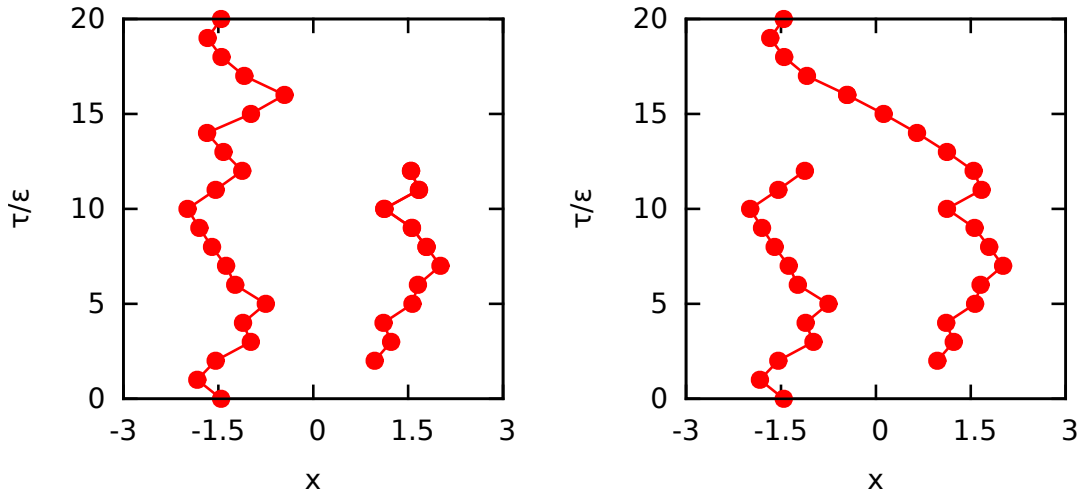

Figure 9: ***Illustration of the Swap update:*** Two configurations are plotted in the x-τ-plane. The left and right picture show the paths before and after the *Swap* update, respectively.

6. ***Swap***: Without the *Swap* update, the only possibility to sample particle exchange with the other introduced moves would be to advance a worm for several β in imaginary time, which is, obviously, very inefficient. The following update is self-balanced and requires an off-diagonal configuration with more than P beads, i.e., more than one particle. The particle exchange is a local and completely ordinary move in the worm picture. The basic idea is illustrated in Fig. 9, where two configurations are plotted in the x-τ-plane. The left image shows the configuration before the update, consisting of a single, closed particle and an eleven beads long worm. The right image is a snapshot taken after the update. $M = 3$ beads have been erased from the closed path, starting one time slice ahead of the old head τ_Ψ. The worm's head has been connected to the formerly closed particle instead. The result is a worm with a length $l > P$ which, when getting closed, becomes an exchange cycle of two particles. The exact update scheme is executed as follows:

   - Consider the time slice $\tau_M = \tau_\Psi + M$. Create a list $\chi_1(k)$ which contains the kinetic density matrix elements $\rho(\mathbf{r}_\Psi, \mathbf{r}_{k,M}, M\epsilon)$ for all $k = 1, \ldots, N$ particles on the target slice τ_M.
   - Draw one bead from the list at random according to the probability $P(k) = \chi_1(k)/\Sigma_1$, with the normalization $\Sigma_1 = \sum_{k=1}^{N} \chi_1(k)$.
   - Find the bead which will be the new head after the update by moving M steps backwards from the target bead k. Erase all the beads in between.
   - Connect the old head to the target bead according to the usual bisection scheme from Eq. (37).
   - Finally, calculate a second list $\chi_2(k)$ which contains the $\rho(\mathbf{r}_\Psi^{\text{new}}, \mathbf{r}_{k,M}, M\epsilon)$ between the position of the new head $\mathbf{r}_\Psi^{\text{new}}$ and all the beads on the target slice. The normalization is given by $\Sigma_2 = \sum_{k=1}^{N} \chi_2(k)$.

The transition probability for such a move can be written as

$$T_{\text{Swap}}(\mathbf{X} \to \tilde{\mathbf{X}}) = \frac{\rho(\mathbf{r}_\Psi, \mathbf{r}_{k,M}, M\epsilon)}{\Sigma_1} \frac{\prod_{i=0}^{M-1} \rho(\mathbf{r}_i^{\text{new}}, \mathbf{r}_{i+1}^{\text{new}}, \epsilon)}{\rho(\mathbf{r}_\Psi, \mathbf{r}_{k,M}, M\epsilon)} \quad , \tag{41}$$

with $\mathbf{r}_M^{\text{new}} = \mathbf{r}_{k,M}$. The ratio of the new and old configuration weight is given by

$$\frac{W(\tilde{\mathbf{X}})}{W(\mathbf{X})} = \frac{\prod_{i=0}^{M-1} \rho(\mathbf{r}_i^{\text{new}}, \mathbf{r}_{i+1}^{\text{new}}, \epsilon)}{\prod_{i=0}^{M-1} \rho(\mathbf{r}_i, \mathbf{r}_{i+1}, \epsilon)} e^{\epsilon V(\mathbf{X} \to \tilde{\mathbf{X}})} \quad .$$

The transition probability for the inverse move corresponds to Eq. (41) with the old coordinates in the kinetic density matrix elements and the normalization from the second list Σ_2. Hence, the Metropolis solution of the detailed balance equation reads

$$A_{\text{Swap}}(\mathbf{X} \to \tilde{\mathbf{X}}) = \frac{\Sigma_1}{\Sigma_2} e^{\epsilon \Delta V(\mathbf{X} \to \tilde{\mathbf{X}})} \quad ,$$

since all the ρ_{kin} cancel. The great advantage of the *Swap* update compared to other exchange mechanisms, as e.g. described by Ceperley [5], is the local nature of the move which makes it, in principle, not less probable than *Advance* or *Close* if exchange is wanted by the system. This is due to the fact that only a single connection is sampled at a time and the trajectories can be deformed many times until the configuration is closed.

The PIMC worm algorithm scheme consists of a relatively small set of local updates, which are able to efficiently generate every possible configuration $\mathbf{X}$. The significantly enhanced sampling of particle exchange makes the WA superior to the usual techniques.

2.5 Calculation of Observables

In the following subsection, the general approach to calculate observables from PIMC simulations is discussed. The canonical expectation value of an arbitrary observable $\hat{A}$ in the spatial representation is given by

$$\langle \hat{A} \rangle = \frac{1}{Z_{\text{c}}} \int \mathrm{d}\mathbf{R} \ \langle \mathbf{R}| \hat{A} e^{-\beta \hat{H}} |\mathbf{R}\rangle \approx \frac{1}{N_{\text{MC}}} \sum_{j=1}^{N_{\text{MC}}} A(\mathbf{X}_j) \quad ,$$

with the canonical partition function Z_{c} and the Markov chain of canonical configurations $\{\mathbf{X}_j\}$ created by the Monte Carlo procedure. However, the worm algorithm operates in an extended configuration space. Therefore, one needs a scheme to extract canonical data for a fixed particle number N from such a Markov chain[3].

2.5.1 Measurements of canonical observables

The most widely used canonical measurement scheme consists of the following steps:

- Count all configurations of the Markov chain, including open paths and all particle numbers N.
- Check every M steps, if the configuration is diagonal. If this is the case, then measure all canonical observables (e.g. energies, densities, etc.) and determine N. Include the data into the canonical set $\{A(\mathbf{X}_j(N, V, T))\}$. One is allowed to measure the MGF if the configuration is off-diagonal.

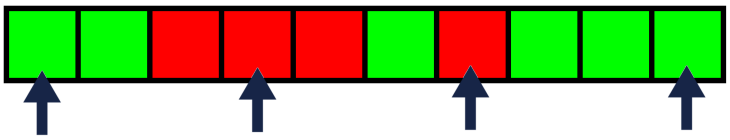

Figure 10: ***Extraction of canonical data:*** The extended Markov chain, which consists of both diagonal (green) and off-diagonal (red) configurations, is visualized. The dark arrows symbolize attempted canonical measurements.

- Repeat the first two steps until enough data is collected.

This approach is illustrated in Fig. 10. The image shows the extended Markov chain consisting of both diagonal (green) and off-diagonal (red) configurations. The dark blue arrows symbolize the attempted measurements every $M = 3$ steps. Canonical observables may only be measured at the first and the last one. The measurement frequency M should be chosen of the order of the autocorrelation time τ_{AC} (see section 2.6) to reduce correlations in the dataset. In order to prove that the described process does indeed generate a dataset of canonically distributed configurations (and, thus, measurements), one must show that the result $\langle A \rangle_{\mathrm{C}}$ can be written as the expectation value of some modified observable in the extended configuration space. This can be accomplished in two similar steps. First, consider the grandcanonical expectation value of $\hat{A}$,

$$\begin{aligned} \langle A \rangle_{\mathrm{GC}} &= \frac{1}{Z_{\mathrm{GC}}} \int \mathrm{d}\mathbf{R}_{\mathrm{GC}} \ \langle \mathbf{R}_{\mathrm{GC}} | \, \hat{A} \, | \mathbf{R}_{\mathrm{GC}} \rangle \\ &= \frac{1}{Z_{\mathrm{ext}}} \int \mathrm{d}\mathbf{R}_{\mathrm{ext}} \ \langle \mathbf{R}_{\mathrm{ext}} | \, \hat{B} \, | \mathbf{R}_{\mathrm{ext}} \rangle \qquad , \end{aligned} \tag{42}$$

where the equality holds for the modified observable

$$\hat{B} = \hat{A} \frac{Z_{\mathrm{ext}}}{Z_{\mathrm{GC}}} \delta_{\mathrm{GC}} \left(\mathbf{R}_{\mathrm{ext}} \right) \qquad ,$$

with the definition

$$\delta_{\mathrm{GC}} \left(\mathbf{R}_{\mathrm{ext}} \right) = \begin{cases} 1, & \text{if } \mathbf{R}_{\mathrm{ext}} \in \{ \mathbf{R}_{\mathrm{GC}} \} \\ 0, & \text{otherwise.} \end{cases}$$

Equation (42) implies that, by performing a Monte Carlo average of $\hat{B}$ in the extended configuration space, one effectively generates a grandcanonical dataset of the observable $\hat{A}$:

$$\langle B \rangle_{\mathrm{ext}} \approx \frac{1}{N_{\mathrm{MC}}} \sum_{j=1}^{N_{\mathrm{MC}}} B_j = \frac{1}{N_{\mathrm{MC}}} \sum_{j=1}^{N_{\mathrm{MC}}} A_j \frac{Z_{\mathrm{ext}}}{Z_{\mathrm{GC}}} \delta_{\mathrm{GC}} \left(\mathbf{R}_j \right) \qquad . \tag{43}$$

The ratio of the two normalizations $Z_{\mathrm{ext}}/Z_{\mathrm{GC}} \to N_{\mathrm{MC}}/N_{\mathrm{GC}}$ approaches the ratio of the numbers of all and only closed configurations for $N_{\mathrm{MC}} \to \infty$, and Eq. (43) reduces to

$$\langle B \rangle_{\mathrm{ext}} \approx \frac{1}{N_{\mathrm{GC}}} \sum_{j=1}^{N_{\mathrm{GC}}} A_j = \langle A \rangle_{\mathrm{GC}} \qquad .$$

[3]The proofs of the extraction schemes have been worked out together with S. Groth and T. Schoof.

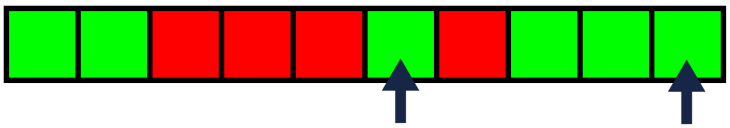

Figure 11: ***Illustration of the canonical cycles scheme:*** The presented Markov chain is identical to the one from Fig. 10. The consideration of canonical configurations only results in different measurements.

The same consideration can be repeated to extract canonical data from the grandcanonical set and the proof is completed.

Another useful possibility is the implementation of canonical cycles. The idea is to only count canonical configurations with a specific N and consider all steps in between, which means both off-diagonal and diagonal paths with another particle number, as one combined Monte Carlo update. The latter, obviously, fulfills the detailed balance condition since this is true for all the WA updates as well and, in the ratio of the new and old weights $W(\tilde{\mathbf{X}})/W(\mathbf{X})$, all terms that include μ cancel. The measurement algorithm can be implemented as follows:

- Check if the configuration is diagonal. If this is true, then determine the particle number N. Increase the canonical counter $c(N) \to c(N) + 1$.
- If $c(N) = M$, then all diagonal observables are measured, added to the canonical dataset and the counter is set back to zero: $c(N) \to c(N) = 0$.
- Repeat the first two steps until enough data is collected.

The canonical cycles scheme is illustrated in Fig. 11, where the same Markov chain as in Fig. 10 is shown. For simplicity, it is assumed that all diagonal (green) configurations exhibit the same particle number, N. The off-diagonal (red) configurations are neglected and measurements are performed every $M = 3$ steps.

There is no general answer to which one of the two extraction schemes is more efficient. In this work, the first presented approach is used.

2.5.2 Examples

A well known approach to calculate an observable by PIMC is to use an explicit connection to the partition function Z, e.g. the system's total energy

$$E = -\frac{\partial}{\partial \beta} Z \quad .$$

Using the expression for Z in the path integral picture from Eq. (22) and inserting the thermal de Broglie wavelength leads to

$$\begin{aligned} E \;=\; & -\int \mathrm{d}\mathbf{R}_0 \ldots \mathrm{d}\mathbf{R}_{P-1} \; \frac{\partial}{\partial \beta} \left(\frac{1}{\lambda_\beta^{dN}} \right) \exp\left(-\frac{mP}{\hbar^2 2\beta} \sum_{i=0}^{P-1} \sum_{k=1}^{N} \left(\mathbf{r}_{k,i} - \mathbf{r}_{k,i+1} \right)^2 - \right. \\ & \left. -\frac{\beta}{P} \sum_{i=0}^{P-1} V(\mathbf{R}_i) \right) \\ & -\int \mathrm{d}\mathbf{R}_0 \ldots \mathrm{d}\mathbf{R}_{P-1} \; \frac{1}{\lambda_\beta^{dN}} \frac{\partial}{\partial \beta} \exp\left(-\frac{mP}{\hbar^2 2\beta} \sum_{i=0}^{P-1} \sum_{k=1}^{N} \left(\mathbf{r}_{k,i} - \mathbf{r}_{k,i+1} \right)^2 - \frac{\beta}{P} \sum_{i=0}^{P-1} V(\mathbf{R}_i) \right) \quad . \end{aligned} \tag{44}$$

The evaluation of all the derivatives gives the usual expression for the energy as the sum of the three contributions [28]

$$E = \frac{dNP}{2\beta} - \frac{mP}{2\hbar^2\beta^2}\langle\sum_{i=0}^{P-1}\sum_{k=1}^{N}(\mathbf{r}_{k,i}-\mathbf{r}_{k,i+1})^2\rangle + \frac{1}{P}\langle\sum_{i=0}^{P-1}V(\mathbf{R}_i)\rangle \quad . \tag{45}$$

The last term can, obviously, be identified with the total potential energy, while the first two correspond to the thermodynamic estimator of the kinetic energy. The very first term is similar to the classical value, i.e., $E_{\mathrm{cl,kin}} = 3Nk_{\mathrm{B}}T/2$ for a $3D$ system and the second term can be interpreted as a purely quantum mechanical correction. In the classical limit, i.e., a single imaginary time slice $P = 1$, the double sum vanishes and the kinetic energy becomes $E_{\mathrm{cl,kin}}$. It is very interesting to note that particles which propagate over a long distance in the imaginary time in the path integral picture actually have a small kinetic energy since this is related to the quantum mechanical extension of the particles and absolutely not to any real time propagation. A well known shortcoming of the estimator from Eq. (45) is that the kinetic energy suffers from a very high variance and, thus, a big statistical uncertainty. One possibility to overcome this issue is based on the virial theorem. However, there exist pros and cons for both the virial and thermodynamic estimator and the optimal way to estimate the kinetic energy is discussed e.g. in [41].

Diagonal observables can be calculated in an even more straightforward way, that is, by making direct use of the definition of the expectation value

$$\langle A\rangle = \frac{1}{Z}\int \mathrm{d}\mathbf{R}\,\langle\mathbf{R}|\,e^{-\beta\hat{H}}\hat{A}\,|\mathbf{R}\rangle \quad ,$$

and translating it into the path integral picture in precisely the same way as the partition function Z in section 2.1.2, i.e., by factorizing $\hat{\rho}$ and inserting again the $P-1$ unities:

$$\langle A\rangle = \frac{1}{Z}\int \mathrm{d}\mathbf{R}_0\ldots\mathrm{d}\mathbf{R}_{P-1}\ \langle\mathbf{R}_0|\,e^{-\epsilon\hat{H}}\,|\mathbf{R}_1\rangle\ldots\langle\mathbf{R}_{P-1}|\,e^{-\epsilon\hat{H}}\hat{A}\,|\mathbf{R}_0\rangle \quad .$$

The Metropolis algorithm generates the configurations $\{\mathbf{X}\}$ according to the correct configuration weights, and if $\hat{A}$ is diagonal, it can be evaluated on e.g. the last time slice in every configuration of the Markov chain. In addition, there is nothing special about any particular time slice, and, hence, it makes sense to average $\hat{A}$ over all imaginary time slices to obtain better statistics. An obvious example is the density

$$\langle\rho(\mathbf{r}_\alpha)\rangle \approx \frac{1}{N_{\mathrm{MC}}}\sum_{i=1}^{N_{\mathrm{MC}}}\frac{1}{PV_\alpha}\sum_{j=0}^{P-1}\sum_{k=1}^{N}\delta(\mathbf{r}_{j,k},\mathbf{r}_\alpha) \quad ,$$

calculated on some discrete spatial positions $\mathbf{r}_\alpha$ in the center of bins with the volume V_α and the definition

$$\delta(\mathbf{r}_{j,k},\mathbf{r}_\alpha) = \begin{cases} 1, & \text{if } \mathbf{r}_{j,k}\in V_\alpha \\ 0, & \text{otherwise.} \end{cases}$$

The calculation of other observables like superfluid properties or estimators for the quantum breathing mode are discussed in the corresponding sections.

2.6 Error analysis of Monte Carlo data

A very important point for every simulation method is the availability of reasonable errorbars to evaluate the quality of any obtained result. This is a non-trivial task in the case of PIMC data since correlation effects between configurations in the Markov chain must be taken into account. The following introduction applies to every Metropolis Monte Carlo simulation technique and is mainly based on the overview by Janke [42].

The expectation value of an observable $\hat{A}$ is approximated by the MC average

$$\langle A \rangle \approx \overline{A} = \frac{1}{N_{\mathrm{MC}}} \sum_{j=1}^{N_{\mathrm{MC}}} A_j \tag{46}$$

over all N_{MC} elements of the generated Markov chain. According to the **C**entral **L**imiting **T**heorem (CLT), which becomes valid for a sufficiently large number of single measurements A_j, $\overline{A}$ is normally distributed around the exact expectation value $\langle A \rangle$. For uncorrelated measurements the variance of the mean value is given by

$$\sigma^2_{\overline{A}} = \frac{\langle A_j^2 \rangle - \langle A_j \rangle^2}{N_{\mathrm{MC}}} = \frac{\sigma^2_{A_j}}{N_{\mathrm{MC}}} \quad , \tag{47}$$

with the variance of individual measurements $\sigma^2_{A_j}$. Equation (47) implies that the error scales as $\sigma_{\mathrm{MC}} \propto 1/\sqrt{N_{\mathrm{MC}}}$. This means that one needs one hundred times the computation time to gain an additional digit of accuracy.

2.6.1 Autocorrelation time

However, Eq. (47) neglects correlation effects. This can be shown by inserting Eq. (46) into the former and, after some conversions, one obtains:

$$\sigma^2_{\overline{A}} = \langle \overline{A}^2 \rangle - \langle \overline{A} \rangle^2 = \frac{1}{N_{\mathrm{MC}}^2} \sum_{i,j=1}^{N_{\mathrm{MC}}} \langle A_i A_j \rangle - \frac{1}{N_{\mathrm{MC}}^2} \sum_{i,j=1}^{N_{\mathrm{MC}}} \langle A_i \rangle \langle A_j \rangle \quad . \tag{48}$$

By decomposing Eq. (48) into diagonal and off-diagonal elements and doing some algebra, one arrives at

$$\sigma^2_{\overline{A}} = \frac{\sigma^2_{A_j}}{N} 2\tau_{\mathrm{int}} \quad ,$$

with the integrated autocorrelation time

$$\tau_{\mathrm{int}} = \frac{1}{2} + \sum_{k=1}^{N_{\mathrm{MC}}} A(k) \left(1 - \frac{k}{N_{\mathrm{MC}}} \right) \quad , \tag{49}$$

and the normalized autocorrelation function

$$A(k) = \frac{\langle A_j A_{j+k} \rangle - \langle A_j \rangle \langle A_j \rangle}{\langle A_j^2 \rangle - \langle A_j \rangle \langle A_j \rangle} \quad .$$

Equation (49) is a measure for the distance between two independent configurations in the Markov chain. Hence, the Monte Carlo error can be written as

$$\sigma_{\overline{A}} = \frac{\sigma_{A_j}}{\sqrt{N_{\mathrm{eff}}}} \quad ,$$

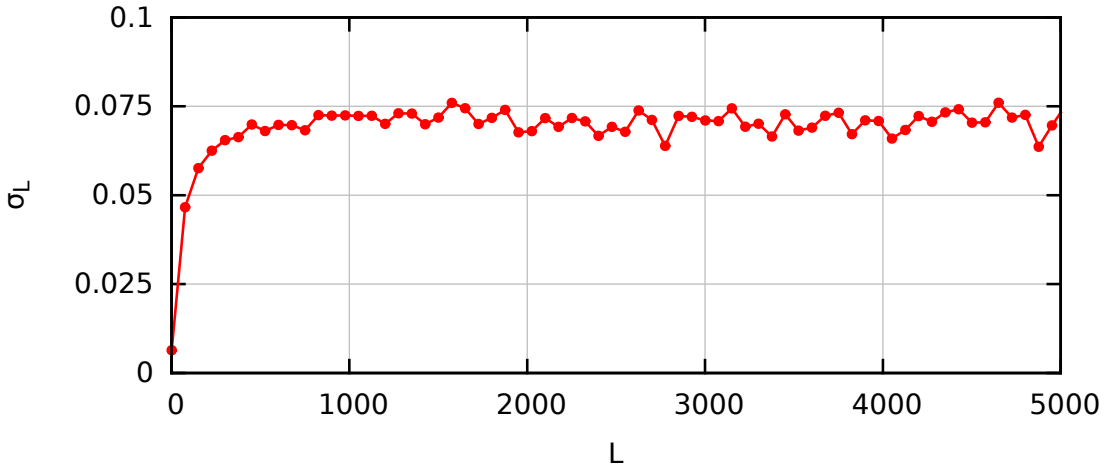

Figure 12: ***Binning analysis of MC data:*** The error σ_L of the binned data sets is plotted over the blocklength L for the potential energy of $N = 10$ Coulomb interacting particles in $2D$.

with the number of effective (independent) measurements $N_{\text{eff}} = N_{\text{MC}}/2\tau_{\text{int}} < N_{\text{MC}}$. This means that correlation effects of the samples increase the statistical error of the MC averages. This is also quite intuitive since correlated configurations cannot contain the same amount of information as uncorrelated ones.

2.6.2 Binning analysis

The remaining question for this subsection is how to numerically estimate τ_{int} from the Monte Carlo data. It turns out that a straightforward calculation of Eq. (49) is both time consuming and afflicted with large statistical noise. An alternative approach is the binning analysis procedure, which can be implemented as follows:

- Bin the dataset $\{A_j\}$ into $M = N_{\text{MC}}/L$ blocks of L measurements. Create a new dataset $\{A_k(L)\}$ with

$$A_k(L) = \frac{1}{L}\sum_{j=1}^{L} A_{kL+j} \qquad .$$

- Consider the $A_k(L)$ as the new measurement values and calculate the uncorrelated error σ_L according to Eq. (47).
- Repeat the first two steps for different blocklengths L.

The result of this procedure for $N_{\text{MC}} = 4.5 \cdot 10^5$ measurements of the potential energy for $N = 10$ Coulomb-interacting particles in a $2D$ harmonic trap is shown in Fig. 12, where σ_L is plotted over L and measurements have been performed in every diagonal configuration. For small L, the error increases with L until, for $L \sim 500$, the curve saturates. For small blocklengths, the blockaverages are still correlated with each other and the error is underestimated. With increasing L correlations are reduced until, finally, all values are independent and the error fluctuates around $\sigma_L \approx 0.07$. Hence, the plot in Fig. 12 reveals both the autocorrelation time τ_{int} and the correct correlated error. The binning analysis is used to calculate every errorbar in this work.

3 Implementation of PIMC

In this section, all practical aspects concerning the implementation of the worm algorithm path integral Monte Carlo scheme are discussed. The code is written in C++, which is a modern object oriented language and widely used for scientific calculations [43]. The section begins with a brief introduction of the system of units and some practical details, followed by a presentation of different checks of the implementation, including the comparison with analyical solutions and results from another code. Afterwards, some improvements to the usual worm algorithm are motivated and discussed and the section is completed by a short summary of the possible and missing capabilities of the presented PIMC implementation.

3.1 System of units

The systems of interest in this work are given by N harmonically confined particles and can be described by a Hamiltonian of the form

$$\hat{H} = \frac{-\hbar^2}{2m}\sum_{k=1}^{N}\nabla_k^2 + \frac{1}{2}m\Omega^2\sum_{k=1}^{N}\mathbf{r}_k^2 + \sum_{j<k}^{N} w(j,k) \quad , \tag{50}$$

with the pair interaction

$$w(j,k) = \begin{cases} \frac{q^2}{4\pi\epsilon_0|\mathbf{r}_k-\mathbf{r}_j|}, & \text{Coulomb,} \\ \frac{D}{4\pi|\mathbf{r}_k-\mathbf{r}_j|^3}, & \text{polarized dipoles.} \end{cases} \tag{51}$$

For a more convenient numerical handling, it is useful to transform Eqs. (50) and (51) into a dimensionless form. Lengths are expressed in units of the characteristic oscillator length,

$$l_0 = \sqrt{\frac{\hbar}{m\Omega}} \quad ,$$

and energies in units of $\hbar\Omega$. This gives the modified Hamiltonian

$$\hat{H} = \frac{1}{2}\sum_{k=1}^{N}\left(-\nabla_k^2 + \mathbf{r}_k^2\right) + \lambda\sum_{j<k}\frac{1}{|\mathbf{r}_k-\mathbf{r}_j|^\alpha} \quad , \tag{52}$$

with $\alpha = 1, 3$ for Coulomb- and dipole-interaction, respectively, and the definition of the coupling parameter λ as the ratio of the characteristic energies

$$\begin{aligned} E_0 &= \hbar\Omega \quad , \\ E_{\text{Clmb}} &= \frac{q^2}{4\pi\epsilon_0 l_0} \quad \text{and} \\ E_{\text{dip}} &= \frac{D}{4\pi l_0^3} \quad , \\ \Rightarrow \lambda &= \begin{cases} \frac{q^2}{4\pi\epsilon_0 l_0\hbar\Omega}, & \text{Coulomb,} \\ \frac{D}{4\pi l_0^3\hbar\Omega} & \text{polarized dipoles.} \end{cases} \end{aligned} \tag{53}$$

Equation (53) implies that the coupling strength λ can be tuned experimentally by the modification of the trap frequency Ω. All simulation parameters and results in this work are given in these characteristic oscillator units.

3.2 Practical details

The first functioning implementation of WA-PIMC consists of the following steps:

1. Read the input parameters like the chemical potential μ, inverse temperature β, number of time slices P, etc. and initialize all the data structures.
2. Start with an empty system and let the worm algorithm adjust the particle number according to μ.
3. Optimize the free parameters like the maximum number of displaced beads, M, and the control variable C for the ratio of off- and diagonal sector.
4. Spend N_{eq} Monte Carlo steps without measuring any observables to let the system equilibrate.
5. Check every N_{m} steps wether the system is diagonal or not and measure the corresponding observables.
6. Write all obtained observables on the disk, e.g. every $\sim 10^4$ measurements.
7. Stop the program after collecting the desired number of measurements.

One possibility to perform the adjustment of C in step 3 is to pre-define some ratio κ_{input} of steps in the diagonal and off-diagonal sector and choose C in a way that the real ratio κ is within some interval around the desired value. Although one might, in principle, argue that high quality data of diagonal observables requires a lot of diagonal measurements and, hence, a lot of time in the closed path sector, this is not necessarily true. The sampling of particle exchange only happens in off-diagonal configurations. Thus, spending only little time in this sector will result in very high correlations of quantities that are sensitive to exchange like e.g. the superfluid fraction, and the larger number of measurements will hardly reduce the statistical error. Empirically, it turns out to be reasonable to spend approximately three times as much steps in the off-diagonal than in the diagonal sector. Step 6 is needed to get the measured observables out of the random access memory (RAM) and, in addition, allows to check the quality of the observables before the PIMC simulation is finished.

The presented algorithm is already complete in the sense that it - if implemented correctly - will calculate correct observables. In the following section, the correctness of the code will be validated before some improvements are introduced in section 3.4.

3.3 Checks of the implementation

There exist several powerful criteria that can be implemented into the code to verify its validity. Each time an update is proposed, one might immediately consider the inverse update and check if the acceptance probability for the two moves satisfies Eq. (28) from section 2.3. If this is not the case, then the particular updates are not in detailed balance and the algorithm does not work. Another good check is to introduce some variable E_{update} and add the change in the potential energy $\Delta V(\mathbf{X} \to \tilde{\mathbf{X}})$ onto it every time an update is accepted. In the diagonal sector, E_{update} must coincide with the total potential energy calculated by hand. In this case, the bookkeeping of $V(\mathbf{X})$ in the updates is correct. The connections between different beads might be checked by considering their next and previous IDs and the latter's time slices as well. Only the head and tail of the worm do not have a next and previous neighbour, respectively.

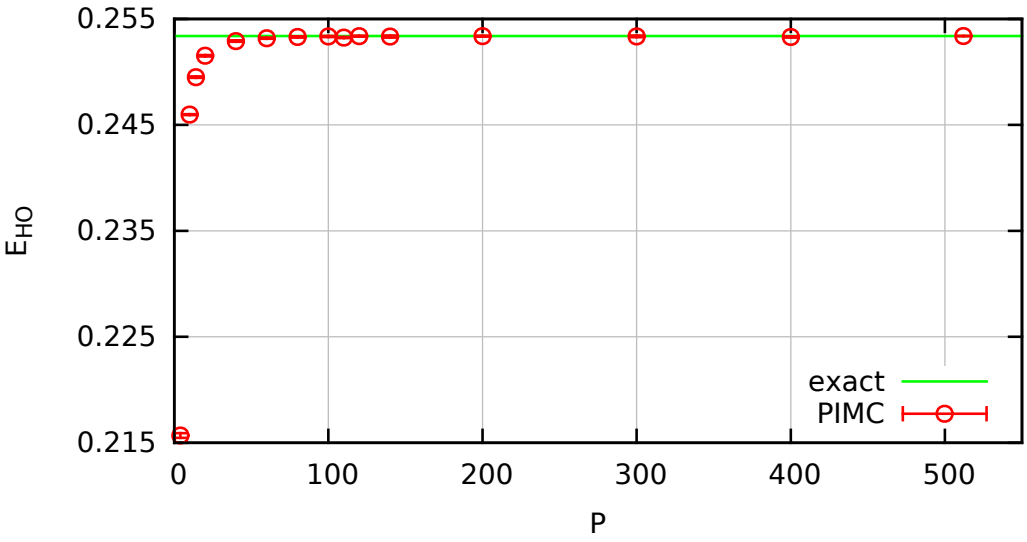

Figure 13: ***Convergence with*** P***:*** The potential energy E_{HO} is plotted over the number of time slices P for a single particle in $1D$ at $\beta = 5$. The PIMC results are visualized as red points and the analytical value corresponds to the green line.

3.3.1 One particle harmonic oscillator

If all the above checks are fulfilled, one might calculate some observables of a test system to compare them to analytically known values. Such an example is provided by a single particle in a $1D$ harmonic oscillator potential. The parameters for the simulation are chosen as $\lambda = 10$, $\mu = 2$ and $\beta = 5$ and the convergence of the potential energy E_{HO} with respect to the number of time slices P is investigated. The results are visualized in Fig. 13 where E_{HO} is plotted with errorbars over P. The horizontal green line corresponds to the analytical value $E_{\mathrm{exact}} = 0.25339....$ For small P, the red points strongly deviate from the green line since the commutator terms missing in the primitive approximation are not negligible. With an increasing number of time slices, this difference decreases until, for $P \sim 80$, the curve saturates. This means that the error terms have become smaller than the statistical errors and the results are quasi-exact. The convergence behaviour is in complete agreement with data published by Sakkos et al. [34] and a simulation with $P = 512$ and $N_{\mathrm{MC}} > 7 \cdot 10^8$ measurements gave a potential energy with a statistical error on the sixth digit and the exact value within single errorbars.

Another quantity to be investigated for the convergence is the density n, which is plotted in the left image of Fig. 14 over the spatial coordinate x. All four curves exhibit a similar gaussian-like form. The result for $P = 4$ time slices (red) significantly deviates from the other three curves. The green dataset corresponds to $P = 10$ and nearly equals the density for $P = 60$ (blue) and $P = 110$ (purple) and the latter cannot be distinguished with the naked eye. The radial density can be compared to the ground state function

$$n_0(x) = \frac{1}{\sqrt{\pi}} \exp\left(-x^2\right) \quad .$$

The deviation $\Delta n(x) = n(x) - n_0(x)$ between the simulation results and n_0 is shown in the right image with errorbars. The red curve corresponds to $\beta = 5$ and exhibits a non-monotonous behaviour. The PIMC results are below the ground state density for $x < 0.7$ and above otherwise. This implies that higher states significantly contribute to n. The green curve corresponds to

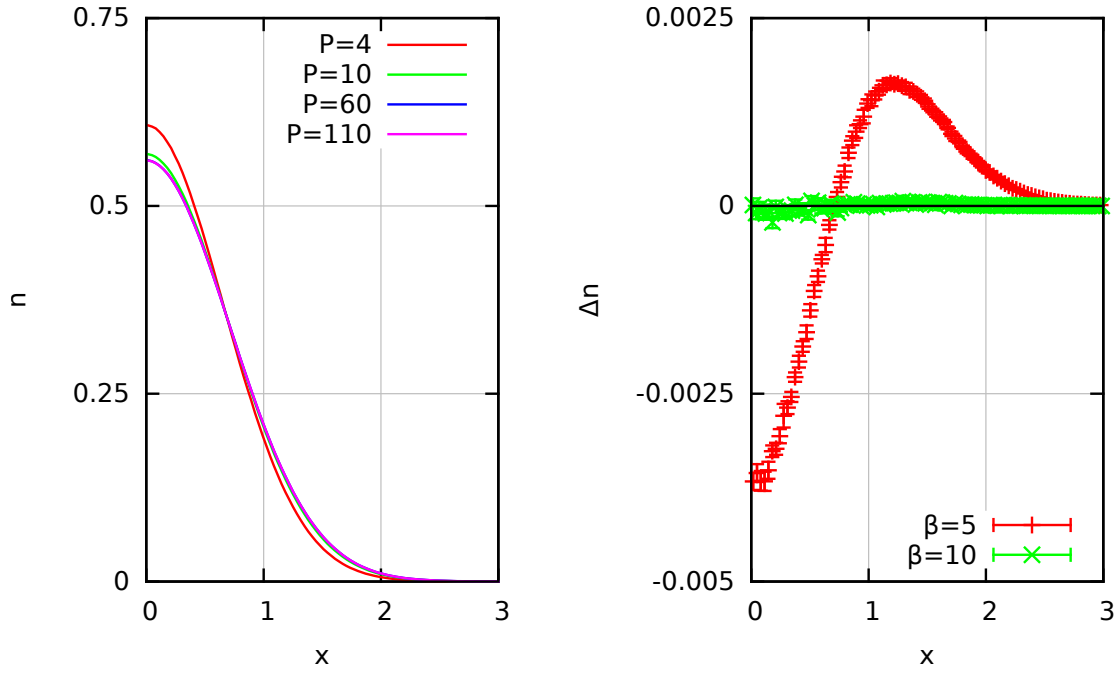

Figure 14: ***Comparison of the densities:*** The left image shows the density n plotted over x for $P = 4$ (red), $P = 10$ (green), $P = 60$ (blue) and $P = 110$ (purple) time slices. In the right image, the difference Δn to the ground state density n_0 is plotted for the inverse temperatures $\beta = 5$ (red) and $\beta = 10$ (green).

Insert	Remove	Open	Close	Advance	Recede	Bisection	Swap	Move
0.75559	0.2548	0.15232	0.37201	0.46981	0.46970	0.59833	0.11174	0.82572

Table 1: Acceptance ratios of the PIMC simulation from Fig. 13 with $P = 200$.

$\beta = 10$ and the difference Δn vanishes within the errorbars. Evidently, the probability to occupy higher states is so small that their contribution to n can hardly be resolved with the accuracy of the presented PIMC results. Finally, table 1 lists the acceptance ratios from the simulation with $\beta = 5$ and $P = 200$. It is a common misconception that there should be some optimum acceptance ratio which is valid for all systems, as it is demonstrated in more detail in section 3.4.2. Still, one can conclude that all updates enjoy medium to high probabilities which indicates that there is no ergodicity problem and small autocorrelations in the Markov chain.

3.3.2 Comparison to another PIMC code

At this point, one may conclude that the PIMC code works correctly for a single particle or, equivalently, ideal systems. Unfortunately, there is no analytical benchmark for correlated many-body systems. The best possible check in those cases is the comparison with already existing code, in this case a WA-PIMC implementation by A. Filinov, see e.g. [13], over a wide parameter range. A selected test case to be presented in this section is a $2D$ Coulomb system with $\lambda = 10$, $\beta = 5$, $P = 80$ and $N = 7$. The resulting radial density n is plotted in Fig. 15 over the distance to the center of the trap, r. The red curve corresponds to the implementation by Filinov and the blue points to the author's code. The outcome of the two independent calculations for n are in

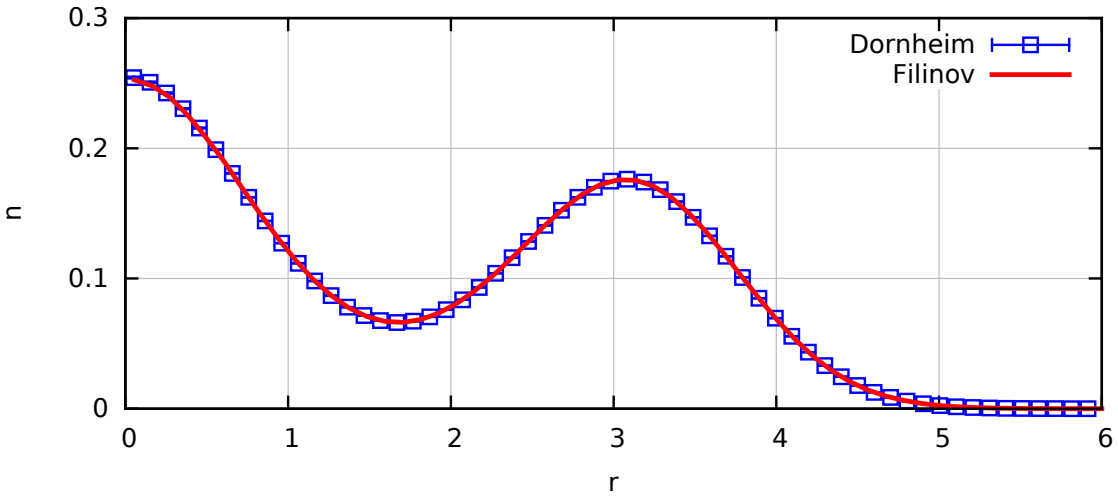

Figure 15: ***Comparison of the radial density:*** The radial density n is plotted over the distance to the center of the trap r for a $2D$ Coulomb system with $N = 7$, $\lambda = 10$, $\beta = 5$ and $P = 80$. The red curve has been obtained with a PIMC implementation by A. Filinov and the blue points with the author's code.

perfect agreement, that is, within the errorbars. The same is true for the energies. This means that both codes seem to be able to correctly produce results in the canonical ensemble. To verify grandcanonical results, one may consider the probability distribution $P(N)$ of configurations with a specific particle number N. Such a comparison is shown in Fig. 16 where P is plotted over N for a $2D$ Coulomb system with $\lambda = 0.25$, $\mu = 4.6$, $\beta = 5$ and $P = 80$. The color assignment is the same as in Fig. 15 and, again, the two data sets coincide.

3.3.3 The virial theorem

The virial theorem provides a connection between a system's kinetic, confinement and interaction energy. For a Hamiltonian like Eq. (52), it states

$$E_{\text{kin}} = E_{\text{HO}} - \frac{\alpha}{2} E_{\text{int}} \quad . \tag{54}$$

It is immediately clear from Eq. (54) that only two of the three energies are needed to know all of them. On the other hand, one can calculate all energies from the PIMC simulation and check the validity of the virial theorem, i.e., if the left and right hand side of Eq. (54) are within each others errorbars. The result for such a check is shown in Fig. 17, where the kinetic energy - normalized to the result from the thermodynamic estimator - is plotted over the particle number N for a $2D$ Coulomb system with $\lambda = 3$ and $\beta = 5$. The red points correspond to the thermodynamic estimator itself and the green points to the virial theorem. All points are within each others single or double errorbars and the results from Eq. (54) fluctuate around unity. This means that no systematic deviation occurs and the virial theorem is indeed fulfilled.

3.3.4 Effect of bad random numbers

In section 2, it has been concluded that the path integral Monte Carlo method delivers quasi-exact results if a sufficient number of time slices P is used. However, this is, strictly speaking,

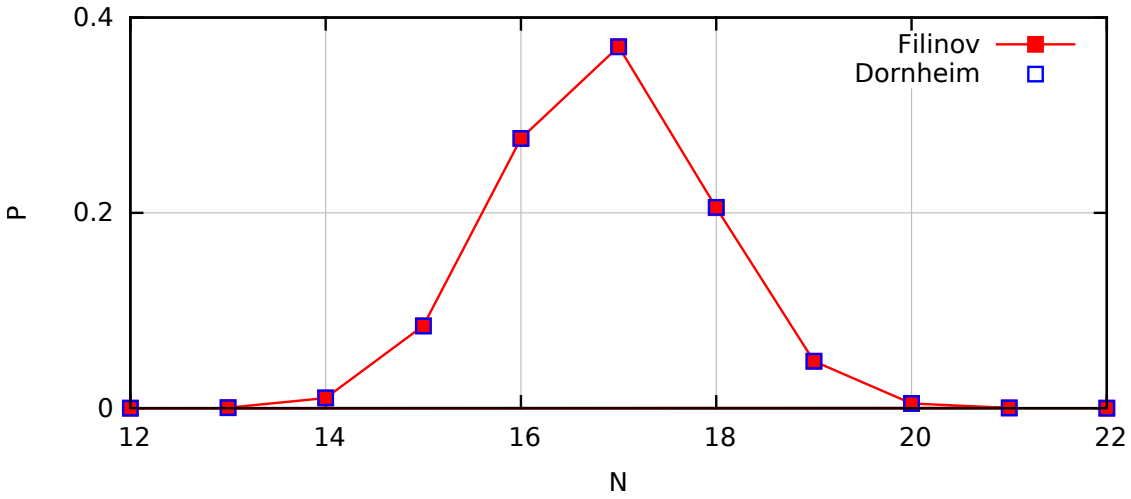

Figure 16: ***Comparison of the grandcanonical data:*** The probability $P(N)$ for a specific particle number N is plotted over the latter for a $2D$ Coulomb system with $\lambda = 0.25$, $\beta = 5$, $P = 80$ and $\mu = 4.6$. The red curve has been obtained with the code by A. Filinov and the blue points with the author's.

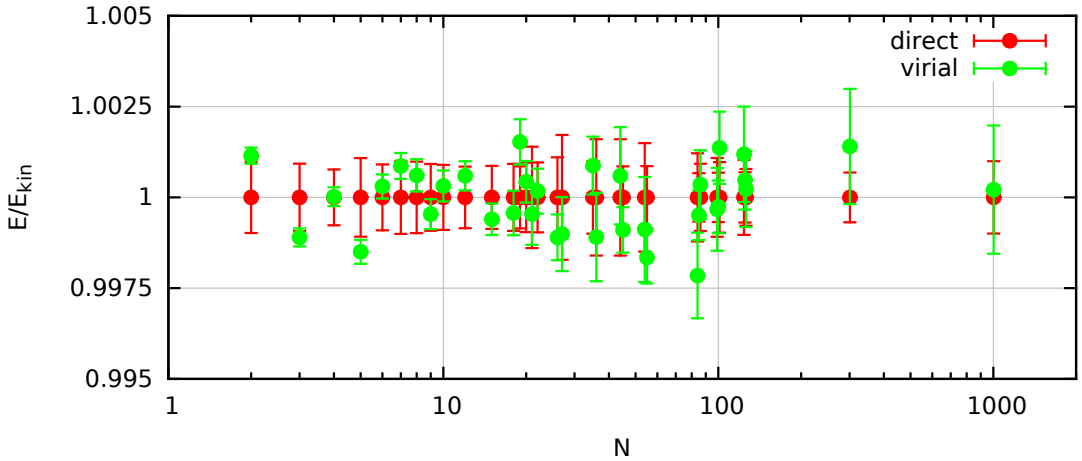

Figure 17: ***Check of the virial theorem:*** The kinetic energy - normalized to the result of the thermodynamic estimator - is plotted over the particle number N for a $2D$ Coulomb system with $\lambda = 3$ and $\beta = 5$. The red points have been obtained with the thermodynamic estimator and the green points with the virial theorem.

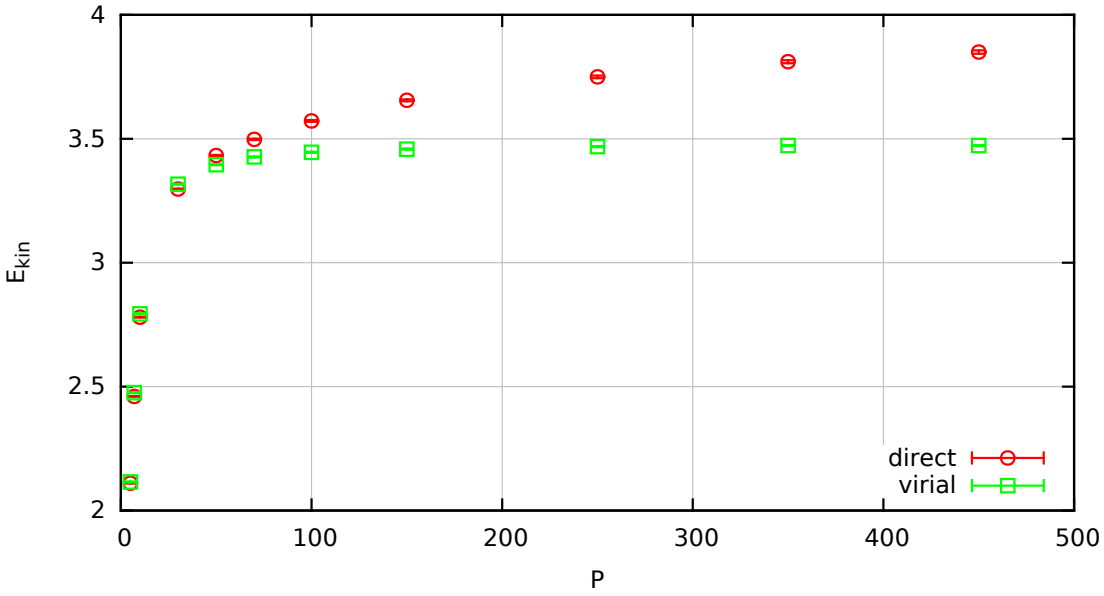

Figure 18: ***Effect of bad random numbers:*** The kinetic energy E_{kin} is plotted over the number of time slices P for a $2D$ Coulomb system with $N = 7$, $\beta = 5$ and $\lambda = 5$. The red curve has been obtained using the thermodynamic estimator and the green curve with the virial theorem.

not true. Any Monte Carlo algorithm assumes the availability of perfect random numbers which are not only correctly distributed but also completely uncorrelated. This would require the conduction of quantum mechanical measurements, like a double slit setup, for example. Such an approach is, however, not feasible for practical purposes. The solution is given by the development of pseudo random number generators, see e.g. [44]. These generate a deterministic chain of uniformly distributed numbers which are uncorrelated enough to be used in MC simulations. The quality of pseudo random numbers might be checked with the Kendall tests, as described in the textbook [24]. It is important for any developer of Monte Carlo code to be aware of this problem since it might drastically effect the quality of the simulation results. An example of the effect of bad random numbers is shown in Fig. 18, where the kinetic energy E_{kin} is plotted over the number of time slices P for a $2D$ Coulomb system with $\beta = 5$, $N = 7$ and $\lambda = 10$. The red points have been obtained using the thermodynamic estimator and the green points with the virial theorem. For $P < 50$, the virial results are systematically higher but for an increasing number of time slices the red curve seems to diverge. The discrepancy between the two kinetic energy datasets exceeds the magnitude of the errorbars, which means that the outcome of the simulation must be incorrect. The explanation for the wrong data is the application of the C++ default random number function rand(). The latter is based on a very simple algorithm with a short period and a high degree of correlation and is absolutely inappropriate for Monte Carlo simulations [45]. A suitable alternative is given by the Mersenne Twister [46], as implemented in the C++11 library ⟨rand⟩.

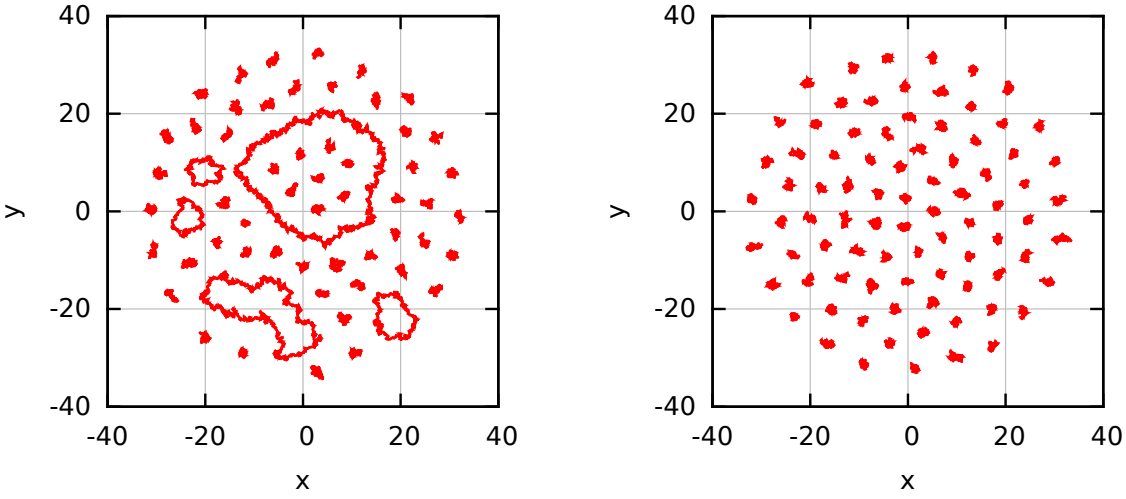

Figure 19: ***Example for artefacts:*** Two PIMC snapshots of $N = 84$ particles are plotted in the x-y-plane. The left and right image have been obtained without and with additional Boltzmannon equilibration steps, respectively. The simulation parameters are $\lambda = 300$, $\beta = 4$ and $P = 100$.

3.4 Improvements

In computational physics, there usually is no such thing as the perfect algorithm and some useful improvements to the standard worm algorithm are discussed in the following section.

3.4.1 Boltzmannon equilibration steps

One possible and relatively simple improvement is to start the simulation with an equilibration procedure without any particle exchange. In the implemented scheme, the particles are inserted as closed trajectories on all P time slices. The other possible updates in this phase are the single particle *Move*, *Bisection* and a modified *Remove*, which deletes an entire particle. This means that no off-diagonal configurations and macroscopic paths occur. Hence, the generated configurations correspond to a grandcanonical ensemble of Boltzmannons. The Boltzmannon equilibration is an indenspensible tool for the simulation of very strongly correlated systems. This is demonstrated in Fig. 19 where two snapshots from PIMC simulations with $N = 84$ particles are plotted in the x-y-plane for a $2D$ Coulomb system with $\lambda = 300$, $\beta = 4$ and $P = 100$. The left image has been obtained without the Boltzmannon equilibration and five exchange cycles occur. However, these are not physical effects but rather undesireable artefacts. In the beginning of the simulation, a first worm is inserted into the empy system. Since there are no other particles to interact with, there is a very high probability that it will advance several times P long in the imaginary time because the chemical potential μ is dominating. Similar update cycles might happen a few times until, finally, a balance between μ and the potential energy is achieved and all the new particles will behave classically. The problem is that in order to remove the long exchange cycles from the first few updates, the trajectory must be openend and a *Swap* or several *Recede*s have to be accepted. The strong coupling will, with a high probability, prevent the *Swap* and the chemical potential the *Recede* since the latter corresponds to the removal of a particle. The right image of the figure shows a snapshot of the same system but with the Boltzmannon equilibration procedure. In this case, the artefacts,

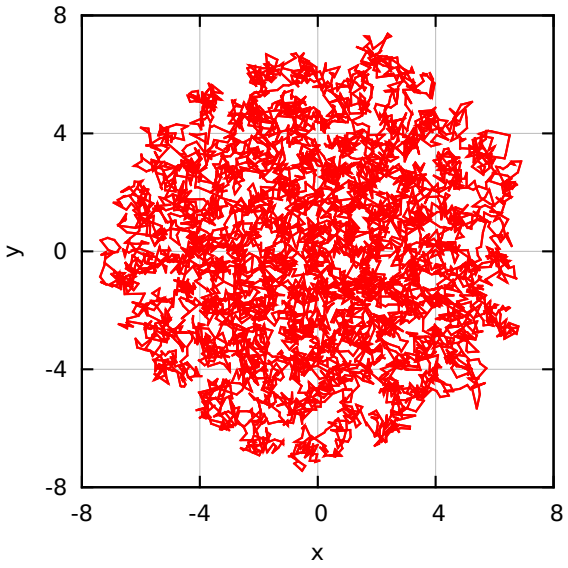

Figure 20: ***PIMC snapshot of a strongly degenerate system:*** A random configuration is shown for a $2D$ dipole system with $\lambda = 2.5$, $\beta = 4$, $P = 80$ and $N \approx 88$.

obviously, cannot be created in the beginning and the resulting configurations can be used to perform measurements.

It is also noteworthy that this equilibration does not cause any errors or artefacts for very degenerate systems, where macroscopic exchange cycles are expected. This is because, in such cases, the usual worm algorithm will sample the exchange starting from Boltzmannons as well. The only slight disadvantage is that the total equilibration of the system might take a little longer since all the exchange has to be sampled after the creation of the particles and is not generated in the beginning. Nevertheless, starting with Boltzmannons is always the safe thing to do.

3.4.2 Artificial potential between head and tail

Another difficulty for the WA-PIMC algorithm occurs in strongly degenerate systems. A PIMC snapshot from such an example is shown in Fig. 20 for a $2D$ dipole system with $\lambda = 2.5$, $\beta = 4$, $P = 80$ and $N \approx 88$. Nearly all particles are involved in exchange cycles and, thus, form macroscopic trajectories over the entire system. This means that the *Swap* update enjoys a high probability since the mean interparticle distance is smaller than the thermal de Broglie wavelength. The bottleneck of this feature is that the worm's head might be swapped several times until there appears a large difference between $\mathbf{r}_\Psi$ and $\mathbf{r}_{\Psi^\dagger}$. When the two are spatially separated too much, the trajectory cannot be closed any more. In such a case, one has to wait until head and tail are swapped together closely enough by chance and hope that, in this particular configuration, *Close* is proposed and accepted. This means that changes between the off-diagonal and diagonal sector will only seldomly occur, which causes higher autocorrelation times. A possible solution to this problem is the introduction of an additional artifical potential term $U(\mathbf{r}_\Psi, \mathbf{r}_{\Psi^\dagger})$ which influences the relative distribution of head and tail [47]. A natural choice

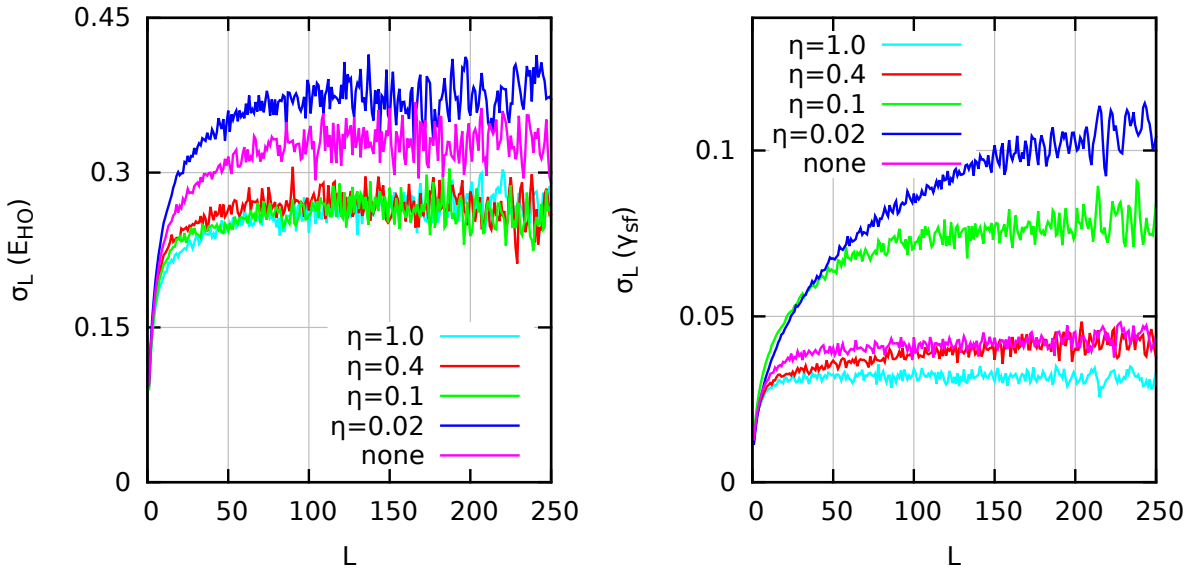

Figure 21: ***Autocorrelation effects with and without the artifical potential:*** The outcome of a binning analysis is shown for the system from Fig. 20 for the potential energy due to the confinement E_{HO} (left) and the superfluid fraction γ_{sf} (right). The color assignment distinguishes different artifical potentials.

is

$$U(\mathbf{r}_\Psi, \mathbf{r}_{\Psi^\dagger}) = \frac{1}{\Omega} \exp\left(-\frac{(\mathbf{r}_\Psi - \mathbf{r}_{\Psi^\dagger})^2}{2\eta\lambda_{\mathrm{dB}}^2}\right) \quad , \tag{55}$$

with the unimportant normalization Ω and a control factor η which can be used to tune the effects. With $\eta = 1$, Eq. (55) is simply a gaussian distribution of $\mathbf{r}_\Psi$ around $\mathbf{r}_{\Psi^\dagger}$ with the thermal de Broglie wavelength as the variance. This choice is well suited to the problem since it is ensured that the head and tail will be most probably in a range towards each other where the closing of the trajectory is at least possible. Decreasing η will narrow the gaussian and, therefore, head and tail will be located even more closely together. However, a too small choice of the control parameter can prevent exchange in cases where it is actually wanted by the system and, thus, create ergodicity problems or at least drastically increase the autocorrelation time. Hence, the implementation and tuning of the artifical potential needs to be considered carefully.

The effect of the artifical potential is illustrated in Fig. 21, where the results of a binning analysis for the system from Fig. 20 are presented for the potential energy due to the harmonic trap E_{HO} (left) and the superfluid fraction γ_{sf} (right). As usual, the error σ_L is plotted over the corresponding blocklength L and for all five simulations the same number of measurements have been obtained. The left picture reveals that the lowest error and, thus, autocorrelation time occurs for an activated potential between head and tail with the control parameters $\eta = 1.0$ (turquoise), $\eta = 0.4$ (red) and $\eta = 0.1$ (green). A too strict potential indeed dramatically increases correlation effects and the corresponding dark blue curve indicates even more correlation effects than in the simulation without the additional term (purple). The right picture shows the same analysis for the superfluid fraction, but with a different outcome. Here, the choice $\eta = 0.4$ only slightly reduces the autocorrelation time, while $\eta = 0.1$ and $\eta = 0.02$ both dramatically increase the correlated error. The blue curve has not even converged yet, which means that

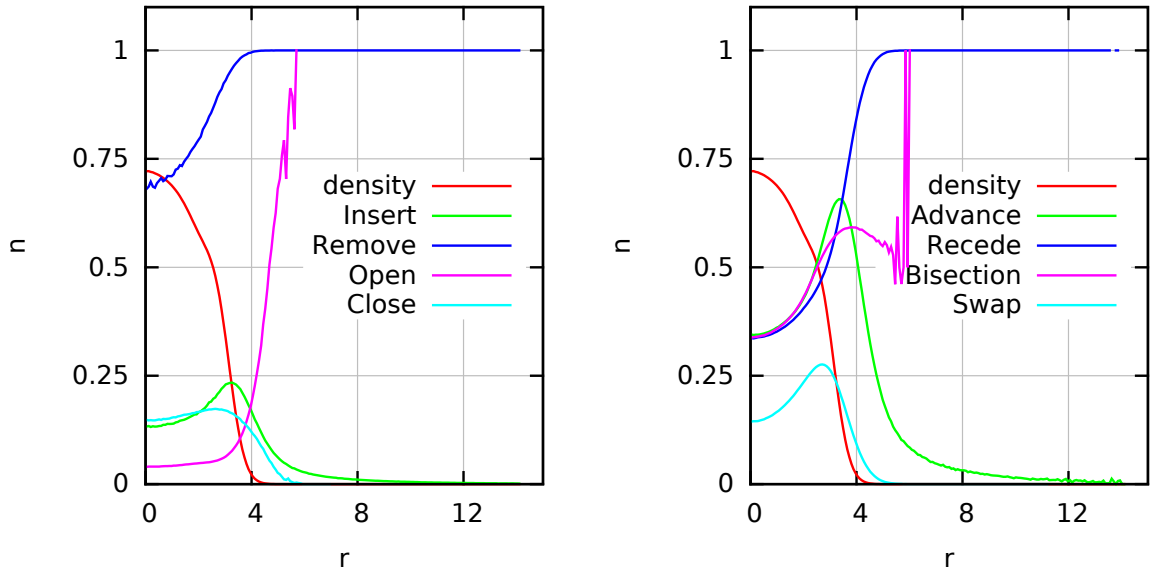

Figure 22: ***Local acceptance ratios for a small system:*** The radial density n and the local acceptance ratios of the updates are plotted over the distance to the center of the trap r for a $2D$ system of $N \approx 19$ dipole-interacting particles with $\lambda = 0.5$, $P = 300$, $\beta = 5$ and $\mu = 7.4$.

the corresponding Markov chain is not a representative selection from the entire configuration space since some region with a characteristic feature for the superfluid fraction is not sufficiently included. Only the natural choice of $\eta = 1.0$ leads to a significant improvement. The potential energy E_{HO} is only sensitive to the spatial distribution of the single beads which are updated in both the off- and diagonal sector nearly equally. Hence, it does not strongly matter for this quantity how often the interparticle exchange in the system is updated. The superfluid fraction, on the other hand, strongly depends on the quality of the exchange cycles since the latter are essential for the area which is enclosed by the paths, see section 4.2 for a detailed discussion. A too strict artifical potential between head and tail only allows for a sampling of exchange in a close circle around $\mathbf{r}_{\Psi^\dagger}$ and, thus, significantly reduces the ergodicity of macroscopic trajectories. It is also very interesting to note that the critical update pair *Open*/*Close* enjoys the highest acceptance ratios for $\eta = 0.02$. This means that high acceptance ratios do not guarantee an efficient algorithm.

3.4.3 Local acceptance ratios

The last extension of the PIMC implementation to be presented in this work does not enhance the performance but provides a better insight into some difficulties that appear for the simulation of strongly inhomogenous systems. The probability to accept a particular update from the worm algorithm scheme depends on the spatial location of the worm's head or the entire particle of interest. This implies that, at some positions in the trap, the configurations are less efficiently updated than elsewhere. The first testcase is a $2D$ system of $N \approx 19$ dipole-interacting particles with $\lambda = 0.5$, $\beta = 5$ and $P = 300$. The system is in the superfluid phase and the density is shown as the red curve in Fig. 22. The other datasets correspond to the spatially resolved acceptance ratios of several updates. The radial density exhibits a parabola-like form and vanishes around $r \approx 4$. The highest probability to insert a new piece of trajectory (green) is at the boundary

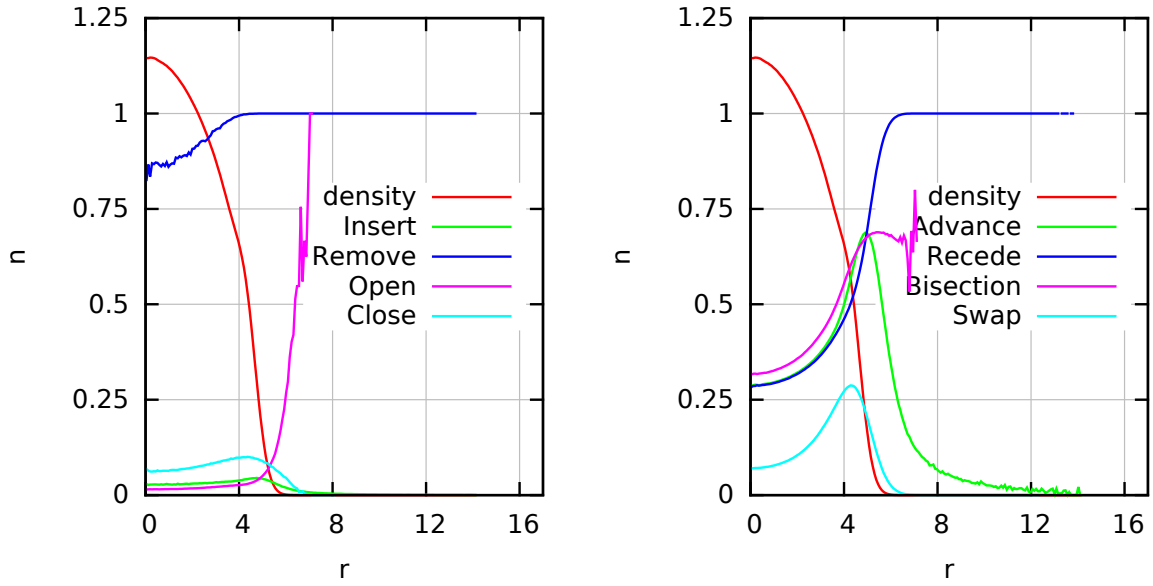

Figure 23: ***Local acceptance ratios for a medium system:*** The radial density n and the local acceptance ratios of the updates are plotted over the distance to the center of the trap r for a $2D$ system of $N \approx 59$ dipole-interacting particles with $\lambda = 0.5$, $P = 300$, $\beta = 5$ and $\mu = 14.4$.

of the system, where the density is already significantly decreased, while the confinement is not too high. In the center of the trap, the acceptance ratio is still quite high, while it vanishes for increasing r. The local acceptance ratio for the *Close* (turquoise) update has a similar shape for the same reasons. The updates *Remove* (blue) and *Open* (purple), however, exhibit the opposite behaviour since here already existing pieces of trajectory are attempted to be removed. This is most probable for large r, where the external confinement causes large punishments, and both ratios decrease with the distance to the center of the trap. The *Recede* update (blue) is very similar to the purple and blue curve in the left image and *Swap* (turquoise) and *Advance* (green) to the green one. Only the *Bisection* move behaves a little differently since it is nothing else than a combination of opening and closing a path and, therefore, combines the behaviour of those two updates.

The inhomogeneity of the acceptance ratios increases for larger systems, as it is illustrated by Fig. 23, where the same information is shown for a similar system as Fig. 22 but with $\mu = 14.4$ and $N \approx 59$ particles. The most worrysome changes are the decreased acceptance ratios of *Open*, *Close* and *Insert* and the reduced probability for *Swap* in the center of the trap. It is, in principle, possible to adjust the free algorithmic parameter M in a way to achieve any desired total acceptance ratio for the latter update. However, the inhomogeneity of the spatially resolved quantity remains and the system's inner core is more correlated than the boundaries. Finally, Fig. 24 shows two random PIMC snapshots for the small (left) and medium (right) system. It is not hard to imagine that a path in the dense center of the right image is much harder to deform than in the left one.

The most trivial solution to overcome this bottleneck is the implementation of two different update lists (i.e., Swap_1 and Swap_2, etc.) with differently chosen free algorithmic parameters M_i and C_i. The first list can be optimized to deliver good acceptance ratio at the center of the trap and the second one at the boundaries. In this way, all parts of the system will be efficiently updated. The inefficiency of the second list for small r is not a serious problem since, in the

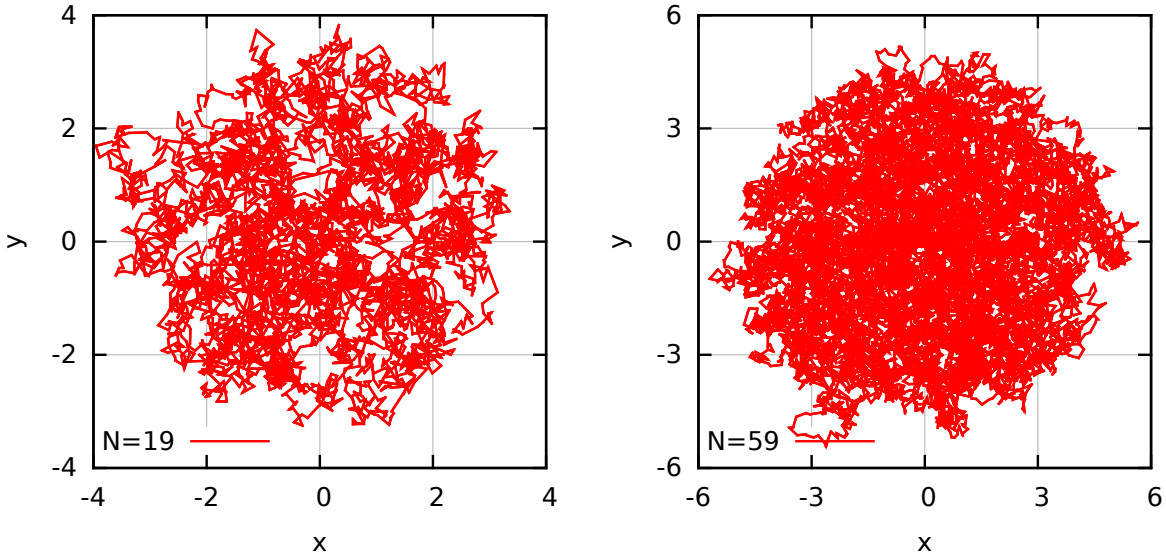

Figure 24: ***PIMC snapshots of the two test systems:*** Two random configurations are shown for the systems from Fig. 22 (left) and 23 (right).

worst case, the required number of Monte Carlo steps has to be doubled (assuming that updates from both lists have the same probability to be selected and that updates from list two will always be rejected), which is feasible in every case.

3.5 Capability of the implementation

The presented implementation of the worm algorithm path integral Monte Carlo scheme is able to simulate particles at arbitrary temperature T, pair-interaction and coupling parameter λ and in any confinement potential. Although all results in this work are obtained for harmonic confinements, even highly irregular systems require no additional effort. Only recently, Bhattacharya and Ghosal [48] have used PIMC to investigate the melting of Coulomb-interacting Boltzmannons in a $2D$ confinement of the form

$$V_{\text{trap}} = \left(\frac{x^4}{b} + by^4 - 2\eta x^2 y^2 + \gamma(x-y)xy\sqrt{(x^2+y^2)} \right) \quad . \tag{56}$$

The outcome of the simulation of such a system with the author's code and Eq. (56) replacing V_{HO} in the Hamiltonian is presented in Fig. 25 for $N = 75$ particles with $\beta = 1$, $P = 80$ and $\lambda = 10$ and the potential parameters $b = \pi/4$, $\gamma = 0.15$ and $\eta = 0.6$. The left picture shows the density profile $n(x, y)$ and nicely demonstrates the system's irregularity. There appear four pronounced maxima in the corners and a local minimum in the center of the trap. The right image shows a random snapshot from the PIMC simulation and one can easily recognize that the extension of the particle's paths are of the same order as the mean interparticle distance. This means that exchange effects play a dominant role and the system behaves differently than the corresponding Boltzmannon pendant. The superfluid fraction (see section 4.2) is calculated as $\gamma = 0.415 \pm 0.005$ and the fermionic sign (see section 6) fluctuates around zero.

A missing feature in the code is the implementation of periodic boundary conditions to simulate homogenous systems. However, this feature is not needed for the systems of interest in this

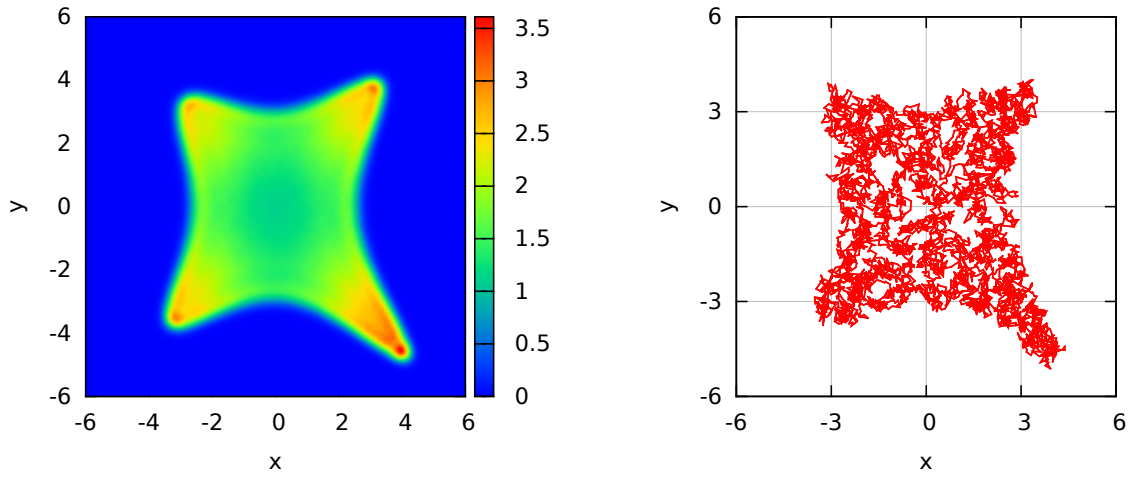

Figure 25: ***Simulation of a highly irregular trap:*** The density $n(x, y)$ (left) and a PIMC snapshot (right) with the confinement from Eq. (56) are shown for a $2D$ Coulomb system with $N = 75$, $\lambda = 10$, $\beta = 1$, $P = 80$ and the parameters $b = \pi/4$, $\gamma = 0.15$ and $\eta = 0.6$.

work and for e.g. Coulomb-interacting particles additional, nontrivial effort is required, namely the Ewald summation for the repression of boundary effects. Therefore, a further discussion of this matter is beyond the scope of this thesis and the interested reader is referred to [49]. The difficulties of simulating strongly coupled systems at low temperature are discussed in the appendix A.

4 General properties of confined bosons

Ensembles of mutually repelling bosonic particles in a harmonic confinement potential are strongly inhomogenous systems and exhibit many interesting features like e.g. Bose Einstein condensation [9]. For small systems, some properties like energies and superfluidity explicitly depend on the exact number of particles and, hence, the symmetry [18, 50, 51]. The following section starts with some brief examples of different phases of Coulomb-interacting particles in $2D$. Afterwards, the purely quantum mechanical phenomenon of superfluidity [52, 53, 54, 55] which manifests by the reduction of the system's moment of inertia due to exchange effects is introduced and investigated for both $2D$ and $3D$ systems. The analysis is extended by the consideration of a spatially resolved superfluid density [56] which provides a good insight to the inhomogeneity of the superfluid phase transition. Finally, spatial correlations are discussed considering the example of a strongly coupled Coulomb system which exhibits solid shells and superfluidity at the same time.

4.1 Radial density and shell structures

The shape of any trapped system is the result of the competition between the mutual repulsion between the particles and the confinement potential. The combination of different coupling parameters and temperatures yields several interesting regimes. In Fig. 26, three $2D$ systems of $N = 15$ Coulomb-interacting particles are presented in a solid, liquid and superfluid phase. The left column corresponds to the radial density n and, in the right one, random snapshots from the PIMC simulations are shown. The top row shows results for the inverse temperature $\beta = 10$, coupling parameter $\lambda = 100$ and number of time slices $P = 300$. The density exhibits two very clearly pronounced peaks with almost no overlap and, in the corresponding random configuration, two shells with five and ten particles appear. The solidity of the system is caused by the strong inter-particle interaction which makes disordered movements of individual particles improbable and separates different particles at a larger distance than their spatial extension, hence, exchange effects are suppressed. For completeness, it should be noted that the information presented in Fig. 26 is not sufficient to decide wether the system is completely solid or not, since rotations of the two shells with respect to each other might still occur. However, the application of more sophisticated spatial correlation functions is discussed in section 4.3. The central row corresponds to a system with $\beta = 0.75$, $\lambda = 10$ and $P = 100$. Here, the density profile is more or less flat and no distinct shell structure emerges. The random configuration in the right image directly reveals the lack of order in the system and the particle's extensions are, again, much smaller than their spatial separations. Hence, a system with such parameters might be categorized as a liquid. Finally, the bottom row shows the results for a system with $\lambda = 0.3$, $\beta = 5$ and $P = 300$. The density profile exhibits a parabola like shape with a smooth decay at the boundaries and a high density at the center of the trap. In this case, the repulsion between the particles is too weak to separate them and the random configuration in the right image reveals that all particles overlap. This implies that particle exchange plays a dominant role and indeed long exchange cycles involving several particles occur. The system is in the superfluid phase, as will be explained in section 4.2.

4.2 Superfluidity

Superfluidity, see e.g. [52, 53, 54, 57], is a purely quantum mechanical phenomenon. As early as 1937, the independent groups of Kapitsa and Misener discovered that liquid Helium below some critical temperature T_c partly behaves as if it had zero viscosity. Hence, the resulting frictionless

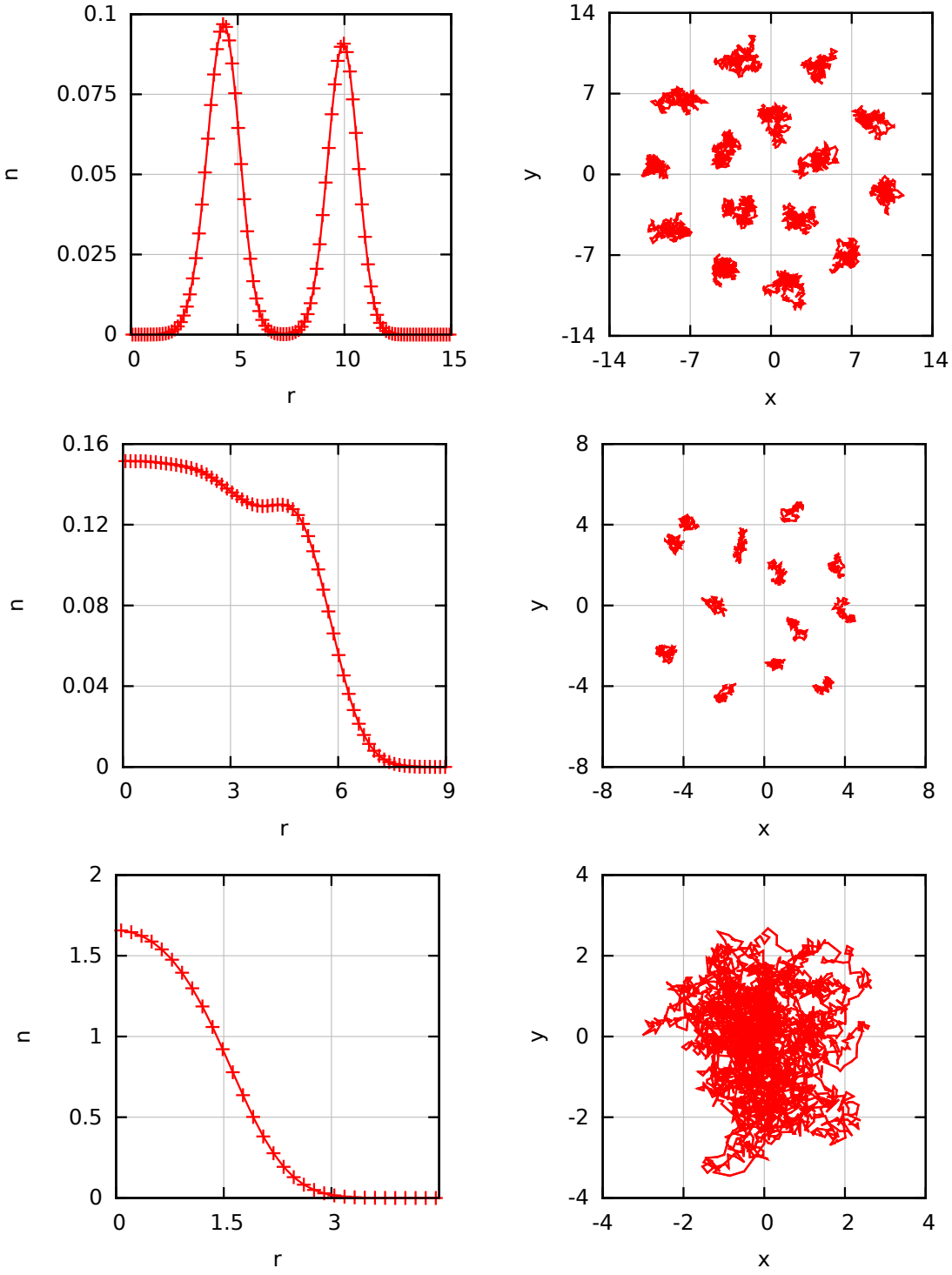

Figure 26: ***Comparison of different phases of*** $N = 15$ ***Coulomb-interacting particles in*** $2D$***:*** In the left column, the radial density n is plotted over the distance to the center of the trap r and, in the right column, random PIMC configurations are shown. The top row corresponds to a solid with $\beta = 10$, $\lambda = 100$ and $P = 300$, the center row to a liquid with $\beta = 0.75$, $\lambda = 10$ and $P = 100$ and the bottom row to a superfluid with $\beta = 5$, $\lambda = 0.3$ and $P = 300$.

flow of this *superfluid* component is the eponym of this peculiar phenomenon. Today, after more than seventy years of time to find a satisfying theoretical description, it has been shown that superfluidity in bulk systems is closely related (but not equal) to Bose Einstein condensation, i.e., the macroscopic occupation of the ground state due to Bose statistics [58], and a direct consequence of **O**ff-**D**iagonal **L**ong **R**ange **O**rder (ODLRO) of the density matrix throughout the entire system [55]. ODLRO, however, cannot directly apply to finite and, in particular, very small systems and the cause, consequences and even definition of superfluidity for few particles in a trap might be different, see e.g. [59] for an overview. In this work, the term is defined to describe the reduction of the system's moment of inertia due to quantum mechanical effects, regardless of any collective behaviour caused by the bosonic nature of the particles.

To investigate the predicted **N**on **C**lassical **R**otational **I**nertia (NCRI) one usually considers an experimental setup by Andronikashvili where the entire system is placed in a rod and rotated with an infinitesimally small angular frequency ω around the z-axis. The moment of inertia I, which explicitly depends on the temperature T, is directly accessible by measurements of the cycle duration T_p. For high T, the system behaves classically and I_cl is simply given by the usual expression

$$I_\mathrm{cl} = m \sum_{k=1}^{N} \left(\mathbf{r}_k^\perp \right)^2 \quad ,$$

with $\mathbf{r}_k^\perp$ being the $\mathbf{r}_k$-component in the x-y-plane. In the quantum mechanical regime, below some critical value T_c, however, not all particles participate in the rotation and the moment of inertia is reduced, i.e., NCRI. In the classical regime, the cycle duration

$$T_p = \frac{2\pi}{\omega} \propto \sqrt{I_\mathrm{cl}} \propto \sqrt{n}$$

is proportional to the squareroot of the moment of inertia and, therefore, to the total density, n. Below T_c, in the superfluid phase, the rotation is only sensitive to those particles which participate in the angular motion:

$$T_p \propto \sqrt{I(T)} \propto \sqrt{n_\mathrm{n}} = \sqrt{n - n_\mathrm{sf}} \quad ,$$

with the normal and superfluid density n_n and n_sf, respectively. The quantity of interest is the superfluid fraction γ_sf which is defined as the ratio of the superfluid and total density

$$\gamma_\mathrm{sf} = \frac{n_\mathrm{sf}}{n} = 1 - \frac{I(T)}{I_\mathrm{cl}} \quad . \tag{57}$$

The open task to investigate superfluidity with PIMC is the derivation of a connection between Eq. (57) and the path integral picture which has been achieved by Sindzingre et al. [35]. The basic idea is the consideration of the definition of the moment of inertia as the derivative of the angular momentum, L_z, at the limit of zero angular motion

$$I(T) = \left. \frac{\mathrm{d} \langle L_z \rangle}{\mathrm{d}\omega} \right|_{\omega \to 0} \quad . \tag{58}$$

The expectation value in Eq. (58) is then written in the path integral picture via the usual decomposition of $\hat{\rho}$ and the insertion of the $P-1$ unities and, after applying some algebra, one finally arrives at the desired expression

$$\gamma_\mathrm{sf} = \frac{4m^2 \langle A_z^2 \rangle}{\hbar^2 \beta I_\mathrm{cl}} \quad . \tag{59}$$

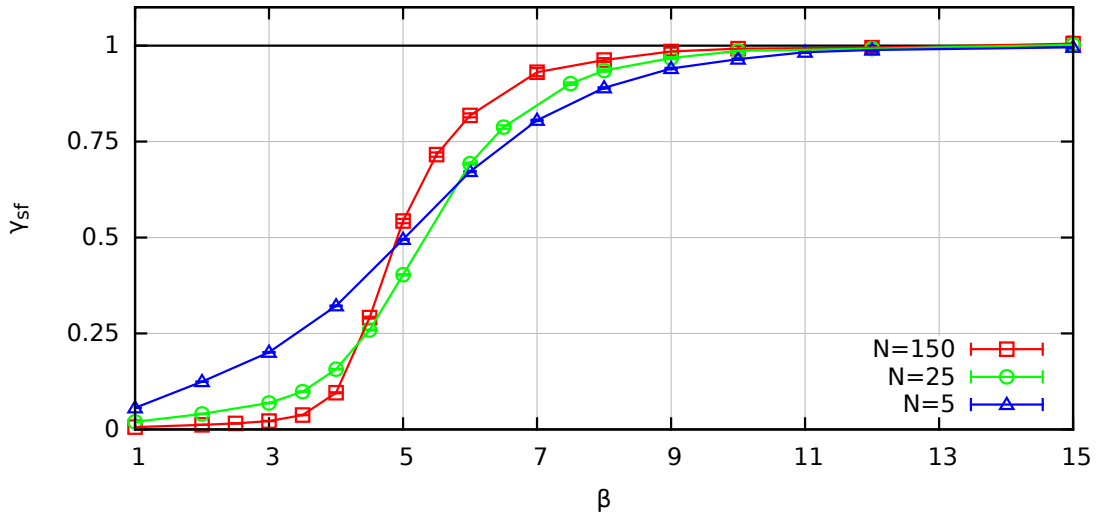

Figure 27: ***Superfluid phase transition of a*** $3D$ ***Coulomb system:*** The superfluid fraction γ_{sf} is plotted over the inverse temperature β for a $3D$ Coulomb system with $\lambda = 10$ and $N = 150$ (red), $N = 25$ (green) and $N = 5$ (blue) particles. The data for $N = 150$ is published in [60].

Here, A_z denotes the area which is enclosed by the paths of all particles in the x-y-plane and the total area vector is given by

$$\mathbf{A} = \frac{1}{2} \sum_{k=1}^{N} \sum_{i=0}^{P-1} (\mathbf{r}_{k,i} \times \mathbf{r}_{k,i+1}) \qquad .$$

Equation (59) implies that the transition to the superfluid phase is directly connected to the formation of macroscopic exchange cycles between multiple particles since this dramatically increases $\mathbf{A}$. In the classical phase, however, the particles are point-like and no exchange occurs. Therefore, the area vanishes and the superfluid fraction becomes zero.

The superfluid phase transition of a $3D$ Coulomb system with relatively strong coupling, $\lambda = 10$, is illustrated in Fig. 27, where γ_{sf} is plotted over the inverse temperature β for $N = 5$ (blue), $N = 25$ (green) and $N = 150$ (red) particles. All three curves start from a very low superfluid fraction at $\beta = 1$ and monotonically increase until they converge towards $\gamma_{\mathrm{sf}} = 1$, i.e., a completely superfluid system. The red curve exhibits a much sharper transition than the other two datasets. This is expected since, for small particle numbers, finite size effects play an important role and the transition is broadened, see e.g. [61]. Above $\beta = 5$, the largest system has the largest superfluid fraction because the density in the center of the trap is higher than for fewer particles, which leads to more particle exchange. For small β, the blue curve clearly exceeds the other two since here, even without particle exchange throughout the entire system, the finite extension of the trajectories in the path integral picture significantly contributes to A_z, while, for $N = 150$, the classical moment of inertia in Eq. (59) dominates, if not (almost) all particles are involved in macroscopic exchange cycles. The aforementioned manifestations of the onset of superfluidity are nicely illustrated by the comparison of random PIMC snapshots for different β. In Fig. 28, such random configurations for the transition of $N = 150$ particles are plotted, namely for $\beta = 1$ (top left), $\beta = 3$ (top right), $\beta = 5$ (bottom left) and $\beta = 7$ (bottom right). For $\beta = 1$, the particle extension is much smaller than the mean interparticle distance

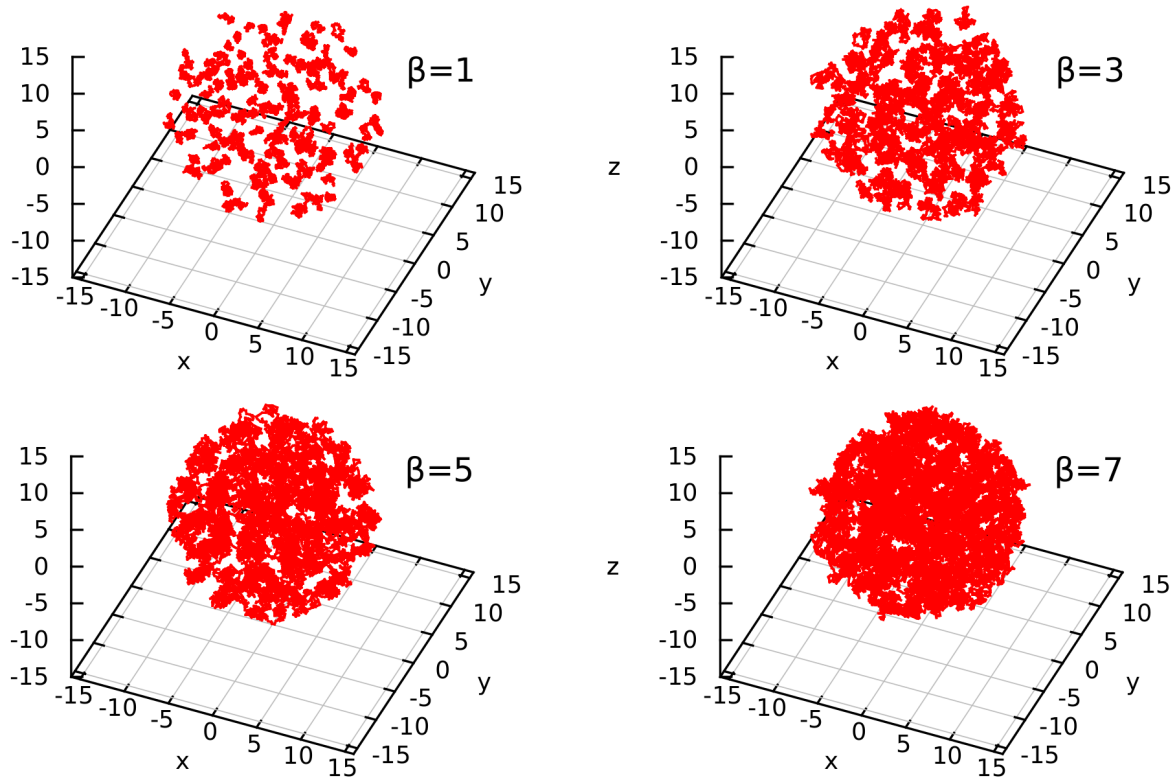

Figure 28: ***PIMC snapshots at different temperatures:*** Random PIMC snapshots from the simulations of $3D$ Coulomb systems with $N = 150$ particles and $\lambda = 10$ are shown for $\beta = 1$, $\beta = 3$, $\beta = 5$ and $\beta = 7$.

and the system behaves almost classically. The snapshot at $\beta = 3$ exhibits clearly extended particle paths but the mean interparticle distance is still slightly larger and almost no exchange is visible. Hence, the superfluid fraction nearly equals zero, again. For $\beta = 5$, a lot of exchange cycles occur and the system is in the middle of the superfluid phase transition with $\gamma_{\text{sf}} > 0.5$. Finally, at $\beta = 7$, the system is almost completely superfluid and the snapshot clearly reveals macroscopic exchange cycles with multiple particles involved.

A related topic is the investigation of possible connections of other static properties to the phase transition. In Fig. 29, the radial density n is plotted over the distance to the center of the trap r for the same system and $\beta = 1$ (turquoise), $\beta = 2$ (purple), $\beta = 3$ (blue), $\beta = 5$ (green) and $\beta = 10$ (red). All shown curves exhibit a quite similar behaviour, that is, a flat structure at the center of the trap and a shell-like oscillation at the boundary. The latter feature becomes more pronounced for smaller temperatures due to increased correlation effects. For $\beta = 10$, the system is completely superfluid and n does approximately represent the ground state density. At $\beta = 5$, in the middle of the phase transition, the radial density is still nearly equal to the red curve. This is a very interesting result since it implies that, in this case, the system's spatial properties are not drastically affected by superfluidity. This notion becomes even clearer by considering the curve for $\beta = 3$, i.e., the density of a system without any superfluidity. The blue curve only slightly deviates from the red and green ones as well, despite the phase transition. Finally, for $\beta = 1$, the density changes more significantly and the shell-like oscillations near the center of the trap are lost, only the outermost maximum is still pronounced, although decreased. Another interesting research topic is the comparison of the superfluid phase transition between

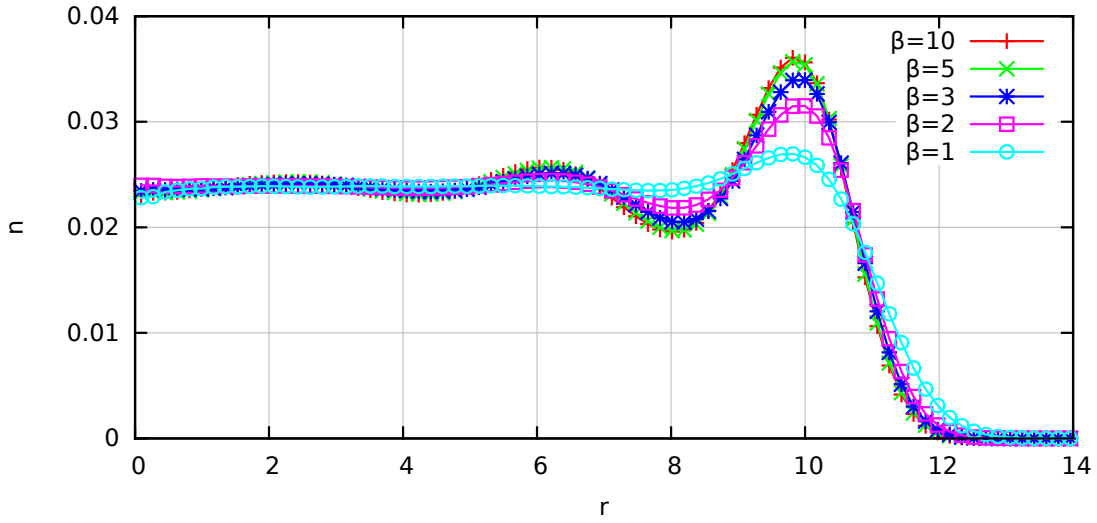

Figure 29: ***Temperature dependence of the radial density:*** The radial density n is plotted over the distance to the center of the trap r for a $3D$ Coulomb system with $N = 150$, $\lambda = 10$ and different β.

$2D$ and $3D$ systems. In Fig. 30, the superfluid fraction γ_{sf} is plotted for the system with $N = 150$ particles from Fig. 27 (red) and the $2D$ pendant (green) with the same parameters. Both curves exhibit a similar behaviour, that is, a γ_{sf} which runs between zero and unity with roughly the same slope. The $2D$ system, however, enters the phase transition much earlier and, hence, becomes a complete superfluid for lower inverse temperatures. This interesting feature could be caused by different effects. The most intuitive explanation is a lower density in the $3D$ case which results in less exchange and, therefore, a smaller total area in every direction. The later onset of superfluidity would then simply be a degeneracy effect. Another possible explanation is the explicit three dimensional nature of the particle exchange. The superfluid fraction is sensitive only to the component of the total area vector in the plane perpendicular to the axis of rotation, e.g. the x-y-plane. However, if a particle is already involved in an exchange cycle which mainly contributes to the **A**-component in another plane, the probability to include the former into another cycle might be reduced. This implies that the availability of an additional dimension effectively reduces the area in a particular plane and, hence, the superfluid fraction. To answer which (if any) of the two proposed explanations is correct, one might consider a degeneracy parameter of the form

$$\chi_0 = n_0 \lambda_\beta^d \quad , \tag{60}$$

with the dimensionality d. Equation (60) provides a measure for the number of particles within the approximate extension of a single particle wavefunction, with the density at the center of the trap $n_0 = n(r = 0)$ serving as a reference. Fig. 31 shows χ_0 as a function of the inverse temperature for the system of interest and reveals that the characteristic value of $\gamma_{\text{sf}} = 0.5$, which might be used to define the critical temperature of the phase transition and is illustrated by the blue triangles, requires an even slightly higher degeneracy parameter in the $2D$ system. Although this result should not be overinterpreted, since the densities in both systems are not constant and, thus, making the choice of χ_0 arbitrary to some degree, it nevertheless rules out the second explanation for the later phase transition in $3D$. For the latter, the same value of the

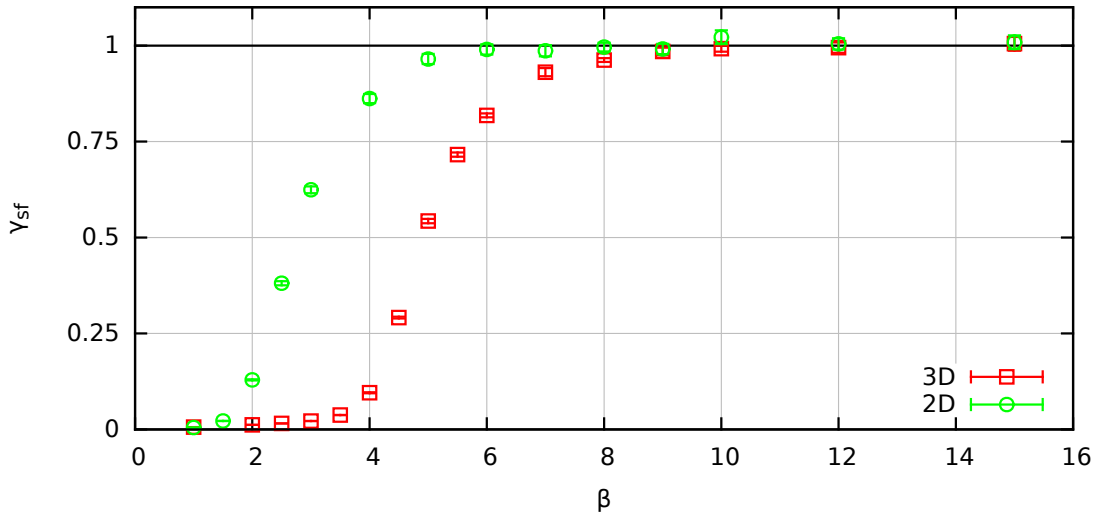

Figure 30: ***Superfluid phase transition in*** $2D$ ***and*** $3D$***:*** The superfluid fraction γ_{sf} is plotted over the inverse temperature β for a Coulomb system with $N = 150$ and $\lambda = 10$. The red and green curve correspond to three and two dimensions, respectively. This data is published in [60].

total superfluid fraction would have required a clearly higher degeneracy parameter in the $3D$ system. Fig. 32 shows another degeneracy parameter χ where the density n_0 from Eq. (60) has been replaced by an average over the approximate extension of the system. Here, the correlation between the superfluid fraction and the degeneracy is even more clear and both the $2D$ and $3D$ system exhibit roughly the same χ for the phase transition at $\gamma_{\mathrm{sf}} = 0.5$. In conclusion, the later onset of superfluidity in the three dimensional system has been revealed as a degeneracy effect and is not caused by the availability of an additional direction for the particle exchange. These results are published in [60], and the additional analysis of the sampling frequency of exchange cycles confirms this explanation.

4.2.1 The local superfluid density

Trapped quantum particles, even in the case of a purely harmonic oscillator confinement, are strongly inhomogenous systems. Therefore, it is highly desireable to obtain spatially resolved information about the system of interest. In the case of superfluidity, such a tool is given by the local superfluid density estimator by Kwon et al. [56]. Filinov et al. [50] have used this quantity to investigate the ground state radial distribution of superfluidity in small clusters of strongly coupled Coulomb-interacting bosons in a $2D$ harmonic confinement. It was found that the superfluid density n_{sf} is decreased and pushed to the outer shell if the system size corresponds to a magic number $N = 12, 19, \ldots$ with strong hexagonal symmetry in the center of the trap. For other particle numbers, like e.g. $N = 21$, the maximum of n_{sf} is located in the inner shells. Khairallah et al. [62] have analyzed the influence of these magic numbers on parahydrogen clusters, although here the reduction of superfluidity mainly occured for larger systems with $N \geq 23$. Mezzacapo and Boninsegni [63] and Idowu and Boninsegni [64] have applied the superfluid density estimator to the investigation of parahydrogen clusters and found that, at low temperature, the superfluidity is distributed almost uniformly among the pronounced shell structure of the system, due to the formation of exchange cycles involving all the molecules. Only

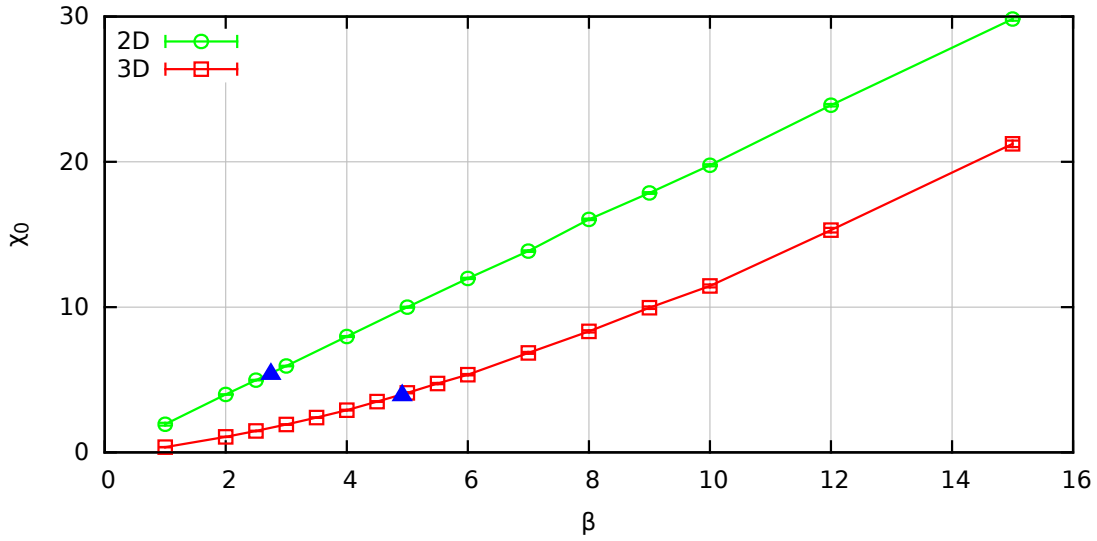

Figure 31: ***The degeneracy parameter in*** $2D$ ***and*** $3D$***:*** The degeneracy parameter χ_0 is plotted over the inverse temperature β for the system from Fig. 30. The green and red curve correspond to $2D$ and $3D$, respectively, and the blue triangles mark the critical inverse temperature.

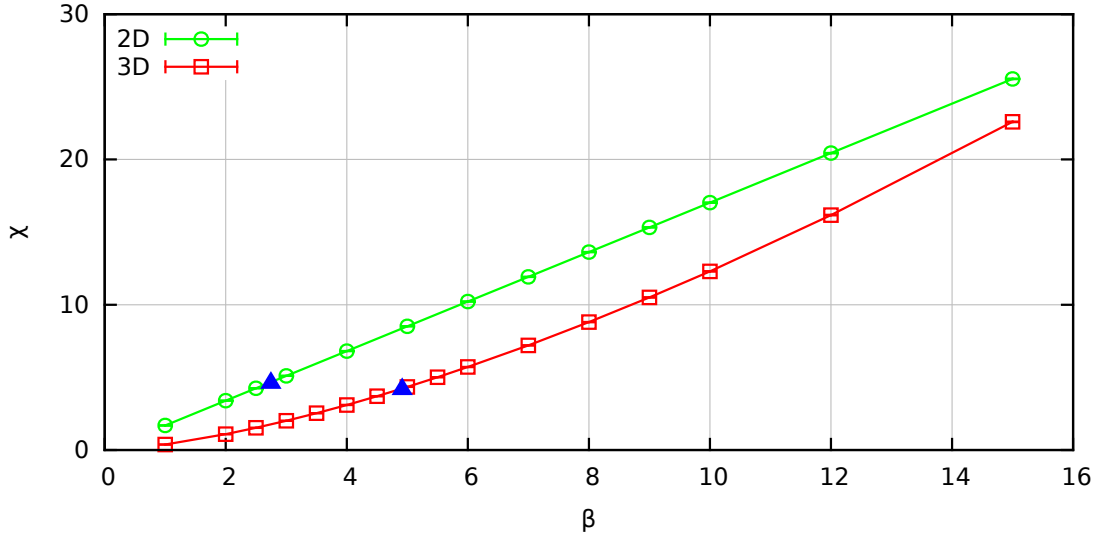

Figure 32: ***The averaged degeneracy parameter in*** $2D$ ***and*** $3D$***:*** The averaged degeneracy parameter χ is plotted over the inverse temperature β for the system from Fig. 30. The green and red curve correspond to $2D$ and $3D$, and the blue triangles mark the critical inverse temperature. This data is published in [60].

recently, Kulchytskyy et al. [65] have simulated ^{4}HE in a nanopore and it has been revealed that the finite superfluid fraction, even at low temperature, is due to a suppression of superfluidity near the pore walls. In this work, the superfluid density is investigated for larger particle numbers of Coulomb-interacting bosons in a $2D$ harmonic confinement at finite temperature.

The basic idea behind the estimator is to make use of the Landau two fluid model, where the total density is decomposed into the normal and superfluid contribution [57]:

$$n = n_\mathrm{n} + n_\mathrm{sf} \quad .$$

Hence, the moment of inertia might be written as

$$I(T) = m \int \mathrm{d}\mathbf{r} \;\; (n(\mathbf{r}) - n_\mathrm{sf}(\mathbf{r}))\, \mathbf{r}_\perp^2 \quad . \tag{61}$$

The first term can be identified with the classical moment of inertia

$$I_\mathrm{cl} = m \int \mathrm{d}\mathbf{r} \; n(\mathbf{r}) \mathbf{r}_\perp^2 \quad .$$

A combination of the Eqs. (57) and (59) with (61) implies

$$m \int \mathrm{d}\mathbf{r} \; n_\mathrm{sf}(\mathbf{r}) \mathbf{r}_\perp^2 \stackrel{!}{=} \frac{4m^2}{\beta\hbar^2} \langle A_z \rangle^2 \quad ,$$

which yields the following expression for the superfluid density

$$n_\mathrm{sf}(\mathbf{r}) = \frac{4m}{\beta\hbar^2 I_\mathrm{cl}(\mathbf{r})} \langle A_z A_{z,\mathrm{loc}}(\mathbf{r}) \rangle \quad , \tag{62}$$

with the local area

$$\mathbf{A}_\mathrm{loc}(\mathbf{r}) = \frac{1}{2} \sum_{k=1}^{N} \sum_{i=0}^{P-1} (\mathbf{r}_{k,i} \times \mathbf{r}_{k,i+1})\, \delta(\mathbf{r} - \mathbf{r}_{k,i}) \quad .$$

For completeness, it is reported that the estimator from Eq. (62) integrates to the correct moment of inertia $I(T)$, whereas other suggested quantities are inconsistent and, therefore, neglected in this work. The superfluid density has, in general, six spatial dependencies, namely the three coordinates for the position of the evaluation, $\mathbf{r}$, and the rotational axis, $\mathbf{e}_z$. In a harmonic confinement, however, the situation simplifies and for a $2D$ system it is sufficient to consider $\mathbf{e}_z$ always as perpendicular to the trap and to average the other spatial dependence over the angle, like for the usual radial density distribution n.

Fig. 33 shows the total and superfluid density of a $2D$ Coulomb system with $N = 16$ and $\lambda = 10$ for different inverse temperatures. The top left graph corresponds to $\beta = 12$ and the total density, n, (red) exhibits a more or less pronounced shell structure with two minima. The superfluid fraction has been calculated as $\gamma_\mathrm{sf} = 0.993 \pm 0.002$, which means that the system is completely superfluid. Thus, the red and green datapoints are nearly identical. The superfluid density is afflicted with a much larger statistical uncertainty than n since the local area has both positive and negative contributions and, hence, n_sf suffers from a sign problem. For $\beta = 5$ (top right), n nearly coincides with the $\beta = 12$ result but the superfluid fraction $\gamma_\mathrm{sf} = 0.544 \pm 0.002$ is considerably smaller. The superfluid density exhibits a shell structure as well but the ratio of n_sf and n is larger for small r. This is expected since particles which are not located in the outermost shell have more neighbours available for an exchange. This increases the local

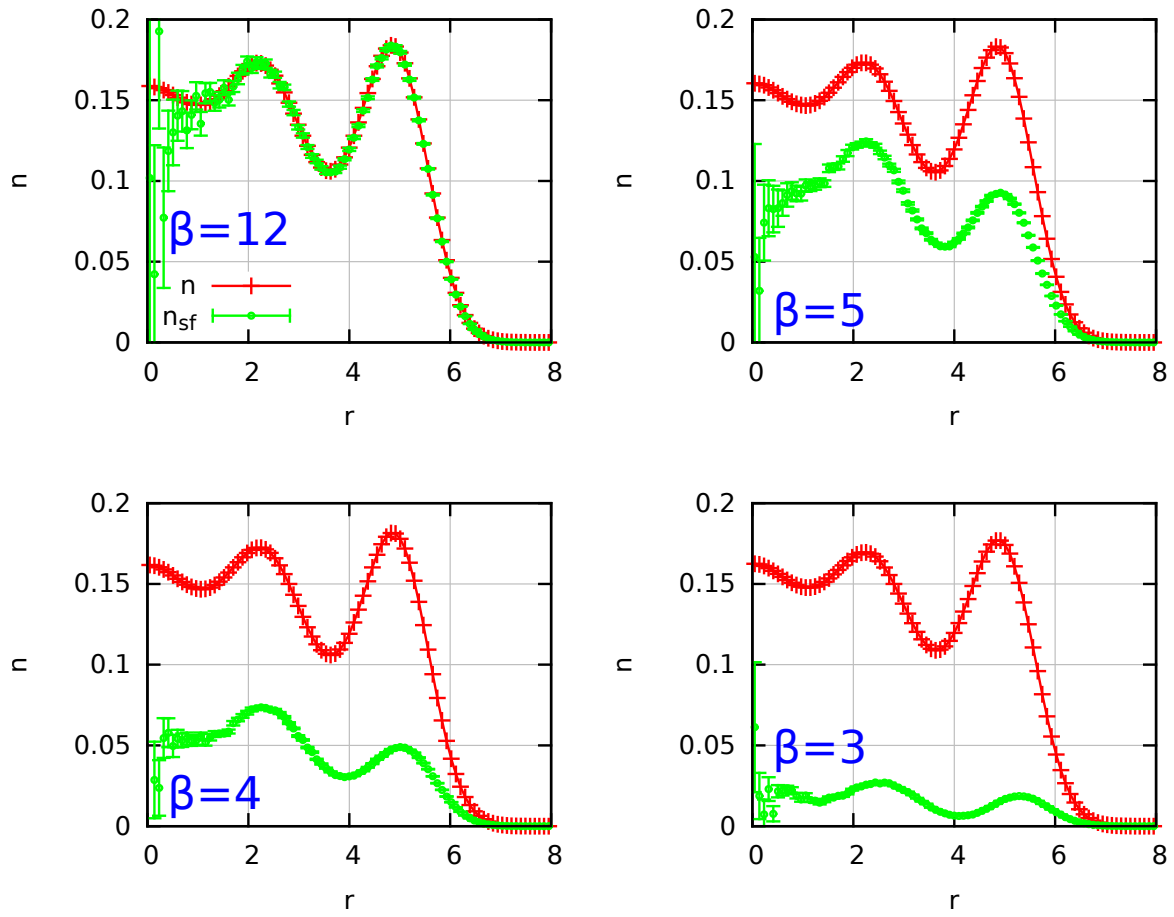

Figure 33: ***Local superfluid density of a*** $2D$ ***Coulomb system:*** The total and superfluid density n and n_{sf}, respectively, are plotted over the distance to the center of the trap r for a system with $\lambda = 10$ and $N = 16$. The four graphs correspond to the inverse temperatures $\beta = 12$, $\beta = 5$, $\beta = 4$ and $\beta = 3$.

area and, therefore, the superfluid density as well. At $\beta = 4$ (bottom left), the picture looks very similar. The superfluid fraction is now decreased to $\gamma_{\mathrm{sf}} = 0.305 \pm 0.001$ but the spatial distribution is almost the same. The last picture (bottom right) corresponds to $\beta = 3$ and $\gamma_{\mathrm{sf}} = 0.119 \pm 0.0005$. Despite the total decrease of the superfluidity, it is interesting to note that the two outermost maxima in n_{sf} appear at slightly larger r than in n. A possible explanation for this feature is a competition between shell configurations with different occupation numbers. The local area in a particular shell is increased if the number of particles and, thus, the density within it is higher. An additional particle, however, makes the shell a little more extended than the average density, which manifests in the superfluid density as described. Finally, Fig. 34 shows two random configurations from the simulations at $\beta = 12$ (left) and $\beta = 3$ (right). The particle distribution looks very similar in both pictures but the particle extension is much larger for $\beta = 12$ and long exchange cycles are present. In the right image, more than half of the particles are not involved in exchange. It again seems that the transition to the superfluid phase and the connected formation of macroscopic trajectories does not directly affect the total density distribution of the system.

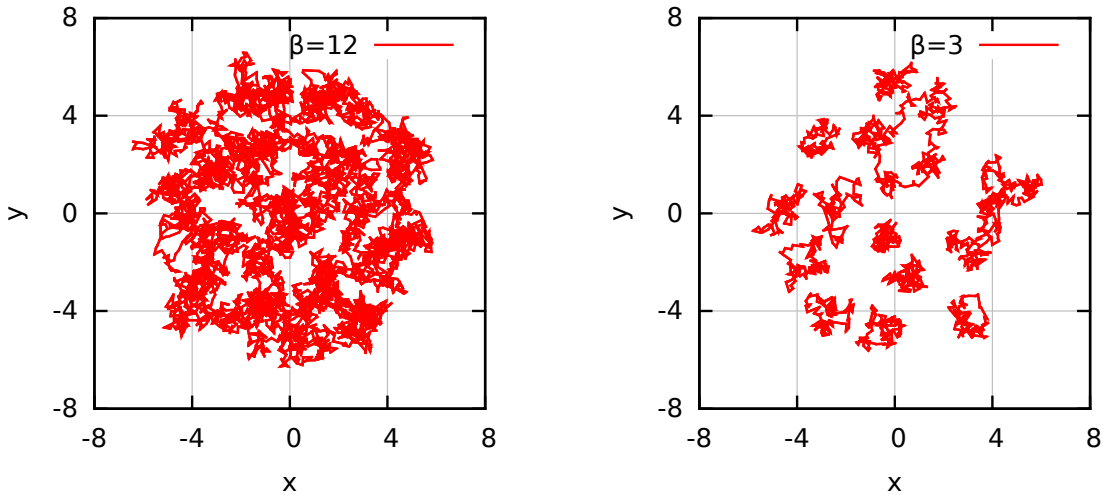

Figure 34: ***PIMC snapshots of a*** $2D$ ***Coulomb system:*** Two random configurations are shown from the simulation of the system in Fig. 33 for the inverse temperatures $\beta = 12$ (left) and $\beta = 3$ (right).

An even more interesting application of the superfluid density estimator is given by the locally resolved investigation of the superfluid phase transition of a larger system. The system of interest is again given by the $N = 150$ Coulomb-interacting particles with $\lambda = 10$ in $2D$ from Fig. 27 and, in Fig. 35, the corresponding densities are plotted over the distance to the center of the trap, r. The red curve corresponds to the total density n at $\beta = 9$ and the other datasets to n_{sf} at different inverse temperatures. For $\beta = 9$, the system is completely superfluid and the green curve is identical to the red one within the errorbars. At $\beta = 4$, however, the total superfluid fraction is calculated as $\gamma_{\mathrm{sf}} = 0.86 \pm 0.01$ and the superfluid density (blue) is significantly decreased in the outermost region, while it seems to be unaffected near the center of the trap. A similar effect appears at $\beta = 3$ with $\gamma_{\mathrm{sf}} = 0.62 \pm 0.01$ and the purple curve is even more reduced for large r. Finally, at $\beta = 2$, the superfluid fraction equals $\gamma_{\mathrm{sf}} = 0.129 \pm 0.002$ and nearly no superfluidity (turquoise) is located in the outermost region of the system.

Before attempting to explain the aforementioned behaviour, it is useful to take a look at the system in the path integral picture. Fig. 36 shows two random PIMC snapshots of the system for $\beta = 4$ (left) and $\beta = 2$ (right). In the left image, most of the particles are involved in exchange cycles, while only in the outer shell many particles form single trajectories. In the right image, almost all exchange cycles are located at $r < 5$. The spatially resolved behaviour of the superfluid phase transition can be explained by the static properties of the system, in particular the total density in Fig. 35. For small r, the density profile stays nearly flat, while near the boundary a shell-like oscillation appears. In this region, the particles are more localized and, hence, the formation of exchange cycles becomes less probable. In other words, the individual particles have to be more extended to overcome their spatial separation. The effect is enhanced for the particles at the outermost part of the boundary since here, in radial direction, no neighbours are available which again reduces the local area and the superfluid density. The stronger coupling in the outermost region is typical for Coulomb systems because, in mean field approximation, the particles at the center of the trap do not experience interactions from other particles with a larger r. This "Faraday cage" effect is observed in classical Coulomb systems, as well [66], and the new results are published in [60]. In conclusion, the total density distribution n is nearly

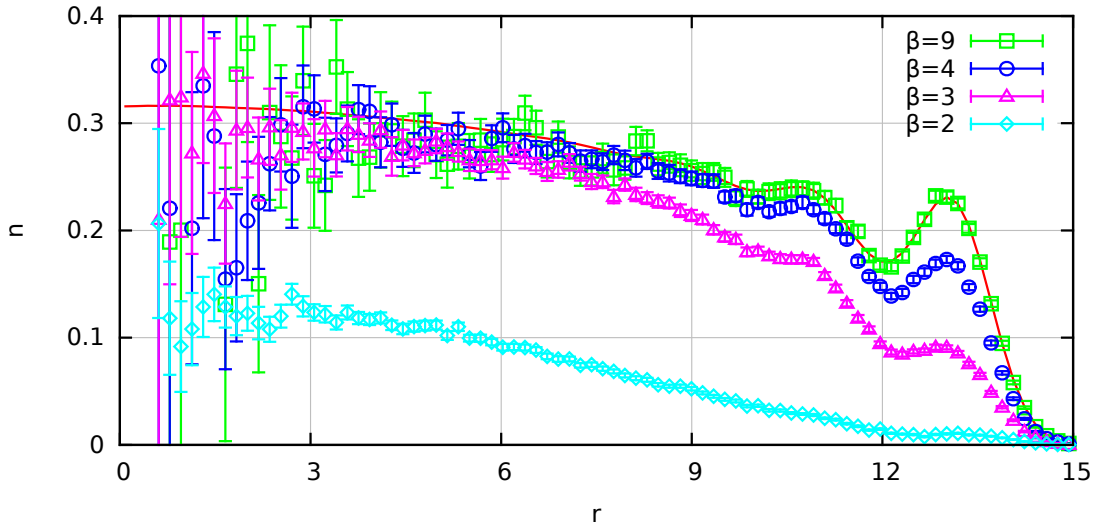

Figure 35: ***Local superfluid density of a*** $2D$ ***Coulomb system:*** The total and superfluid density n and n_{sf}, respectively, are plotted over the distance to the center of the trap r. The red curve corresponds to n at $\beta = 9$ and approximately equals the ground state density. The other four datasets symbolize n_{sf} for $\beta = 9$ (green), $\beta = 4$ (blue), $\beta = 3$ (purple) and $\beta = 2$ (turquoise).

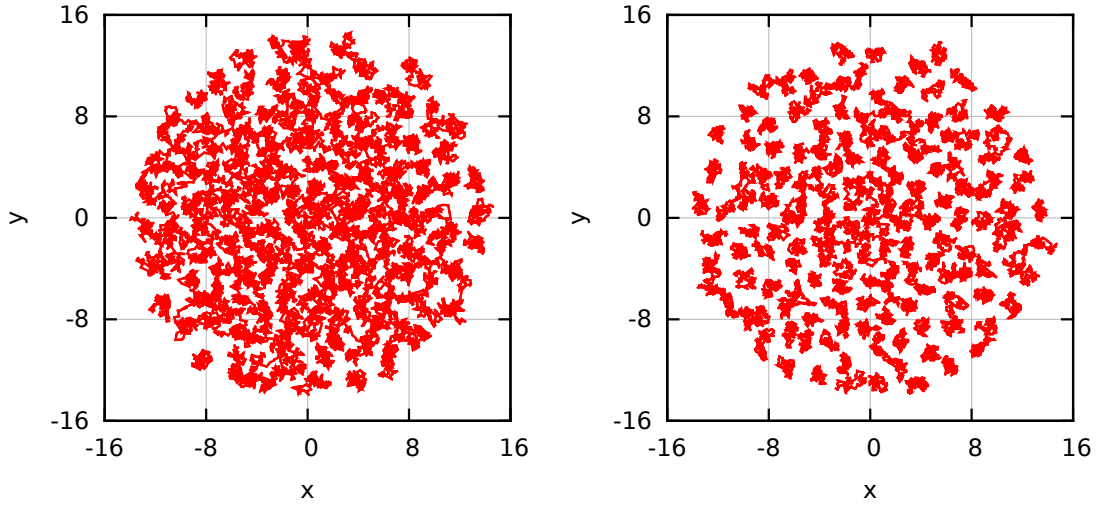

Figure 36: ***PIMC snapshots of a*** $2D$ ***Coulomb system:*** Two random configurations are shown of a $2D$ Coulomb system with $N = 150$, $\lambda = 10$ and $P = 110$. The left image corresponds to an inverse temperature $\beta = 4$ and the right one to $\beta = 2$.

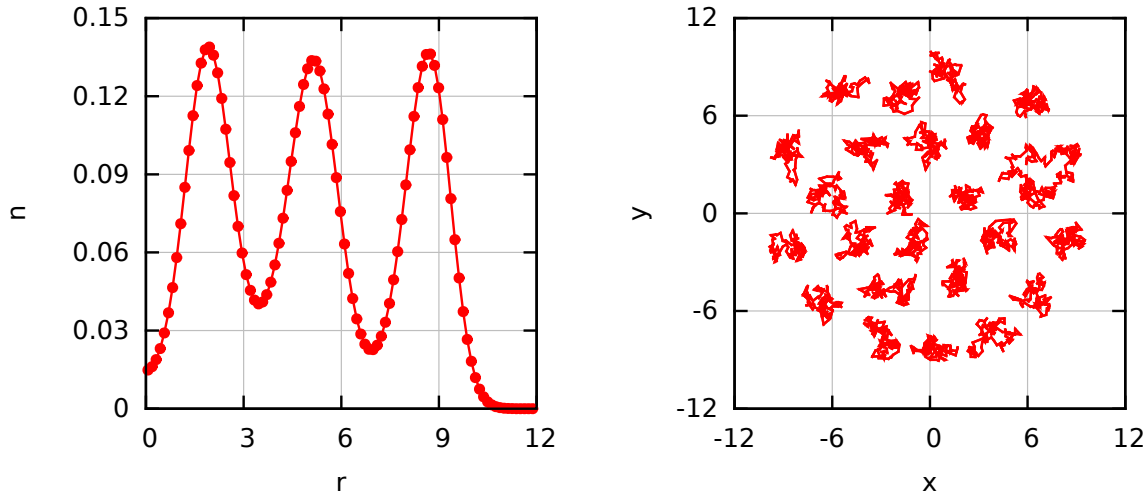

Figure 37: ***Strongly correlated*** $2D$ ***Coulomb system:*** The left image shows the radial density n plotted over the distance to the center of the trap r for a system with $N = 25$, $\beta = 5$, $\lambda = 30$ and $P = 110$. The right picture features a random PIMC snapshot.

invariant to the superfluid phase transition but its shape can have a strong influence on the probability for the formation of exchange cycles and, hence, the distribution of superfluidity and the critical temperature of the phase transition itself.

4.3 Spatial correlation functions

Another interesting topic for the investigation of trapped systems is the consideration of spatial correlations. The left image of Fig. 37 shows the radial density n of a $2D$ Coulomb system with $\beta = 5$, $\lambda = 30$, $N = 25$ and $P = 110$. There appear three very clearly pronounced shells with a relatively small overlap. The right image of the figure shows a random PIMC snapshot from the corresponding simulation and one does indeed spot a shell structure, although especially the top region seems a little disordered. It is highly desireable to gain further insight into the stability of such a system, i.e., if the relative distances between multiple particles are fixed and if different shells can be rotated with respect to each other. The most trivial quantity providing information about a system's spatial properties is the density profile $n(x, y)$, which is shown in the left image of Fig. 38. However, the Hamiltonian from Eq. (52) is invariant under a rotation of all particles and the averaged density profile contains exactly the same information as the radial density n. This means that any knowledge about intra-shell and inter-shell correlations is lost. To preserve the spatial correlations, one might try to identify some symmetry axis in each random configuration from the Markov chain and rotate the system with respect to it. A trivial choice is a fragmentation into angular segments and to define the symmetry axis as the center of the segment with the highest density in the particular configuration. The result of this quantity for the system of interest is shown in the right image of Fig. 38. One immediately recognizes the symmetry breaking and the appearance of individual particles within a single shell. At the top of the image, the density maxima are very sharp and pronounced since this part corresponds to the special segment with the highest density in each configuration. With an increasing angular distance towards it, the correlations become weaker and the density profile smeers out. This appears especially clear in the central shell and implies that particles at opposite positions within a shell are much weaker correlated than next neighbours, as it is expected. Hence, the applied

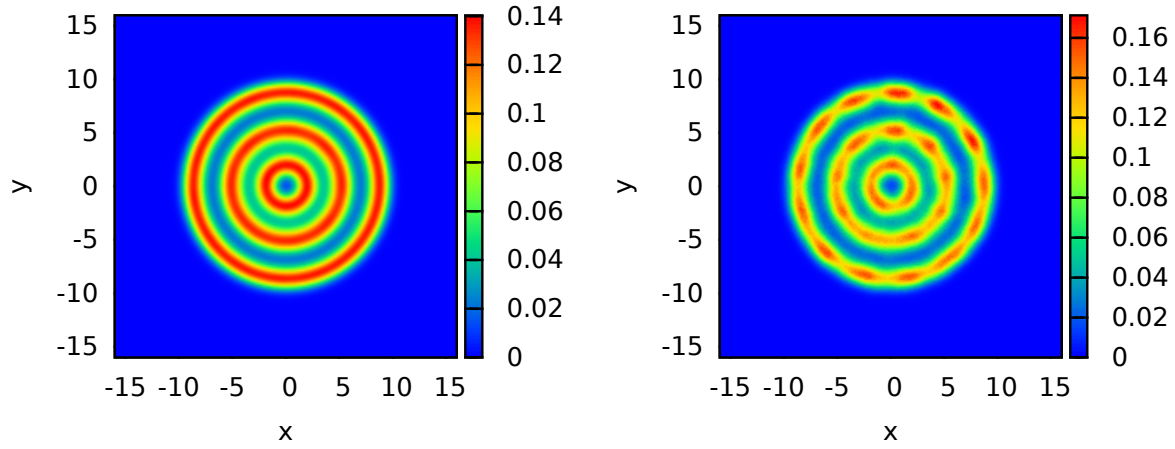

Figure 38: ***Averaged density profiles of a*** $2D$ ***Coulomb system in a harmonic trap:*** The system of interest is the same as in Fig. 37 and the left image shows the averaged density profile $n(x, y)$. For the right picture, the density is binned into angular segments in each measured configuration. Afterwards, the entire system is rotated with respect to the bin containing the most beads. This achieves the depicted symmetry break.

symmetry breaking has worked at least to some degree for the system of interest and spatial correlations are visible. Difficulties appear when there are several configurations with a similar energy but differently occupied shells. In such a case, this quantity will always give pronounced maxima in all shells in the top sector and the rest of the profile will be smeered out. This implies that again all real spatial correlations in the system are lost and the resulting profile is just an average over completely different configurations.

A natural approach for the investigation of correlations is the consideration of spatial correlation functions, like the two particle quantity

$$g_2(\mathbf{R}, \mathbf{r}) = \frac{1}{2NP} \sum_{i=0}^{P-1} \sum_{j=1}^{N} \sum_{k=1}^{N} \delta\left(\mathbf{R} - \frac{\mathbf{r}_{j,i} + \mathbf{r}_{k,i}}{2}\right) \delta\left(\mathbf{r} - (\mathbf{r}_{j,i} - \mathbf{r}_{k,i})\right) \quad ,$$

which gives the probability for two particles to be located at $\mathbf{R}$ and $\mathbf{r}$. Here, $\mathbf{R}$ denotes the center of mass of two particles and $\mathbf{r}$ the relative difference. Due to the symmetry of the harmonic trap, the angular dependence of $\mathbf{R}$ can be dropped and the correlation function g_2 depends on three spatial coordinates. Such a quantity seems to be impractical and one usually integrates over the modulus of the center of mass and the angular orientation of $\mathbf{r}$ as well, hence, tayloring a correlation function which depends on the modulus of the difference between the positions of two particles only:

$$g_2(r_h) = \frac{1}{2NP\Delta r} \sum_{i=0}^{P-1} \sum_{j=1}^{N} \sum_{k=1}^{N} \delta(r_h, |\mathbf{r}_{j,i} - \mathbf{r}_{k,i}|) \quad . \tag{63}$$

In practice, it is, obviously, unfeasible to obtain g_2 as a continuous function and in Eq. (63) a uniform grid of width Δr is used. This quantity is shown in Fig. 39 for the system of interest and exhibits a smooth progression with several relatively pronounced peaks. The latter mark some characteristic differences in the most probable shell configurations. For a completely disordered

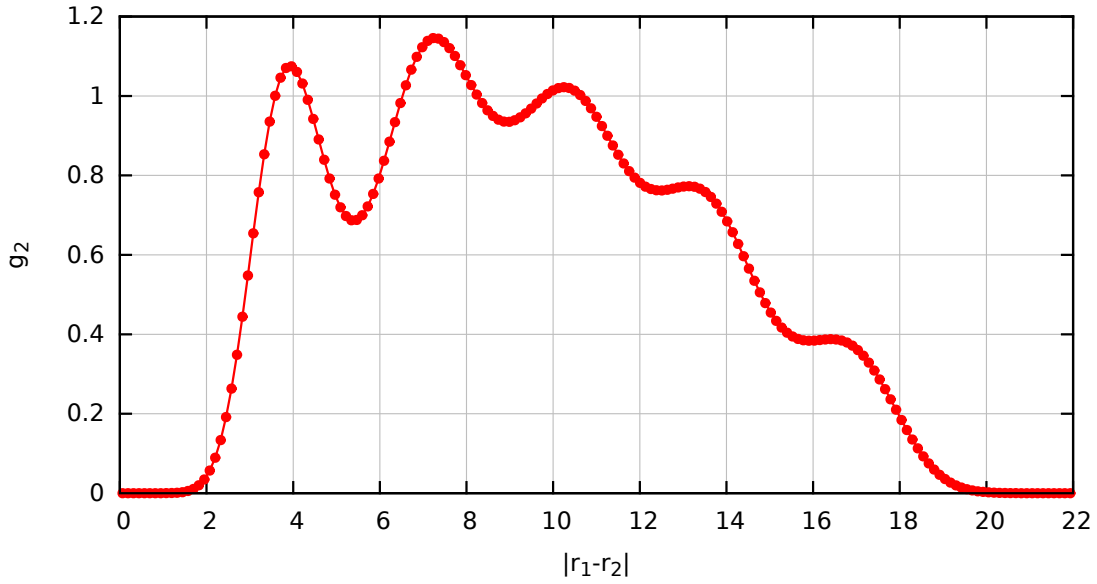

Figure 39: ***The two-particle correlation function:*** The averaged two-particle correlation function g_2 is plotted over the distance between two particles r for the system from Fig. 37.

system, on the other hand, the function g_2 would be flat. Another interesting feature is that the two-particle correlation function equals zero for $r < 1.5$, which implies that the particles cannot directly collide due to the Coulomb repulsion. The averaged two-particle correlation function still does not directly provide information about inter-shell correlations, for example.

A better quantity has recently been suggested by Thomsen et al. [11]. In principle, it incorporates three spatial coordinates and, therefore, the complete information about all spatial two-particle correlations. The idea behind this center two-particle correlation function is illustrated in Fig. 40, where the same configuration as in Fig. 37 is shown. The calculation of the new correlation function requires the consideration of all pairs of particles (which are on the same time slice) and the creation of a histogram according to their distances to the center of the trap r_1 and r_2 and angular differences α. Such a quantity can be defined as

$$\tilde{g}_2(r_1, r_2, \alpha) = \frac{1}{2P\Delta r^2 \Delta\alpha} \sum_{i=0}^{P-1} \sum_{j=1}^{N} \sum_{k=1}^{N} \delta(r_1 - r_{i,j}) \delta(r_2 - r_{i,k}) \delta(\alpha_{i,jk} - \alpha) \quad , \tag{64}$$

with the angular difference $\alpha_{i,jk}$. Equation (64) gives the probability to have a pair of two particles with some specific r_1, r_2 and α. However, it is even more interesting to investigate the relative correlation. This is achieved via a division by the uncorrelated density, i.e., a two particle quantity without correlations beyond the single particle density profile [11]:

$$\begin{aligned} n_2(r_1, r_2, \tilde{\alpha}) &= \int_{|\mathbf{r}_a|=r_1} d\mathbf{r}_a \int_{|\mathbf{r}_b|=r_2, \alpha(\mathbf{r}_a,\mathbf{r}_b)=\tilde{\alpha}} d\mathbf{r}_b \; n(r_a) n(r_b) \\ &= 4\pi n(r_1) r_1 n(r_2) r_2 \\ \Rightarrow T(r_1, r_2, \alpha) &= \frac{\tilde{g}_2(r_1, r_2, \alpha)}{n_2(r_1, r_2, \alpha)} \quad . \end{aligned} \tag{65}$$

The quantity from Eq. (65) is still hard to handle. Thus, it is useful to integrate both the numerator and denominator over one of the distances r_1 and r_2, e.g. over one of the shells.

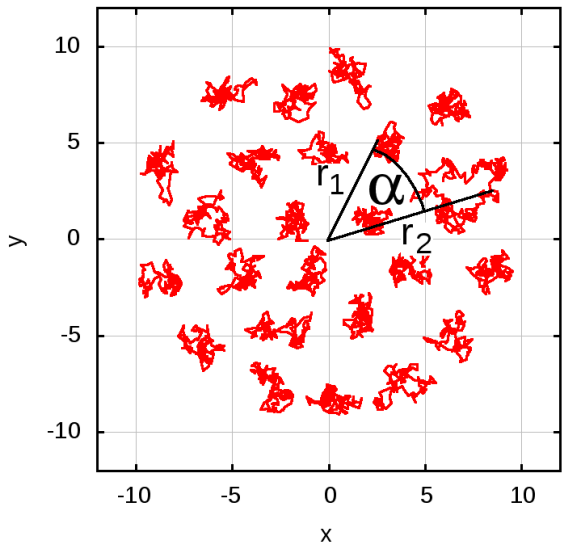

Figure 40: ***Illustration of the center-two particle correlation function:*** Knowledge about all spatial two-particle correlations requires the consideration of three coordinates, e.g. the distances to the center of the trap r_1 and r_2 and the angular difference α.

This means that one of the two considered particles is definetly located within the selected shell and the correlation with respect to the angular difference and the second coordinate, which still ranges over the entire system, is analyzed.

The results for this integrated center two-particle correlation function for the system of interest are presented in Fig. 41. The left panels show the radial density n and the two blue lines mark the integrated interval of one spatial coordinate. The right panels correspond to the integrated center two-particle correlation function for the innermost (top), center (center) and outermost (bottom) shell. All plots of this quantity are symmetric with respect to $\alpha = 180$, as it is, of course, expected. In the top image, two clear maxima appear near the center of the trap since the shell usually contains three particles. However, there also appear correlations to the other shells and the minima between them. Of particular interest is the minimum between the innermost and the center shell, where the two bottom maxima have split into three. This indicates that there is a competition between different shell configurations and four instead of three particles inside the inner shell are also possible. In this case, the shell is a little more extended. The center image exhibits eight distinct maxima in the middle shell, corresponding to the nine particles which are usually located within it. There do appear some correlations to the other two shells but they are much weaker. This indicates that the center shell can be rotated with respect to the other ones. Finally, the bottom image shows the quantity for the outermost shell, in which twelve maxima appear which again correspond to the thirteen particles witihin it. There are almost no correlations to the center shell and the correlations for angles around $\alpha = 180$ are blurred, as it is expected.

Another interesting application for the center-two particle correlation function is the investigation of the system's temperature dependence. This is shown in Fig. 42, where the center shell is considered for $\beta = 0.75$ (top), $\beta = 5$ (center) and $\beta = 20$ (bottom). For $\beta = 0.75$, the system is in the liquid phase and no shell structure appears in both the density (left panel) and the correlation function. The latter is almost constant apart from the minimum at $\alpha = 0$

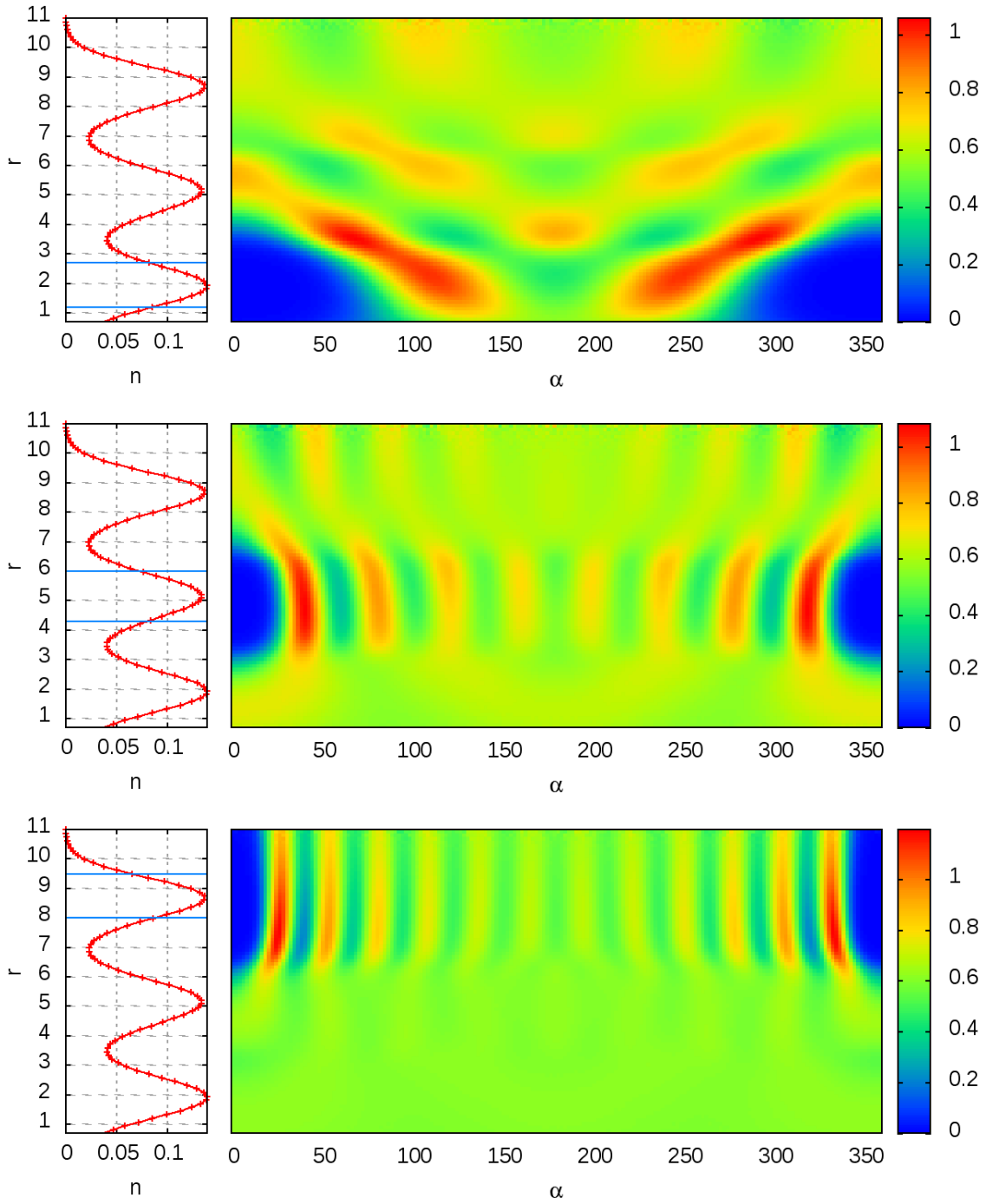

Figure 41: ***The center-two particle correlation function:*** The integrated center two-particle correlation function $T(r_2, \alpha)$ is plotted with respect to the inner (top), middle (center) and outer (bottom) shell for the system from Fig. 37. The left panel shows the radial density n and the two blue lines represent the integrated intervall of the second spatial coordinate r_1.

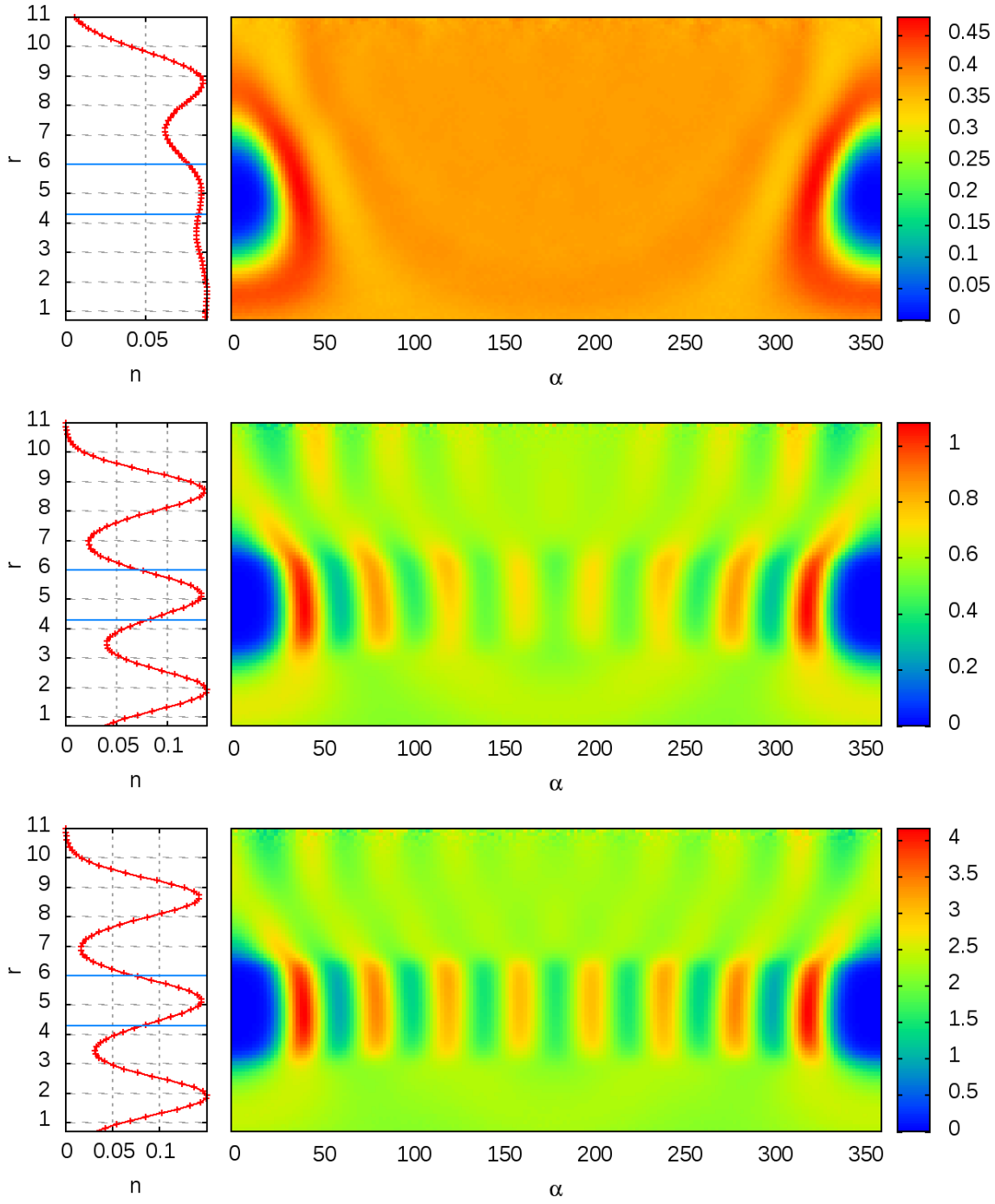

Figure 42: ***The center-two particle correlation function:*** The integrated center two-particle correlation function $T(r_2, \alpha)$ is plotted with respect to the middle shell for the system from Fig. 37 with $\beta = 0.75$ (top), $\beta = 5$ (center) and $\beta = 20$ (bottom). The left panel shows the radial density n and the two blue lines represent the integrated intervall of the second spatial coordinate r_1.

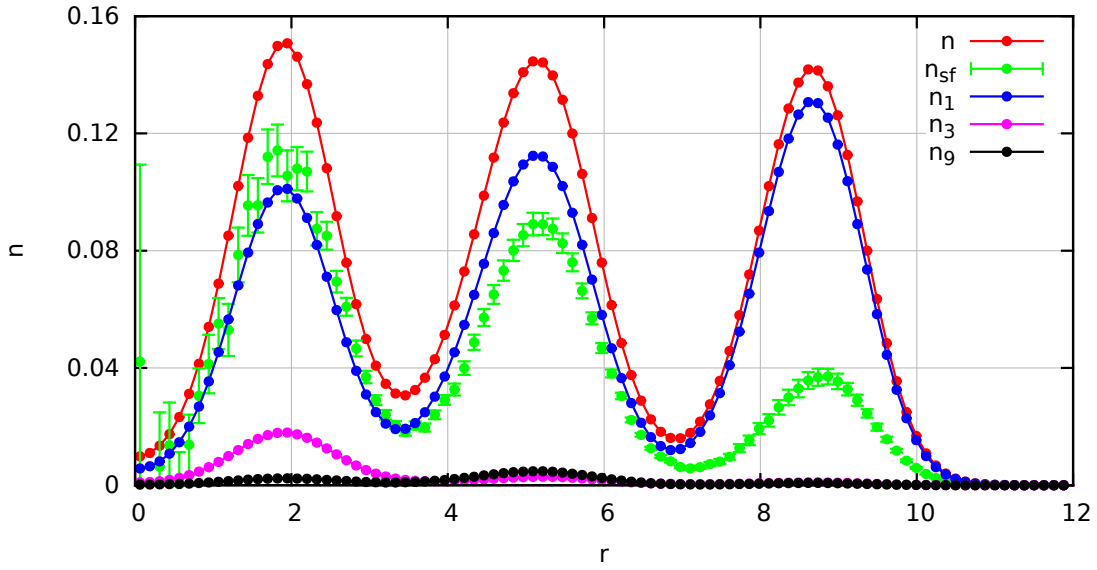

Figure 43: ***Density profiles for low temperature:*** The density n is plotted over the distance to the center of the trap r for the system of interest at $\beta = 17$ and $P = 410$. The red and green curve correspond to the total and superfluid density, respectively, and the blue, purple and black datasets show the fraction of n which is involved in exchange cycles of the lenghts $l = 1$, $l = 3$ and $l = 9$.

and the weak maximum structure around it. The center image corresponds to $\beta = 5$ and is the same as in Fig. 41 and just shown as a reference. The bottom image has been obtained for $\beta = 20$ and the density is almost equivalent to the $\beta = 5$ result. The main differences in the integrated center two-particle correlation function are the much more pronounced maxima within the center shell, indicating that the particles within it behave as a solid. Nevertheless, there still appear no clear correlations to the other two shells which implies that the total system is not crystallized and rotations of the shells with respect to each other do occur. This is a quite interesting feature and one might ask, wether such a system exhibits superfluidity and how the latter is realized in the path integral picture. To answer this question the system is simulated with the usual parameters and $\beta = 17$ and $P = 410$. The total superfluid fraction is calculated as $\gamma_{\mathrm{sf}} = 0.34 \pm 0.02$ and the density profiles are shown in Fig. 43. The total density (red) exhibits the same shape as in Fig. 37 and the superfluid density (green) decreases with increasing distance to the center of the trap. This behaviour can be explained by considering those fractions n_l of n which are due to particles being involved in exchange cycles of a particular length l. The blue curve corresponds to $l = 1$, i.e., single particles which are not involved in any exchange at all. In the outermost shell, the blue and red datasets nearly coincide since exchange is much less propable at the boundary as discussed in section 4.2.1. However, for decreasing r, particle exchange becomes more likely and there appears a significant difference between n and n_1. The purple curve corresponds to n_3 and exhibits a distinct global maximum in the innermost shell since the latter usually contains three particles. However, exchange cycles consisting of three particles occur in the center shell as well, although with highly reduced probability. Finally, the black curve corresponds to n_9. Here, the global maximum is clearly located in the center shell.

The analysis of the densities in Fig. 43 has revealed that n_1 and n_{sf} show a complementary

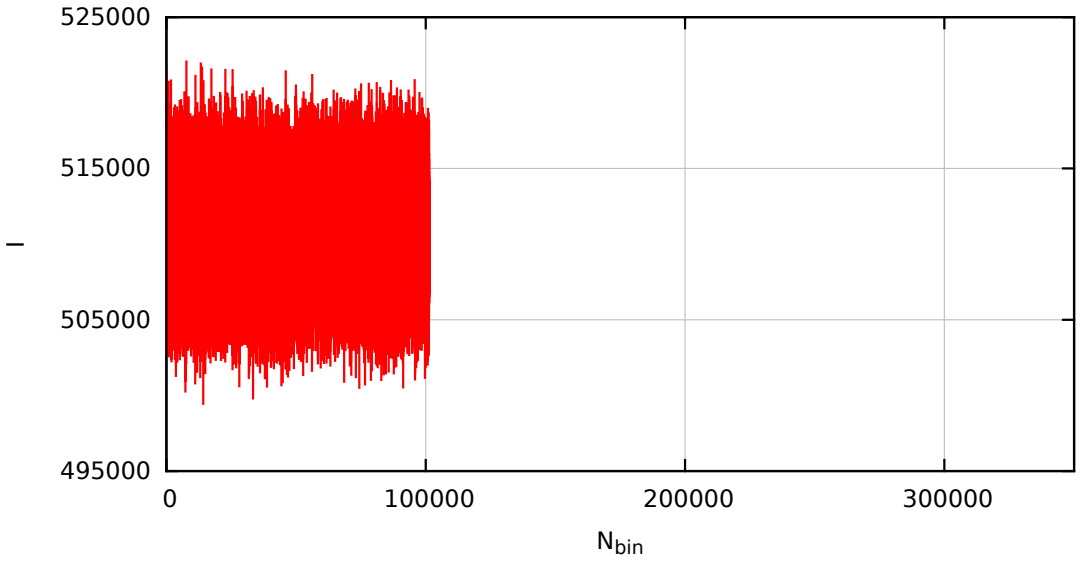

Figure 44: ***The classical moment of inertia:*** The classical moment of inertia I_{cl} is plotted over the number of bins N_{bin} for the system from Fig. 43. Each bin corresponds to the average over one hundred Monte Carlo samples.

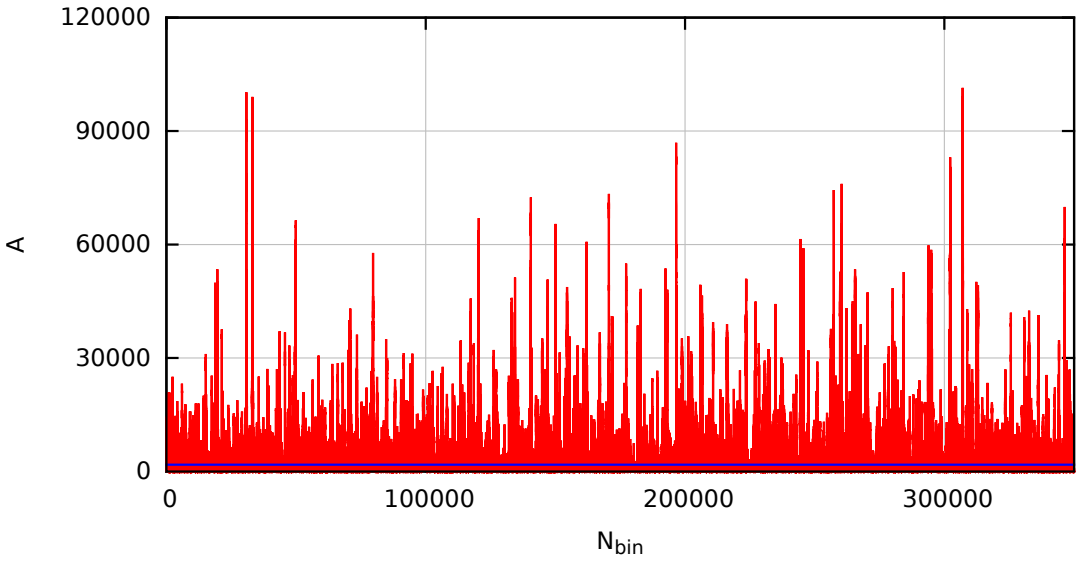

Figure 45: ***The total area:*** The total area A_z in the x-y-plane is plotted over the number of bins N_{bin} for the system from Fig. 43. Each bin corresponds to the average over one hundred Monte Carlo samples and the blue line to the average value $\overline{A}_z = 1810 \pm 10$.

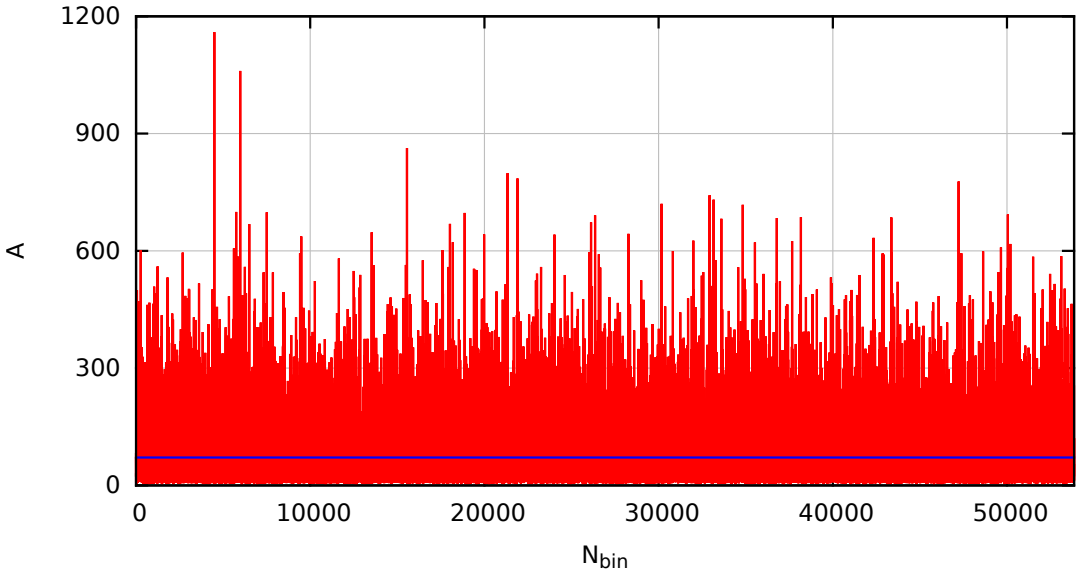

Figure 46: ***The total area of the Boltzmannon system:*** The total area in the x-y-plane A_z is plotted over the number of Monte Carlo bins N_{bin} for the system from Fig. 45, but simulated with Boltzmannons. The blue line corresponds to the average value $\overline{A}_z = 71.4 \pm 0.5$.

behaviour, which is a strong hint that the superfluidity in this system is caused by particle exchange and not any finite size effects due to the larger extension of individual particles at low temperature. This conclusion is confirmed by the consideration of the two quantities which determine the total superfluid fraction γ_{sf}, namely the total area in the x-y-plane A_z and the classical moment of inertia I_{cl}. The latter is plotted in Fig. 44 over the number of bins N_{bin}, where each bin corresponds to the average over one hundred Monte Carlo samples. The plot exhibits a rather smooth behaviour with relatively small deviations from the mean value because the system's static properties do not drastically change. An entirely different picture occurs for the total area A_z, which is shown in Fig. 45. It turns out that this quantity heavily fluctuates and a number of sharp peaks exceed the average value $\overline{A}_z = 1810 \pm 10$, which is visualized as the blue line, by orders of magnitude. This behaviour of the area is accounted to the occurence of larger exchange cycles. The most probable configurations consist of single particles or small exchange cycles in the center of the trap. However, in the improbable case of an exchange cycle which involves all the particles in the center or outermost shell, the enclosed area becomes much larger and causes the maxima in Fig. 45. In comparison, Fig. 46 shows the area for the same system of boltzmannons, i.e., distinguishable particles without any exchange. Here, no large peaks appear and the average value is calculated as $\overline{A}_z = 71.4 \pm 0.5$, leading to a total superfluid fraction $\gamma_{\mathrm{sf}} = 0.0135 \pm 0.0002$. The moment of inertia is roughly the same as in Fig. 44. Thus, it has been demonstrated that the superfluidity in the bosonic system, at $\beta = 17$, is caused by macroscopic exchange cycles and, therefore, a collective response of the system. Finally, Fig. 47 shows a comparison of the total densities for boltzmannons (blue) and bosons (red). The two curves nearly coincide but the bosonic density exhibits a slightly larger overlap between the shells, as it is expected. In conclusion, the center-two particle correlation function has revealed the appearance of solid-like intra-shell behaviour at low temperature, but different shells are still free to be rotated with respect to each other. The latter degree of freedom allows for a

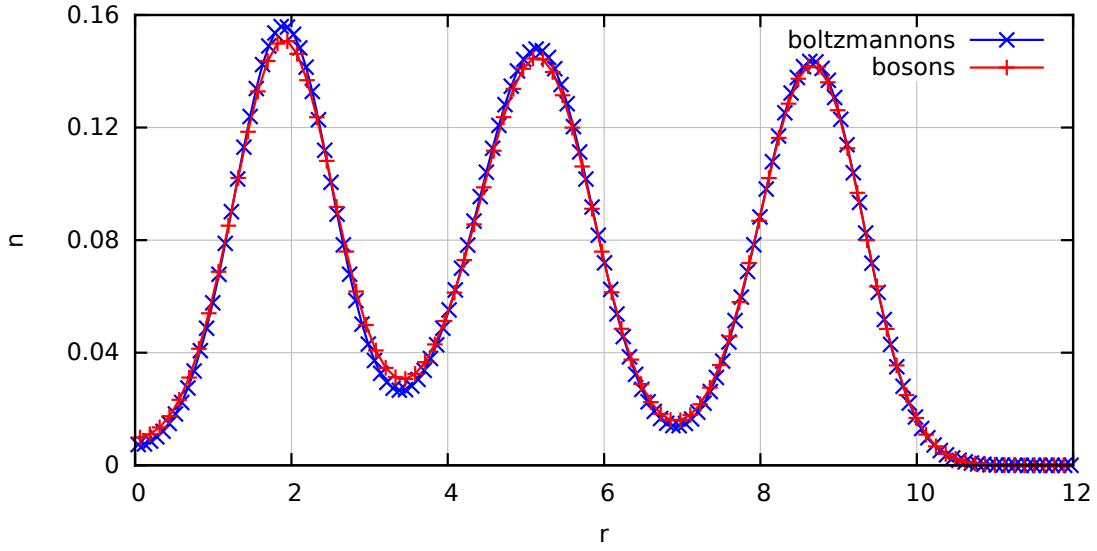

Figure 47: ***Comparison of the densities:*** The density n is plotted over the distance to the center of the trap r for the system from Fig. 43 for bosons (red) and boltzmannons (blue).

finite superfluid response, which is consistent with the findings by Filinov et al. [50] and also Khairallah et al. [62] in the case of parahydrogen clusters. However, the classification of such a system as a supersolid, i.e., a combination of density order and superfluidity [67], does not seem to be appropriate since there is no real order throughout the entire system, as it is observed e.g. for a parahydrogen cluster of the same size by Idowu and Boninsegni [64].

Another useful application of the center-two particle correlation function is the investigation of the melting process of a finite sized trapped system, which is a notoriously hard task, especially for small systems, see e.g. [61]. A relatively robust melting criterion, which is based on the variance of the block averaged interparticle distance fluctuations, has been proposed by Böning et al. [68]. The idea is to perform averages over L Monte Carlo steps of the changes of interparticle distances. In the transition region between the liquid and solid phase, the variance of this quantity should increase because both solidlike intervals with few and liquidlike intervals with many fluctuations occur and, hence, the phase transition is detected. However, the shortcoming of such an approach is the dependence of the results on the particular update scheme of the applied Monte Carlo method. The pseudo-dynamics created by the MC updates are, in general, not related to the real-time dynamics of the physical system of interest and an estimator should be independent of the implementation or choice of the update scheme. A better alternative, which has been suggested by Thomsen and Bonitz [69] for the investigation of classical systems, is the calculation of the information entropy [70] from the center-two particle correlation function. Being a physical quantity, it can be equivalently evaluated with any simulation method. In addition, it is expected that the latter approach provides more detailed and spatially resolved information about phase transitions in or between different shells of the system. Therefore, the application of this melting criterion to quantum mechanical systems is of major interest for future research and might provide even more insight into the connection between superfluidity and static properties of harmonically confined particles.

5 The quantum breathing mode

The central theme of the following section is the calculation of dynamic properties of trapped bosons from Quantum Monte Carlo data. The problem of interest is given by the quantum **B**eathing **M**ode (BM), i.e., the system's response to a monopole perturbation. The latter can be excited by a short lowering of the confinement potential which causes the particles to oscillate. The BM is of fundamental interest for the investigation of trapped systems in the quantum mechanical regime since it allows to obtain all characteristic energies [71] and, hence, might serve as a tool of diagnostics.

Bauch et al. [72] have shown that the breathing mode behaves differently for quantum systems and is composed of two independent oscillations, namely of the system's center of mass and a relative oscillation between the particles. The former has a constant value while the latter undergoes a transition between a classical and an ideal limit. The presented results of a numerical integration of the time dependent Schrödinger equation have confirmed those predictions. However, such an exact approach is limited to small particle numbers, i.e., a two particle system in this case. The application of time dependent Multi-configuration-Hartree-Fock methods has allowed Bauch et al. [73] to obtain results for up to six particles for both Coulomb and polarized dipole interaction, but this does still not qualify as a real many body system. Abraham et al. [74] presented results for up to $N = 20$ Coulomb interacting fermions in a $1D$ trap, using a time dependent Hartree Fock approach. The latter is numerically much less costly, but at the expense of an only approximate treatment of correlation effects, thus limiting the method to weakly coupled systems. It has been found that the breathing mode of the $1D$ system exhibits a minimum around $N \approx 6$ particles which might seem like a rather peculiar result. However, the presented analysis has revealed that the trend of ω_{BM} directly corresponds to several non-ideality parameters which characterize the deviation from the non-interacting system. Schmitz et al. [75] have used a recently published multilayer multiconfiguration time-dependent Hartree method for bosons to investigate the breathing mode in a $1D$ trap with contact-interacting particles.

A very interesting approach to the calculation of dynamic properties in the context of this thesis are the sum-rules, which have already been successfully applied to the investigation of collective modes in nuclei, see e.g. [76] and references therein. The idea is to express an accurate upper bound for the frequency of interest solely in terms of equilibrium properties of the system. The numerical treatment of the stationary problem is, obviously, much less involved, which allows for the investigation of larger systems. Abraham et al. [12] have used this approach to obtain results for the quantum breathing mode for both Coulomb- and dipole-interacting fermions in $1D$ and $2D$ traps. The equilibrium properties have been calculated with Hartree-Fock and Thomas-Fermi methods for small and large particle numbers, respectively. Finally, the last noteworthy approach to the breathing mode is the reconstruction of the spectrum from imaginary time correlation functions. The latter are easily accessible with PIMC and an ill-posed inverse problem has to be solved, as it has already been very successfully conducted for other dynamic properties like the dynamic structure factor and the single particle spectrum, see e.g. [13]. A review of the quantum breathing mode, including detailed sum-rule results for fermions, can be found in [10].

The following section 5.1 starts with a brief revision of the pictures of quantum mechanics and the linear response formalism. The latter includes the introduction of response and correlation functions which provide the basis for both the sum-rules and the reconstruction of the spectral function and the necessary theoretical background for both approaches will be provided. Being equipped with these tools, numerical results for the quantum breathing mode from the sum-rules are presented in section 5.2 and the dependencies on the system parameters (i.e., N, λ and β)

are analyzed in detail for both Coulomb- and dipole-interacting particles. Finally, in section 5.3, the reconstruction of the entire spectrum is discussed.

5.1 Linear Response Theory

In the following section, some fundamentals about the linear response formalism are introduced based on [77, 78, 79]. The system of interest is decribed by a Hamiltonian of the form

$$\hat{H}(t) = \hat{H}_0 + \hat{V}(t) \quad ,$$

where $\hat{H}_0$ corresponds to the unperturbed system at $t \to -\infty$ and $\hat{V}(t) = -f(t)\hat{B}$ is an explicitly time dependent perturbation, coupling to the scalar function $f(t)$. In case of the breathing mode, $\hat{B}$ is given by the monopole operator

$$\hat{B} = \sum_{k=1}^{N} \mathbf{r}_k^2 \quad . \tag{66}$$

It is the goal of the linear response formalism to derive an expression for the effect of $\hat{V}(t)$ on some not explicitly t-dependent observable $\hat{A}$ which, in case of the breathing mode, is given by the monopole operator $\hat{B}$ itself. The choice $\hat{B} = \hat{A}$ is used because it provides a measure of the mean extension of the system which fluctuates when the BM is excited. However, first it is necessary to repeat some basics about the three pictures of quantum mechanics.

5.1.1 Pictures of quantum mechanics

The expectation value of an observable $\langle \hat{A} \rangle$ must, by definition, be equal in all formulations since it can be experimentally measured. In the Schrödinger picture, the states $|\Psi_S(t)\rangle$ carry the entire time dependence and the expectation value is written as

$$\begin{aligned} \langle \hat{A}(t) \rangle &= \langle \Psi_S(t)| \hat{A}_S |\Psi_S(t)\rangle \\ &= \langle \Psi_S(t_0)| \hat{U}^\dagger(t,t_0) \hat{A}_S \hat{U}(t,t_0) |\Psi_S(t_0)\rangle \quad , \end{aligned} \tag{67}$$

with the time evolution operator

$$\hat{U}(t,t_0) = \hat{T} \exp\left(-\frac{i}{\hbar} \int_{t_0}^{t} d\bar{t}\ \hat{H}_S \right) \quad , \tag{68}$$

and the time ordering operator $\hat{T}$. The operators $\hat{A}_S$ are constant in time and the equation of motion for the states is given by the Schrödinger equation:

$$i\hbar \frac{\partial}{\partial t} |\Psi_S(t)\rangle = \hat{H}_S |\Psi_S(t)\rangle \quad .$$

Special attention must be paid to the density matrix which might be written in the eigenstate respresentation as

$$\hat{\rho}_S(t) = \sum_i p_i |\Psi_S^i(t)\rangle \langle \Psi_S^i(t)| \quad , \tag{69}$$

and, thus, is time dependent. The equation of motion for Eq. (69) is given by the von Neumann equation

$$\frac{\mathrm{d}\hat{\rho}_S(t)}{\mathrm{d}t} = \frac{1}{i\hbar} \left[\hat{H}_S, \hat{\rho}_S \right](t) \quad .$$

The second well known picture of quantum mechanics is the Heisenberg picture. Here, the product of the three operators in Eq. (67) is combined into a single operator $\hat{A}_{\mathrm{H}}(t)$

$$\langle \hat{A}(t) \rangle = \langle \Psi_{\mathrm{S}}(t_0) | \, \hat{A}_{\mathrm{H}}(t) \, | \Psi_{\mathrm{S}}(t_0) \rangle \qquad . \tag{70}$$

Equation (70) implies that the entire t-dependence is carried by the operator, while the states remain unchanged and coincide with the initial ones from the Schrödinger picture. The density matrix $\hat{\rho}_{\mathrm{H}}$ is constant as well and the equation of motion for the operators is given by the Heisenberg equation

$$\frac{\mathrm{d}\hat{A}_{\mathrm{H}}(t)}{\mathrm{d}t} = \frac{i}{\hbar} \left[\hat{H}_{\mathrm{S}}, \hat{A}_{\mathrm{H}}(t) \right] + \frac{\partial \hat{A}_{\mathrm{H}}(t)}{\partial t} \qquad .$$

It should be noted that the brackets (t) indicate the time dependence due to the Heisenberg (and later also Dirac) picture, while $\hat{H}_{\mathrm{S}}$ might implicitly depend on t as well. A third useful representation is given by the Dirac picture, which is also denoted as interaction picture in the literature. The idea is to distribute the time evolution to both the states and operators by splitting $\hat{U}(t, t_0)$ from Eq. (68) into two parts:

$$\hat{U}(t, t_0) = \hat{U}_0(t, t_0) \hat{U}_V(t, t_0).$$

Here, $\hat{U}_0(t, t_0) = \hat{U}_0(t - t_0)$ corresponds to the time evolution of the unperturbed system and, hence, only depends on the t-difference and $\hat{U}_V(t, t_0)$ is governed by the perturbation itself. The operators in the Dirac picture are defined as

$$\hat{A}_{\mathrm{D}}(t) = \hat{U}_0^{\dagger}(t, t_0) \hat{A}_{\mathrm{S}} \hat{U}_0(t, t_0) \qquad ,$$

which means that they coincide with the Heisenberg picture if there is no perturbation. The equation of motion is given by the modified Heisenberg equation

$$\frac{\mathrm{d}\hat{A}_{\mathrm{D}}(t)}{\mathrm{d}t} = \frac{i}{\hbar} \left[\hat{H}_0, \hat{A}_{\mathrm{D}}(t) \right] + \frac{\partial \hat{A}_{\mathrm{D}}(t)}{\partial t} \qquad .$$

The states can be expressed as

$$| \Psi_{\mathrm{D}}(t) \rangle = \hat{U}_V(t, t_0) \, | \Psi_{\mathrm{S}}(t_0) \rangle \qquad ,$$

and $\hat{U}_V(t, t_0)$ fulfills a Schrödinger equation of the form

$$i\hbar \frac{\mathrm{d}\hat{U}_V(t, t_0)}{\mathrm{d}t} = \hat{V}_{\mathrm{D}}(t) \hat{U}_V(t, t_0) \qquad . \tag{71}$$

Finally, it should be noted that a formal solution of Eq. (71) is given by

$$\hat{U}_V(t, t_0) = \hat{T} \exp\left(-\frac{i}{\hbar} \int_{t_0}^{t} \mathrm{d}\bar{t} \; \hat{V}_{\mathrm{D}}(\bar{t}) \right) \qquad . \tag{72}$$

5.1.2 Response functions

The basic idea of linear response theory is to consider a perturbation $\hat{V}(t)$ which is small enough to be negligible beyond linear terms in Eq. (72). This gives

$$\hat{U}_V(t, t_0) = \hat{1} - \frac{i}{\hbar} \int_{t_0}^{t} \mathrm{d}\bar{t} \; \hat{V}_{\mathrm{D}}(\bar{t}) + \mathcal{O}(\hat{V}_{\mathrm{D}}^2) \qquad , \tag{73}$$

where all terms in $\mathcal{O}(\hat{V}_\mathrm{D}^2)$ will be dropped. The goal of this subsection is the derivation of an expression for the change in an observable $\hat{A}$ due to the external field:

$$\delta \langle \hat{A}(t) \rangle = \langle \hat{A}(t) \rangle - \langle \hat{A}(t) \rangle_0 \quad .$$

The non-equilibrium expectation value can be written in the Heisenberg picture as

$$\langle \hat{A}(t) \rangle = \mathrm{Tr} \left(\hat{\rho}_\mathrm{H} \hat{A}_\mathrm{H}(t) \right) \quad . \tag{74}$$

Inserting the identity[4]

$$\hat{A}_\mathrm{H}(t) = \exp\left(\frac{i}{\hbar} \int_{t_0}^{t} \mathrm{d}\bar{t}\ \hat{V}_\mathrm{D}(\bar{t}) \right) \hat{A}_\mathrm{D}(t) \exp\left(-\frac{i}{\hbar} \int_{t_0}^{t} \mathrm{d}\bar{t}\ \hat{V}_\mathrm{D}(\bar{t}) \right)$$

into Eq. (74) and simultaneously considering only linear terms in Eq. (73) leads to the expression

$$\begin{aligned} \langle A(t) \rangle &\approx \mathrm{Tr} \left(\hat{\rho}_\mathrm{H} \left[1 + \frac{i}{\hbar} \int_{t_0}^{t} \mathrm{d}\bar{t}\ \hat{V}_\mathrm{D}(\bar{t}) \right] \hat{A}_\mathrm{D}(t) \left[1 - \frac{i}{\hbar} \int_{t_0}^{t} \mathrm{d}\bar{t}\ \hat{V}_\mathrm{D}(\bar{t}) \right] \right) \\ &= \mathrm{Tr} \left(\hat{\rho}_\mathrm{H} \hat{A}_\mathrm{D}(t) \right) - \frac{i}{\hbar} \mathrm{Tr} \left(\hat{\rho}_\mathrm{H} \int_{t_0}^{t} \mathrm{d}\bar{t}\ \left[\hat{A}_\mathrm{D}(t), \hat{V}_\mathrm{D}(\bar{t}) \right] \right) + \mathcal{O}(\hat{V}_\mathrm{D}^2) \quad . \end{aligned} \tag{75}$$

The first term in Eq. (75) is identified with the unperturbed expectation value $\langle \hat{A}(t) \rangle_0$. Inserting the explicit expression for $\hat{V}_\mathrm{D}$ and again neglecting all $\mathcal{O}(\hat{V}_\mathrm{D}^2)$ contributions leads to

$$\langle \hat{A}(t) \rangle \approx \langle \hat{A}(t) \rangle_0 + \frac{i}{\hbar} \int_{t_0}^{t} \mathrm{d}\bar{t}\ \left\langle \left[\hat{A}_\mathrm{D}(t), \hat{B}_\mathrm{D}(\bar{t}) \right] \right\rangle_0 f(\bar{t}) \quad .$$

Hence, the desired expression for the effect of the perturbation on an observable $\hat{A}$ is given by

$$\delta \langle \hat{A}(t) \rangle = \frac{i}{\hbar} \int_{t_0}^{t} \mathrm{d}\bar{t}\ \left\langle \left[\hat{A}_\mathrm{D}(t), \hat{B}_\mathrm{D}(\bar{t}) \right] \right\rangle_0 f(\bar{t}) \quad , \tag{76}$$

and the index $\langle \ldots \rangle_0$ indicates the expectation value of the unperturbed system. It should be noted that Eq. (76) depends on equilibrium averages only, which is already a great simplification. This implies that the reaction to the external field depends on system properties (i.e., material constants) only. The latter are often introduced as response functions of the form

$$\chi''_{AB}(t_1, t_2) = \frac{1}{2\hbar} \left\langle \left[\hat{A}_\mathrm{D}(t_1), \hat{B}_\mathrm{D}(t_2) \right] \right\rangle_0 \quad ,$$

thus, reducing (76) to

$$\delta \langle \hat{A}(t) \rangle = 2i \int_{t_0}^{t} \mathrm{d}\bar{t}\ \chi''_{AB}(t, \bar{t}) f(\bar{t}) \quad . \tag{77}$$

There exist a number of useful relations and properties of $\chi''_{AB}(t_1, t_2)$ which, however, can be found in any textbook about advanced statistical mechanics. The most important one in the context of this work is that the response function only depends on the time difference $\theta = t_1 - t_2$:

$$\chi''_{AB}(t_1, t_2) = \chi''_{AB}(t_1 - t_2) = \chi''_{AB}(\theta) \quad . \tag{78}$$

[4]For simplicity, the time ordering operator $\hat{T}$ is neglected.

A change from the real time θ to the frequency ω domain is achieved by a **F**ourier **T**ransformation (FT)

$$\tilde{\chi}''_{AB}(\omega) = \int_{-\infty}^{\infty} \mathrm{d}\theta \; \chi''_{AB}(\theta) \; \exp\left(i\omega\theta\right) \qquad ,$$

and the other way around with the inverse FT

$$\chi''_{AB}(\theta) = \frac{1}{2\pi} \int_{-\infty}^{\infty} \mathrm{d}\omega \; \tilde{X}''_{AB}(\omega) \; \exp\left(-i\omega\theta\right) \qquad .$$

Another useful quantity is the dynamic susceptibility

$$\chi_{AB}(\theta) = 2i\theta_{\mathrm{H}}(\theta)\chi''_{AB}(\theta) \qquad , \tag{79}$$

where the Heaviside stepfunction

$$\theta_{\mathrm{H}}(x) = \begin{cases} 1, & \text{if } x \geq 0 \\ 0, & \text{otherwise} \end{cases}$$

is not to be confused with the relative time difference $\theta = t_1 - t_2$. Equation (79) allows to replace the lower integration boundary in (77) to minus infinity:

$$\delta \left\langle \hat{A}(t) \right\rangle = \int_{-\infty}^{t} \mathrm{d}\bar{t} \; \chi_{AB}(t - \bar{t}) f(\bar{t}) \qquad .$$

5.1.3 Correlation functions

Another important class of quantities from the linear response theory are correlation functions $C_{AB}(t_1, t_2)$ with the definition

$$C_{AB}(t_1, t_2) = \langle \hat{A}_{\mathrm{D}}(t_1) \hat{B}_{\mathrm{D}}(t_2) \rangle_0 \qquad . \tag{80}$$

They are connected to the response function $\chi''_{AB}(t_1, t_2)$ from the last section by

$$\chi''_{AB}(t_1, t_2) = \frac{1}{2\hbar} \left(C_{AB}(t_1, t_2) - C_{BA}(t_2, t_1) \right) \qquad . \tag{81}$$

Equation (81) directly implies that an observable $\hat{A}$ must be correlated to the perturbation operator $\hat{B}$ for the latter to cause a nonzero effect $\delta \left\langle \hat{A}(t) \right\rangle$. The correlation functions only depend on the relative time difference between the two arguments as well

$$C_{AB}(\theta) = C_{AB}(t_1 - t_2) = C_{AB}(t_1, t_2) \qquad ,$$

and the representation in the frequency space is given by

$$\tilde{C}_{AB}(\omega) = \int_{-\infty}^{\infty} \mathrm{d}\theta \; C_{AB}(\theta) \; \exp\left(i\omega\theta\right) \qquad .$$

The complementary step back to the time domain is again given by the inverse FT. Of major importance is the correlation function's spectral representation [77]

$$\tilde{C}_{AB}(\omega) = 2\pi \sum_{m \neq n} p_m \left\langle m \right| \hat{A}_{\mathrm{S}} \left| n \right\rangle \left\langle n \right| \hat{B}_{\mathrm{S}} \left| m \right\rangle \delta\left(\omega - \omega_{nm}\right) \qquad , \tag{82}$$

with the Hamiltonian's eigenstates $\{|n\rangle\}$, the probability to occupy a specific $|m\rangle$, p_m, and the frequency difference $\omega_{nm} = \omega_n - \omega_m$. Thus, this spectral function consists of a superposition of sharp peaks located at the allowed transitions. In addition, it is important to note that the double sum in Eq. (82) does not include the diagonal elements $m = n$. For the case of a single Hermitean operator $\hat{A} = \hat{B}$, as it is the case for the breathing mode, the spectral representation simplifies to

$$\tilde{C}_A(\omega) = 2\pi \sum_{m \neq n} p_m |\langle m| \hat{A}_\mathrm{S} |n\rangle|^2 \delta(\omega - \omega_{nm}) \quad , \tag{83}$$

which might be interpreted as follows: Equation (83) is the sum over all initial states $|m\rangle$, weighted with their corresponding occupation probability p_m. The matrix element's squares give the transition probability to get from $|m\rangle$ to $|n\rangle$, induced by the operator $\hat{A}$ and the delta distribution ensures the energy conservation. Until this point, all considerations have dealt with the real time (or the inverse, i.e., real time frequency) dynamics of slightly perturbed systems. However, real time response and correlation functions cannot be obtained with path integral Monte Carlo since the latter is restricted to the calculation of ensemble averages in the TD equilibrium, i.e., in the imaginary time. For completeness, it is reported that the PIMC calculation in the real time is possible in theory but its applicability to interesting systems is heavily reduced by a dynamical sign problem, see e.g. [80]. Therefore, it is the task for the remainder of this subsection to derive a connection between the real time dynamical quantity $\tilde{C}_A(\omega)$ and a correlation function which can be obtained in the imaginary time.

The correlation function from Eq. (80) can be written in the canonical ensemble with $p_m = \exp(-\beta E_m)/Z$ as

$$\begin{aligned}
C_{AB}(\theta) &= \langle \hat{A}_\mathrm{D}(\theta) \hat{B}_\mathrm{D}(0) \rangle_0 \\
&= \frac{1}{Z} \sum_m e^{-\beta E_m} \langle m| e^{\frac{i}{\hbar}\hat{H}_0\theta} \hat{A}_\mathrm{S} e^{-\frac{i}{\hbar}\hat{H}_0\theta} \hat{B}_\mathrm{S} |m\rangle \\
&= \frac{1}{Z} \sum_{m,n} e^{-\beta E_m} \langle m| e^{\frac{i}{\hbar}\hat{H}_0\theta} \hat{A}_\mathrm{S} e^{-\frac{i}{\hbar}\hat{H}_0\theta} |n\rangle \langle n| \hat{B}_\mathrm{S} |m\rangle \\
&= \frac{1}{Z} \sum_{m,n} e^{-\beta E_m} \langle m| e^{\frac{i}{\hbar}E_m\theta} \hat{A}_\mathrm{S} e^{-\frac{i}{\hbar}E_n\theta} |n\rangle \langle n| \hat{B}_\mathrm{S} |m\rangle \\
&= \frac{1}{Z} \sum_{m,n} e^{-\beta E_m} e^{\frac{i}{\hbar}(E_m - E_n)\theta} \langle m| \hat{A}_\mathrm{S} |n\rangle \langle n| \hat{B}_\mathrm{S} |m\rangle \quad .
\end{aligned} \tag{84}$$

For the quantum breathing mode, it holds $\hat{A} = \hat{B} = \hat{A}^\dagger$ and, hence,

$$C_A(\theta) = \frac{1}{Z} \sum_{m,n} e^{-\beta E_m} e^{\frac{i}{\hbar}(E_m - E_n)\theta} \left| \langle m| \hat{A}_\mathrm{S} |n\rangle \right|^2 \quad .$$

To make a transition to the imaginary time, the argument is chosen as $\theta = -i\tau$, which leads to

$$\begin{aligned}
C_A(\tau) &= \frac{1}{Z} \sum_{m,n} e^{-\beta E_m} e^{\frac{i}{\hbar}(E_m - E_n)(-i\tau)} \left| \langle m| \hat{A}_\mathrm{S} |n\rangle \right|^2 \\
&= \frac{1}{Z} \sum_{m,n} e^{-\beta E_m} e^{\frac{E_m - E_n}{\hbar}\tau} \left| \langle m| \hat{A}_\mathrm{S} |n\rangle \right|^2 \\
&= \frac{1}{Z} \sum_{m,n} e^{-\beta E_m} e^{-\omega_{nm}\tau} \left| \langle m| \hat{A}_\mathrm{S} |n\rangle \right|^2 \quad ,
\end{aligned} \tag{85}$$

where the sloppy, but commonly used, notation $C_A(\theta = -i\tau) = C_A(\tau)$ is applied. Most terms in Eq. (85) can be identified with parts from the spectral representation (83). The connection between the two is given by

$$C_A(\tau) - \frac{1}{Z}\sum_m e^{-\beta E_m}\left|\langle m|\,\hat{A}_S\,|m\rangle\right|^2 = \frac{1}{2\pi}\int_{-\infty}^{\infty} \mathrm{d}\omega\; e^{-\omega\tau}\tilde{C}_A(\omega) \qquad , \tag{86}$$

as can be easily verified by inserting Eq. (83) into (86):

$$\begin{aligned} C_A(\tau) &= \frac{1}{Z}\sum_m e^{-\beta E_m}\left|\langle m|\,\hat{A}_S\,|m\rangle\right|^2 + \\ &\quad + \frac{1}{2\pi}\int_{-\infty}^{\infty}\mathrm{d}\omega\; e^{-\omega\tau} 2\pi \frac{1}{Z}\sum_{m\neq n} e^{-\beta E_m}|\,\langle m|\,\hat{A}_S\,|n\rangle\,|^2\delta(\omega-\omega_{nm}) \\ &= \frac{1}{Z}\sum_m e^{-\beta E_m}\left|\langle m|\,\hat{A}_S\,|m\rangle\right|^2 + \\ &\quad + \frac{1}{Z}\sum_{m\neq n}\int_{-\infty}^{\infty}\mathrm{d}\omega\;\delta(\omega-\omega_{nm}) e^{-\beta E_m} e^{-\omega\tau}|\,\langle m|\,\hat{A}_S\,|n\rangle\,|^2 \\ &= \frac{1}{Z}\sum_{m,n} e^{-\beta E_m} e^{-\omega_{nm}\tau}|\,\langle m|\,\hat{A}_S\,|n\rangle\,|^2 \qquad . \end{aligned}$$

Eq. (86) is of major importance since it provides a direct connection between desireable dynamic information and an imaginary time function which can be easily obtained with a suitable QMC method, e.g. PIMC for finite temperature. The remaining task is to reconstruct a function $\tilde{C}_A(\omega)$ which, when being inserted into (86), results in a correlation function within the errorbars of the Monte Carlo result, i.e., the left hand side. This turns out to be an ill-posed problem and is discussed in detail in section 5.3. Finally, it should be noted that it does not matter if one reconstructs the response or correlation function because the two are connected by the fluctuation dissipation theorem [81]

$$\tilde{\chi}''_A(\omega) = \frac{1}{2\hbar}\left[\tilde{C}_A(\omega) - \tilde{C}_A(-\omega)\right] \qquad .$$

In this work, $\tilde{C}_A(\omega)$ is reconstructed from Eq. (86) but one is free to choose otherwise.

5.1.4 The sum-rule formalism

Another possibility to obtain spectral information from quantities calculated in thermodynamic equilibrium are the sum-rules, see e.g. [12, 79] and the references therein. Here, one considers the energy weighted moments from the spectral function which are defined as

$$\begin{aligned} m_k &= \frac{1}{2\pi}\int_{-\infty}^{\infty}\mathrm{d}\omega\;(\hbar\omega)^k\tilde{C}_A(\omega) \\ &= \frac{1}{Z}\sum_{n\neq m} e^{-\beta E_m}(\hbar\omega_{nm})^k\left|\langle m|\,\hat{A}\,|n\rangle\right|^2 \qquad . \end{aligned} \tag{87}$$

The breathing mode at low temperature is nothing else but the lowest excitation from the ground state due to the monopole operator. Hence, one can use different moments to calculate an estimated excitation energy as

$$\hbar\omega(k,k-l) = E_{k,l} = \left(\frac{m_k}{m_{k-l}}\right)^{\frac{1}{l}} \qquad , \quad l>0 \qquad . \tag{88}$$

For completeness, it is mentioned that the different estimates from Eq. (88) fulfill the relation

$$\cdots \geq E_{k+2,1} \geq E_{k+2,2} \geq E_{k+1,1} \geq E_{k+1,2} \geq \ldots \quad , \tag{89}$$

which is useful to check the quality of the obtained results. If one assumes the system to be in the ground state, i.e., by choosing a sufficiently high β in the path integral Monte Carlo simulation, Eq. (88) provides an accurate upper bound for the lowest excitation energy, which corresponds to the breathing mode:

$$\hbar\omega_{\mathrm{BM}} \leq E_{k,l} \quad . \tag{90}$$

For too high temperature, however, the lowest energy excitation will probably occur between some higher states and (90) is not valid anymore. This is discussed in detail in section 5.2. The great advantage of the sum-rule formalism is that one does not have to explicitly evaluate the entire sum in Eq. (87), which is not feasible indeed. Instead, there exist expressions for several m_k in terms of equilibrium expectation values which can be easily obtained with PIMC.

In this work, the following four energy weighted moments are used:

- $m_3 = 8E_{\mathrm{kin}} + 8E_{\mathrm{HO}} + 2\alpha^2 E_{\mathrm{int}}$
- $m_1 = 4E_{\mathrm{HO}}$
- $m_0 = C_A(0) - \frac{1}{\beta}\left(\int_0^\beta \mathrm{d}\tau\ C_A(\tau) - 2m_{-1}\right)$
- $m_{-1} = \frac{\beta}{2}\left(\langle\hat{A}^2\rangle - \langle\hat{A}\rangle^2\right)$.

A detailed derivation of these expressions is presented in the appendix B.

5.1.5 Relative and center of mass mode

The breathing mode is dominated by two independent frequencies [72], as will be shown in the following. The starting point of this consideration is the decoupling of the system's wavefunction into relative and **c**enter-**o**f-**m**ass (COM) coordinates, respectively:

$$\begin{aligned} \mathbf{r}_{ij} &= \mathbf{r}_i - \mathbf{r}_j \quad , \\ \mathbf{R} &= \frac{1}{N}\sum_{k=1}^{N} \mathbf{r}_i \quad , \\ |\Psi_{\mathrm{S}}(t)\rangle &= |\Psi_{\mathrm{S,com}}(t)\rangle \otimes |\Psi_{\mathrm{S,rel}}(t)\rangle \quad . \end{aligned} \tag{91}$$

Splitting the monopole operator $\hat{A}$ into relative and center of mass contributions as well yields independent excitations in the two subsystems from Eq. (91) and the expectation value of the energies at an arbitrary time t can be written as

$$\begin{aligned} \langle\hat{V}_{\mathrm{HO}}\rangle(t) &= \langle\Psi_{\mathrm{S,com}}(t)|\,\hat{V}_{\mathrm{HO,com}}\,|\Psi_{\mathrm{S,com}}(t)\rangle + \langle\Psi_{\mathrm{S,rel}}(t)|\,\hat{V}_{\mathrm{HO,rel}}\,|\Psi_{\mathrm{S,rel}}(t)\rangle \quad , \\ \langle\hat{T}\rangle(t) &= \langle\Psi_{\mathrm{S,com}}(t)|\,\hat{T}_{\mathrm{com}}\,|\Psi_{\mathrm{S,com}}(t)\rangle + \langle\Psi_{\mathrm{S,rel}}(t)|\,\hat{T}_{\mathrm{rel}}\,|\Psi_{\mathrm{S,rel}}(t)\rangle \quad , \\ \langle\hat{V}_{\mathrm{int}}\rangle(t) &= \langle\Psi_{\mathrm{S,rel}}(t)|\,\hat{V}_{\mathrm{int,rel}}\,|\Psi_{\mathrm{S,rel}}(t)\rangle \quad . \end{aligned}$$

The interaction energy is independent from the COM system and, hence, the latter is simply an ideal harmonic oscillator system with an analytical solution. It directly follows from the monopole operator's selection rules that the COM contribution to the breathing mode spectrum

has a constant frequency, namely $\omega_{\text{com}} = 2$ in oscillator units. This means that the frequency estimate from Eq. (90) is an upper bound to the lowest transition in the combined spectrum from relative and COM oscillations. However, since one is only interested to get an as accurate as possible value for ω_{rel}, it is highly desireable to get rid of all com contributions. This is indeed possible since the latter are known explicitly and one finally arrives at the following expression for the relative part of the energy weighted moment [12]:

$$m_k^* = m_k - 2^{k-1} d \quad , \tag{92}$$

with d being the dimensionality. Equation (92) yields the improved estimate for the relative oscillation frequency:

$$\hbar\omega_{\text{rel}} \leq \hbar\omega^*(k, k-l) = \left(\frac{m_k^*}{m_{k-l}^*} \right)^{1/l} \quad . \tag{93}$$

There exist different limits of ω_{rel} for ideal and strongly coupled systems. For $\lambda = 0$, it holds

- $\omega_{\text{ideal}} = 2$.

For $\lambda \to \infty$, on the other hand, the classical limit of the breathing mode frequency explicitly depends on the type of interaction:

- Coulomb: $\omega_{\text{classical}} = \sqrt{3}$
- polarized dipoles: $\omega_{\text{classical}} = \sqrt{5}$.

The transition between the two will be investigated in the following subsections.

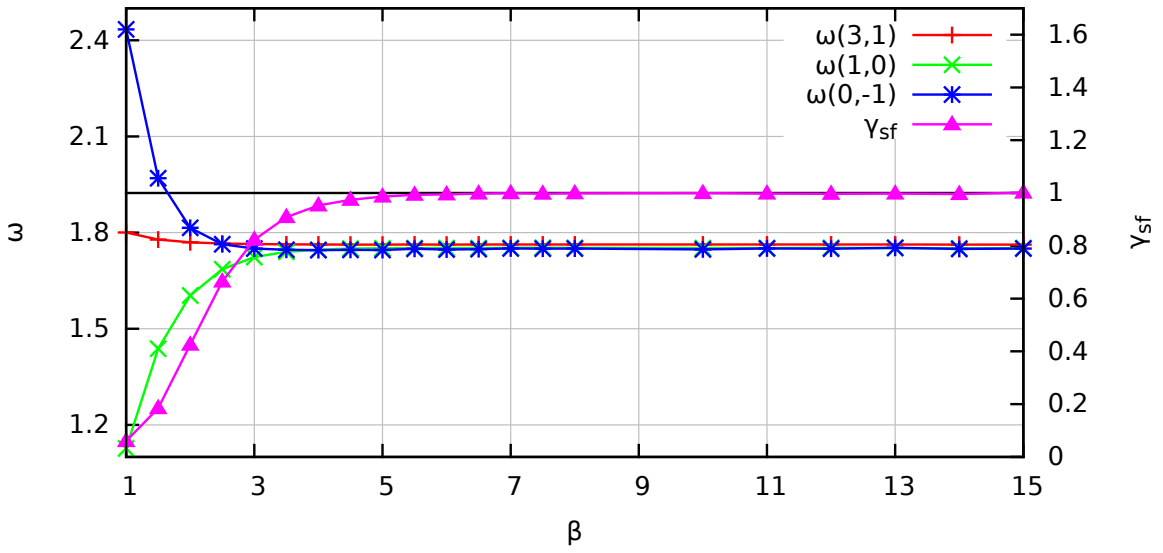

Figure 48: ***Temperature dependence of the sum-rule estimators:*** On the left ordinate, the three sum-rule estimators $\omega(3,1)$ (red), $\omega(1,0)$ (green) and $\omega(0,-1)$ (blue) are plotted over the inverse temperature β. The right ordinate corresponds to the superfluid fraction γ_{sf} which is visualized as the purple curve. The results have been obtained for a $2D$ Coulomb system with $N = 16$ and $\lambda = 3$.

5.2 Sum-rule results

In this section, several dependencies of the sum-rule estimators are analyzed in detail.

5.2.1 2D Coulomb systems

The first interesting question to be addressed is the temperature dependence of the estimators $\omega^*(k, k-l)$ from Eq. (93). It is important to understand that the T (β) dependent behaviour of those quantities does not directly correspond to the real physical behaviour of the breathing mode spectrum. The estimators provide an upper bound to the lowest excitation in the spectrum. For the ground state, i.e., $T = 0$ ($\beta \to \infty$), that transition is equal to the quantum breathing mode. For finite T, however, some higher states are populated with a non zero probability and transitions between them might have a lower energy difference. In that case, the sum-rule estimators provide an upper bound to those transitions and not to ω_{rel}. Therefore, one needs to check, if the inverse temperature β is chosen high enough to ensure the validity of the considered estimator. In Fig. 48, the BM estimators $\omega(3,1)$ (red), $\omega(1,0)$ (green) and $\omega(0,-1)$ (blue) are plotted on the left ordinate over the inverse temperature β for a system of $N = 16$ particles with $\lambda = 3$. The right ordinate corresponds to the superfluid fraction γ_{sf} (purple). All three frequency estimates exhibit a convergence to very similar values for increasing β, as it is expected. At high temperature, however, they behave quite differently. The blue and green curve start at $\omega > 2.4$ and $\omega < 1.2$, respectively, which are clearly out of the possible interval of the breathing mode, $\omega_{\text{rel}} \in [\sqrt{3}, 2]$. In contrast, the red curve only slightly changes with the inverse temperature. Hence, the $\omega(3,1)$ sum-rule provides the most stable estimation of the breathing mode frequency with respect to the temperature and, in addition, is afflicted with the smallest statistical errors. All three $\omega(i,j)$ approach their final value around $\beta = 4$.

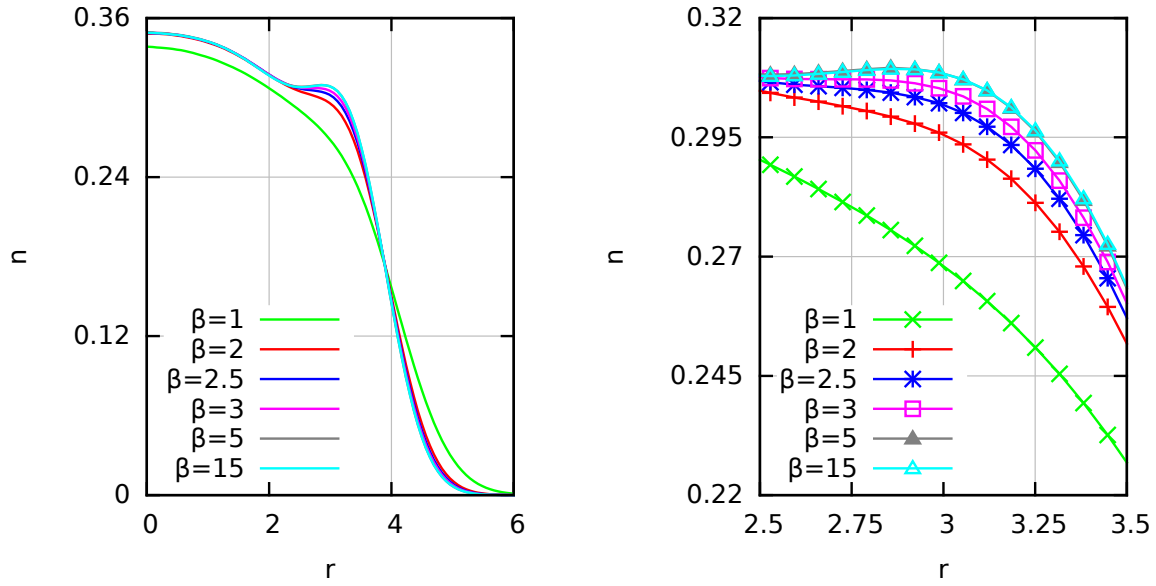

Figure 49: ***Temperature dependence of the radial density:*** The radial density n is plotted over the distance to the center of the trap r for a $2D$ Coulomb system with $\lambda = 3$ and $N = 16$. The color assignment distinguishes the inverse temperature and the right image shows a magnified segment from the left one.

For completeness, it is reported that for the converged frequencies the relation from Eq. (89) is fulfilled, i.e., $\omega(3,1) > \omega(1,0) > \omega(0,-1)$. The superfluid fraction exhibits the usual phase transition and approaches unity around $\beta = 6$. This implies that the onset of superfluidity does not seem to be directly connected to the convergence of the sum-rule estimators. In Fig. 49, the radial density n of the same system is shown for several inverse temperatures. In the left image, only the curves for $\beta = 1$ (green) and $\beta = 2$ (red) can easily be distinguished from the other curves, which look very similar. The right image shows a magnified segment of the density profile and, here, most differences can be resolved. The two curves which correspond to $\beta = 15$ (turquoise) and $\beta = 5$ (grey), however, appear to be equal, which means that they are approximately equal to the ground state density of the system. The purple and blue curves, which correspond to $\beta = 3$ and $\beta = 2.5$, respectively, slightly deviate. This is interesting because the sum-rule estimators from Fig. 48 also exhibit a deviation from the converged values of a similar magnitude around this inverse temperature. The red curve ($\beta = 2$) deviates a little stronger than the aforementioned datasets but clearly the largest difference to the ground state density appears for $\beta = 1$, i.e., the green curve. This, again, fits to the behaviour of the $\omega(i,j)$ from Fig. 48. To find a more systematical connection between the convergence of the breathing mode estimators and the density n one might define an integrated density difference as

$$\Delta n(\beta) = 2\pi\Delta r \sum_{i=1}^{N_{\text{bin}}} r_i |n_i(\beta) - n_i(\beta = 15)| \quad , \tag{94}$$

where $n(\beta = 15)$ is assumed to be equal to the ground state distribution. The results for the quantity from Eq. (94) for the system from Fig. 48 are shown in Fig. 50, where, in the left and right image, the sum-rule estimator $\omega(1,0)$ and integrated density difference Δn, respectively, are plotted over the inverse temperature. The red points visualize the corresponding datasets

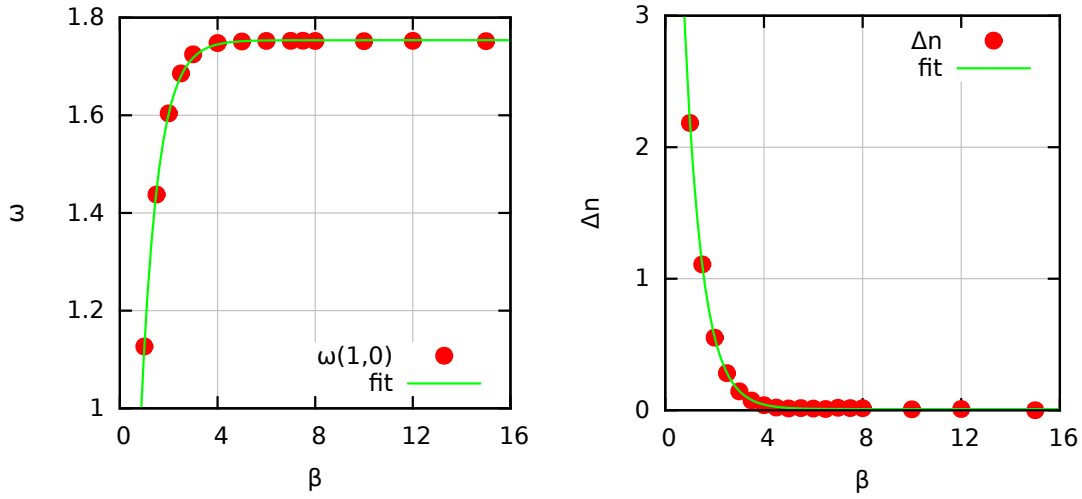

Figure 50: ***Convergence of the BM estimators compared to the density:*** In the left and right image, the breathing mode estimator $\omega(1,0)$ and the integrated density difference Δn are plotted over the inverse temperature β for the same simulation parameters as in Fig. 48. The red points correspond to the PIMC results and the green curves to fitted exponential functions according to Eq. (95).

and both curves seem to exhibit an exponential decay towards the ground state result. This suggests an exponential fit of the form

$$f(x) = a + be^{-x/c} \quad ,$$

with the characteristic decay inverse temperature c. The results of such a fit are given by the green curves in both images and the agreement with the datasets appears to be excellent. The c parameters have been calculated as

- $\omega(3,1)$: $c = 0.70 \pm 0.01$
- Δn: $c = 0.723 \pm 0.004$

and are in each others double errorbars. Hence, it can be concluded that the convergence of some of the breathing mode estimators is directly connected to the convergence of the density of the system. However, this does not hold for e.g. $\omega(0,-1)$ which exhibits a non-monotonous behaviour as explained in the discussion of Fig. 56. Finally, in Fig. 51, four random configurations from the PIMC simulation are shown. For $\beta = 1$ (top left), the system exhibits a liquidlike disorder and the extension of the particles is clearly smaller than their average distance towards each other. This means that exchange only seldomly occurs and, therefore, the system exhibits almost no superfluidity. In the $\beta = 2$ configuration (top right), there does appear significant particle exchange, in particular around the center of the trap, and the system is in the middle of the phase transition. For $\beta = 3$ (bottom left), nearly all the particles seem to be involved in exchange cycles and the superfluid fraction has almost approached $\gamma_{\text{sf}} = 0.8$. A similar behaviour, but with even more extended particle trajectories, appears for $\beta = 5$ (bottom right) and this system is almost a complete superfluid. However, the behaviour of the densities from Fig. 49 and the connected convergence of the sum-rule estimators from Fig. 48 is not obvious from the four presented random configurations.

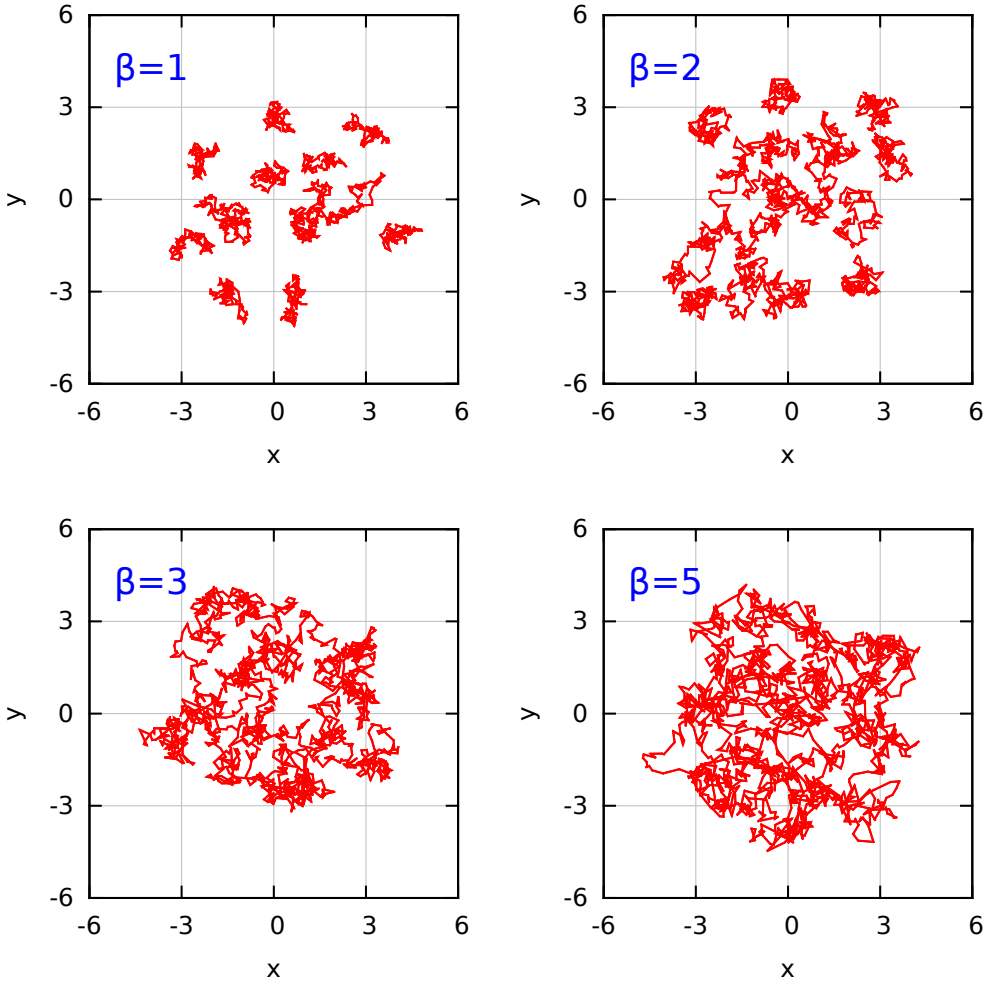

Figure 51: ***PIMC snapshots at different temperatures:*** Four random snapshots from PIMC simulations of $2D$ Coulomb systems with $N = 16$, $\lambda = 3$ and $P = 110$ are plotted for the inverse temperatures $\beta = 1$, $\beta = 2$, $\beta = 3$ and $\beta = 5$.

To verify that the correct convergence of the sum-rule estimators is a general feature and not just a coincidence for the selected system, one might investigate the temperature behaviour of $\omega(i, j)$ for different coupling parameters. This is shown in the left image of Fig. 52, where the breathing mode estimator $\omega(3, 0)$ is plotted over the inverse temperature for $N = 16$ particles with $\lambda = 0.3$ (red), $\lambda = 1$ (green), $\lambda = 3$ (blue) and $\lambda = 10$ (purple). Again, all curves exhibit a convergence towards their final value around $\beta = 4.5$. It is also interesting to note that, for large β, the four curves are ordered with decreasing λ, that is, the smaller the coupling parameter, the larger the breathing mode frequency. This is expected since for Coulomb-interacting particles the ideal limit $\omega = 2$ is larger than the classical pendant $\omega = \sqrt{3}$, which is attained at strong coupling. For high temperature, however, the order of the four curves is reversed and one cannot extract information about the true beathing mode frequency from the sum-rule estimators. In the right image of Fig. 52, the corresponding superfluid fractions γ_{sf} are plotted over the inverse temperature with the same color assignment. All curves exhibit the expected superfluid phase transition but with quite different slopes and critical temperatures. For the smallest

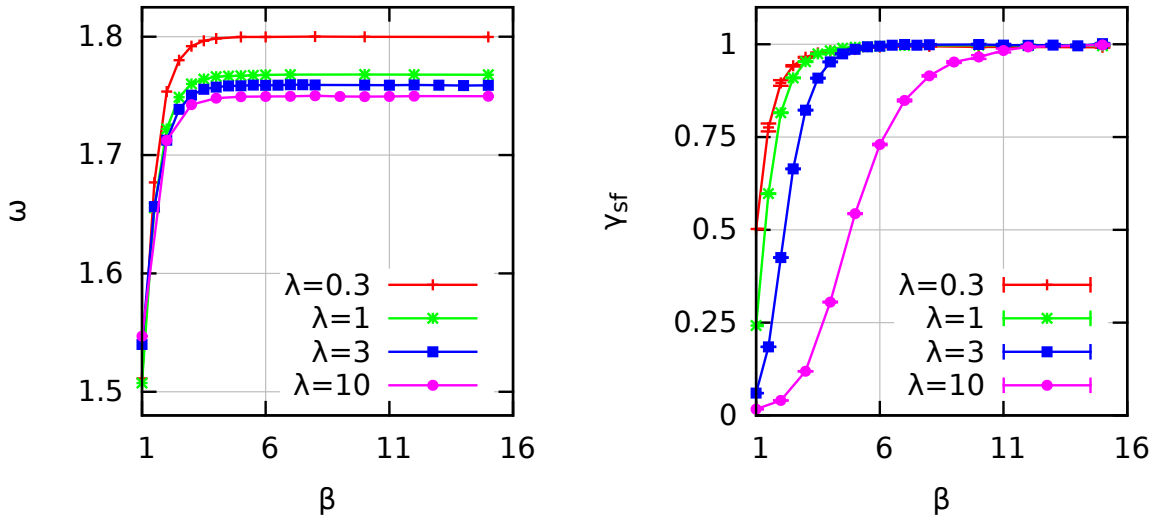

Figure 52: ***Estimator convergence for different coupling:*** The breathing mode estimator $\omega(3,0)$ (left image) and superfluid fraction γ_{sf} (right image) are plotted over the inverse temperature β for a $2D$ Coulomb system with $N = 16$ particles for different coupling parameters, namely $\lambda = 0.3$ (red), $\lambda = 1$ (green), $\lambda = 3$ (blue) and $\lambda = 10$ (purple).

coupling parameter, $\lambda = 0.3$ (red curve), the system enters the superfluid phase for the highest temperature because the average interparticle distances are smaller and, hence, the degeneracy for a particular β higher than for the other values of λ. For $\lambda = 10$, on the other hand, the system is not completely superfluid even for $\beta = 10$. Therefore, the results presented in Fig. 52 nicely demonstrate that the superfluid phase transition is in no way connected to the convergence of the sum-rule estimators for the breathing mode.

Another important check for the sum-rule formalism is the investigation of the convergence behaviour for different particle numbers. The results of such a comparison are shown in Fig. 53, where the breathing mode estimator $\omega(3,0)$ is plotted over the inverse temperature β for $N = 3$ (red), $N = 16$ (green) and $N = 60$ (blue) particles and the coupling parameter $\lambda = 3$. All three curves exhibit a similar behaviour, that is, a convergence towards some final value with increasing β, as it is expected. The red curve, however, converges slightly later than the other two. This implies that, for fewer particles in the system, less temperature is needed to populate states with a higher energy than the ground state. This is a nice feature since it means that, for systems with more particles, it is sufficient to obtain sum-rule results for smaller β and, hence, less time slices P are needed.

In the first part of this subsection, the convergence behaviour of the sum-rule estimators and the connection to other properties of the system has been analyzed. Another benchmark for the correctness of the applied formalism is the comparison to exact results, which is possible for $N = 2$ particles where it is feasible to directly diagonalize the Hamiltonian. In Fig. 54, the breathing mode frequency ω is plotted over the coupling parameter λ for two particles. The turquoise curve corresponds to the exact solution which has been calculated by Abraham and Bonitz [10] and exhibits a smooth transition between the quantum and classical limits, which are illustrated by the two straight lines. The other four curves correspond to the sum-rule estimators $\omega(3,1)$ (green), $\omega(3,0)$ (blue), $\omega(3,-1)$ (purple) and $\omega(1,0)$ and have been obtained with PIMC for $\beta = 15$ and $P = 410$. Again, the order of the different sum-rules fulfills Eq. (89),

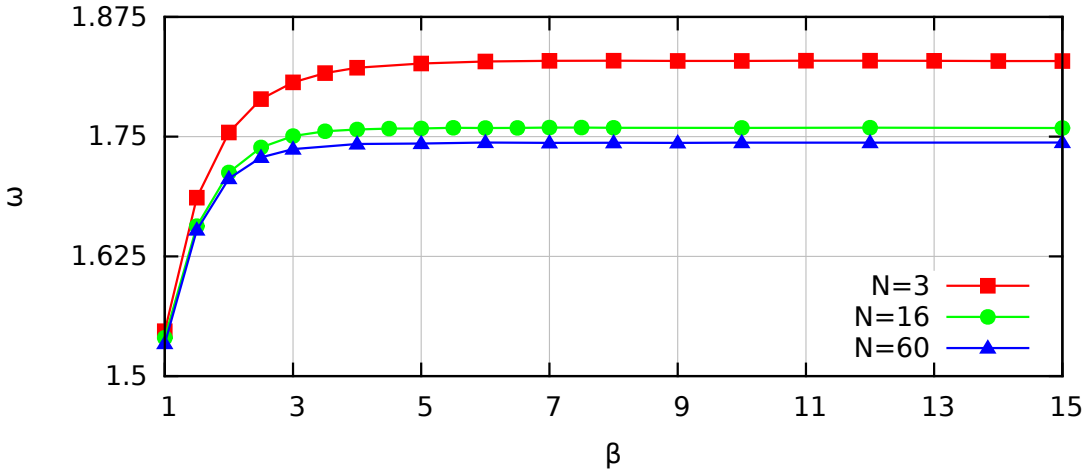

Figure 53: ***Estimator convergence for different particle numbers:*** The breathing mode estimator $\omega(3,0)$ is plotted over the inverse temperature β for a $2D$ Coulomb system with $\lambda = 3$ and the particle numbers $N = 3$ (red), $N = 16$ (green) and $N = 60$ (blue).

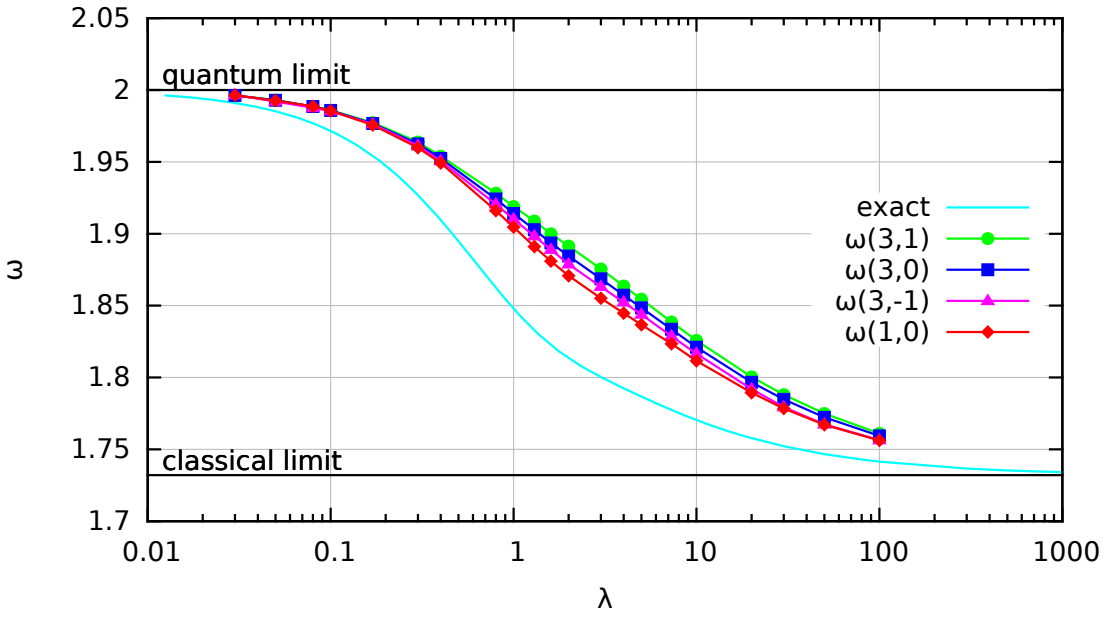

Figure 54: ***Coupling dependence of the unimproved breathing mode estimators for two Coulomb particles in*** $2D$***:*** Four breathing mode estimators and the exact solution by Abraham and Bonitz [10] are plotted over the coupling parameter λ for $N = 2$ Coulomb-interacting particles in $2D$ for $\beta = 15$.

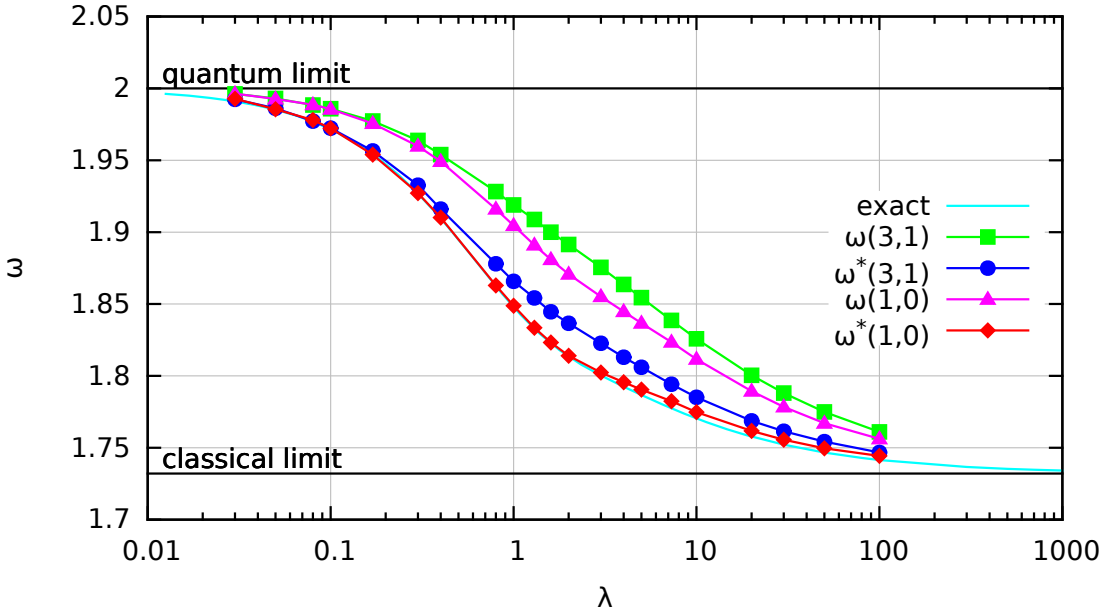

Figure 55: ***Coupling dependence of the un- and improved breathing mode estimators for two Coulomb particles in*** $2D$***:*** Two unimproved breathing mode estimators, their improved pendants and the exact solution by Abraham and Bonitz [10] are plotted over the coupling parameter λ for the system from Fig. 54.

as it is expected. However, there appears a large gap between between the turquoise and the other curves in the middle of the transition. Hence, the presented sum-rule results only provide information about the qualitative behaviour of the breathing mode but the difference to the exact value is significant. The explanation for this seemingly unfortunate feature is given by the center of mass contribution to the monopole spectrum at $\omega = 2.0$. This additional peak enters the usual sum-rules, as explained in section 5.1.5, and shifts the estimates to higher frequencies. Therefore, it is inevitable to consider the improved sum-rule estimators from Eq. (93) which are no longer afflicted with the center of mass contribution.

The results are shown in Fig. 55, where, again, the breathing mode frequency is plotted over the coupling parameter for the same system. This time, however, the four sum-rule results provide a comparison between the standard and the improved frequency moments. The green and blue curve correspond to $\omega(3,1)$ and $\omega^*(3,1)$, respectively, and the latter is much closer to the exact solution than the unimproved pendant. The purple and red curve exhibit the same behaviour for $\omega(1,0)$ and $\omega^*(1,0)$ and the latter almost perfectly coincides with the turquoise dataset. Hence, getting rid of the center of mass contribution is an indenspensible tool to obtain the correct breathing mode for two particles. Thus, it can be concluded that the improved sum-rule estimators provide an accurate upper bound to the relative oscillations in the monopole spectrum. For completeness, it is reported that the improved estimator $\omega^*(0,-1)$ exhibits a slightly non-monotonous behaviour and, for the parameters from Fig. 55, it is not always an upper bound to the exact values. This, however, is not an error of the sum-rule formalism or the implementation, but can be explained with the temperature dependence. In Fig. 56, the breathing mode frequency is plotted over the inverse temperature for two particles with $\lambda = 30$. The red and green curves correspond to the improved estimators $\omega^*(0,-1)$ and $\omega^*(1,0)$, respectively. Both datasets seem to exhibit the expected convergence for increasing β. The right

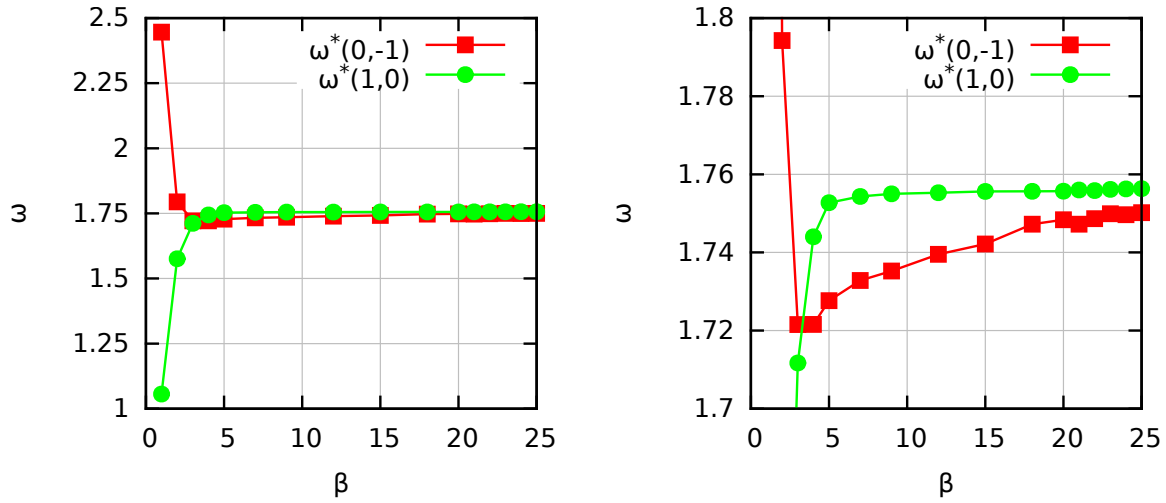

Figure 56: ***Temperature dependence of two improved breathing mode estimators:*** The improved breathing mode estimators $\omega^*(0,-1)$ and $\omega^*(1,0)$ are plotted over the inverse temperature β for $N = 2$ Coulomb-interacting particles in $2D$ with $\lambda = 30$. The right image shows a magnified segment from the left one.

image from the figure shows a magnified segment and it becomes clear that, even for $\beta = 25$, the two particle system has not fully reached the ground state, yet. The green curve only slightly increases from $\beta = 15$, which corresponds to the results from Fig. 55, to $\beta = 25$. This is consistent with the interpretation of the improved sum-rules as an accurate upper bound. The red curve, however, clearly increases in the same interval and, hence, it is obvious that the peculiar results at $\beta = 15$ do not correspond to the correct estimates of the breathing mode frequency. In conclusion, the comparison of the sum-rules with the exact solution has nicely illustrated the necessity of the improved estimators and the obtained PIMC results are in excellent agreement with the true breathing mode frequency.

A very interesting topic to be investigated with the sum-rule formalism is the dependence of the breathing mode frequency on the particle number N. This is shown in Fig. 57, where the improved estimator $\omega^*(3,1)$ is plotted over N for the coupling parameters $\lambda = 10$ (red), $\lambda = 3$ (green), $\lambda = 1$ (blue) and $\lambda = 0.3$ (purple). All results have been obtained for $\beta = 5$ and $P = 110$. The four curves exhibit a decay towards the classical limit with an increasing particle number. This implies that the adding of particles to an otherwise unchanged system leads to more collective behaviour, which is in excellent agreement with the results for fermions by Abraham and Bonitz [10]. A natural quantity to confirm this interpretation are degeneracy and non-ideality parameters, which are analyzed in subsection 5.2.4 for $2D$ and $3D$ Coulomb and $2D$ dipole systems. For completeness, it is reported that the four curves in Fig. 57 are ordered with increasing λ, as it is expected. Only for $N = 1000$, this order is marginally violated. This could be caused by either a small temperature effect, i.e., a not completely converged estimator $\omega^*(3,1)$, or the upper bound nature of the sum-rules themselves. However, the latter do not provide the exact breathing mode anyway and this minor peculiarity is clearly below the expected accuracy of the formalism. Finally, the red curve exhibits some slightly unsmooth features for small N because the properties of few-particle systems explicitly depend on the shell configurations. This effect, obviously, increases with the coupling parameter λ.

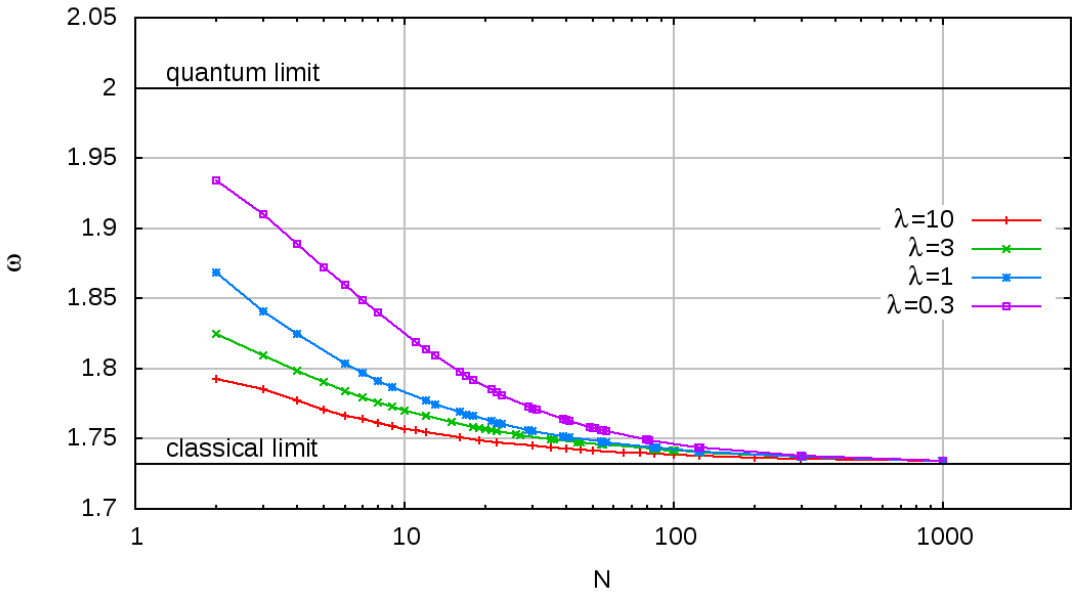

Figure 57: ***Particle number dependence of the breathing mode for*** $2D$ ***Coulomb systems:*** The improved breathing mode estimator $\omega^*_{\mathrm{BM}}(3,1)$ is plotted over the particle number N for a $2D$ Coulomb system at $\beta = 5$. The red, green, blue and purple curve correspond to $\lambda = 10$, $\lambda = 3$, $\lambda = 1$ and $\lambda = 0.3$, respectively.

5.2.2 Comparison of Coulomb systems in $2D$ and $3D$

Like in the $2D$ case, it is a useful check to compare the convergence of different sum-rule estimators and verify their order. This is shown in Fig. 58, where the breathing mode frequency is plotted over the inverse temperature for $N = 16$ Coulomb-interacting particles in $3D$ with the coupling parameter $\lambda = 10$. The red curve corresponds to the estimator $\omega(3,1)$ and exhibits a monotonous decay towards its final value and the slightest deviations of all three curves from the latter at high temperature. The green curve belongs to $\omega(1,0)$ and, again, a monotonous convergence appears, although with a positive slope and much larger deviations at small β. The blue curve corresponds to $\omega(0,-1)$ and exhibits a rather peculiar, non-monotonous behaviour. For small inverse temperatures, it declines until around $\beta \approx 5$ a minimum appears and the estimator approaches its final value from below. The same behaviour has been observed for $2D$ systems, as shown in Fig. 56. The ordering of the three presented estimators fulfills the theoretical prediction from Eq. (89) and the correctness of the applied sum-rule formalism seems to be confirmed for $3D$ systems, as well.

Another interesting question is the impact of an additional dimension on the coupling strength dependence of the breathing mode. To provide an answer, $N = 2$ particles are simulated at $\beta = 15$ and, in Fig. 59, the improved sum-rule estimator $\omega^*(1,0)$ is plotted over λ. The green curve corresponds to the $2D$ and the red one to the $3D$ system. Both curves exhibit a similar transition between the quantum and classical limit, where they are equal. For intermediate coupling, however, the results significantly deviate and the red curve clearly exceeds the green one. This implies that in this regime the three dimensional system exhibits less collective behaviour than the two dimensional pendant. This is expected since, due to the additional available dimension, the particles can avoid each other more effectively. For completeness, it is also reported that the chosen small system which consists of two particles only is probably the

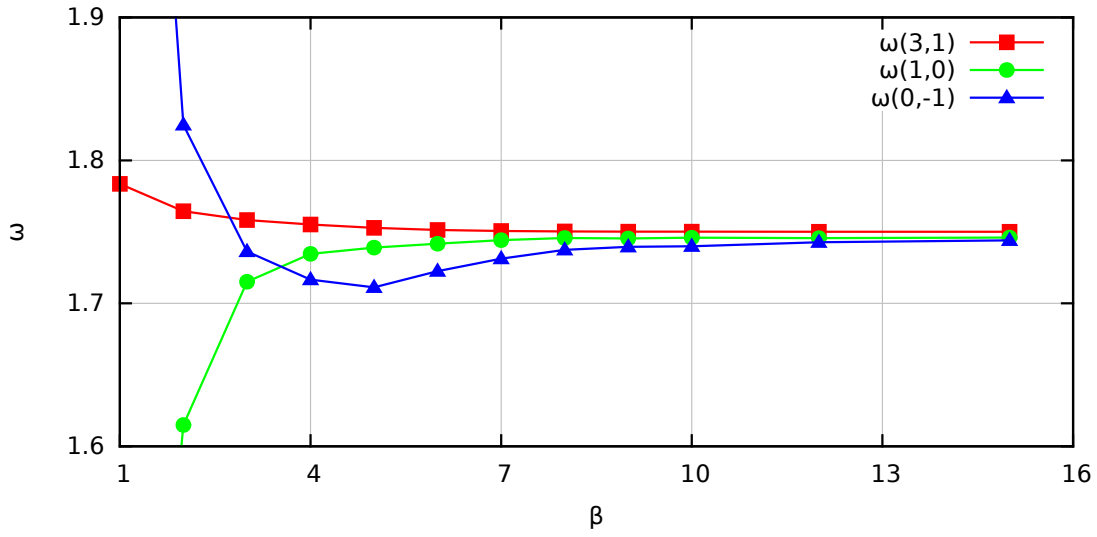

Figure 58: ***Comparison of different BM estimators of a*** $3D$ ***system:*** Three breathing mode estimators are plotted over the inverse temperature β for a $3D$ Coulomb system with $\lambda = 10$ and $N = 16$.

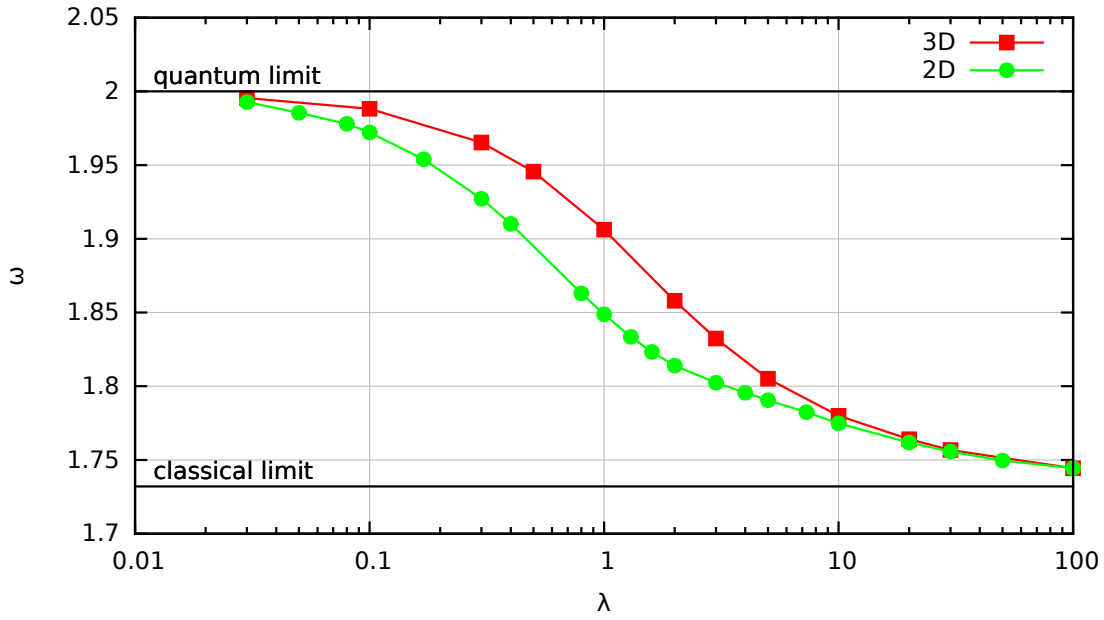

Figure 59: ***Comparison of the breathing mode in*** $2D$ ***and*** $3D$***:*** The improved estimator $\omega^*(1,0)$ is plotted over the coupling parameter λ for two particles in both $2D$ (green) and $3D$ (red) at the inverse temperature $\beta = 15$ and $P = 410$ time slices.

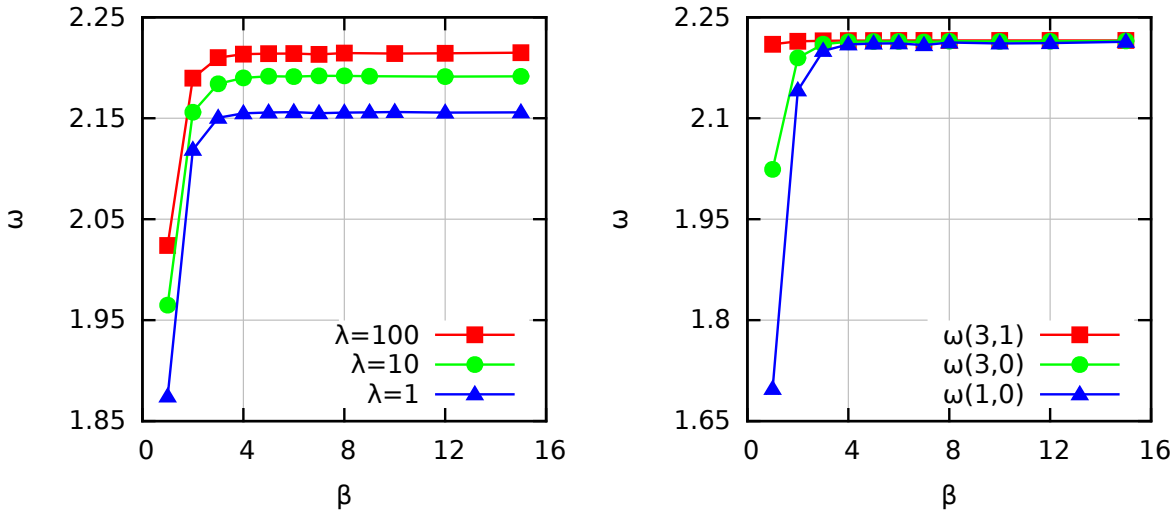

Figure 60: ***Sum-rule convergence of*** $2D$ ***dipole systems:*** The estimated BM frequency ω is plotted over the inverse temperature β for a $2D$ dipole system with $N = 16$. In the left image, results for the estimator $\omega(3,0)$ are shown for $\lambda = 100$, $\lambda = 10$ and $\lambda = 1$. The right image solely corresponds to $\lambda = 100$ and the color assignment distinguishes three different estimators.

optimal example to illustrate the difference between the breathing mode of $2D$ and $3D$ systems. The reason for this claim is the decrease of ω_{BM} with an increasing particle number N, which could prevent the reported difference between the two curves in Fig. 59 from being detected. The sum-rules do provide an (accurate) upper bound for the true transition frequency. If the real difference between the frequencies for the selected $2D$ and $3D$ system is smaller than the inaccurateness due to the upper bound nature of the sum-rule formalism, the correct behaviour cannot be resolved any more and even the opposite trend could appear. This has been observed for both $N = 16$ and $N = 150$ particles with $\lambda = 10$. This, however, is an exclusive feature of the estimator $\omega(3,1)$, which has the largest systematic error of all $\omega(i,j)$. The other sum-rule results suffer from a significantly larger statistical error and fluctuate within each others errorbars. The dependence of the quantum breathing mode on the particle number N of a $3D$ system is discussed in subsection 5.2.4.

5.2.3 2D dipole systems

The last class of systems to be considered for the investigation of the quantum breathing mode in this work are dipole-interacting particles in $2D$. An example is presented in Fig. 60 and the left image shows the convergence of the sum-rule estimator $\omega(3,0)$ for $N = 16$ particles and the coupling parameters $\lambda = 100$ (red), $\lambda = 10$ (green) and $\lambda = 1$ (blue). All curves approach a final value which is located within the correct interval $\omega \in [2, \sqrt{5}]$ around $\beta = 5$ from below. The estimated breathing mode frequency increases for stronger coupling, as it is expected for dipole-interacting particles. In the right image of Fig. 60, PIMC results from the breathing mode estimators $\omega(3,1)$ (red), $\omega(3,0)$ (green) and $\omega(1,0)$ (blue) are plotted over the inverse temperature for $N = 16$ strongly coupled particles with $\lambda = 100$. As usual, all three curves converge with increasing β and, again, approach their final value from below around $\beta = 5$. The order of the three estimators fulfills Eq. (89). In Fig. 61, the corresponding densities n for the same parameters and $\beta = 15$ (red), $\beta = 4$ (green), $\beta = 3$ (blue), $\beta = 2$ (purple) and

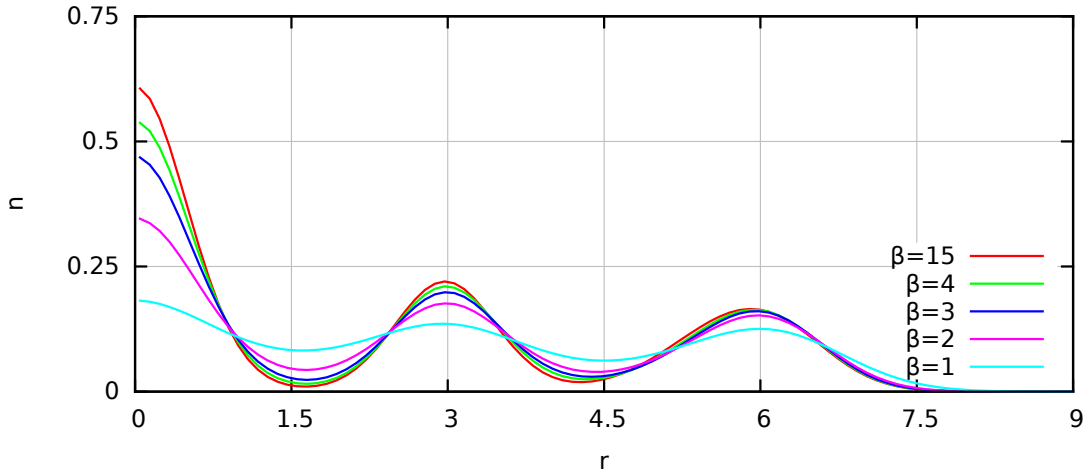

Figure 61: ***Comparison of densities for different temperatures:*** The radial density n is plotted over the distance to the center of the trap r for a $2D$ dipole system with $N = 16$ and $\lambda = 100$. The color assignment distinguishes the different inverse temperatures β.

$\beta = 1$ (turquoise) are shown. All except the latter curve exhibit a clearly pronounced shell structure with relatively small overlap. The red curve approximately equals the ground state density and, with increasing temperature, the shells become flatened. The deviations to the $\beta = 15$ result at different inverse temperatures do reasonably coincide with the behaviour of the sum-rule estimators from Fig. 60, as it has already been discussed for Coulomb interaction. The turquoise curve exhibits a rather smooth progression and, for $\beta = 1$, the spatial order of the system seems to be almost entirely lost. Further results for the quantum breathing mode of $2D$ dipole systems are presented in subsections 5.2.4 and 6.3.3, where the particle number dependence and a comparison between bosons and fermions, respectively, are discussed.

5.2.4 Transition towards collective behaviour

The last sum-rule results to be discussed in this work concern the dependence of the quantum breathing mode on the system size, i.e., the particle number N. Abraham and Bonitz [10] have found that weakly coupled Fermi systems in two dimensions exhibit a transition towards the classical limit of ω_{rel}. In this section, a similar analysis is conducted for bosons with both dipole and Coulomb interaction and in $2D$ and $3D$ for the latter. In the left image of Fig. 62, the PIMC results for the improved estimator $\omega^*(3,1)$ are plotted over the particle number N for $\lambda = 10$. The red and blue curves correspond to Coulomb- and dipole-interacting particles in $2D$, respectively, and have been obtained for the inverse temperature $\beta = 5$. The green curve corresponds to $3D$ Coulomb systems and $\beta = 10$. For completeness, it is again mentioned that, for few particles (i.e., $N < 10$), the BM estimators are not fully converged. However, the selected $\omega^*(3,1)$ exhibits a rather small temperature dependence and the behaviour for larger N is expected to be accurate and the uncertainty due to the upper bound nature of the sum-rules themselves is distinctly larger. The blue curve starts at $\omega \approx 2.162$ for two particles and monotonically increases with N. Hence, the quantum breathing mode for two dimensional dipole systems seems to converge towards the classical limit $\omega = \sqrt{5}$. The red and green curve exhibit a similar behaviour, that is, a monotonical decreasing from $\omega \approx 1.79$ at $N = 2$ towards the classical limit for Coulomb-interaction $\omega = \sqrt{3}$. Both datasets appear to be nearly equal but the

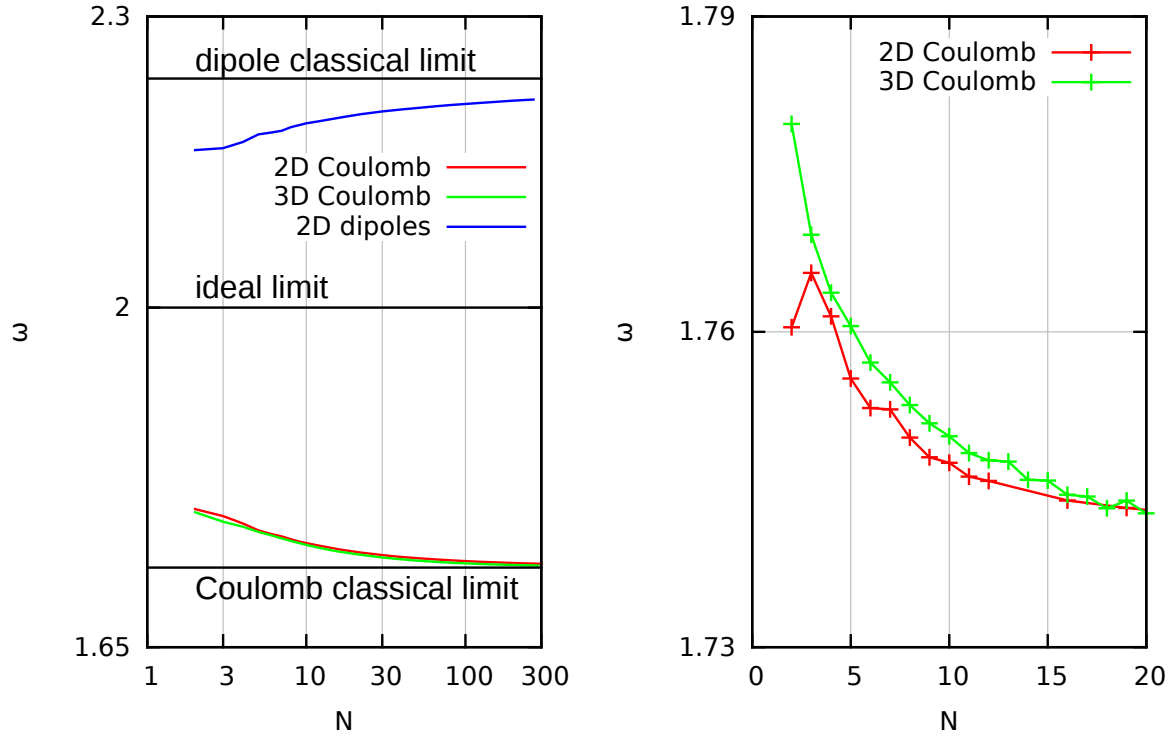

Figure 62: ***Particle number dependence of the quantum breathing mode:*** In the left image, the improved breathing mode estimator $\omega^*(3,1)$ is plotted over the particle number N for $\lambda = 10$ and $2D$ and $3D$ Coulomb systems and $2D$ dipoles. The right image shows the estimator $\omega^*(1,0)$ for few particles.

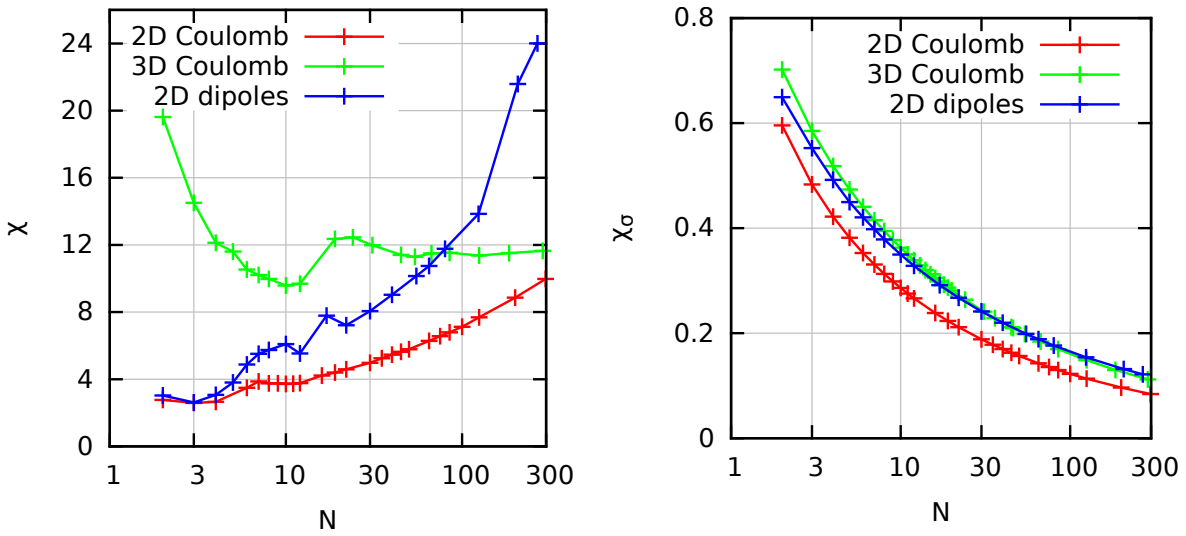

Figure 63: ***Comparison of degeneracy and non-ideality parameters:*** In the left and right image, the averaged degeneracy parameter χ and non-ideality parameter χ_σ, respectively, are plotted over the particle number for the system from Fig. 62 with the same color assignment.

$2D$ results always exceed the $3D$ pendants. However, this is not a physical effect, but can safely be accounted to the upper bound nature of the sum-rules as it has already been pointed out in section 5.2.2. This explanation is confirmed by the right image of Fig. 62, where the improved estimator $\omega^*(1,0)$ is plotted over N for up to twenty particles for both dimensionalities. Indeed, the more accurate upper bounds reveal that the breathing mode adopts higher values in $3D$ and, in addition, provide a better insight into the non-monotonous behaviour due to finite size effects, i.e., shell configurations. The latter effect is clearly more pronounced in two dimensions. In summary, all three systems exhibit a transition towards their respective classical limit of the relative frequency. To explain this trend, one might investigate degeneracy and non-ideality parameters. In the left image of Fig. 63, the averaged degeneracy parameter χ, see also section 4.2 and Fig. 32 in particular, is plotted for the same systems as in Fig. 62. All three curves exhibit a seemingly irregular behaviour for small N, which is again due to the aforementioned finite size effects. The degeneracy of the dipole systems almost monotonically increases with the particle number. The same is true for the $2D$ Coulomb systems, but with a reduced slope. The $3D$ Coulomb system, on the other hand, seems to converge towards a constant value and the higher χ for few particles are due to the increased inverse temperature compared to the other curves. Therefore, the observed behaviour of the breathing mode is not directly connected to the degeneracy of the system. Abraham and Bonitz [10] have suggested a non-ideality parameter χ_σ which can be defined as

$$\begin{aligned} \chi_\sigma &= \frac{\sigma_0}{\sigma} \quad \text{, with} \\ \sigma &= \sqrt{2E_{\mathrm{HO}}} \quad \text{and} \\ \sigma_0 &= \begin{cases} \sqrt{N}, & \text{for } 2D \\ \sqrt{\frac{3N}{2}}, & \text{for } 3D \end{cases} . \end{aligned} \tag{95}$$

Here, σ can be interpreted as the mean extension of the correlated system and σ_0 as the ideal pendant. Hence, the non-ideality parameter from Eq. (95) equals unity for ideal systems and eventually vanishes with increasing coupling strength λ. The results for the simulations from Fig. 62 are plotted in the right image of Fig. 63, where χ_σ is plotted over N. All three curves start at relatively high values around $\chi_\sigma = 0.65$ and monotonically decrease with N. The modulus of the slope decreases with N as well, which is similar to the behaviour of the breathing mode. Thus, the findings by Abraham and Bonitz [10] for fermions, that the transition of ω_{rel} towards the classical limit for large systems is a consequence of the increasing non-ideality, are confirmed for bosons in all three presented cases. However, to what extend the explicit choice of χ_σ can be exploited for diagnostic purposes, is unclear. The dipole curve always exceeds the $2D$ Coulomb pendant, which fits the fact that the breathing mode for the former converges slowlier. The $3D$ Coulomb data, on the other hand, exhibits even larger values for $N < 100$ particles than the blue curve, although the BM frequency in the former case is probably already closer to the classical limit. The non-ideality parameter is, similar to the degeneracy parameter χ, arbitrary to some degree and the definition from Eq. (95) might not have the same significance for $2D$ and $3D$ systems.

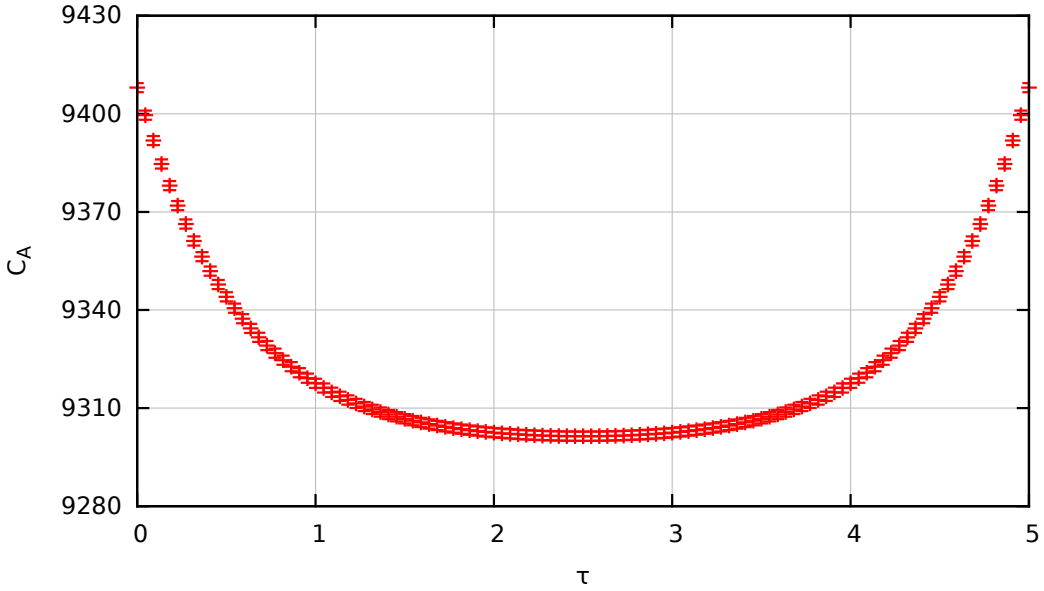

Figure 64: ***PIMC result for the imaginary time correlation function:*** The monopole operator's CF C_A is plotted over the imaginary time τ for a $2D$ Coulomb system with $N = 30$, $\lambda = 0.3$, $\beta = 5$ and $P = 110$.

5.3 Reconstruction of the spectral function

The sum-rules provide an accurate upper bound for the lowest transition in the spectrum of interest. However, the investigation of temperature effects requires knowledge about the entire spectrum, because new peaks will emerge and existing ones might be broadened and their spectral weight changed. The only known approach to obtain such detailed dynamic information from equilibrium simulations is the reconstruction of the spectral function from the corresponding imaginary time autocorrelation function. The latter might be easily obtained with PIMC with the estimator

$$C_A(\tau = m\epsilon) \approx \frac{1}{PN_{\mathrm{MC}}} \sum_{k=1}^{N_{\mathrm{MC}}} \sum_{j=0}^{P-1} A_{k,j} A_{k,j+m} \quad ,$$

and an example for $N = 30$ Coulomb-interacting particles in $2D$ with $\beta = 5$, $\lambda = 0.3$ and $P = 110$ is shown in Fig. 64. The remaining task to be discussed in the following section is the solution of the inverse problem given by Eq. (86). The reconstruction is a well known tool not only for the investigation of the quantum breathing mode, but has already been successfully applied to calculate e.g. the dynamic structure factor and the single particle spectrum. The corresponding correlation functions in these cases are the density-density CF and the Matsubara Green function, respectively, and a detailed analysis for both examples can be found in [13].

5.3.1 Problem statement

The general problem which has to be solved is of the form

$$G(\tau_i) = \int_{-\infty}^{\infty} \mathrm{d}\omega \; S(\omega) K(\omega, \tau_i) \quad . \tag{96}$$

The input data is given by the PIMC result for an imaginary time correlation function $G(\tau_i)$ which is calculated on the discrete time slices τ_i with $i = 1, \ldots, M$. However, these results are not exact, but afflicted with the corresponding statistical errors $\delta G(\tau_i)$. The right hand side of Eq. (96) is given by the integral over the desired spectral function $S(\omega)$ times an integration kernel $K(\omega, \tau_i)$, depending on both the frequency and the imaginary time. A comparison of Eqs. (96) and (86) reveals the particular form of K for the quantum breathing mode:

$$K(\omega, \tau_i) = e^{-\omega\tau_i} \quad .$$

The connection between $S(\omega)$ and $\tilde{C}_A(\omega)$ is given by a constant factor which can be neglected. The task to be solved is the calculation of a model spectral function $\tilde{S}(\omega)$ which, when being inserted into (96), results in a correlation function $\tilde{G}(\tau_i)$ which is within the errorbars of the Monte Carlo results. The quality of the reconstructed quantity can be characterized with a deviation measure of the form

$$\chi^2 = \frac{1}{M} \sum_{i=1}^{M} \frac{\left(G(\tau_i) - \tilde{G}(\tau_i)\right)^2}{\delta G^2(\tau_i)} \quad , \tag{97}$$

which should be of the order of unity. The trivial approach would be to implement some suiting gradient method and simply minimize Eq. (97). However, the ill-posed nature of the reconstruction causes the existence of an infinite number of reconstructed correlation functions within the errorbars of the PIMC data, which means that there is no unique solution. The difficulty is that most functions fulfilling the deviation measure are afflicted with unphysical sawtooth noise which is caused by an overfitting to the input data. Therefore, it is a challenge to minimize χ^2 and get rid of any unphysical noise at the same time, which is a hard problem, indeed.

In order to test any reconstruction method, one can simply create a suiting testcase by hand and use, in principle, any positive function as a trial spectrum $S(\omega)$. A convenient choice is a superposition of η gaussians:

$$S(\omega) = \sum_{l=1}^{\eta} \frac{A_l}{\sqrt{2\pi}\sigma_l} \exp\left(-\frac{(\omega - P_l)^2}{2\sigma_l^2}\right) \quad .$$

The corresponding correlation function $G(\tau)$ can be trivially calculated using Eq. (96). However, a realistic input for the reconstruction is afflicted with statistical errors, which have to be artifically generated for the testcase. It is sufficient to choose the same variance for every point τ_i:

$$G_{\text{test}}(\tau_i) = G(\tau_i) + \alpha\sigma G(0) \quad , \tag{98}$$

with a normally distributed random number α. Fig. 65 shows the result of the primitive reconstruction, i.e., only the minimization of χ^2, for such a testcase, and the spectrum is plotted over ω. The input function consists of two broad gaussians, while the reconstructed curve exhibits two very sharp peaks, centered at different positions. The reconstruction has, obviously, failed to reproduce the test spectrum. In the left image of Fig. 66, the correlation function G is plotted over τ. The red points again correspond to the perturbed input dataset according to Eq. (98) and the green curve has been reconstructed. Both datasets seem to coincide and exhibit the same exponential decay. The right image shows a magnified segment and the reconstructed correlation function nicely extrapolates between the fluctuating input. The deviation measure

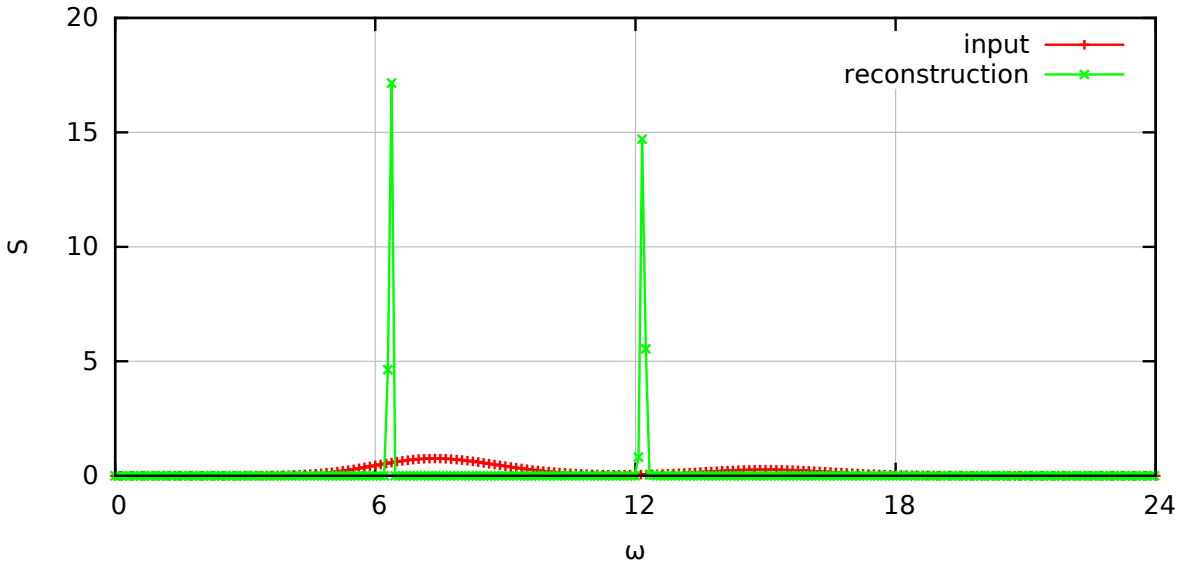

Figure 65: ***Example for the sawtooth noise:*** The spectral function S is plotted over the frequency ω. The red curve corresponds to the exact model spectrum and the green curve has been reconstructed.

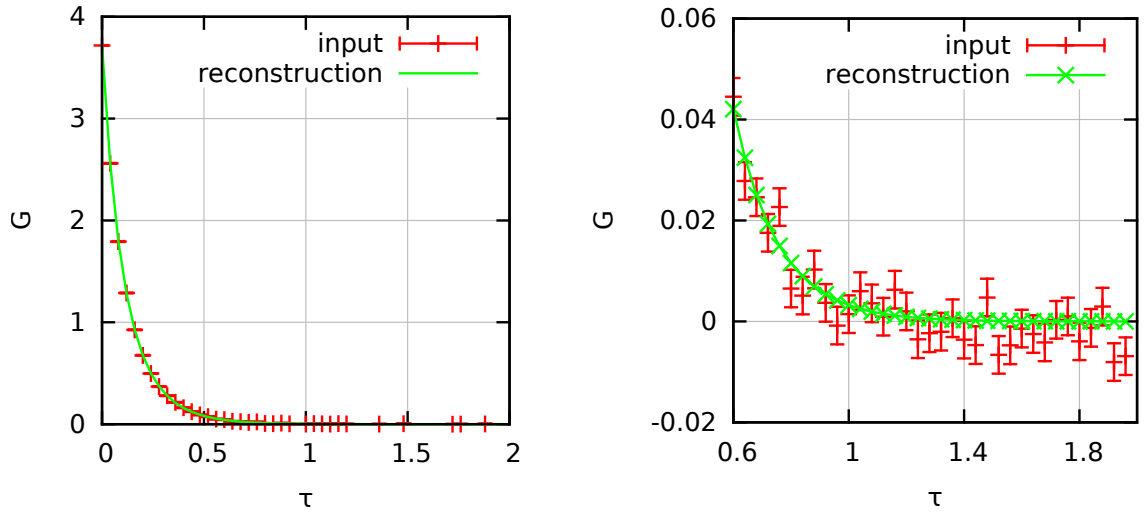

Figure 66: ***Example for the sawtooth noise:*** The correlation function G is plotted over the imaginary time τ. The red curve corresponds to the perturbed input data and the green curve has been reconstructed. The right image shows a magnified segment from the left one.

has been calculated as $\chi^2 \approx 0.98$. Hence, it must be concluded that a deviation measure below unity and a smooth extrapolation between the input data is insufficient. The solution of this ill-posed problem requires additional effort and three different approaches will be introduced in the following subsections.

5.3.2 The Maximum Entropy Method

The **M**aximum **E**ntropy **M**ethod (MEM) is a widely used regularization method [82]. The basic idea is to make use of any information about the spectrum of interest which is available in advance. This is justified by the Bayes theorem [83]

$$P[S|G]P[G] = P[G|S]P[S] \quad ,$$

with $P[x]$ being the a-priory probability for a specific x and the likelihood function $P[y|x]$, i.e., the probability to obtain y under the condition of an already given x. The problem of reconstruction as stated in Eq. (96) is nothing else than the task to find the most probable spectrum $S(\omega)$ for a given correlation function G, described by $P[S|G]$. This rather difficult problem can be transformed into the more trivial task to find G for a given S, if a-priory knowledge about the spectrum is available:

$$P[S|G] \propto P[G|S]P[S] \quad .$$

The reality, however, is not just as nice since this simplification comes at a high price. The inclusion of assumed knowledge about the spectrum leads to a biased outcome of the reconstruction because an expected absence of sharp peaks might lead to a suppression of the latter, although they could be physically motivated and, hence, be an exciting new discovery. The likelihood function is typically defined as

$$P[G|S] \propto \exp\left(-\frac{\chi^2}{2}\right) \quad ,$$

with the usual deviation measure χ^2 given by Eq. (97). The crucial function in the Maximum Entropy Method is the prior knowledge about the spectrum

$$P[S] \propto \exp\left(\alpha E[S]\right) \quad ,$$

with the free control parameter α and the entropy functional

$$E[S] = \int \mathrm{d}\omega \; S(\omega) \log\left(\frac{S(\omega)}{T(\omega)}\right) \quad .$$

Any preknown information about the spectrum is put into the target function $T(\omega)$. The definitions of $P[S]$ and $E[S]$ yield that the prior knowledge function for a particular spectrum $S(\omega)$ is maximized for $S(\omega) = T(\omega)$. Therefore, the amount of new information which is revealed by the reconstruction crucially depends on the choice of the control parameter α since, for $\alpha = 0$, the regularization has no effect and the result is again afflicted with sawtooth noise and, for $\alpha \to \infty$, one just receives T and the reconstruction is futile. There exist several possibilities, like e.g. a weighted averaging over several α.

The Maximum Entropy Method is well suited to get smooth spectra without any sawtooth noise if enough prior knowledge about $S(\omega)$ is provided in advance. However, the regularization comes at a high cost because the outcome is always biased and, therefore, the amount of new information limited. A practical application of the method is presented in [84], where the dynamic structure factor is reconstructed from PIMC results for a system of liquid ^{4}He at finite T. The analysis revealed new information beyond the scope of variational ground state methods which had been used before. State of the art enhancements to MEM might be found in [85].

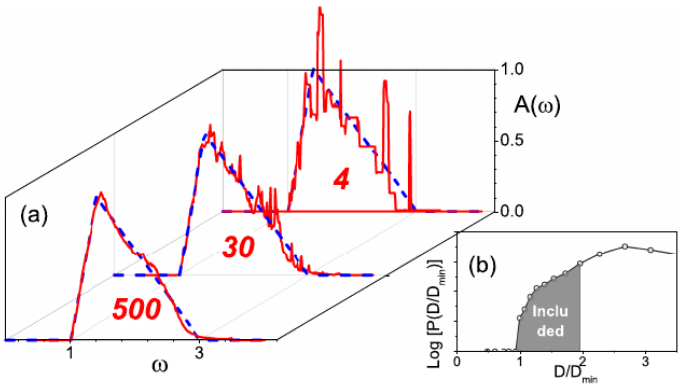

Figure 67: ***Illustration of the composition of the final spectrum:*** In graph (a), the spectral function S - here denoted as A - is plotted over the frequency ω. The three red curves correspond to different numbers of included trial solutions $S_k(\omega)$ and the dotted blue ones to the exact spectrum. Graph (b) shows the logarithmic probability for a ratio of the deviation measure D and the minimum $D_{\mathbf{min}}$, plotted over the latter. The shaded area marks all trial functions which are included in the final average. The figure has been obtained from [87].

5.3.3 The Stochastic Optimization Method

The **S**tochastic **O**ptimization **M**ethod (SOM) has been introduced by Mishchenko et al. [86] and requires no prior knowledge about the spectral function of interest. Since no regularization is used, the SOM guarantees unbiased results. The main idea is to randomly generate a large set of independent trial spectra $S_k(\omega)$, with the only criterion being the minimization of the χ^2 measure. Every single solution S_k will be afflicted with the sawtooth noise. However, the final result of the SOM is given by an average over all trial spectra below a specific deviation measure, which means that all unphysical noise should be averaged out if enough functions are included. The big advantage of this method is that even extremely sharp peaks can be recovered, while the outcome will be at least relatively smooth.

Another difference compared to other reconstruction methods is that the spectrum $S(\omega)$ is not represented by a set of discrete values S_i at frequencies ω_i but is instead given by the superposition of B continuous rectangular basis functions:

$$S_k(\omega) = \sum_{y=1}^{B} \eta_y(\omega) \qquad .$$

The rectangles $\eta_y(\omega)$ can be parametrized by their height h_y, width w_y and position of the center of mass c_y:

$$\eta_y(\omega) = \begin{cases} h_y, & \text{if } \omega \in [c_y - \frac{w_y}{2}, c_y + \frac{w_y}{2}] \\ 0, & \text{otherwise.} \end{cases}$$

To obtain a reconstructed spectrum which fulfills the deviation measure and, thus, fits the PIMC errorbars, one needs to implement an update scheme which is able to reach all possible configurations, i.e., by deforming, moving and deleting existing basis functions and inserting new ones. In addition, it is very important to have some kind of annealing procedure which allows a temporary increase of χ^2 to escape local minima. However, the particular choice of the updates

is not of major interest for this work and the interested reader is referred to the overview by Mishchenko [87]. Fig. 67 illustrates the composition of the final result and in image (a) the exact spectral function (blue) is compared to the SOM result (red) for three different numbers of included individual solutions N_s. Four functions are clearly not sufficient to get rid of the sawtooth noise and the spectrum fluctuates heavily. For $N_\mathrm{s} = 30$, the curve looks much smoother already but there still appear clear fluctuations. Finally, for $N_\mathrm{s} = 500$, the reconstructed spectral function almost perfectly coincides with the exact curve and the fluctuations are relatively small. In image (b), the logarithmic probability for a particular ratio of the deviation measure D and the minimum $D_\mathbf{min}$ is plotted over the latter. The shaded area marks all trial functions which are included into the final average.

In conclusion, the Stochastic Optimization Method is able to deliver relatively smooth spectral functions without heavy sawtooth noise. The great advantage in comparison to regularization methods, like the aforementioned MEM, is that, in principle, no prior knowledge about S is required and, hence, no bias is introduced. Nevertheless, it is possible to include any knowledge about the spectrum, like e.g. sum-rule results for some frequency moments, into the reconstruction to improve the performance. The original application of the Stochastic Optimization Method has been the investigation of the Fröhlich polaron by Mishchenko et al. [86]. The system of interest is an electron, coupled to nondispersive phonons of a dielectric medium via its polarization, and the reconstruction has revealed a nontrivial spectrum with pronounced peaks, which are associated with unstable excited states of the polaron. Another interesting example for the usage of the SOM is the investigation of both the single particle spectrum and the dynamic structure factor of ultracold dipole-interacting bosons by Filinov and Bonitz [13]. Here, the influence of Bose-Einstein-Condensation on both quantities has been analyzed in detail.

5.3.4 The Method of Consistent Constraints

Until recently, there has been a trade-off between having a maximum smooth spectral function, as provided by regularization methods, or obtaining a completely unbiased solution with e.g. the Stochastic Optimization Method which, on the other hand, might still be afflicted with fluctuations. The **M**ethod of **C**onsistent **C**onstraints (MCC) by Prokof'ev and Svistunov [88] promises to solve this dilemma and allows for the calculation of the smoothest possible spectral function which is in agreement with the deviation measure. The basic idea of this new approach is to minimize an objective function $O[S(\omega)]$ which consists of the usual χ^2 measure from Eq. (97) and, in addition, several regularization terms which artifically smoothen the spectral function. However, the smoothening does not introduce any bias because the regularization terms are adjusted by an additional iteration loop. Artificial punishments for e.g. sharp peaks are only possible if they do not compromise the deviation measure.

The spectral function is represented by a set of values S_k at discrete frequency values $\omega_k = k\Delta\omega$ and $k = 1, \ldots, N$. The original objective function by Prokof'ev and Svistunov [88] consists of four terms:

$$O[S(\omega)] = \sum_{j=1}^{4} O_j[S(\omega)] \quad .$$

The first term is simply given by the usual deviation measure

$$O_1[S(\omega)] = \frac{1}{M} \sum_{i=1}^{M} \frac{\left(G(\tau_i) - \tilde{G}(\tau_i)\right)^2}{\delta G^2(\tau_i)} \quad , \tag{99}$$

and is the only physically motivated influence on the reconstructed spectral function. The second term is a punishment for sharp peaks and, therefore, high first derivatives

$$O_2[S(\omega)] = \sum_{k=1}^{N-1} D_k^2 d_k^2 \qquad ,$$

with the trivial approximation

$$d_k = \frac{S_{k+1} - S_k}{\Delta\omega}$$

for the derivatives and explicitly k-dependent coefficients D_k. The last point is very important since it allows to decrease the punishment at positions in the spectrum, where sharp peaks are necessary to decrease Eq. (99) and increase it elsewhere to enforce a smooth curve. The third term of the objective function is a punishment for high amplitudes in the spectral function:

$$O_3[S(\omega)] = \sum_{k=1}^{N} A_j^2 S_k^2 \qquad .$$

Finally, the last term in $O[S(\omega)]$ is related to the maximum entropy idea and punishes the deviations from some target spectral function $S^{\mathrm{T}}(\omega_k) = S_k^{\mathrm{T}}$:

$$O_4[S(\omega)] = \sum_{k=2}^{N-1} T_k^2 \left(S_k^{\mathrm{T}} - S_k\right)^2 \qquad .$$

The last missing ingridient of the MCC scheme is some procedure to minimize the objective function. Possible approaches include gradient methods [89], genetic algorithms [90] or Monte Carlo procedures as described in section 5.3.5.

The basic idea behind the iteration loop is to analyze the punishments in the objective function and adust them in a way that the deviation measure is minimized with as much regularization as possible. The trial solution is denoted as $S_k^{(j)}$, with (j) being the number of iterations. A possible target solution is just an average of two adjacent frequency points from the last iteration:

$$S_k^{\mathrm{T}(j+1)} = \frac{S_{k+1}^{(j)} + S_k^{(j)}}{2} \qquad .$$

This choice will prevent too rapid changes of the trial spectrum $S_k^{(j+1)}$ in a single iteration. The initial coefficients $D_k^{(0)}$ should be chosen large enough to ensure a smooth trial spectrum after the first iteration. Prokof'ev and Svistunov [88] find it sufficient to always set $D_k^{(j)} = T_k^{(j)}$, although this is a degree of freedom which might be exploited for optimization. The initial coefficients for the punishments of large amplitudes $A_k^{(0)}$ are set to zero. The iteration is implemented as follows:

1. Start with an arbitrary (or sophisticated) initial guess for the spectral function $S_k^{(0)}$.

2. Minimize the objective function $O^{(j)}[S^{(j)}(\omega)]$ and increase the iteration counter by one, $j \to j + 1$.

3. Adjust all constraints in the last three terms of $O^{(j)}[S^{(j)}(\omega)]$ which compromise the deviation measure. If the minimization of the objective functions suffers from a large punishment $D_k^2 d_k^2$, then it is likely that a physically motivated sharp peak is located at ω_k or at least nearby. In this case, the constraint must be reduced. Otherwise, a flat spectrum does not compromise the χ^2 measure and, therefore, the punishment is too weak and might be increased:

$$D_k^{(j+1)} = \begin{cases} \frac{C}{d_k^{(j)}} & \text{if } d_k^{(j)} > \frac{C}{D_k^{(j)}} \\ 2D_k^{(j)}, & \text{otherwise.} \end{cases}$$

Here, $C \sim 0.1$ denotes a free algorithmic parameter. To prevent a divergence of the coefficients $D_k^{(j)}$, one should implement an additional cutoff condition:

$$D_k^{(j+1)} = \begin{cases} rD_{\min} & \text{if } D_k^{(j+1)} > rD_{\min} \\ D_k^{(j+1)}, & \text{otherwise,} \end{cases}$$

with some large number $r \sim 10^4$.

4. Adjust the third term to prevent negative values in the spectral function:

$$A_k^{(j+1)} = \begin{cases} A_{\max} \sim 10^8 & \text{if } S_k^{(j)} < 0 \\ \frac{A_k^{(j)}}{10}, & \text{otherwise.} \end{cases}$$

If the trial spectral function exhibits a negative value at some frequency ω_k, then every deviation from zero at this point will be severely punished. Otherwise, the punishment will be decreased in every step until it approaches zero.

5. Update the target function to

$$S_k^{\mathrm{T}(j+1)} = \frac{S_{k+1}^{(j)} + S_k^{(j)}}{2} \quad ,$$

and return to step 2.

The iteration is completed when the spectral function has converged.

In conclusion, the Method of Consistent Constraints starts with a strict regularization to suppress all sawtooth noise. However, in order not to introduce any bias, all regularization coefficients are adjusted in a self consistent iteration loop. This means that the final result for the spectral function will both deliver a deviation measure of the order of unity and exhibit no unphysical fluctuations, hence, being the smoothest possible solution within the PIMC errorbars of the autocorrelation function.

5.3.5 Implementation

The implementation of the spectral analysis to be presented in this section is a Monte Carlo scheme which is, in principle, suited to minimize any objective function, as e.g. required for the Method of Consistent Constraints. However, for sufficiently low temperatures, the monopole spectrum should consist solely of the two peaks due to the relative and COM motion of the particles. Therefore, it is not appropriate to apply any regularization since sharp peaks are

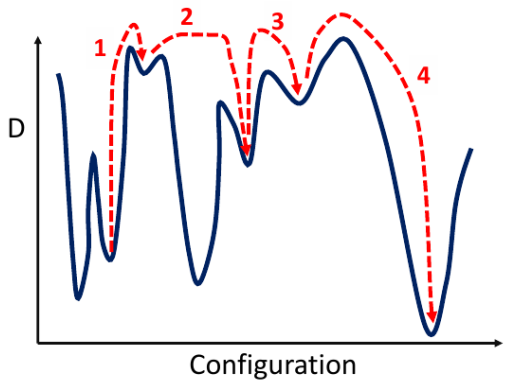

Figure 68: ***Switching between local minima in the configuration space:*** The deviation measure - here denoted as D - is plotted over some arbitrary variable of the configuration space. The dotted red arrows symbolize the movement between several local minima. The figure has been obtained from [87].

explicitly expected. The spectral function $S(\omega)$ is represented by a set of values $\{S_k\}$ at the discrete frequency grid $\omega_k = k\Delta\omega$ with $k = 1, \ldots, N$. To minimize the deviation measure, a set of updates is needed which is able to reach any possible trial spectrum. This is achieved by the following list:

1. *Exchange*: Choose a random frequency point ω_k with $k \in [1, N-2]$ and exchange the spectral function values S_k and $S_{k\pm1}$. The update allows delta-like peaks, which always appear in the beginning of the minimization, to move very efficiently in the frequency space.

2. *Single Slot*: Choose a random frequency point ω_k with $k \in [0, N-1]$ and calculate the proposed change in the spectrum as

$$\Delta S = \alpha S_k c_{\max} \quad , \tag{100}$$

   with the uniformly distributed random number $\alpha \in [0, 1)$ and the free algorithmic parameter $c_{\max} \sim 1$, which determines the maximum change in a single update. The change from Eq. (100) is substracted from S_k and added to one of the adjacent values $S_{k\pm1}$. The update allows extended peaks of any shape to be arbitrarily deformed.

3. *Double Slot*: Procede as for the *Single Slot* update, but add the change to an arbitrary point $j \in [0, N-1]$, $j \neq k$. This update allows for a redistribution of the spectral weight between different peaks which are separated from each other in the frequency domain.

For the MCC, one would need additional updates to ensure that smooth spectra can be manufactured in a relatively small amout of Monte Carlo steps. However, for the sole minimization of the χ^2 measure, the three presented updates are already sufficient.

The last missing ingredient for the spectral analysis procedure is some criterion to decide wether to accept or reject a proposed update. The most trivial approach would be to accept only those moves which result in a decreased deviation measure. However, such a realization will be very inefficient since one might easily get stuck is a local minimum in the configuration space. This is illustrated in Fig. 68, where the deviation measure, which is denoted as D, is plotted over an arbitrary variable of the configuration space. The curve exhibits numerous local

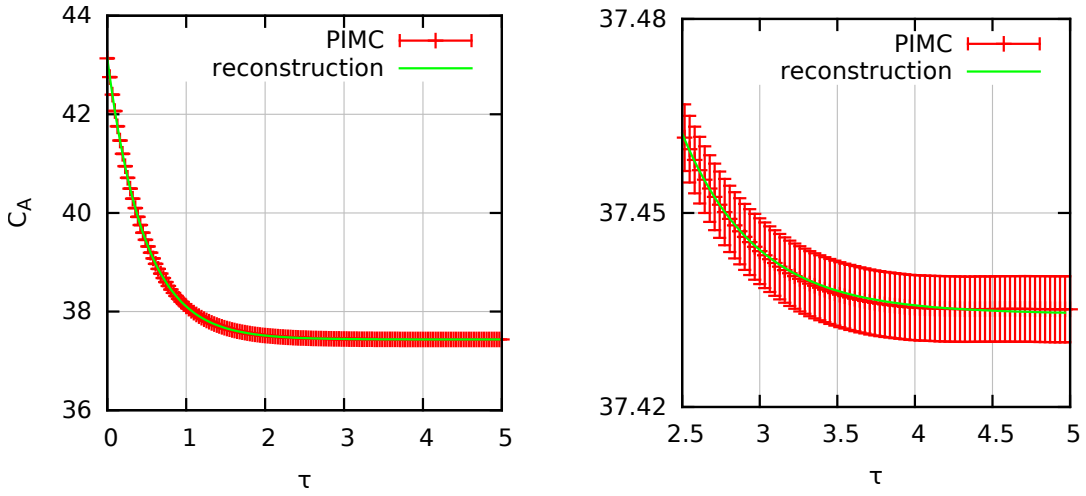

Figure 69: ***The imaginary time autocorrelation function for two dipoles:*** The correlation function C_A is plotted over the imaginary time τ for a $2D$ system of $N = 2$ dipole-interacting particles with $P = 310$, $\lambda = 30$ and $\beta = 10$. The red curve corresponds to the PIMC results and the green one has been reconstructed. In the right image, a magnified segment is shown.

minima. It is, obviously, very improbable to escape from a very deep one with just a single update of the spectrum because multiple peaks might have to be changed. Therefore, the red, dashed arrows represent combinations of more than one update, where the deviation measure is temporarily increased. There exist several schemes to take this into account. In this work, an annealing procedure similar to the one described in [87] in the context of SOM is used. The acceptance ratio for an update with the change in the deviation measure

$$\Delta\chi^2 = \chi^2_{\text{new}} - \chi^2_{\text{old}}$$

is given by

$$A(\Delta\chi^2) = \begin{cases} 1, & \text{if } \Delta\chi^2 \leq 0 \\ \left(\frac{\chi^2_{\text{old}}}{\chi^2_{\text{new}}}\right)^x, & \text{otherwise.} \end{cases} \tag{101}$$

Equation (101) implies that every decrease of χ^2 is accepted but increases are included with a finite probability as well. The exponent x should be chosen small in the beginning to ensure an efficient hopping between local minima and can be increased in the end to find the best spectrum within a single one of them.

5.3.6 Results

A suitable testcase for the spectral analysis is a $2D$ system of $N = 2$ dipole-interacting particles with $\beta = 10$, $\lambda = 30$ and $P = 310$. For this system, the exact value of the breathing mode is known to be $\omega_{\text{exact}} \approx 2.1866$ and, thus, is clearly separated from the COM peak at $\omega_{\text{com}} = 2.0$, which is still expected to exhibit a relatively high spectral weight since the un- and improved BM estimators significantly deviate. The autocorrelation function C_A is plotted in Fig. 69, where the red points correspond to the PIMC result with errorbars and the green curve has been reconstructed. It is sufficient to consider the interval $\tau \in [0, \beta/2]$ due to the function's

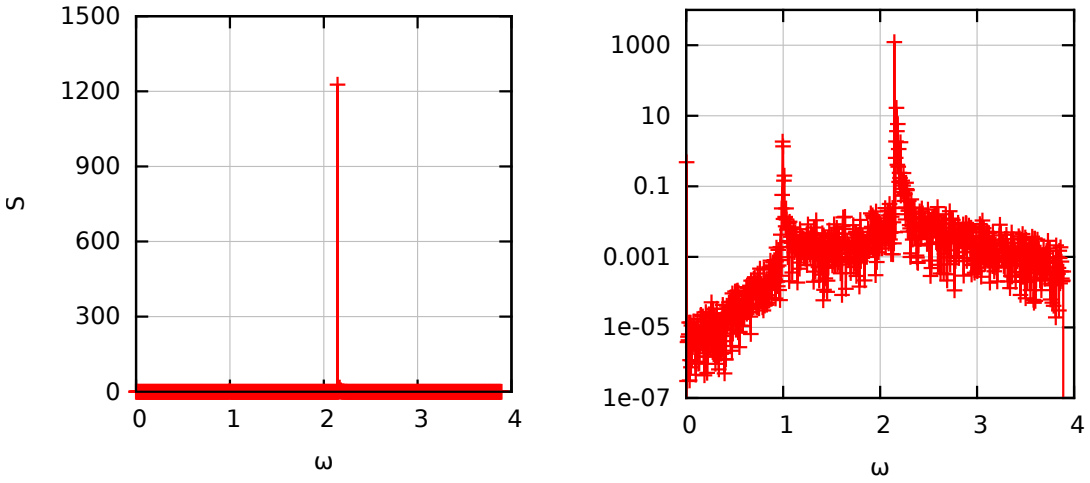

Figure 70: ***Reconstructed BM spectrum:*** The reconstructed spectral function S is plotted over the frequency ω for the system from Fig. 69. The BM peak appears at $\omega \approx 2.14651$.

symmetry, see also Fig. 64. The right image shows a magnified segment from the left one and the two datasets seem to be in perfect agreement, that is, within a tenth of the errorbars. The deviation measure is calculated as $\chi^2 \approx 0.007$ and, hence, much smaller than unity. Fig. 70 shows the corresponding spectral function which is plotted logarithmically in the right image. There appears a single delta-like peak in the expected interval $\omega_{\mathrm{BM}} \in [2, \sqrt{5}]$ at $\omega \approx 2.1465$ but the expected splitting into two separate maxima does not occur. The logarithmic plot reveals another pronounced peak at $\omega = 1.0$, which corresponds to the thermally excited slothing mode, see e.g. [10]. The third visible peak at $\omega = 0$ has no physical meaning, as will be explained below. The reconstructed peak position of the breathing mode, however, is in agreement with the unimproved sum-rule results, like $\omega(1,0) \approx 2.1455$, for example. This implies that the accuracy of C_A is not sufficient to resolve the two different monopole excitations and the obtained spectrum exhibits a single peak between both. The right image of Fig. 69 reveals that the reconstruction has overfitted the statistical errorbars from the PIMC simulation. This is due to the fact that the path integral Monte Carlo simulation allows only for the direct calculation of the imaginary time correlation function which includes both diagonal and off-diagonal contributions. The problem of reconstruction as stated in Eq. (86), however, requires access to the off-diagonal contributions only. This is, in principle, no problem because the diagonal contribution to the ACF can be calculated separately with PIMC as well, see appendix B. Therefore, the resulting input for the reconstruction is given by the difference between two large quantities. This, obviously, results in a higher uncertainty of the off-diagonal correlation function and the errorbars in Fig. 69 are reasonable and correspond rather to the uncertainty of the entire ACF than to the fluctuations of adjacent data points. The reconstructed peak at $\omega = 0$ is simply a constant offset in C_A, which is caused by the statistical uncertainty of the diagonal contribution to the latter. A resolution of the two breathing mode peaks would require orders of magnitude smaller errorbars, which is unfeasible even for small systems. Hence, the calculation of the spectral function is a too difficult task for the monopole operator since the spectrum consists of two very narrow peaks and the input of the reconstruction is given by the difference between two large numbers which increases the uncertainty. For completeness, it is reported that the slothing mode at $\omega = 1$ does not appear for all considered systems and, in some cases, sawtooth instabilities with a comparable weight occur at seemingly random positions.

6 Simulation of fermions

Another challenging topic is the investigation of the thermodynamic properties of fermions. These exhibit many interesting features like Wigner crystallization [61] or the formation of particle pairs which act like bosons and allow for Bose Einstein condensation and superfluidity [15]. Quantum Monte Carlo methods suffer from the notorious fermion sign problem [7] which might render even small systems unfeasible and, therefore, drastically limits the applicability of PIMC. Troyer and Wiese [91] have shown that the former is a NP hard problem, i.e., that no deterministic polynomial time algorithm exists for its solution. However, there do exist several approaches with different benefits and shortcomings as will be discussed in the following section.

6.1 Theoretical background

The central quantity for the derivation of the path integral Monte Carlo scheme is the partition function Z, which, according to section 2, can be written as the integral

$$Z = \int \mathrm{d}\mathbf{X}\; W(\mathbf{X})$$

over the weights $W(\mathbf{X})$ of all configurations $\mathbf{X}$. However, Eq. (24) states that for fermionic particles both negative and positive weights W occur. This seems to be a serious problem since the Metropolis algorithm requires strictly positive weights. To overcome this obstacle, one usually uses the standard PIMC procedure to generate configurations distributed according to the moduli $|W(\mathbf{X})|$, which are nothing else than the correct configuration weights of bosons. The thermodynamic expectation values for fermions are calculated as

$$\langle \hat{A} \rangle_{\mathrm{f}} = \frac{\int \mathrm{d}\mathbf{X}\; S(\mathbf{X})|W(\mathbf{X})|A(\mathbf{X})}{\int \mathrm{d}\mathbf{X}\; S(\mathbf{X})|W(\mathbf{X})|} = \frac{\langle \hat{A}\hat{S} \rangle_{\mathrm{b}}}{\langle \hat{S} \rangle_{\mathrm{b}}} \quad , \tag{102}$$

with the indices f and b referring to Fermi- and Bose-statistics, respectively, and the definition of the sign,

$$S(\mathbf{X}) = \frac{W(\mathbf{X})}{|W(\mathbf{X})|} \quad ,$$

as the ratio of fermionic and bosonic weights. It is a well known fact that the expectation value of the sign behaves as

$$\langle \hat{S} \rangle_{\mathrm{b}} = \frac{Z_{\mathrm{f}}}{Z_{\mathrm{b}}} = e^{-N\beta\Delta f} \quad , \tag{103}$$

with the difference between the free energies $\Delta f = f_{\mathrm{f}} - f_{\mathrm{b}}$. Equation (103) directly implies that the denominator in Eq. (102) exponentially decreases with both the particle number and the inverse temperature, which is highly problematic since a small sign results in large relative statistical errors of the quantity of interest. An optimal Monte Carlo method should sample configurations in the fermionic configuration space with the partition function Z_{f}. However, the Metropolis algorithm generates a Markov chain which corresponds to Z_{b}. Hence, a vanishing ratio (103) indicates that the fermionic space is unsufficiently sampled because most of the data from the bosonic space cancels. For completeness, it is reported that the Monte Carlo error corresponding to the expectation value from Eq. (102) cannot be trivially calculated by error propagation of the two expectation values. Hatano [92] has shown that cross-correlations between the sign and the observable of interest lead to an effective reduction of the true error

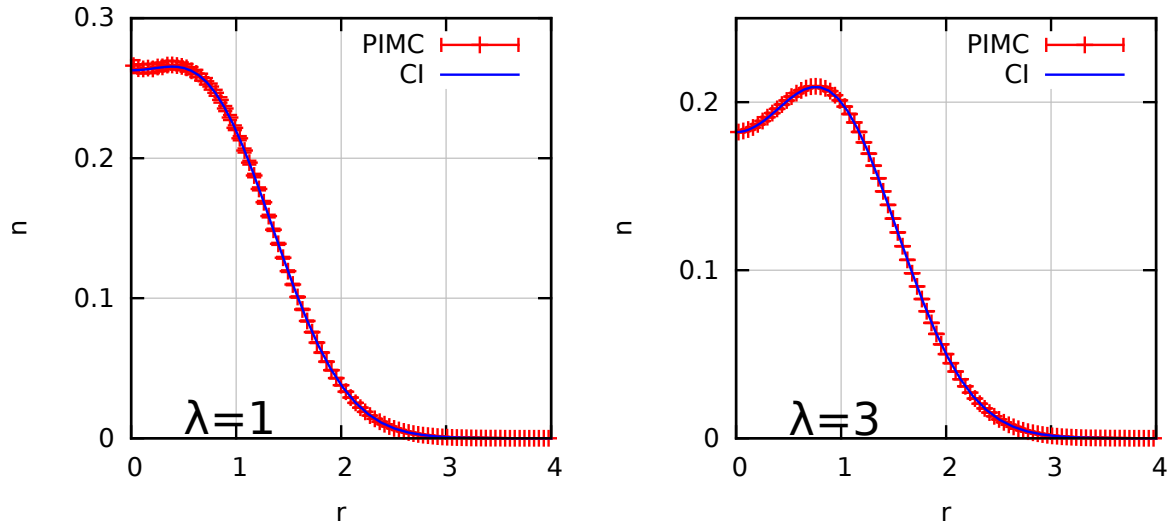

Figure 71: ***Radial density distribution of two fermions:*** The density n is plotted over the distance to the center of the trap r for two Coulomb-interacting fermions at $\beta = 3$ with $\lambda = 1$ (left) and $\lambda = 3$ (right). The blue curve has been calculated with CI and the red datasets corresponds to the PIMC results.

for small $\langle \hat{S} \rangle_{\mathrm{b}}$. However, the consideration of cross-correlations cannot be trivially combined with the binning analysis from section 2.6 and, therefore, is neglected in this work.

The only additional feature which is required to extend the presented implementation of the worm algorithm path integral Monte Carlo scheme to fermions is the calculation of the sign. The most straightforward approach is the evaluation of all permutation lengths as stated in Eq. (24). This is, however, unnecessary since the sign of the current configuration might also be obtained by the application of some bookkeeping during the updates. Every time, when exchange is created or annihilated, some variable is multiplied by minus unity which is the case for the update *Swap* and also *Advance* and *Recede*, when the head surpasses the tail. With this new extension, the implemented code is able to obtain results for both bosons and fermions within the same simulation with negligible additional computational effort.

6.2 Checks of the implementation

The simulation of fermions is not only a highly interesting topic for research but, in addition, provides a very powerful benchmark for the path integral Monte Carlo code. For small systems (e.g. $N = 2$ particles), the results can be compared to exact **C**onfiguration **I**nteraction (CI) data, see e.g. [93], and the calculation of fermionic densities is not only sensitive to the spatial distribution of the beads but also to the formation of exchange cycles in the system. Therefore, a correct radial density is much more unlikely for fermions if the implementation is afflicted with some error. The result of such a comparison is plotted in Fig. 71, where the radial density n is plotted for $N = 2$ Coulomb-interacting particles in $2D$ for $\beta = 3$, $P = 300$ and the coupling parameters $\lambda = 1$ (left) and $\lambda = 3$ (right). The blue curves have been obtained with a CI implementation by Hochstuhl [94] and the red points correspond to the PIMC results. In both curves, the two datasets cannot be distinguished with the naked eye. The errorbars in the left picture are significantly larger than in the right one due to the sign problem and the average signs have been calculated as $S(\lambda = 3) \approx 0.685$ and $S(\lambda = 1) \approx 0.326$. Table 2 provides a comparison

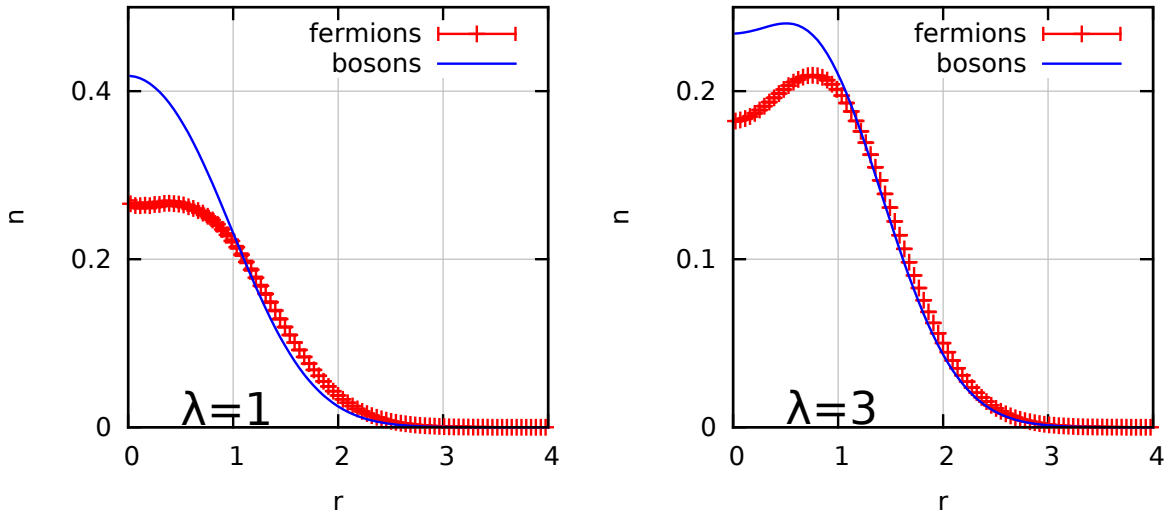

Figure 72: ***Radial density distribution of bosons and fermions:*** The density n is plotted over the distance to the center of the trap r for two Coulomb-interacting particles at $\beta = 3$ with $\lambda = 1$ (left) and $\lambda = 3$ (right). The blue curve corresponds to bosons and the red one to fermions.

λ	3	2	1
CI	4.776319739	4.266088657	3.715753739
PIMC	4.776 ± 0.008	4.265 ± 0.008	3.72 ± 0.02

Table 2: The total energy E is listed for $N = 2$ fermions with $\beta = 3$ (see Fig. 71) for three coupling parameters. The results have been obtained with CI and PIMC.

of the total energies from both CI and PIMC and the deviations are within the errorbars. Fig. 72 shows results for the same system as Fig. 71 but here the blue curve corresponds to the bosonic density. For both coupling parameters, the bosonic density exceeds its fermionic pendant at the center of the trap since the Pauli blocking effectively separates fermions. The difference between the two curves is larger for small λ because here exchange effects are more important.

6.3 Results

In the following section, a few selected simulation results are presented to illustrate the differences between bosons and fermions and the difficulties which are imposed by the sign problem.

6.3.1 The sign problem for dipole and Coulomb interaction

In Fig. 73, the average sign S is plotted logarithmically over the inverse temperature β for a $2D$ system with $N = 2$ and $\lambda = 3$. The red and green curve correspond to Coulomb and dipole interaction, respectively. Both curves exhibit a nearly linear decay as it is expected according to Eq. (103). For dipolar interaction, however, the average sign always exceeds its Coulomb pendant, which makes fermionic dipole systems better suited to be investigated with PIMC. The reason for this feature is illustrated in Fig. 74, where, in the left image, the bosonic density is shown for the simulation from Fig. 73 with $\beta = 8$. The red curve, which again corresponds

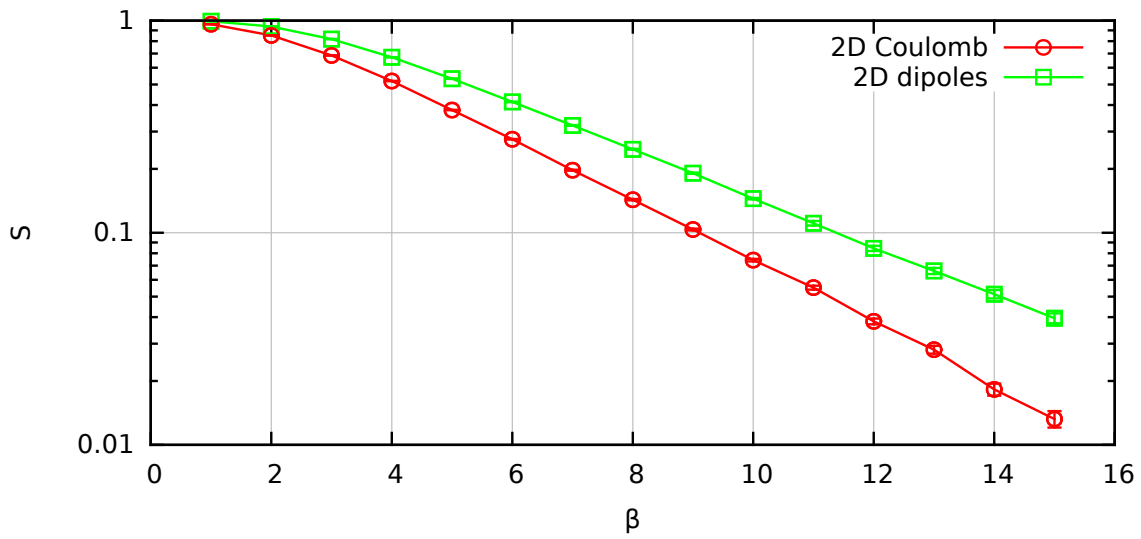

Figure 73: ***Investigation of the sign problem:*** The average sign S is plotted logarithmically over the inverse temperature β for a $2D$ system with $N = 2$, $\lambda = 3$ and $P = 300$ for $\beta \leq 10$ and $P = 400$ otherwise. The red and green curve correspond to Coulomb and dipole interaction, respectively.

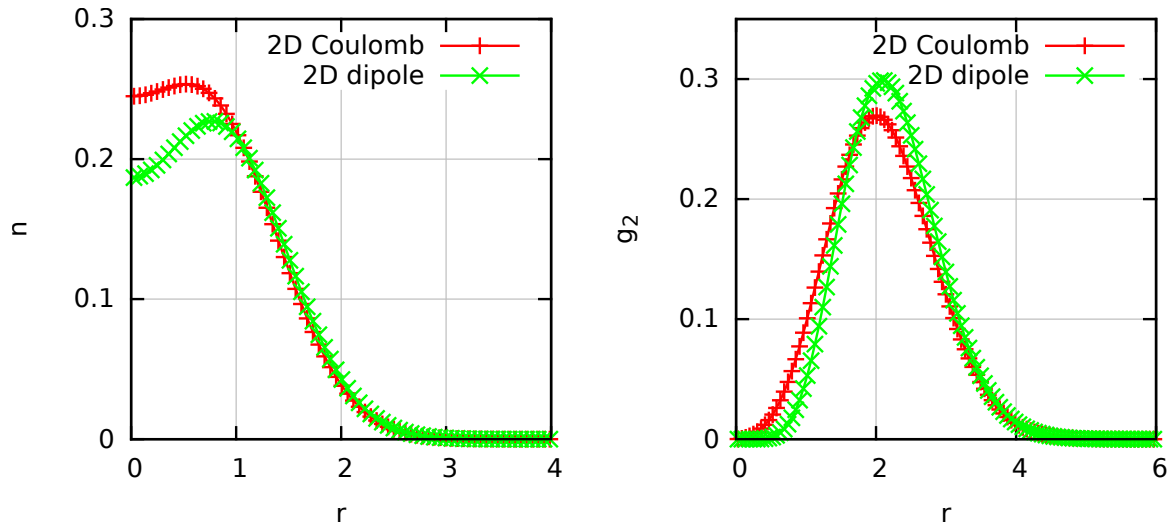

Figure 74: ***Comparison of Coulomb and dipole interaction:*** In the left image, the bosonic density n is plotted over the distance to the center of the trap r for a $2D$ system with $N = 2$, $\beta = 8$, $\lambda = 3$ and $P = 300$. The red and green curve correspond to Coulomb and dipole interaction, respectively. In the right image, the averaged pair correlation function g_2 is plotted over the relative particle distance for the same system.

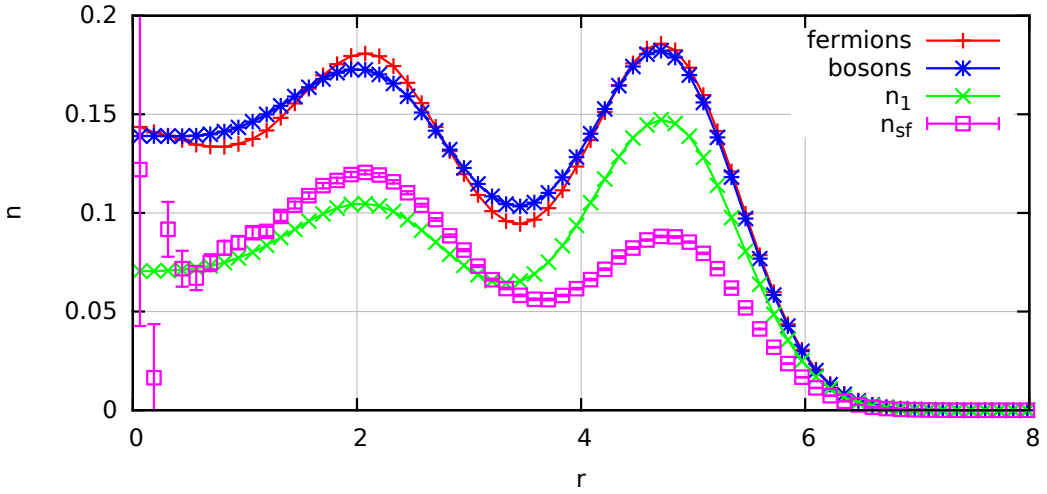

Figure 75: ***Radial densities for a*** $2D$ ***Coulomb system of bosons and fermions:*** The density n is plotted over the distance to the center of the trap r for a $2D$ system of $N = 15$ Coulomb-interacting particles with $\lambda = 10$, $\beta = 5$ and $P = 210$. The red and blue curve correspond to the total density of fermions and bosons, respectively, the green curve to the bosonic density of particles not involved in any exchange cycles n_1 and the purple points to the superfluid density n_{sf}.

to Coulomb interaction, exhibits a significantly larger overlap at the center of the trap than the green one. This can be explained by the different exponents of the interaction power laws, i.e., $\alpha = 1$ and $\alpha = 3$ for Coulomb and dipoles, respectively. For relative distances $r < 1$ between two particles, the Coulomb interaction is weaker than for dipoles. This makes it more unlikely for two dipoles to come much closer together than this threshold and, thus, the exchange is suppressed. The influence of the two exponents is directly visible in the density profile since both curves intersect almost exactly at $r = 1$. The right image of the same figure shows the averaged pair distribution g_2 and the two dipoles are indeed more clearly separated than two Coulomb-interacting particles.

6.3.2 2D Coulomb system

A suitable system to analyze the different impact of Bose- and Fermi-statistics is a $2D$ system of $N = 15$ Coulomb-interacting particles with $\lambda = 10$, $\beta = 5$ and $P = 210$. Even such a small system with a relatively strong coupling turns out to be very difficult to simulate and the average sign has been calculated as $S = 0.069 \pm 0.001$. The radial density is shown in Fig. 75 and the red and blue curve correspond to fermions and bosons, respectively. Both datasets exhibit a shell structure with two minima, which is more pronounced for fermions. This is again a direct consequence of the Pauli blocking. However, the difference between the two curves increases towards the center of the trap, thus, indicating that exchange effects are more important here. This is expected and can be easily verified by the consideration of the bosonic density of particles which are not involved in any exchange cycles, n_1 (green). Indeed, the green curve is much closer to the total density in the outermost shell. The purple curve corresponds to the superfluid density n_{sf} and exhibits the opposite behaviour than n_1, for the same reasons. For completeness, it is reported that the total superfluid fraction is calculated as $\gamma_{\mathrm{sf}} = 0.525 \pm 0.002$. Finally, Fig. 76 shows the averaged pair distribution function g_2 and it is

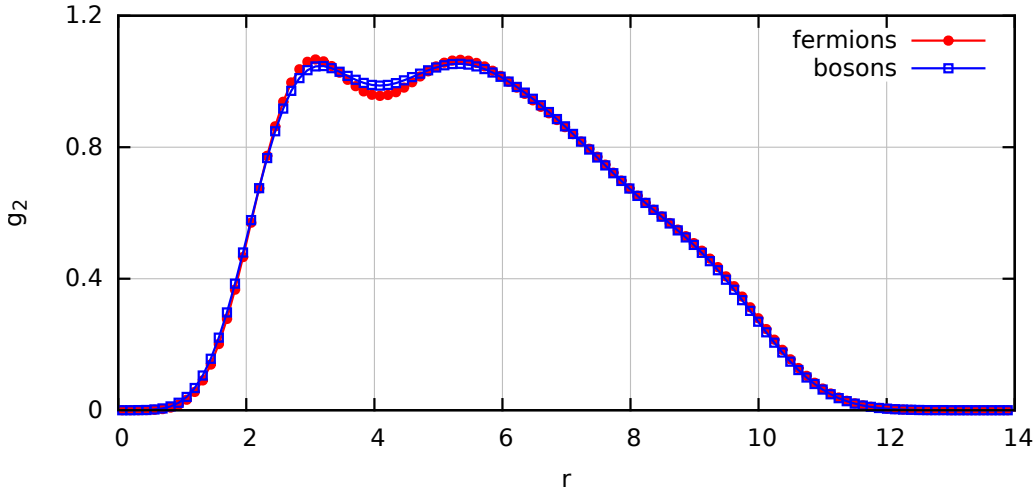

Figure 76: ***Pair distributions for a*** $2D$ ***Coulomb system of bosons and fermions:*** The averaged pair distribution function g_2 is plotted over the relative distance r between two particles for the system from Fig. 75. The red and blue curve correspond to fermions and bosons, respectively.

again revealed that fermions are more spatially separated than bosons, which manifests in the more pronounced peaks at $r \approx 3$ and $r \approx 5.5$.

6.3.3 The breathing mode

One obvious application of fermionic PIMC in the context of this work is the investigation of the breathing mode of fermions. However, the sign problem prohibits the simulation of large systems and low temperatures, which makes path integral Monte Carlo not the best suited method for this task. This is demonstrated in Fig. 77, where, in the left image, the breathing mode frequency ω is plotted over the coupling parameter λ for $N = 2$ Coulomb-interacting particles in $2D$. The blue and purple curve correspond to the exact solution for bosons and fermions, respectively, and both curves exhibit a transition from the ideal limit, $\omega = 2$, to the classical one, $\omega = \sqrt{3}$. Only in the middle of the transition the two curves deviate and the fermionic breathing mode frequency clearly exceeds its bosonic pendant. This is a consequence of the Pauli blocking which effectively causes fermions to exhibit less collective behaviour. The red and green curve correspond to the improved breathing mode sum-rule estimates $\omega^*(3,1)$ and have been obtained with PIMC for the inverse temperature $\beta = 5$. Both datasets clearly reproduce the behaviour of the exact curves, that is, the splitting for intermediate coupling parameters. However, it should be noted that, for $\beta = 5$, two particles are not fully in the ground state, as explained in section 5.2.1 and Fig. 56 in particular. The right image of Fig. 77 shows the average sign which has been obtained within the same simulations. For $\lambda < 0.5$, S drops below 0.05 and the fermionic results are afflicted with large statistical errors. Fig. 78 shows similar results, but for dipole-interacting particles. The blue and purple curve again correspond to the exact results for bosons and fermions, respectively, and exhibit a transition between the ideal and classical limits. This time, however, the bosonic breathing mode frequency exceeds its fermionic pendant for intermediate λ, but for the same reasons as discussed above. The red and green curve correspond to the improved sum-rule estimates $\omega^*(3,0)$ for $\beta = 5$ and qualitatively reproduce the behaviour of the exact datasets. Again, the inverse temperature is too low to reach the ground state and, hence,

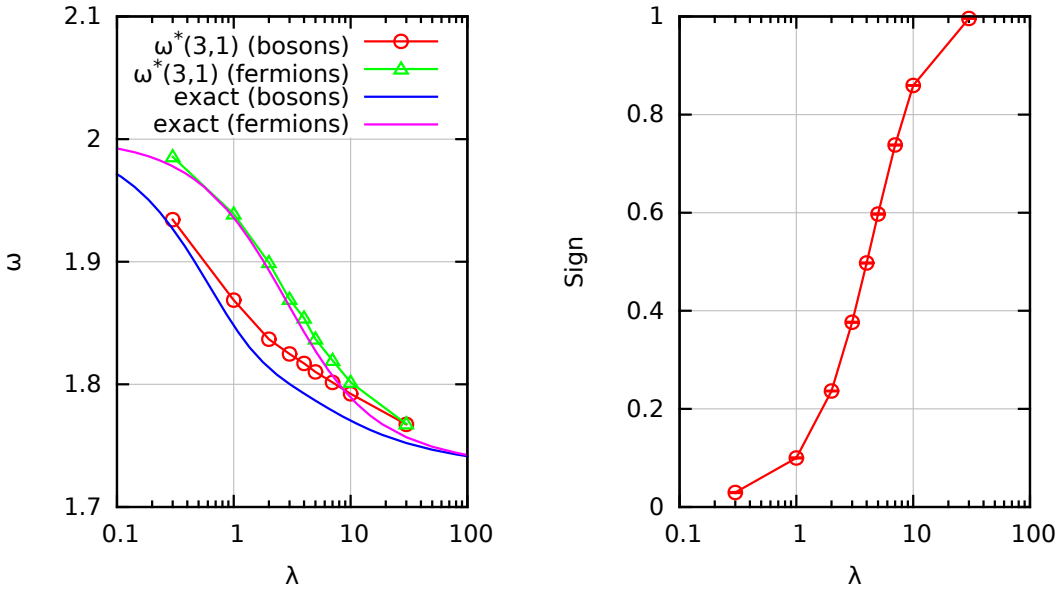

Figure 77: ***Breathing mode for bosons and fermions in a*** $2D$ ***Coulomb system:*** In the left image, the breathing mode frequency ω is plotted over the coupling paramter λ for $N = 2$ Coulomb-interacting particles in $2D$. The blue and purple curve correspond to the exact solution by Abraham and Bonitz [10] for bosons and fermions, respectively, and the red and green curve to the improved sum-rule results $\omega^*(3,1)$ for $\beta = 5$ and $P = 110$. In the right image, the corresponding expectation values of the sign S are shown.

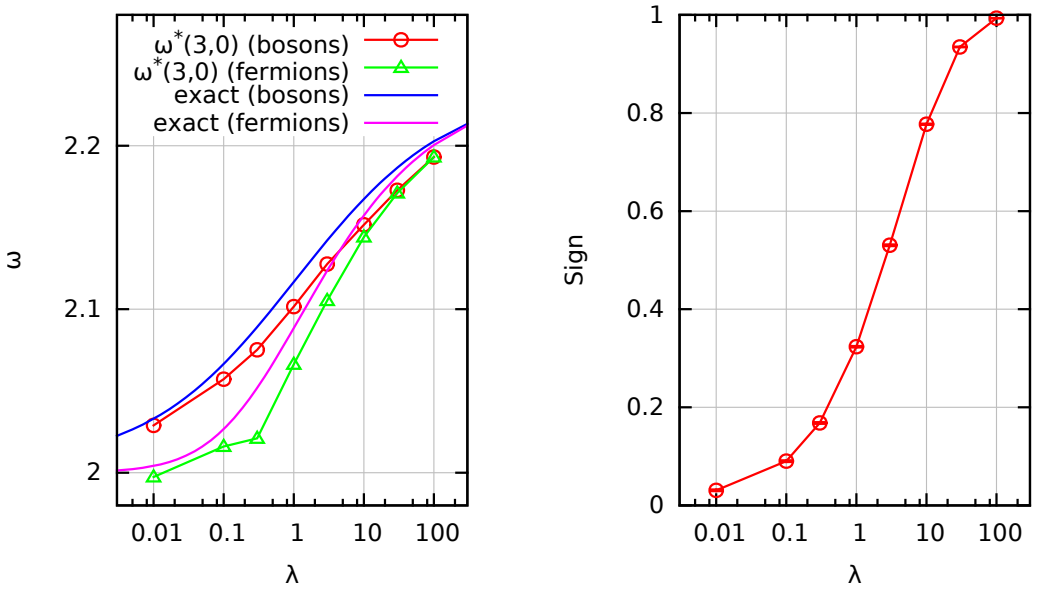

Figure 78: ***Breathing mode for bosons and fermions in a*** $2D$ ***dipole system:*** In the left image, the breathing mode frequency ω is plotted over the coupling paramter λ for $N = 2$ dipole-interacting particles in $2D$. The blue and purple curve correspond to the exact solution by Abraham and Bonitz [10] for bosons and fermions, respectively, and the red and green curve to the improved sum-rule results $\omega^*(3,0)$ for $\beta = 5$ and $P \in [110, 210]$. In the right image, the corresponding expectation values of the sign S are shown.

the sum-rules do not provide an upper bound. The corresponding average sign is shown in the right image and it is again revealed that the simulation of dipole-interacting particles is feasible for smaller λ compared to their Coulomb-interacting pendants.

6.4 Comparison to other methods

There exist several approaches to overcome or at least relieve the fermion sign problem. The probably most ambitious proposal has been announced by Feynman [95], namely the development of a quantum computer, where the elementary units of information, i.e., qubits (quantum bits), are represented by quantum mechanical two-level systems, for an introduction see e.g. [96]. Only recently, Temme et al. [97] have suggested a Quantum Metropolis algorithm which has to be executed on such a device and is completely free of any sign problem since it allows for a direct sampling from the eigenstates of the Hamiltonian. However, the most advanced realization of quantum computation to the author's knowledge consists of 14 qubits [98] and it remains unclear, when sufficiently large devices might be available. A widely used method to overcome the sign problem in the usual spatial representation of PIMC is the fixed node approximation, which is also known as **R**estricted PIMC (RPIMC), see e.g. [99]. Here, the configuration space is divided into regions with positive and negative contributions to the wavefunction which are seperated by the nodal surfaces on which the latter vanishes. However, the obtained results are only claimed to be correct if the exact nodes of the system of interest are known, which is a difficult requirement, indeed. In practice, one has to rely on approximations and the ab initio character of the QMC method is lost. In addition, it has been shown analytically that the fixed node restriction does not reproduce the exact fermionic density matrix for ideal systems [100, 101] and it is concluded that systematic errors appear for increasing degeneracy. About thirty years ago, Takahashi and Imada [102] suggested another PIMC technique in the spatial representation, known as **D**irect **P**ath **I**ntegral **M**onte **C**arlo (DPIMC). Instead of explicitly sampling the exchange cycles, as it is done in standard PIMC, only single particle paths appear and the antisymmetry is taken into account by the inclusion of determinants into the configuration weights. A similar approach for bosons would require the calculation of permanents instead, which is not useful because the worm algorithm allows for a very efficient sampling of particle exchange and without a sign problem there is no need to avoid that. For fermions, however, it was found to be profitable to use this approach. There still appears a sign problem because the determinants can be both positive and negative as well but the average sign for degenerate systems can be significantly increased. This might be understood more intuitively by comparing the magnitude of the total configuration space of PIMC and DPIMC, which is reduced for the latter since exchange cycles are not included. Hence, DPIMC allows for a sampling which is closer to the true fermionic distribution than standard PIMC, which relieves the sign problem. Filinov et al. [103] have presented a similar method with further improvements and DPIMC might in fact be considered as a promising candidate for the future investigation of hitherto unfeasible systems. The final approach to be mentioned in this work is the recently developed **C**onfiguration **P**ath **I**ntegral **M**onte **C**arlo (CPIMC) technique [14, 104]. Here, one makes use of the second quantization (i.e., annihilation and creation operators, see e.g. [39]) and evaluates the partition function in the occupation number representation. It is very interesting to note that the CPIMC method is afflicted with a sign problem as well, which, however, manifests in an entirely different way. Actually, there appear even three different sources for sign changes which have to be taken into account. The advantage of this method lies in the simulation of highly degenerate fermionic systems (i.e., small coupling), where the usual PIMC is no longer applicable. Therefore, the two ab initio approaches are complementary to some degree as will

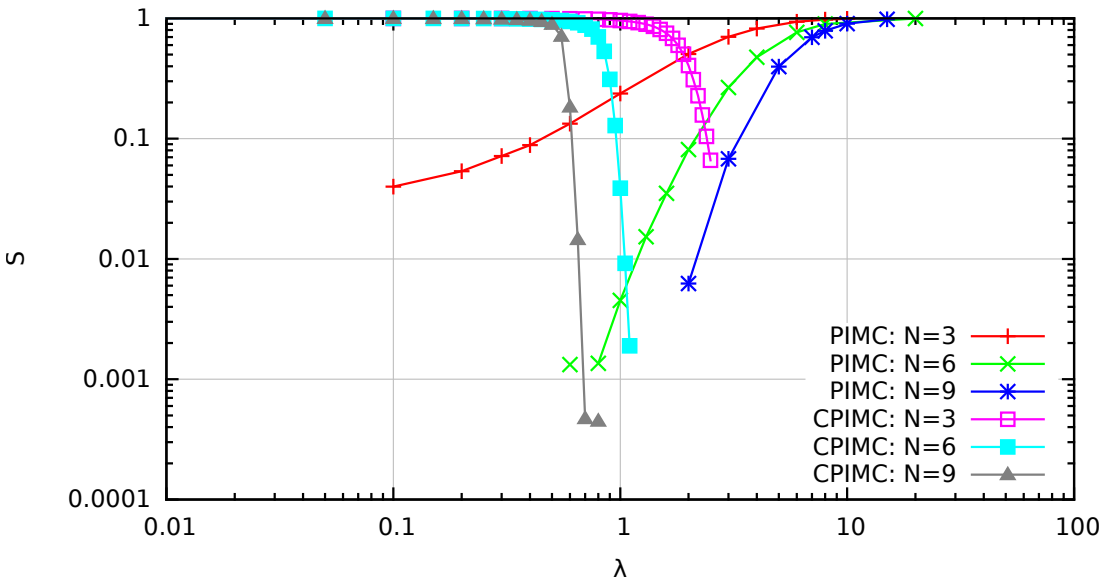

Figure 79: ***Sign problem for PIMC and CPIMC:*** The average sign is plotted over the coupling parameter λ for a $2D$ Coulomb system with the inverse temperature $\beta = 2$. The color assignment distinguishes the particle numbers $N = 3$, $N = 6$ and $N = 9$ and the two applied methods, namely PIMC with $P = 300$ time slices and CPIMC by Groth [104].

be discussed in the following.

6.4.1 Comparison to CPIMC

In this section, the sign problem is investigated for $2D$ Coulomb systems with PIMC and compared to CPIMC data by Groth [104]. In Fig. 79, the average sign is plotted over the coupling parameter λ for the inverse temperature $\beta = 2$ and three different particle numbers. The red, green and blue curve correspond to the PIMC results for $N = 3$, $N = 6$ and $N = 9$, respectively, and all three curves are decreasing for small λ as it is expected. For $N = 6$ and $N = 9$, the average sign approaches zero or even negative values within the statistical uncertainty and those points are neglected in the chosen double logarithmic scale of the plot. The smallest shown system, however, exhibits a finite sign (that is, within the error, the exact sign is always larger than zero) even for vanishing coupling. The CPIMC results are visualized by the purple ($N = 3$), turquoise ($N = 6$) and grey ($N = 9$) curve and exhibit a behaviour which might be denoted as complementary to the PIMC data. Here, the average sign decreases with increasing coupling strength and converges to unity for ideal and weakly interacting systems. For both methods, the sign problem becomes worse for larger particle numbers N. The only overlap, that is, the parameter region where reasonable results can be obtained with both approaches, appears for $N = 3$ and intermediate coupling around $\lambda = 2$. Even a small system with $N = 9$ particles at the relatively small inverse temperature $\beta = 2$ turns out to be a unfeasible for the two Quantum Monte Carlo techniques since, for $\lambda \approx 1.5$, both signs vanish. Fig. 80 shows another comparison of the sign problem between the two methods. The system of interest is given by $N = 3$ particles and the color assignment distinguishes the inverse temperature β. The red, grey and blue curve have been obtained with PIMC for $\beta = 2$, $\beta = 5$ and $\beta = 10$, respectively. Again, the average sign decreases for small λ and it is noteworthy (although, of course, expected) that for lower

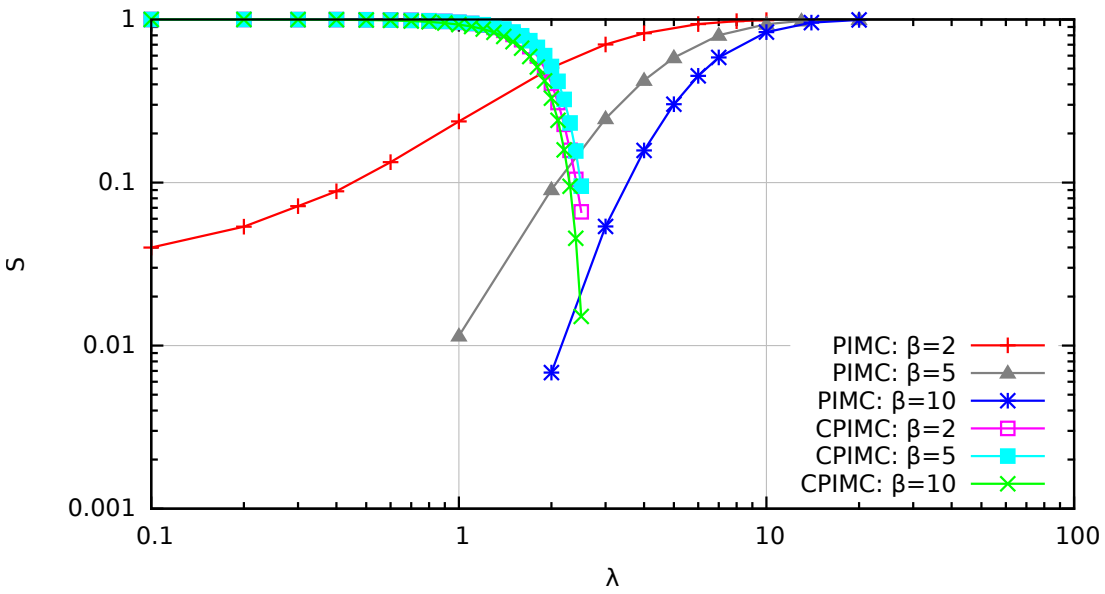

Figure 80: ***Sign problem for PIMC and CPIMC:*** The average sign is plotted over the coupling parameter λ for a $2D$ Coulomb system with $N = 3$ particles. The color assignment distinguishes the inverse temperatures $\beta = 2$, $\beta = 5$ and $\beta = 10$ and the two applied methods, namely PIMC with $P = 300$ time slices and CPIMC by Groth [104].

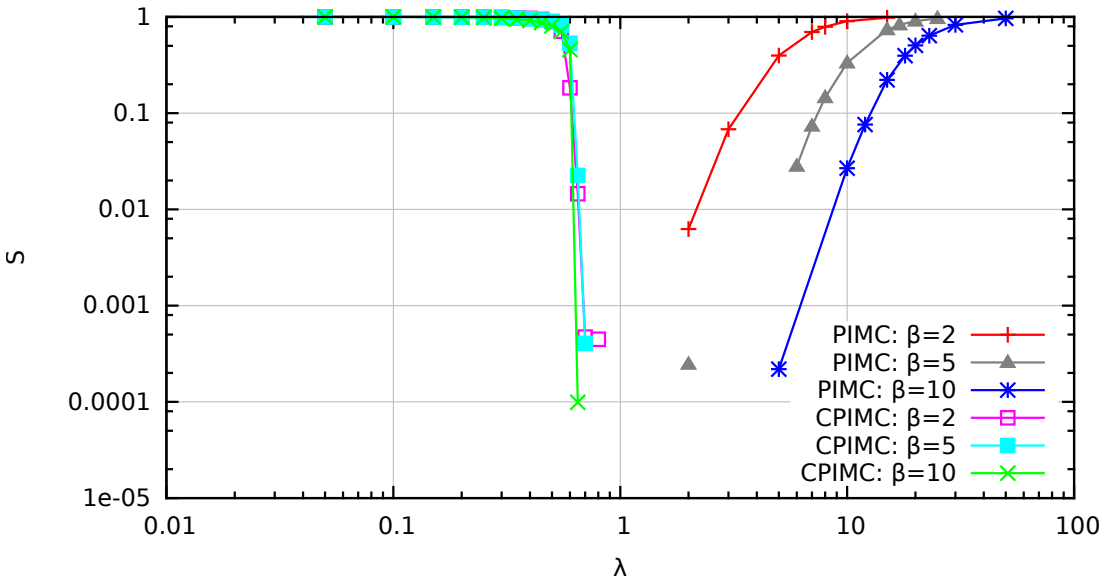

Figure 81: ***Sign problem for PIMC and CPIMC:*** The average sign is plotted over the coupling parameter λ for a $2D$ Coulomb system with $N = 9$ particles. The color assignment distinguishes the inverse temperatures $\beta = 2$, $\beta = 5$ and $\beta = 10$ and the two applied methods, namely PIMC for $P = 300$ time slices and CPIMC by Groth [104].

temperature the curves exhibit a sharper decay at higher coupling parameters. The CPIMC results are plotted as the purple ($\beta = 2$), turquoise ($\beta = 5$) and green ($\beta = 10$) curve and look very similar. For all three inverse temperatures, the average sign decreases for increasing λ and both the slope and location of the decay are very close. The interesting feature is the seemingly peculiar order. The lowest temperature curve exhibits the smallest sign, as it is the case for PIMC as well. The $\beta = 5$ data, however, exceeds the $\beta = 2$ pendant, which seems to contradict the exponential decay from Eq. (103). To understand this behaviour, one must reconsider the different representation of the partition function Z in the CPIMC method. The occupation number representation requires a (in general infinite) set of basis functions as an input. For practical purposes, however, only a finite number of basis functions N_b is included. To preserve the ab initio character of the method, one must make sure to choose N_b large enough that only orbitals with a too high energy to be significantly populated are neglected. This means that the temperature behaviour of the CPIMC method is the result of a competition between two opposite effects. On the one hand, for a fixed number of basis functions N_b, the sign does exponentially decay with β according to Eq. (103). On the other hand, with increasing temperature, more basis functions have to be included, which increases the magnitude of the configuration space and, therefore, reduces the sign as well. In conclusion, CPIMC is best suited for intermediate inverse temperatures, in this case around $\beta = 5$. Finally, Fig. 81 shows the same information as Fig. 80, for $N = 9$ particles instead. The CPIMC data again exhibits a very sharp decay, which is very similar for all three inverse temperatures. The average sign from the PIMC simulations does significantly differ for the three curves and again the situation is worst for $\beta = 10$. There appears no overlap region between the two sign problems, as it has already been concluded for Fig. 79.

The comparison of the fermion sign problem of the standard path integral Monte Carlo (PIMC) and the conceptually completely different configuration path integral Monte Carlo (CPIMC) method has revealed the complementary coupling parameter dependence of their applicability. CPIMC excells at highly degenerate (especially ideal) systems where, to the author's knowledge, no other ab initio results for finite temperature are available. The PIMC approach in the usual spatial representation, which has been presented and used in this work, on the other hand, is efficient for strong coupling, where exchange effects do not yet play a dominant role. Unfortunately, the applicability of both methods overlaps for very small systems only, which means that there still exists a large region at indermediate coupling, where no reliable results are available. It is, of course, highly desireable to fill this gap and a systematic comparison between DPIMC and CPIMC is of major interest for future research.

7 Conclusion

7.1 Summary

The guiding theme of this thesis is the ab initio simulation of correlated, trapped quantum systems at finite temperature. The method of choice is given by the path integral Monte Carlo technique, which allows for the calculation of quasi-exact results in thermodynamic equilibrium. The basic idea of this approach is to perform a Trotter decomposition of the density matrix in the spatial representation and express the partition function as the integral over all possible paths in the imaginary time. The remaining task is the generation of correctly distributed configurations which is achieved by the Metropolis algorithm. A particularly advantageous realization of the latter applied to PIMC is the worm algorithm, which operates in an extended configuration space including both particle number changes and a single open trajectory. The WA is superior to other update schemes since it allows for a highly efficient sampling of particle exchange and does not suffer from critical slowing down problems at phase transitions. A detailed derivation of the acceptance probabilities for the updates from the worm algorithm has been followed by a discussion about the calculation of observables with PIMC, including two methods for the extraction of canonical data from the extended Markov chain. The theoretical background has been completed by the error analysis of Monte Carlo data and the introduction of a method which takes autocorrelation effects into account, namely the binning analysis.

In the third chapter, some practical aspects concerning the implementation of the WA-PIMC method in C++ have been discussed. The validity of the developed code has been verified by the consideration of several checks, i.e., a screening of the data structure and comparisons of observables to other results, including a single particle in the harmonic trap and the virial theorem, as well as CI data for fermions in a later section. This rather technical section has been extended with the presentation of several improvements to the standard worm algorithm. All simulations should be started with a boltzmannon equilibration period to prevent artefacts in strongly correlated systems. Special attention has been paid to the inhomogeneity of the systems of interest. The introduction of an artifical potential term between the worm's head and tail can significantly reduce autocorrelation effects and the discussion of spatially resolved acceptance ratios of the Monte Carlo updates has revealed that different regions of a system are updated less efficiently than others. Nevertheless, the section has finished with the conclusion that the presented PIMC implementation is capable to simulate particles in any confinement potential.

The investigation of general properties of confined bosons has started with a brief presentation of three different phases, i.e., solid, liquid and superfluid behaviour. The latter deserves special attention and, in the context of this thesis, the term superfluidity is defined to describe any reduction of the moment of inertia (NCRI) due to quantum effects. The first example to be considered has been a $3D$ Coulomb system at relatively strong coupling and it has been found that larger systems exhibit a sharper phase transition, as it is expected. An even more interesting topic is the comparison of the latter between $2D$ and $3D$ systems and the later onset of superfluidity in three dimensions has been revealed solely as a degeneracy effect, which is independent from the availability of an additional dimension for particle exchange. The strong inhomogeneity yields for the consideration of spatially resolved information about the phase transition which has been provided by a local superfluid density estimator. The application of the latter to $N = 150$ particles with $\lambda = 10$ in $2D$ has revealed that, with decreasing inverse temperature β, the center of the trap tends to stay superfluid, while the boundary sooner starts to behave classically. This has been explained by the stronger localization of the particles in this regions, which makes exchange less likely and, hence, surpresses superfluidity. The final

topic of the section has been the investigation of spatial correlations, which is a nontrivial task. Several presented quantities have failed to reveal the system's inter- and intra-shell correlations. A better alternative is given by the center-two particle correlation function which, in principle, incorporates the complete information. It has, however, turned out to be useful to integrate over one spatial coordinate and the resulting quantity provides information about the correlations between one particle in a particular shell to the rest of the system. Therefore, this integrated center two-particle correlation function provides the desired information, that is, a solid intra-shell behaviour and the lack of correlation between different shells for the system of interest.

The arguably most important section (that is, apart from the theory part, of course) is the investigation of the quantum breathing mode of trapped bosons. It has been shown how dynamical information can be obtained from equilibrium data, using the linear response formalism. The sum-rules allow for the calculation of an accurate upper bound to the frequency of interest solely in terms of equilibrium expectation values which are directly accessible with PIMC. Several dependencies of the sum-rule estimators have been analyzed in detail for Coulomb-interacting particles in $2D$ and $3D$ and dipole systems in $2D$. One of the main results is the increasingly collective behaviour for larger particle numbers in all three aforementioned systems. A second and potentially even more powerful approach is the reconstruction of a spectral function from imaginary time correlation functions. The latter allows not only for the investigation of a single transition between two states, but provides access to the entire spectrum. The spectrum of the quantum breathing mode, however, has turned out to be too difficult. The reconstruction has revealed only a single peak and the predicted splitting into a center of mass and relative contribution has not been resolved. The input for the reconstruction is given by the difference between two large numbers, which results in a relatively high statistical uncertainty. In addition, the spectrum is very narrow and the required accuracy of the PIMC data is unfeasible even for small systems.

The last section of this thesis is devoted to the simulation of harmonically confined fermions, which is a very difficult task due to the notorious sign problem. The latter is caused by the appearance of both positive and negative contributions to the partition function, which might almost cancel each other. This means that only a fraction of the simulation is spent in the remaining configuration space which, hence, is not sufficiently sampled and large statistical uncertainties occur. The aforementioned comparison of PIMC results with CI data has been followed by the investigation of the temperature dependence of the average sign for both Coulomb- and dipole-interacting particles. The latter are better accessible with PIMC, which has been explained by the different interaction power laws. Two dipoles are more spatially separated and, thus, exchange is less probable. However, both systems suffer from an exponentially decreasing sign with increasing inverse temperature β. The brief comparison of the density profiles for $N = 15$ and coupling dependence of the quantum breathing mode for $N = 2$ particles between bosons and fermions has been followed by an overview over other Monte Carlo methods for the simulation of fermions at finite temperature in thermodynamic equilibrium. Special attention has been paid to the recently developed CPIMC technique, which expresses the partition function in the occupation number representation and exhibits a different sign problem with a complementary behaviour compared to standard PIMC. A direct comparison between the two conceptually different methods has revealed that CPIMC excells at weakly coupled and, in particular, ideal systems, while PIMC is better suited for strong coupling, where exchange effects are not yet dominating. However, even for small systems with $N = 9$ particles at a relatively small inverse temperature $\beta = 2$, there exists a coupling parameter region for which both methods fail to provide reasonable results.

7.2 Central results

In the following, the central results of this thesis are briefly listed:

- The worm algorithm path integral Monte Carlo method is well suited for the simulation of trapped quantum particles. However, special attention has to be paid to the strong inhomogeneity of such systems.

- At intermediate Coupling, a $2D$ Coulomb system exhibits superfluidity at higher temperatures than a $3D$ system with the same parameters. This is solely a degeneracy effect and not caused by the availability of an additional dimension for particle exchange [60].

- The local superfluid density is well suited to spatially resolve the phase transition, during which the considered $2D$ Coulomb system has exhibited significantly decreased superfluidity at the boundary. This can be explained by a stronger localization of the particles in this region [60].

- The center-two particle correlation function which has been suggested by Thomsen et al. [11] in the context of classical systems is well suited for the investigation of inter- and intra-shell correlations in quantum systems as well.

- Path integral Monte Carlo allows for the indirect calculation of dynamic properties, as it has been demonstrated for the quantum breathing mode. The sum-rules provide an accurate upper bound for the frequency of interest solely in terms of equilibrium expectation values and have been successfully applied in this thesis. In addition, a spectral function can be reconstructed from imaginary time correlation functions. This, however, is in practice unfeasible for the breathing mode.

- PIMC and CPIMC exhibit a complementary coupling behaviour of the fermion sign problem for confined $2D$ Coulomb systems, which is in agreement with results by Schoof et al. [14] in $1D$. Nevertheless, there do exist parameter regions where both methods are not applicable and no reliable ab initio results exist.

7.3 Outlook

This thesis has merely attempted to provide an overview about different aspects and research topics concerning the simulation of trapped quantum particles and there remain multiple challenging topics for future research:

- It is highly desireable to gain further insight to superfluidity in traps. A substantial analysis of superfluidity in $2D$ and $3D$, which includes parameter scans over the particle number, temperature and coupling strength, could be complemented by the consideration of anisotropic confinement potentials, like pancake and cigar-shaped geometries. In those cases, the superfluid fraction will explicitly depend on the orientation of the rotational axis and interesting behaviour might occur.

- The aforementioned center two-particle correlation function could be used to systematically investigate correlations in quantum systems. Possible extensions of this topic include the consideration of supersolidity, i.e., the appearance of both spatial order and a finite superfluid fraction, and the calculation of the information entropy to describe phase transitions and melting phenomena.

- Path integral Monte Carlo allows for the calculation of multiple imaginary time correlation functions, which could be used to investigate other dynamic properties of traps. An obvious possibility is given by the reconstruction of the single particle spectrum from the Matsubara Green function but possible connections to other transport properties might be derived as well. Another promising tool for the reconstruction itself is given by the **G**enetic **I**nversion by **F**alsification of **T**heories (GIFT) [105], which is introduced in the appendix C.

- The ab initio simulation of fermions at finite temperature remains impossible even for small systems in certain parameter regions. To overcome this extremely unsatisfactory shortcoming, other methods than PIMC or CPIMC have to be applied to the investigation of (not only trapped) fermions. A promising candidate to at least partly fill the gap is the Direct path integral Monte Carlo (DPIMC) technique.

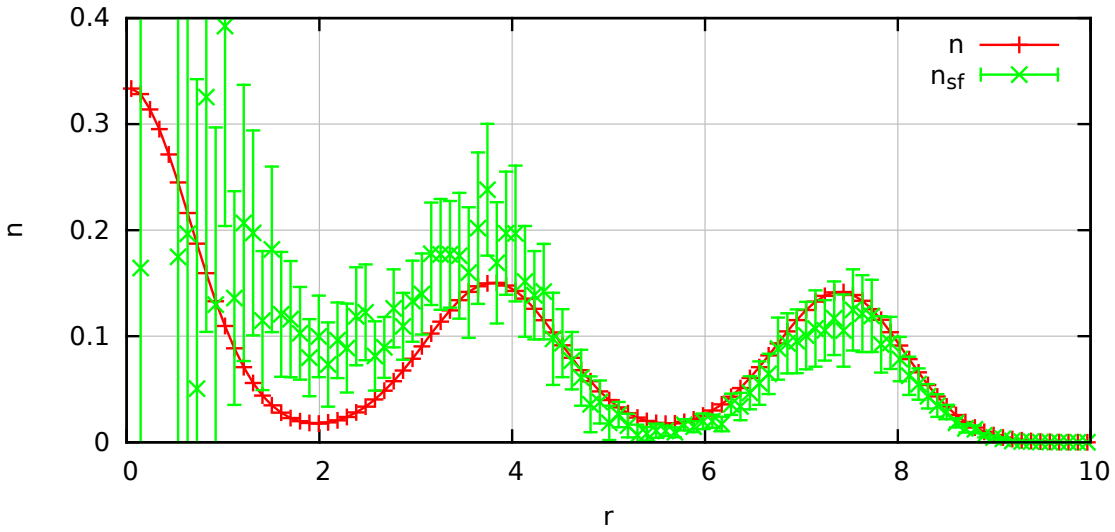

Figure 82: ***Density of the*** $2D$ ***Coulomb system:*** The density is plotted over the distance to the center of the trap r for a $2D$ system with $N = 19$ Coulomb-interacting particles with $\lambda = 28$, $\beta = 100$ and $P = 500$. The red and green curves correspond to the total and superfluid density, respectively.

Appendices

A Problems for strong coupling at low temperature

The worm algorithm PIMC scheme which has been used for all the simulations in this work has proven to be a very efficient tool and has allowed for the calculation of ab initio results for $N \sim 1000$ particles. Nevertheless, there exist disadvantages of the method as well, which will be explained in this section. The system of interest is given by $N = 19$ Coulomb-interacting bosons in $2D$ with $\lambda = 28$, $\beta = 100$ and $P = 500$, which is very similar to an example from [50]. Fig. 82 shows the PIMC result for the total and superfluid density as the red and green curve, respectively. The former exhibits a pronounced shell structure with two deep minima. The superfluid density n_{sf} loosely follows n, indicating that the system is in the superfluid phase. The global superfluid fraction is calculated as $\gamma_{\mathrm{sf}} = 0.87 \pm 0.21$, which is afflicted with a surprisingly high statistical error for $N_{\mathrm{MC}} > 4 \cdot 10^6$ Monte Carlo samples.

To explain this behaviour, one might consider the quantities entering γ_{sf}, that is, the classical moment of inertia I and the total area A. The former is plotted in Fig. 83 over the number of bins N_{MC}. The curve is nearly constant and only minor fluctuations around the expectation value occur. Fig. 84 shows the same plot for the total area A and the behaviour is completely different. There appear three long periods with a large area enclosed by the paths and two minima in between, where A is only slightly above zero. This means that the particle exchange in the system is very correlated. It is apparently very improbable to generate macroscopic exchange cycles but, once they are accepted, it is just as improbable to remove them. Fig. 85 shows two random snapshots form the PIMC simulation. The left image shows a configuration with little exchange and a small area and the right one an exchange cycle in the outer shell, which gives a large contribution to A. The large autocorrelation time of the superfluid fraction is consistent with the acceptance ratios of the standard worm algorithm updates, which are listed

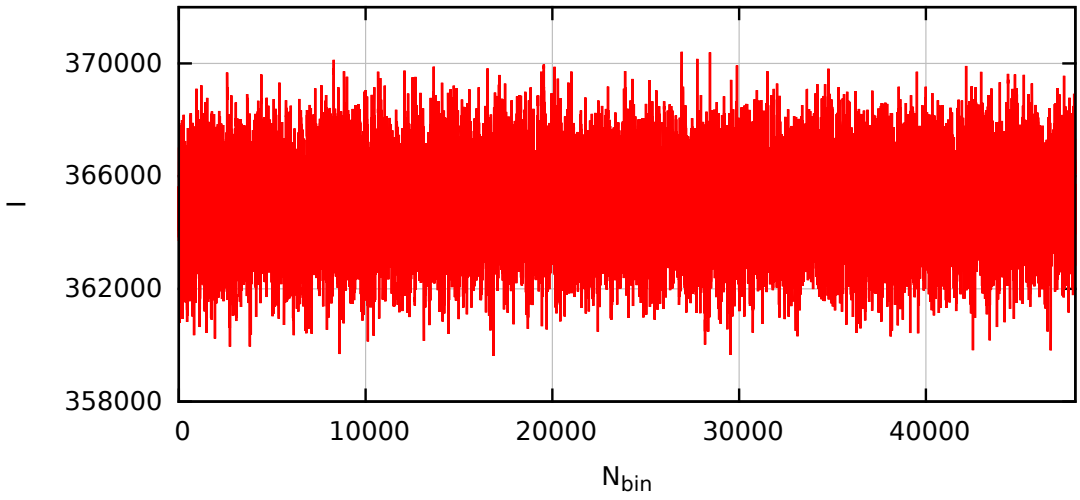

Figure 83: ***Monte Carlo samples of the classical moment of inertia:*** The classical moment of inertia I is plotted over the number of Monte Carlo bins N_{MC} which correspond to the average over one hundred measurements. The simulation parameters are the same as in Fig. 82.

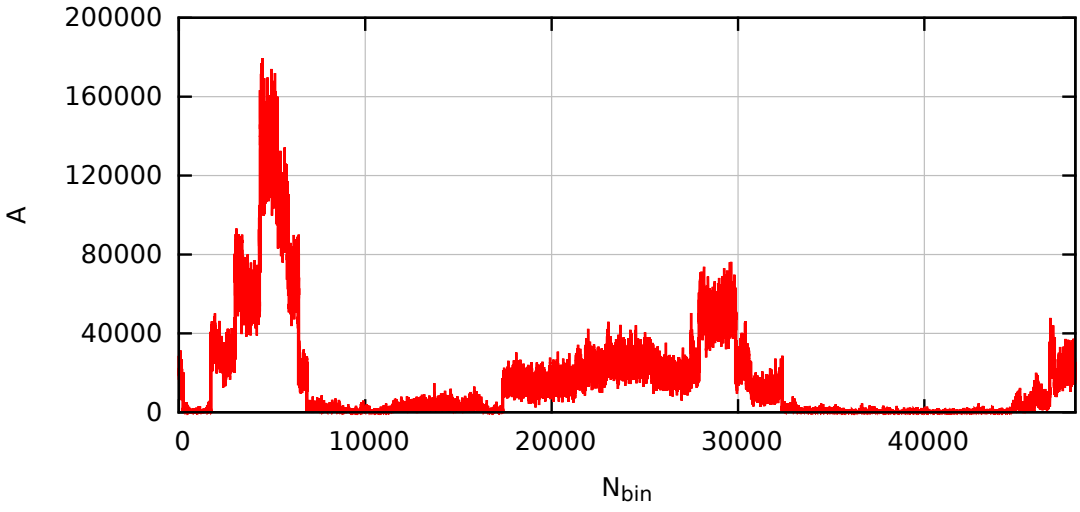

Figure 84: ***Monte Carlo samples of the total area:*** The total area A is plotted over the number of Monte Carlo bins N_{MC} which correspond to the average over one hundred measurements. The simulation parameters are the same as in Fig. 82.

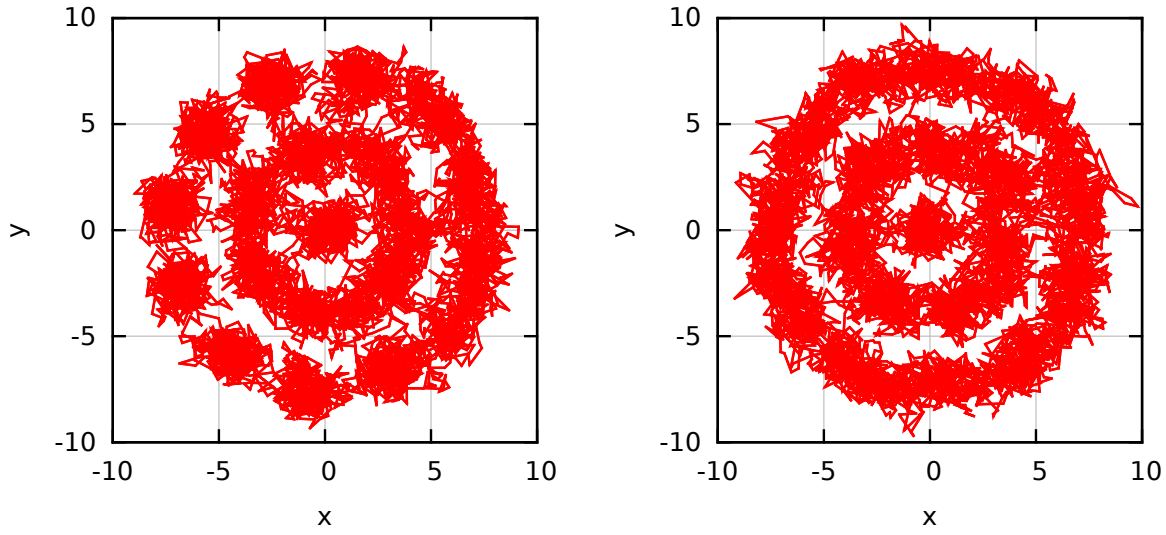

Figure 85: ***PIMC snapshots of the system of interest:*** Two random configurations from the PIMC simulation from Fig. 82 are plotted in the x-y-plane. The left and right images exhibit a small and large total area, respectively.

Insert	Remove	Open	Close	Advance	Recede	Swap
0.0244756	0.00965485	0.03947	0.102744	0.0211126	0.0211332	0.000349175

Table 3: Acceptance ratios of the standard worm algorithm updates from the PIMC simulation from Fig. 82.

in table 3. All values are quite low and the *Swap* move, which is essential for an efficient sampling of particle exchange, is the worst by far. The difficulty of simulating the presented system of interest comes from the combination of strong coupling and low temperature. The thermal de Broglie wavelength is calculated as $\lambda_\beta \approx 25.1$, which is clearly larger than the extension of the entire system. The coordinates of the new beads for any update are sampled from the free particle density matrix and, thus, the displacement of the path sampling scheme is proportional to λ_β. The real paths of single particles, however, are pinned by the Coulomb interaction and much less extended than the latter. This means that during most of the Monte Carlo moves it is suggested to create a new bead which belongs to a specific particle at the opposite direction or completely out of the system. Such proposals are, obviously, rejected, which explains the low acceptance ratios and the large correlations of the total area and the superfluid fraction. One possible solution to this problem is the implementation of a new update set which samples the positions of new beads according to some more suiting distribution function. This would result in more complicated solutions of the detailed balance equation since the ratios of the kinetic terms would have to be taken into account explicitly, but it might just be necessary to allow for an efficient simulation of systems at high coupling and low temperature.

B Derivation of the Sum-Rules

In this section, the sum-rule estimators for the different energy weighted moments are derived following [10, 79] and oscillator units are assumed for all considerations. The first moment m_1 only requires knowledge of the potential energy due to the harmonic oscillator confinement, as will be derived in the following. By assuming to always start from the ground state $|0\rangle$, Eq. (87) simplifies for $k = 1$ to

$$\begin{aligned}
m_1 &= \sum_{i\neq 0} \hbar\omega_{i0} \langle 0|\, \hat{A}\, |i\rangle \langle 0|\, \hat{A}\, |i\rangle^* \\
&= \sum_{i\neq 0} \hbar\omega_{i0} \langle 0|\, \hat{A}\, |i\rangle \langle i|\, \hat{A}\, |0\rangle \\
&= \sum_{i\neq 0} (E_i - E_0) \langle 0|\, \hat{A}\, |i\rangle \langle i|\, \hat{A}\, |0\rangle \\
&= \sum_{i=0}^{\infty} \Big(\langle 0|\, \hat{A}E_i\, |i\rangle - \langle 0|\, E_0\hat{A}\, |i\rangle \Big) \langle i|\, \hat{A}\, |0\rangle \\
&= \sum_{i=0}^{\infty} \Big(\langle 0|\, \hat{A}\hat{H}_0\, |i\rangle - \langle 0|\, \hat{H}_0\hat{A}\, |i\rangle \Big) \langle i|\, \hat{A}\, |0\rangle \\
&= \sum_{i=0}^{\infty} \langle 0|\, [\hat{A}, \hat{H}_0]\, |i\rangle \langle i|\, \hat{A}\, |0\rangle \\
&= \langle 0|\, [\hat{A}, \hat{H}_0]\hat{A}\, |0\rangle \qquad . \qquad (104)
\end{aligned}$$

For the second equality, it is assumed that $\hat{A} = \hat{A}^\dagger$, which is, of course, valid for the monopole operator. The last step makes use of the identity $\hat{1} = \sum_i |i\rangle \langle i|$. A series of very similar steps results in the second expression

$$m_1 = -\langle 0|\, \hat{A}[\hat{A}, \hat{H}_0]\, |0\rangle \qquad . \qquad (105)$$

The combination of Eqs. (104) and (105) gives

$$\begin{aligned}
m_1 &= \frac{1}{2} \Big(\langle 0|\, [\hat{A}, \hat{H}_0]\hat{A}\, |0\rangle - \langle 0|\, \hat{A}[\hat{A}, \hat{H}_0]\, |0\rangle \Big) \\
&= \frac{1}{2} \langle 0|\, [[\hat{A}, \hat{H}_0], \hat{A}]\, |0\rangle \\
&= \frac{1}{2} \langle 0|\, [\hat{A}, [\hat{H}_0, \hat{A}]]\, |0\rangle \qquad . \qquad (106)
\end{aligned}$$

A further simplification of Eq. (106) requires explicit knowledge about the equilibrium Hamiltonian $\hat{H}_0$ and the excitation operator $\hat{A}$. The monopole operator from Eq. (66) is a single particle quantity and the potential energy from $\hat{H}_0 = \hat{T} + \hat{V}$ has a spatial dependence only. This means

$$[\hat{V}, \hat{A}] = 0 \Rightarrow [\hat{H}_0, \hat{A}] = [\hat{T}, \hat{A}] \qquad .$$

The kinetic energy operator can be expressed as

$$\hat{T} = \frac{1}{2} \sum_{k=1}^{N} \hat{\mathbf{p}}_k^2 \qquad ,$$

which has to be inserted into the commutator:

$$[\hat{T},\hat{A}] = \frac{1}{2}\left[\sum_{k=1}^{N}\hat{\mathbf{p}}_k^2, \sum_{j=1}^{N}\hat{\mathbf{r}}_j^2\right] \quad . \tag{107}$$

The operators $\hat{\mathbf{p}}_k$ and $\hat{\mathbf{r}}_j$ commute for different particles $j \neq k$, which simplifies Eq. (107) to

$$[\hat{T},\hat{A}] = \frac{1}{2}\sum_{k=1}^{N}\left[\hat{\mathbf{p}}_k^2, \hat{\mathbf{r}}_k^2\right] \quad .$$

This can be rearranged to

$$\begin{aligned}
[\hat{T},\hat{A}] &= \frac{1}{2}\sum_{k=1}^{N}\left(\hat{\mathbf{p}}_k\hat{\mathbf{p}}_k\hat{\mathbf{r}}_k^2 - \hat{\mathbf{r}}_k^2\hat{\mathbf{p}}_k\hat{\mathbf{p}}_k\right) \\
&= \frac{1}{2}\sum_{k=1}^{N}\left(\hat{\mathbf{p}}_k\hat{\mathbf{p}}_k\hat{\mathbf{r}}_k^2 - \hat{\mathbf{r}}_k^2\hat{\mathbf{p}}_k\hat{\mathbf{p}}_k + \hat{\mathbf{p}}_k\hat{\mathbf{r}}_k^2\hat{\mathbf{p}}_k - \hat{\mathbf{p}}_k\hat{\mathbf{r}}_k^2\hat{\mathbf{p}}_k\right) \\
&= \frac{1}{2}\sum_{k=1}^{N}\left([\hat{\mathbf{p}}_k,\hat{\mathbf{r}}_k^2]\hat{\mathbf{p}}_k + \hat{\mathbf{p}}_k[\hat{\mathbf{p}}_k,\hat{\mathbf{r}}_k^2]\right) \quad .
\end{aligned} \tag{108}$$

The operators are now expressed in spatial representation as $\hat{\mathbf{p}}_k = -i\nabla_k$ and $\hat{\mathbf{r}}_k = \mathbf{r}_k$. The commutators in Eq. (108) can be evaluated with the identity

$$\begin{aligned}
[\hat{\mathbf{p}}_k,\hat{\mathbf{r}}_k^2] &= -i\nabla_k\mathbf{r}_k^2 + i\mathbf{r}_k^2\nabla_k \\
&= -i(\nabla_k\mathbf{r}_k^2) - i\mathbf{r}_k^2\nabla_k + i\mathbf{r}_k^2\nabla_k \\
&= -i(\nabla_k\mathbf{r}_k^2) \quad .
\end{aligned}$$

This leads to

$$\begin{aligned}
[\hat{T},\hat{A}] &= \frac{1}{2}\sum_{k=1}^{N}\left(-i(\nabla_k\mathbf{r}_k^2)(-i\nabla_k) - i\nabla_k(-i(\nabla_k\mathbf{r}_k^2))\right) \\
&= -\frac{1}{2}\sum_{k=1}^{N}\left((\nabla_k\mathbf{r}_k^2)\nabla_k + (\nabla_k^2\mathbf{r}_k^2) + (\nabla_k\mathbf{r}_k^2)\nabla_k\right) \\
&= -\frac{1}{2}\sum_{k=1}^{N}\left(2(\nabla_k\mathbf{r}_k^2)\nabla_k + (\nabla_k^2\mathbf{r}_k^2)\right) \\
&= -\frac{1}{2}\sum_{k=1}^{N}\left(2i(\nabla_k\mathbf{r}_k^2)\hat{\mathbf{p}}_k + (\nabla_k^2\mathbf{r}_k^2)\right) \quad .
\end{aligned}$$

This result can now be inserted into the double commutator from Eq. (106)

$$\begin{aligned}
[\hat{A},[\hat{T},\hat{A}]] &= -\frac{1}{2}\sum_{k=1}^{N}\left(\mathbf{r}_k^2 2i(\nabla_k\mathbf{r}_k^2)\hat{\mathbf{p}}_k - 2i(\nabla_k\mathbf{r}_k^2)\hat{\mathbf{p}}_k\mathbf{r}_k^2\right) \\
&= -i\sum_{k=1}^{N}\left(\mathbf{r}_k^2(\nabla_k\mathbf{r}_k^2)\hat{\mathbf{p}}_k - (\nabla_k\mathbf{r}_k^2)(-i\nabla_k\mathbf{r}_k^2) - (\nabla_k\mathbf{r}_k^2)\mathbf{r}_k^2\hat{\mathbf{p}}_k\right) \\
&= \sum_{k=1}^{N}\left(\nabla_k\mathbf{r}_k^2\right)^2 \quad .
\end{aligned} \tag{109}$$

The spatial derivative in Eq. (109) is simply given by

$$\begin{aligned} \frac{\partial}{\partial x_k}\mathbf{r}_k^2 &= \frac{\partial}{\partial x_k}(x_k^2+y_k^2+z_k^2) = 2x_k \\ \Rightarrow \nabla_k \mathbf{r}_k^2 &= 2\mathbf{r}_k \quad , \end{aligned}$$

and, hence, the first energy weighted moment can be written as

$$\begin{aligned} m_1 &= \frac{1}{2}\langle 0|\,[\hat{A},[\hat{T},\hat{A}]]\,|0\rangle \\ &= \frac{1}{2}\langle 0|\sum_{k=1}^{N} 4\mathbf{r}_k^2\,|0\rangle \\ &= 2\langle 0|\,\hat{\mathbf{R}}^2\,|0\rangle \\ &= 4E_{\mathrm{HO}} \quad . \end{aligned}$$

Thus, it has been demonstrated that m_1 is simply given by four times the potential energy due to the harmonic confinement. This quantity is automatically calculated in every PIMC simulation anyway and, therefore, requires no additional computational effort.

The third moment is given by

$$m_3 = \sum_{i\neq 0}(\hbar\omega_{i0})^3 \left|\langle 0|\,\hat{A}\,|i\rangle\right|^2 \quad ,$$

and can be expressed via nested commutators as well. However, since the derivation of the relation reveals no physical insight and is merely an algebraic task, the interested reader is referred to [79] while here only the final result is presented:

$$m_3 = \frac{1}{2}\langle 0|\,[[[\hat{A},\hat{H}_0],\hat{H}_0],[\hat{H}_0,\hat{A}]]\,|0\rangle \quad . \tag{110}$$

The evaluation of Eq. (110) depends on the explicit form of the particle interaction, i.e., the exponent α from the power law:

$$m_3 = 8E_{\mathrm{kin}} + 8E_{\mathrm{HO}} + 2\alpha^2 E_{\mathrm{int}} \quad .$$

Therefore, the third energy weighted moment can be expressed in terms of the different energies of the system as well.

Another interesting quantity is the inverse frequency moment, which, at finite temperature, is given by

$$m_{-1} = \frac{1}{Z_{\mathrm{c}}}\sum_i\sum_{k\neq i} e^{-\beta E_i}\frac{1}{E_k-E_i}\left|\langle i|\,\hat{A}\,|k\rangle\right|^2 \quad . \tag{111}$$

To find a suitable sum-rule, one usually considers stationary perturbation theory. The perturbed Hamiltonian is given by

$$\hat{H} = \hat{H}_0 + \eta\hat{A} \quad ,$$

with $\eta \ll 1$, meaning that the effect of the perturbation is small. Let $\{|k^{(0)}\rangle\}$ denote the eigenstates of $\hat{H}_0$ with the corresponding eigenvalues $E_k^{(0)}$. The first order correction to the states in perturbation theory is calculated as [106]

$$|i^{(1)}\rangle = \sum_{k\neq i}\frac{\langle k^{(0)}|\,\hat{A}\,|i^{(0)}\rangle}{E_i^{(0)}-E_k^{(0)}}\,|k^{(0)}\rangle \quad . \tag{112}$$

The first order eigenstates of $\hat{H}$ are given by

$$|i_\eta\rangle = |i^{(0)}\rangle + \eta\,|i^{(1)}\rangle \qquad . \tag{113}$$

It is now the goal to connect the Eqs. (112) and (113) with the inverse moment. For this purpose, one considers the diagonal matrix elements of $\hat{A}$ with respect to the states from Eq. (113), which can be expressed as

$$\begin{aligned}
\langle i_\eta|\,\hat{A}\,|i_\eta\rangle &= \left(\langle i^{(0)}| + \eta\sum_{k\neq i}\frac{\left(\langle k^{(0)}|\,\hat{A}\,|i^{(0)}\rangle\right)^\dagger}{E_i^{(0)}-E_k^{(0)}}\langle k^{(0)}|\right)\hat{A}\left(|i^{(0)}\rangle + \eta\sum_{k\neq i}\frac{\langle k^{(0)}|\,\hat{A}\,|i^{(0)}\rangle}{E_i^{(0)}-E_k^{(0)}}|k^{(0)}\rangle\right) \\
&= \langle i^{(0)}|\,\hat{A}\,|i^{(0)}\rangle + \eta\sum_{k\neq i}\frac{\left(\langle k^{(0)}|\,\hat{A}\,|i^{(0)}\rangle\right)^\dagger\langle k^{(0)}|\,\hat{A}\,|i^{(0)}\rangle + \langle k^{(0)}|\,\hat{A}\,|i^{(0)}\rangle\langle i^{(0)}|\,\hat{A}\,|k^{(0)}\rangle}{E_i^{(0)}-E_k^{(0)}} \\
&= \langle i^{(0)}|\,\hat{A}\,|i^{(0)}\rangle + \eta\sum_{k\neq i}\frac{2\left|\langle k^{(0)}|\,\hat{A}\,|i^{(0)}\rangle\right|^2}{E_i^{(0)}-E_k^{(0)}} \qquad ,
\end{aligned} \tag{114}$$

where again all $\mathcal{O}(\eta^2)$ contributions have been neglected. The final expression from Eq. (114) can be identified with a single addend $(m_{-1})_i$ from (111):

$$\frac{Z_c(m_{-1})_i}{e^{-\beta E_i}} = \frac{1}{2\eta}\left(\langle i^{(0)}|\,\hat{A}\,|i^{(0)}\rangle - \langle i_\eta|\,\hat{A}\,|i_\eta\rangle\right) \qquad .$$

The insertion of this connection into the inverse moment leads to

$$\begin{aligned}
m_{-1} &= \sum_i (m_{-1})_i \\
&= \frac{1}{2\eta Z_0}\sum_i e^{-\beta E_i^{(0)}}\left(\langle i^{(0)}|\,\hat{A}\,|i^{(0)}\rangle - \langle i_\eta|\,\hat{A}\,|i_\eta\rangle\right) \qquad .
\end{aligned} \tag{115}$$

It is important to understand that the inverse moment is calculated for the unperturbed Hamiltonian $\hat{H}_0$. This means that in Eq. (115) one has to use the corresponding partition function and configuration weight Z_0 and $\exp\left(-\beta E_i^{(0)}\right)$, respectively. The next step is the identification of two terms in (115) with canonical expectation values, namely

$$\begin{aligned}
\langle\hat{A}\rangle_0 &= \frac{1}{Z_0}\sum_i e^{-\beta E_i^{(0)}}\langle i^{(0)}|\,\hat{A}\,|i^{(0)}\rangle \qquad , \\
\langle\hat{A}\rangle_\eta &\approx \frac{1}{Z_0}\sum_i e^{-\beta E_i^{(0)}}\langle i_\eta|\,\hat{A}\,|i_\eta\rangle \qquad .
\end{aligned} \tag{116}$$

The approximality in Eq. (116) becomes exact if one assumes to start from the ground state, which is valid for the breathing mode:

$$\langle\hat{A}\rangle_\eta = \langle 0_\eta|\,\hat{A}\,|0_\eta\rangle \qquad .$$

This finally allows one to write the inverse energy weighted moment as

$$m_{-1} = -\frac{1}{2}\left(\frac{\langle\hat{A}\rangle_\eta - \langle\hat{A}\rangle_0}{\eta}\right) \qquad . \tag{117}$$

In the limiting case of an infinitely small perturbation, all approximations, i.e., including only linear terms in η, become exact and Equation (117) can be written as the derivative

$$m_{-1} = -\frac{1}{2}\frac{\partial}{\partial\eta}\left\langle\hat{A}\right\rangle_\eta\Big|_{\eta=0} \quad . \tag{118}$$

Equation (118) allows for a straightforward evaluation:

$$\begin{aligned}
\left\langle\hat{A}\right\rangle_\eta &= \frac{1}{Z_\eta}\sum_\alpha \left\langle\alpha\right| \hat{A}e^{-\beta(\hat{H}_0+\eta\hat{A})}\left|\alpha\right\rangle \quad \text{, with} \\
Z_\eta &= \sum_\alpha \left\langle\alpha\right| e^{-\beta(\hat{H}_0+\eta\hat{A})}\left|\alpha\right\rangle \\
\frac{\partial}{\partial\eta}\left(\frac{1}{Z_\eta}\right) &= \frac{-1}{Z_\eta^2}\frac{\partial}{\partial\eta}Z_\eta = \frac{1}{Z_\eta^2}\sum_\alpha \left\langle\alpha\right| \beta\hat{A}e^{-\beta\hat{H}}\left|\alpha\right\rangle \\
\Rightarrow \frac{\partial}{\partial\eta}\left\langle\hat{A}\right\rangle_\eta\Big|_{\eta=0} &= \frac{1}{Z_0^2}\left(\sum_\alpha \left\langle\alpha\right| \beta\hat{A}e^{-\beta\hat{H}_0}\left|\alpha\right\rangle\right)\left(\sum_\gamma \left\langle\gamma\right| \hat{A}e^{-\beta\hat{H}_0}\left|\gamma\right\rangle\right) - \\
&\quad -\frac{1}{Z_0}\sum_\alpha \left\langle\alpha\right| \beta\hat{A}^2e^{-\beta\hat{H}_0}\left|\alpha\right\rangle \\
&= \beta\left\langle\hat{A}\right\rangle^2 - \beta\left\langle\hat{A}^2\right\rangle \quad .
\end{aligned} \tag{119}$$

Inserting Eq. (119) into (118) gives the final result for the inverse energy weighted moment:

$$m_{-1} = \frac{\beta}{2}\left(\left\langle\hat{A}^2\right\rangle - \left\langle\hat{A}\right\rangle^2\right).$$

This means that m_{-1} is simply proportional to the monopole operator's variance.

The last moment to be considered in this work is the zero energy weighted moment, which, at finite T, is given by

$$m_0 = \frac{1}{Z}\sum_{i\neq k} e^{-\beta E_i}\left|\left\langle i\right|\hat{A}\left|k\right\rangle\right|^2 \quad .$$

To find the corresponding sum-rule, one can consider the monopole operator's imaginary time correlation function, which is also needed for the reconstruction:

$$\begin{aligned}
C_A(\tau) &= \left\langle\hat{A}_\mathrm{D}(\tau)\hat{A}_\mathrm{D}(0)\right\rangle \\
&= \frac{1}{Z}\sum_{i,k} e^{-\beta E_i}\left\langle i\right| e^{\frac{i}{\hbar}\hat{H}_0(-i\hbar\tau)}\hat{A}e^{-\frac{i}{\hbar}\hat{H}_0(-i\hbar\tau)}\left|k\right\rangle\left\langle k\right|\hat{A}\left|i\right\rangle \\
&= \frac{1}{Z}\sum_{i,k} e^{-\beta E_i}e^{-\tau(E_k-E_i)}\left|\left\langle i\right|\hat{A}\left|k\right\rangle\right|^2 \\
&= \frac{1}{Z}\sum_{i} e^{-\beta E_i}\left|\left\langle i\right|\hat{A}\left|i\right\rangle\right|^2 + \frac{1}{Z}\sum_{i\neq k} e^{-\beta E_i}e^{-\tau(E_k-E_i)}\left|\left\langle i\right|\hat{A}\left|k\right\rangle\right|^2 \quad .
\end{aligned} \tag{120}$$

The evaluation of Eq. (120) at $\tau = 0$ gives

$$\begin{aligned}
C_A(0) &= \frac{1}{Z}\sum_{i,k} e^{-\beta E_i}\left|\left\langle i\right|\hat{A}\left|k\right\rangle\right|^2 \\
&= m_0 + \frac{1}{Z}\sum_{i} e^{-\beta E_i}\left|\left\langle i\right|\hat{A}\left|i\right\rangle\right|^2 \quad .
\end{aligned} \tag{121}$$

Thus, it is the remaining task to express the diagonal part of $C_A(0)$ in terms of equilibrium expectation values which are accessible with PIMC. The connection can be found by integrating $C_A(\tau)$:

$$\int_0^\beta \mathrm{d}\tau\ C_A(\tau) = \frac{\beta}{Z}\sum_i e^{-\beta E_i}\left|\langle i|\,\hat{A}\,|i\rangle\right|^2 + \frac{1}{Z}\sum_{i\neq k} e^{-\beta E_i}\left|\langle i|\,\hat{A}\,|k\rangle\right|^2 \int_0^\beta \mathrm{d}\tau\ e^{-\tau(E_k-E_i)} \quad . \tag{122}$$

The integral in the second term can be evaluated as

$$\int_0^\beta \mathrm{d}\tau\ e^{-\tau(E_k-E_i)} \quad = \quad \frac{1-e^{-\beta(E_k-E_i)}}{E_k-E_i} \quad ,$$

and the entire integral over the correlation function becomes

$$\begin{aligned}\int_0^\beta \mathrm{d}\tau\ \langle\hat{A}_\mathrm{D}(\tau)\hat{A}_\mathrm{D}(0)\rangle \quad &= \quad \frac{\beta}{Z}\sum_i e^{-\beta E_i}\left|\langle i|\,\hat{A}\,|i\rangle\right|^2 + \\ &\quad + \frac{1}{Z}\sum_{i\neq k} e^{-\beta E_i}\frac{1-e^{-\beta(E_k-E_i)}}{E_k-E_i}\left|\langle i|\,\hat{A}\,|k\rangle\right|^2 \quad . \end{aligned} \tag{123}$$

The second addend in Eq. (123) is twice the inverse moment

$$\begin{aligned}\frac{1}{Z}\sum_{i\neq k} e^{-\beta E_i}\frac{1-e^{-\beta(E_k-E_i)}}{E_k-E_i}\left|\langle i|\,\hat{A}\,|k\rangle\right|^2 \quad &= \quad \frac{1}{Z}\sum_{i\neq k} e^{-\beta E_i}\frac{\left|\langle i|\,\hat{A}\,|k\rangle\right|^2}{E_k-E_i} - \frac{1}{Z}\sum_{i\neq k} e^{-\beta E_k}\frac{\left|\langle i|\,\hat{A}\,|k\rangle\right|^2}{E_k-E_i} \\ &= \quad 2m_{-1} \quad ,\end{aligned}$$

and, hence, the final result is given by

$$\int_0^\beta \mathrm{d}\tau\ \langle\hat{A}_\mathrm{D}(\tau)\hat{A}_\mathrm{D}(0)\rangle = \frac{\beta}{Z}\sum_i e^{-\beta E_i}\left|\langle i|\,\hat{A}\,|i\rangle\right|^2 + 2m_{-1} \quad .$$

Thus, the diagonal part in Eq. (121) is the difference between the integral over the monopole operator's correlation function and twice the inverse energy weighted moment, devided by the inverse temperature β. The desired sum-rule is given by

$$m_0 = C_A(0) - \frac{1}{\beta}\left(\int_0^\beta \mathrm{d}\tau\ C_A(\tau) - 2m_{-1}\right) \quad .$$

C Genetic Inversion by Falsification of Theories

In section 5.3, three quite different methods for the reconstruction of a spectral function have been introduced, namely maximum entropy (MEM), stochastic optimization (SOM) and the method of consistent constraints (MCC). Another powerful approach for this problem has been suggested by Vitali et al. [105]: **G**enetic **I**nversion by **F**alsification of **T**heories (GIFT). Like for SOM, the sawtooth instabilitiy is overcome by composing the final spectrum as an average over individual, noisy solutions, $S_k(\omega)$. The new idea is that the $S_k(\omega)$ are not obtained by fitting the Monte Carlo correlation function $G_{\mathrm{MC}}(\tau)$, but a perturbed CF $\tilde{G}_k(\tau)$ where all points can be displaced within the order of the statistical error. Hence, the individual solutions try to overfit differently fluctuating CFs which results in nearly independent sawtooth peaks for each trial spectrum $S_k(\omega)$. It is the aim to include all forms of spectral functions that fit the input CF into the final solution, whereas all other functions are falsified. To find an appropriate trial spectrum for each perturbed CF, $G_k(\tau)$, a genetic algorithm (GA) is used, see e.g. [90]. The latter is well suited to treat a high dimensional optimization problem and, due to the non-local nature of the "reproduction", local minima can efficiently be avoided. In addition, gradient methods tend to find very similar results in each run, whereas GAs are highly probabilistic and likely to deliver different trial spectral functions even for the same input CF. However, a detailed introduction to GAs and the GIFT method itself is beyond the scope of this work and the interested reader is referred to the apendix of [105].

To demonstrate the capabilities of this method the dynamic structure factor $S(q,\omega)$ is considered for a dipole interacting bilayer system. Here, q denotes the momentum of a density fluctuation and the response within a single layer is investigated. To reconstruct this quantity one must compute the density-density CF, see [13] for a detailed introduction. In addition, it is useful to also include additional information about the shape of the spectra, namely all frequency moments $\langle\omega^k\rangle$ that are known from the sum-rule formalism.

In Fig. 86, results for $S(q,\omega)$ are shown for $q = 0.69813172$ both from a SOM implementation by A. Filinov, see the appendix of [13], and the author's GIFT code. Evidently, the reconstructed structure factors are very similar and consist of two pronounced peaks, which are located around the same position and have approximately the same spectral weights. Both solutions are very smooth and do not exhibit any sawtooth noise. However, the exact shape of the peaks does not coincide. Since the exact solution $S(q,\omega)$ is not known, it is not trivial to decide which of the two results is preferable and one must consider the agreement with the given constraints. Both methods fulfill the frequency moments and Fig. 87 shows the difference between the Monte Carlo CF, $G_{\mathrm{MC}}(\tau)$, and the reconstructed data $G(\tau)$ corresponding to the spectra from Fig. 86. The black curves at the top and bottom of the image represent the statistical uncertainty from the PIMC simulation. However, both reconstructed correlation functions match G_{MC} much better than the latter, which means that the errors are overestimated and the true errorbars are not known. The red and blue curve exhibit a qualitatively similar behaviour, but the total deviation measure from the GIFT solution is significantly smaller than the SOM pendant. In particular, there occurs a very large deviation around $\tau = 0.08$ for the latter, whereas the GIFT data deviates from the Monte Carlo CF within the same order everywhere. This lack of systematic deviations in the red curve makes it preferable to the SOM results. However, it should be noted that both presented results for $S(q,\omega)$ and even reconstructed spectra without the inclusion of the frequency moments deliver two peaks around the same position, only the particular shape of the peaks, especially the second one, varies. This means that dispersion relations, which contain the peak positions as a function of q, can be obtained with high accuracy and from ab initio.

In conclusion, the GIFT algorithm is a powerful approach to reconstruct dynamic information

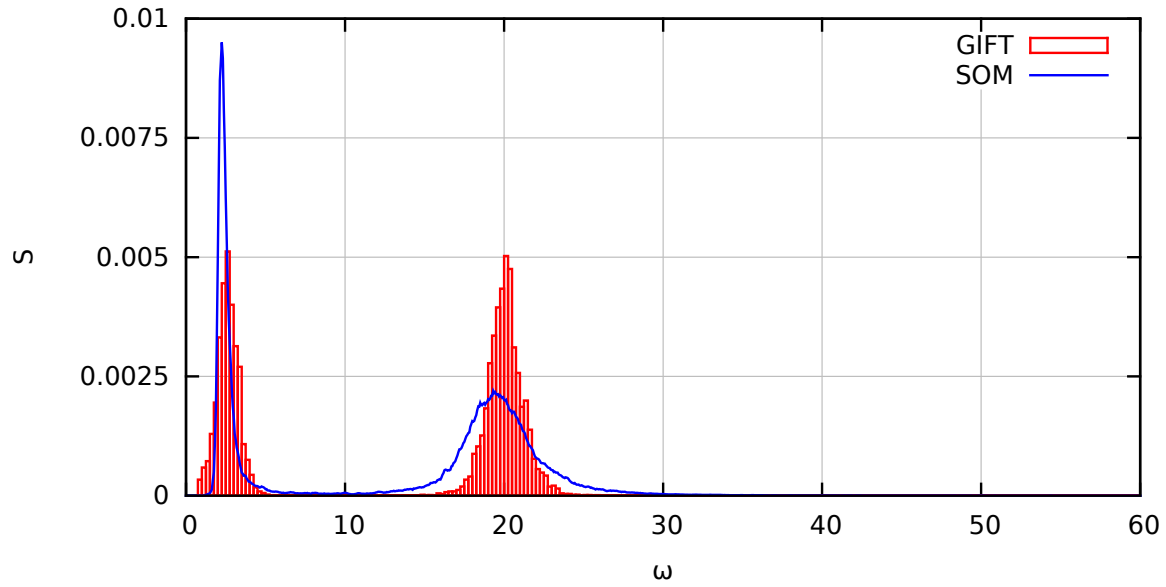

Figure 86: ***Dynamic structure factor of a bilayer system:*** The intra-layer dynamic structure factor $S(q, \omega)$ is plotted over the frequency ω for a bilayer system with dipole interaction. The red curve corresponds to the author's GIFT implementation and the blue curve has been obtained with SOM by A. Filinov.

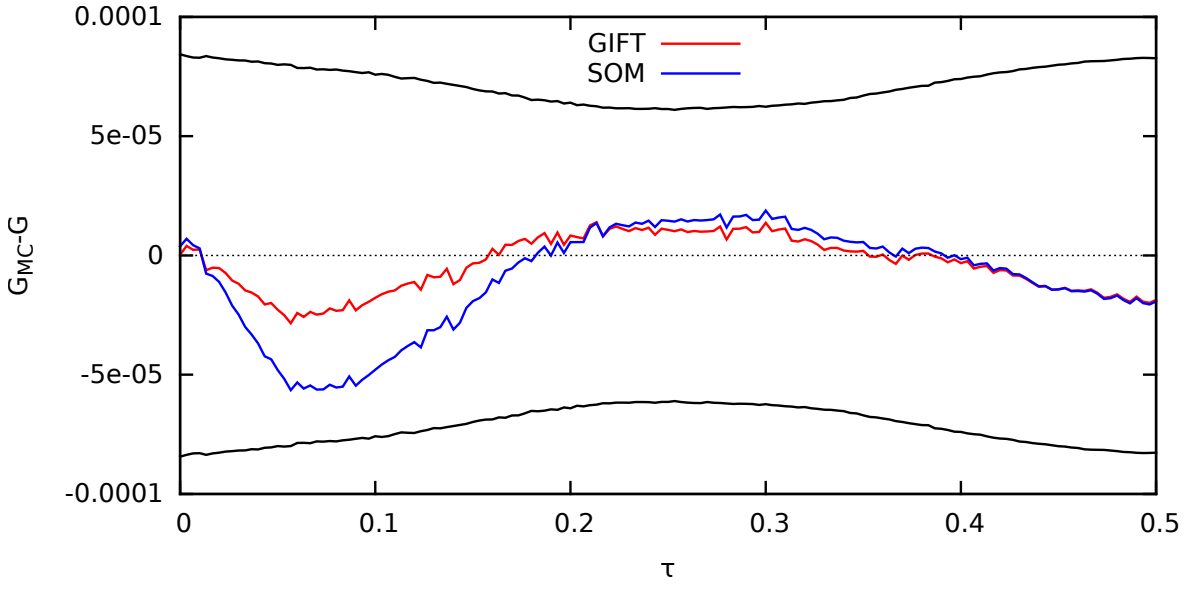

Figure 87: ***Deviation from the Monte-Carlo correlation function:*** The difference between the MC and reconstructed CF, $G_{\mathrm{MC}} - G$, is plotted over the imaginary time τ for the structure factor from Fig. 86. The Monte Carlo data for the density CF has been provided by A. Filinov.

solely from equilibrium information. Contemporary applications include the investigation of the excitation spectrum of a supersolid [107] and the coupling dependence of a many-body system of hard-sphere bosons [108]. However, the reconstruction of the breathing mode spectrum remains out of reach.

References

[1] L. Pareschi and G. Toscani. *Interacting Multiagent Systems: Kinetic Equations and Monte Carlo Methods*. OUP Oxford, 2013. ISBN 9780199655465. 1

[2] C. J. Mode. *Applications of Monte Carlo Methods in Biology, Medicine and other Fields of Science*. intechopen, 2011. ISBN 978-953-307-427-6. 1

[3] M. Morales, R. Clay, C. Pierleoni, and D. Ceperley. *Entropy*, **16**:287–321, 2013. 1

[4] P. Nightingale and C.J. Umrigar. *Quantum Monte Carlo Methods in Physics and Chemistry*. NATO ASI series: Mathematical and physical sciences. Springer, 1998. ISBN 9780792355526. 1

[5] D. M. Ceperley. *Rev. Mod. Phys.*, **67**:279–355, 1995. 1, 11, 21

[6] N. Metropolis, A. W. Rosenbluth, M. N. Rosenbluth, A. H. Teller, and E. Teller. *J. Chem. Phys.*, **21**:1087–1092, 1953. 1, 6, 10

[7] E. Y. Loh, J. E. Gubernatis, R. T. Scalettar, S. R. White, D. J. Scalapino, and R. L. Sugar. *Phys. Rev. B*, **41**:9301–9307, 1990. 1, 8, 97

[8] M. Boninsegni, N. V. Prokof'Ev, and B. V. Svistunov. *Phys. Rev. E*, **74**(3):036701, 2006. 1, 10, 11, 16

[9] F. Dalfovo, S. Giorgini, L. P. Pitaevskii, and S. Stringari. *Rev. Mod. Phys.*, **71**:463–512, 1999. 1, 41

[10] J. W. Abraham and M. Bonitz. *Contrib. Plasma Phys.*, **54**:27–99, 2014. 1, 63, 76, 77, 78, 79, 83, 85, 96, 103, 116

[11] H. Thomsen, J. Schablinski, and M. Bonitz, 2014. *Phase Transitions in Dusty Plasmas*, in *Complex Plasmas: Scientific Challenges and Technological Opportunities*. M. Bonitz, J. Lopez, K. Becker and H. Thomsen (editors). Springer Series on Atomic, Optical, and Plasma Physics. Springer International Publishing. ISBN 9783319054360. 1, 2, 55, 111

[12] Jan Willem Abraham, Michael Bonitz, Chris McDonald, Gianfranco Orlando, and Thomas Brabec. *New J. Phys.*, **16**(1):013001, 2014. 1, 63, 69, 71

[13] A. Filinov and M. Bonitz. *Phys. Rev. A*, **86**(4):043628, 2012. 1, 12, 30, 63, 86, 91, 122

[14] T. Schoof, M. Bonitz, A. Filinov, D. Hochstuhl, and J. W. Dufty. *Contrib. Plasma Phys.*, **51**:687–697, 2011. 1, 2, 104, 111

[15] S. Giorgini, L. P. Pitaevskii, and S. Stringari. *Rev. Mod. Phys.*, **80**:1215–1274, 2008. 1, 97

[16] I. Bloch, J. Dalibard, and W. Zwerger. *Rev. Mod. Phys.*, **80**:885–964, 2008. 1

[17] S. M. Reimann and M. Manninen. *Rev. Mod. Phys.*, **74**:1283–1342, 2002. 1

[18] P. Ludwig. *Structure formation in strongly correlated few-particle systems in traps*. PhD thesis, 2008. 1, 41

[19] C. J. Pethick, N. Chamel, and Sanjay Reddy. *Prog. Theor. Phys. Suppl.*, **186**:9–16, 2010. 1

[20] N. Chamel. *Phys. Rev. Lett.*, **110**:011101, 2013. 1

[21] Gregory Gabadadze and Rachel A Rosen. *J. Cosmol. Astropart. Phys.*, **2008**(10):030, 2008. 1

[22] Paulo F. Bedaque, Evan Berkowitz, and Srimoyee Sen. *Phys. Rev. D*, **89**:045010, 2014. 1

[23] W. Nolting. *Grundkurs Theoretische Physik 6: Statistische Physik*. Grundkurs Theoretische Physik / Wolfgang Nolting. Springer, 2007. ISBN 9783540688709. 3, 11

[24] M. Bonitz and D. Semkat. *Introduction to Computational Methods in Many Body Physics*. Rinton Press, 2006. ISBN 9781589490093. 3, 33

[25] J. Campbell. *Proc. Lond. Math. Soc.*, **28**:381–390, 1898. 4

[26] R.P. Feynman and A.R. Hibbs. *Quantum Mechanics and Path Integrals: Emended Edition*. Dover Publications, Incorporated, 2012. ISBN 9780486134635. 4

[27] H. F. Trotter. *Proc. Am. Math. Soc.*, **10**:545–551, 1959. 4

[28] A. Filinov and M. Bonitz, 2006. *Classical and Quantum Monte-Carlo*, in *Introduction to Computational Methods in Many Body Physics*. M. Bonitz, and D. Semkat (editors). Rinton Press. ISBN 9781589490093. 6, 8, 10, 24

[29] L. de Broglie. *Recherches sur la théorie des quanta*. PhD thesis, 1925. 6

[30] P.A.M. Dirac. *The Principles of Quantum Mechanics*. Igal Meirovich, 2013. ISBN 9781607965602. 7

[31] D. Chandler and P. G. Wolynes. *J. Chem. Phys.*, **74**:4078–4095, 1981. 7

[32] K. Sakkos, J. Boronat, and J. Casulleras. Higher-order actions for path integral monte carlo, 2005. URL `http://simcon.upc.edu/topics/qm/activities/chinfest/boronat.pdf`. 7

[33] S. A. Chin. *Phys. Lett. A*, **226**:344–348, 1997. 8

[34] K. Sakkos, J. Casulleras, and J. Boronat. *J. Chem. Phys.*, **130**(20):204109, 2009. 8, 29

[35] P. Sindzingre, M. L. Klein, and D. M. Ceperley. *Phys. Rev. Lett.*, **63**:1601–1604, 1989. 10, 43

[36] L. Brualla i Barbera. *Path integral Monte Carlo, Algorithms and applications to quantum fluids*. PhD thesis, 2002. 11

[37] S. Wessel, F. Alet, M. Troyer, and G. G. Batrouni. *Phys. Rev. A*, **70**(5):053615, 2004. 11

[38] K. Binder and D. Heermann. *Monte Carlo Simulation in Statistical Physics: An Introduction*. Graduate Texts in Physics. Springer-Verlag, 2010. ISBN 9783642031632. 11

[39] P.R. Surjan. *Second Quantized Approach to Quantum Chemistry: An Elementary Introduction*. Springer London, Limited, 2011. ISBN 9783642747571. 12, 104

[40] A. Filinov, J. Böning, and M. Bonitz. In H. Fehske, R. Schneider, and A. Weiße, editors, *Computational Many-Particle Physics*, volume **739** of *Lecture Notes in Physics, Berlin Springer Verlag*, page 397, 2008. 15

[41] W. Janke and T. Sauer. *J. Chem. Phys.*, **107**:5821–5839, 1997. 24

[42] W. Janke. *Quantum simulations of Complex Many-Body Systems: From Theory to Algorithms*. John von Neumann Institute for Computing, FZ Jülich, 2002. ISBN 3000090576. 25

[43] J. Pitt-Francis and J. Whiteley. *Guide to Scientific Computing in C++*. Undergraduate Topics in Computer Science. Springer, 2012. ISBN 9781447127352. 27

[44] W.H. Press. *Numerical Recipes in C: The Art of Scientific Computing*. Number bk. 4 in Numerical recipes in C : the art of scientific computing / William H. Press. Cambridge University Press, 1992. ISBN 9780521437202. 33

[45] Stephan T. Lavavej. rand() considered harmfull, 2013. URL `http://sdrv.ms/1e11LXl`. 33

[46] Makoto Matsumoto and Takuji Nishimura. *ACM Trans. Model. Comput. Simul.*, **8**(1): 3–30, 1998. 33

[47] N.V. Prokof'ev, B.V. Svistunov, and I.S. Tupitsyn. *J. Exp. Theor. Phys.*, **87**(2):310–321, 1998. 35

[48] D. Bhattacharya and A. Ghosal. *Eur. Phys. J. B*, **86**:499, 2013. 39

[49] Louisa M. Fraser, W. M. C. Foulkes, G. Rajagopal, R. J. Needs, S. D. Kenny, and A. J. Williamson. *Phys. Rev. B*, **53**:1814–1832, 1996. 40

[50] A. Filinov, J. Böning, M. Bonitz, and Y. Lozovik. *Phys. Rev. B*, **77**(21):214527, 2008. 41, 47, 62, 113

[51] M. Boninsegni. *Phys. Rev. A*, **87**(6):063604, 2013. 41

[52] F. London. *Superfluids: Macroscopic theory of superfluid hellium*. Structure of matter series. Wiley, 1954. 41

[53] R. P. Feynman. *Rev. Mod. Phys.*, **29**:205–212, 1957. 41

[54] A. J. Leggett. *Rev. Mod. Phys.*, **71**:S318–S323, 1999. 41

[55] Yu Shi. *Phys. Rev. B*, **72**:014533, 2005. 41, 43

[56] Y. Kwon, F. Paesani, and K. B. Whaley. *Phys. Rev. B*, **74**(17):174522, 2006. 41, 47

[57] L. Landau. *Phys. Rev.*, **60**:356–358, 1941. 41, 49

[58] V. I. Yukalov. *Phys. Part. Nucl.*, **42**:460–513, 2011. 43

[59] J. Böning. Superfluidity in mesoscopic systems of charged bosons, 2007. Diploma thesis. 43

[60] T. Dornheim, A. Filinov, and M. Bonitz, 2014. submitted to Phys. Rev. A, arXiv-eprint 1410.0878. 44, 47, 48, 51, 111

[61] A. V. Filinov, M. Bonitz, and Y. E. Lozovik. *Phys. Rev. Lett.*, **86**:3851–3854, 2001. 44, 62, 97

[62] S. A. Khairallah, M. B. Sevryuk, D. M. Ceperley, and J. P. Toennies. *Phys. Rev. Lett.*, **98**:183401, 2007. 47, 62

[63] Fabio Mezzacapo and Massimo Boninsegni. *Phys. Rev. Lett.*, **100**:145301, 2008. 47

[64] Saheed Idowu and Massimo Boninsegni. *J. Chem. Phys.*, **140**(20):204310, 2014. 47, 62

[65] B. Kulchytskyy, G. Gervais, and A. Del Maestro. *Phys. Rev. B*, **88**:064512, 2013. 49

[66] H. Kählert and M. Bonitz. *Phys. Rev. Lett.*, **104**:015001, 2010. 51

[67] M. Boninsegni and N. V. Prokof'ev. *Rev. Mod. Phys.*, **84**:759–776, 2012. 62

[68] J. Böning, A. Filinov, P. Ludwig, H. Baumgartner, M. Bonitz, and Y. E. Lozovik. *Phys. Rev. Lett.*, **100**(11):113401, 2008. 62

[69] H. Thomsen and M. Bonitz. In preparation, 2014. 62

[70] R.M. Gray. *Entropy and Information Theory*. SpringerLink : Bücher. Springer, 2011. ISBN 9781441979704. 62

[71] C. R. McDonald, G. Orlando, J. W. Abraham, D. Hochstuhl, M. Bonitz, and T. Brabec. *Phys. Rev. Lett.*, **111**(25):256801, 2013. 63

[72] S. Bauch, K. Balzer, C. Henning, and M. Bonitz. *Phys. Rev. B*, **80**(5):054515, 2009. 63, 70

[73] S. Bauch, D. Hochstuhl, K. Balzer, and M. Bonitz. *JPC*, **220**(1):012013, 2010. 63

[74] J. W. Abraham, K. Balzer, D. Hochstuhl, and M. Bonitz. *Phys. Rev. B*, **86**(12):125112, 2012. 63

[75] R. Schmitz, S. Krönke, L. Cao, and P. Schmelcher. *Phys. Rev. A*, **88**(4):043601, 2013. 63

[76] S. Stringari. *Phys. Lett. B*, **108**:232–236, 1982. 63

[77] R.A. Jishi. *Feynman Diagram Techniques in Condensed Matter Physics*. Cambridge University Press, 2013. ISBN 9781107355125. 64, 67

[78] W. Nolting and William D. Brewer. *Fundamentals of Many-body Physics: Principles and Methods*. Springer, 2009. ISBN 9783540719304. 64

[79] M. Herold. Sum-rule approach for collective excitations of ultracold quantum gases, 2012. Bachelor thesis. 64, 69, 116, 118

[80] I. Prigogine and S.A. Rice. *Advances in Chemical Physics, New Methods in Computational Quantum Mechanics*. Advances in Chemical Physics. Wiley, 2009. ISBN 9780470142059. 68

[81] R Kubo. *Rep. Prog. Phys.*, **29**(1):255, 1966. 69

[82] M. Jarrell. *The Maximum Entropy Method, Analytic Continuation of QMC Data*, volume **2** of *Modeling and Simulations*. FZ Juelich, 2012. ISBN 978-3-89336-796-2. 89

[83] Mr. Bayes and Mr. Price. *Philosophical Transactions*, **53**:370–418, 1763. 89

[84] M. Boninsegni and D. M. Ceperley. *J. Low Temp. Phys.*, **104**:339–357, 1996. 89

[85] A. Dirks, J. E. Han, M. Jarrell, and T. Pruschke. *Phys. Rev. B*, **87**(23):235140, 2013. 89

[86] A. S. Mishchenko, N. V. Prokof'ev, A. Sakamoto, and B. V. Svistunov. *Phys. Rev. B*, **62**: 6317–6336, 2000. 90, 91

[87] A. Mishchenko. *Stochastic Optimization Method for Analytic Continuation*, volume **2** of *Modeling and Simulations*. FZ Juelich, 2012. ISBN 978-3-89336-796-2. 90, 91, 94, 95

[88] N.V. Prokof'ev and B.V. Svistunov. *JETP Letters*, **97**(11):649–653, 2013. 91, 92

[89] L.M. Adams, J.L. Nazareth, A.M. Society, I.M. Statistics, and S.I.A. Mathematics. *Linear and Nonlinear Conjugate Gradient-related Methods*. Proceedings in Applied Mathematics Series. Society for Industrial and Applied Mathematics, 1996. ISBN 9780898713763. 92

[90] D.E. Goldberg. *Genetic Algorithms in Search, Optimization, and Machine Learning*. Artificial Intelligence. Addison-Wesley, 1989. ISBN 9780201157673. 92, 122

[91] M. Troyer and U.-J. Wiese. *Phys. Rev. Lett.*, **94**(17):170201, 2005. 97

[92] N. Hatano. *J. Phys. Soc. Jpn.*, **63**:1691, 1994. 97

[93] A. Szabo and N.S. Ostlund. *Modern Quantum Chemistry: Introduction to Advanced Electronic Structure Theory*. Dover Books on Chemistry. Dover Publications, 2012. ISBN 9780486134598. 98

[94] David Hochstuhl. *Multiconfiguration methods for the numerical simulation of photoionization processes of many-electron atoms*. PhD thesis, 2013. 98

[95] R. P. Feynman. *Int. J. Theor. Phys.*, **21**:467–488, 1982. 104

[96] J. Stolze and D. Suter. *Quantum Computing: A Short Course from Theory to Experiment*. Wiley, 2008. ISBN 9783527617777. 104

[97] K. Temme, T. J. Osborne, K. G. Vollbrecht, D. Poulin, and F. Verstraete. *Nature*, **471**: 87–90, 2011. 104

[98] T. Monz, P. Schindler, J. T. Barreiro, M. Chwalla, D. Nigg, W. A. Coish, M. Harlander, W. Hänsel, M. Hennrich, and R. Blatt. *Phys. Rev. Lett.*, **106**(13):130506, 2011. 104

[99] D.M. Ceperley. *J. Stat. Phys.*, **63**(5-6):1237–1267, 1991. 104

[100] V. Filinov. *J. Phys. A: Math. Gen.*, **34**:1665–1677, 2001. 104

[101] V. S. Filinov. *ArXiv e-prints*, art. 1304.0216, 2013. 104

[102] M. Takahashi and M. Imada. *J. Phys. Soc. Jpn.*, **53**:963, 1984. 104

[103] V. S. Filinov, M. Bonitz, W. Ebeling, and V. E. Fortov. *Plasma Phys. Contr. Fusion*, **43**: 743–759, 2001. 104

[104] Simon Groth. Strongly Degenerate Nonideal Fermi Systems: Configuration PIMC Simulation, 2014. Master thesis. 104, 105, 106

[105] E. Vitali, M. Rossi, L. Reatto, and D. E. Galli. *Phys. Rev. B*, **82**:174510, 2010. 112, 122

[106] W. Greiner. *Quantenmechanik: Einführung*. Theoretische Physik. Deutsch, 2005. ISBN 9783817117659. 118

[107] S. Saccani, S. Moroni, and M. Boninsegni. *Phys. Rev. Lett.*, **108**:175301, 2012. 124

[108] R. Rota, F. Tramonto, D. E. Galli, and S. Giorgini. *JPC*, **529**(1):012022, 2014. 124

Acknowledgements

It is a great pleasure to acknowledge all the personal and subject-specific support which has made this work possible.

First of all, I want to thank Prof. Dr. Michael Bonitz for giving me the opportunity to devote my thesis to this interesting topic. During various lectures he got me interested into theoretical physics and, despite a close schedule, always made time for his students. While giving me every freedom to pursue my own research interests, he provided feedback and thought-provoking impulses on short-term.

Further, I am grateful to Priv.-Doz. Dr. Alexei Filinov who introduced me to the broad topic of Monte Carlo simulations. The incredible amount of time that he has devoted to discussions about PIMC, but also the problem of reconstruction, is something special and has significantly improved my understanding of those topics.

My sincerest gratitude goes to Niclas Schlünzen for his friendship during many lectures and practica of the master study, and for proofreading this work. I also thank the entire group and, in particular, my Monte-Carlo-enthusiastic office colleagues Simon Groth and Tim Schoof for a great working climate and many interesting and stimulating discussions. In addition, I am grateful to Simon for his proofreading.

Finally, I want to thank my parents Susanne and Andreas Dornheim for their tremendous support during my study. Without their help, I could not have pursued this degree.

Erklärung

Die vorliegende Arbeit ist von mir selbständig und nur unter Zuhilfenahme der angegebenen Quellen und Hilfsmittel angefertigt worden.

Ort und Datum	Unterschrift